Enhancing laser-induced X-ray emission and ion acceleration with microstructured targets

Zur Erlangung des Grades eines Doktors der Naturwissenschaften (Dr. rer. nat.)
Genehmigte Dissertation von Tina Ebert aus Alsfeld
Tag der Einreichung: 01. Oktober 2021, Tag der Prüfung: 08. November 2021

1. Gutachten: Prof. Dr. Markus Roth
2. Gutachten: Prof. Dr. Oliver Boine-Frankenheim
Darmstadt – D17

TECHNISCHE
UNIVERSITÄT
DARMSTADT

Physics Department
Institut für Kernphysik
Laser- und Plasmaphysik

Enhancing laser-induced X-ray emission and ion acceleration with microstructured targets

Accepted doctoral thesis by Tina Ebert

1. Review: Prof. Dr. Markus Roth
2. Review: Prof. Dr. Oliver Boine-Frankenheim

Date of submission: 01. Oktober 2021
Date of thesis defense: 08. November 2021

Darmstadt – D17

Erklärungen laut Promotionsordnung

§8 Abs. 1 lit. c PromO

Ich versichere hiermit, dass die elektronische Version meiner Dissertation mit der schriftlichen Version übereinstimmt.

§8 Abs. 1 lit. d PromO

Ich versichere hiermit, dass zu einem vorherigen Zeitpunkt noch keine Promotion versucht wurde. In diesem Fall sind nähere Angaben über Zeitpunkt, Hochschule, Dissertationsthema und Ergebnis dieses Versuchs mitzuteilen.

§9 Abs. 1 PromO

Ich versichere hiermit, dass die vorliegende Dissertation selbstständig und nur unter Verwendung der angegebenen Quellen verfasst wurde.

§9 Abs. 2 PromO

Die Arbeit hat bisher noch nicht zu Prüfungszwecken gedient.

Darmstadt, 01. Oktober 2021

Tina Ebert

Abstract

The irradiation of thin, solid foils with a high intensity laser leads to the heating of electrons, which in turn, among other things, generate characteristic X-ray line emission and strong electrostatic fields that can accelerate ions. The induced radiation and particle yield can be enhanced by increasing the energy transfer from the laser to the hot electrons. Potential applications of these laser-induced secondary sources range from non-destructive imaging via proton or X-ray radiography, to the ignition of inertial confinement capsules by focused ion beams, to the generation of directed neutron pulses.

This thesis investigates targets with microstructured front surfaces to enhance the laser matter coupling. In previous studies, targets with micro-engineered surfaces have shown great potential in improving the energy transfer, as they can affect the relevant heating mechanisms, introduce guiding effects and increase the interaction volume and time. Much effort has been spent on investigating fragile structures such as nanowires, however, since these structures are only suited to laser systems with ultrahigh contrast and pulse lengths in the tens of femtoseconds range, high energy lasers with longer pulse lengths call for more durable microstructures. Therefore, in this thesis the surfaces of flat silicon wafers are modified with conical, spike-like microstructures in a randomly distributed, dense array. The structures are produced via ultrashort laser pulse processing. For this, an experimental setup was designed, which allows to create a wide range of spike geometries by changing the processing parameters, including the parameters of the femtosecond laser, the processing medium as well as the target material. In addition, a replication procedure based on molding with polydimethylsiloxane (PDMS) was developed. It enables the fabrication of a master target mold, which is subsequently used to create identical microstructures out of other materials such as polystyrene and copper.

The fabricated targets were studied in experimental campaigns at the PHELIX laser at the GSI Helmholtzzentrum für Schwerionenforschung, Darmstadt, Germany, and the Omega EP laser at the Laboratory for Laser Energetics (LLE), Rochester, NY, USA, with varied laser contrasts, intensities, and pulse lengths. Both laser systems deliver pulse energies above 100 J at pulse lengths exceeding 0.5 ps, thereby fulfilling a main requisite for the generation of powerful radiation and particle sources. The laser-induced X-ray generation and ion acceleration with the microstructured targets was evaluated in comparison to flat foils. In addition to the experiments, complementary 2D particle-in-cell (PIC) simulations were performed to study the impact of the microspikes on the electron heating processes, optimize the target parameters and validate the experimental findings.

The microstructured targets showed both an enhancement of the accelerated proton numbers and their maximum energies. In particular, matching the structures tilt angle to the laser incidence angle resulted in a 40% increase of the maximum energy compared to structures with a relative angle of 30°, which was observed both experimentally and in corresponding simulations. Furthermore, the silicon targets with a microstructured surface generated an up to 13 times stronger He_α emission and a 12 times stronger Ly_α line compared to a flat target at a laser pulse length of 1 ps. The benefit decreases with increasing pulse length, but even at the longest investigated pulse length of 20 ps they showed an enhancement for both lines. In contrast to alternative target types such as foam targets or targets with an attached shield, the presented microspikes generate a well-defined X-ray pulse with a rapidly decaying slope. Using PIC simulations, the importance of target geometry optimization to further enhance the performance is demonstrated and the spiked targets are compared to another microstructure type, namely micropillars, in terms of their ion acceleration efficiency. The results presented in this thesis highlight the potential of microstructured targets for enhancing laser-induced secondary sources.

Zusammenfassung

Die Bestrahlung dünner Folien mit einem Hochintensitäts-Laser führt zur Erzeugung von heißen Elektronen, die anschließend unter anderem charakteristische Röntgenstrahlung produzieren sowie starke elektrostatische Felder hervorrufen, welche ihrerseits Ionen beschleunigen können. Die Strahlungs- und Teilchenausbeute kann dabei durch eine Optimierung des Energietransfers zwischen Laser und Elektronen erhöht werden. Mögliche Anwendungen solcher laserinduzierten Sekundärquellen reichen von zerstörungsfreier Bildgebung mittels Protonen- oder Röntgenradiographie über die Zündung von Trägheitsfusionskapseln durch fokussierte Ionenstrahlen bis hin zur Erzeugung gerichteter Neutronenpulse.

Diese Arbeit widmet sich der Untersuchung mikrostrukturierter Targets zur Verbesserung der Laser-Materie-Kopplung. In vorhergehenden Studien hat die Mikrostrukturierung von Targetoberflächen großes Potenzial zur Steigerung des Energietransfers gezeigt, da dadurch relevante Heizmechanismen beeinflusst und sowohl das Wechselwirkungsvolumen als auch die -zeit vergrößert werden können. Eine typische Strukturart sind sogenannte Nanodrähte. Diese fragilen Strukturen sind jedoch vor allem für Lasersysteme mit ultrahohem Kontrast und Pulslängen im Femtosekundenbereich geeignet, weshalb für Hochenergielaser mit längeren Pulsdauern beständigere Mikrostrukturen benötigt werden. In dieser Arbeit werden hierfür kegelförmige, nadelartige Mikrostrukturen durch ultrakurze Laserpulse auf polierten Silizium-Wafern erzeugt, was zu einer dichten Anordnung der Strukturen mit zufälliger Verteilung führt. Dazu wurde ein Versuchsaufbau konzipiert, mit dem eine große Bandbreite von Nadelgeometrien erzeugt werden kann, indem die Bearbeitungsgsparameter eingestellt werden. Dazu zählen u.a. die Eigenschaften des Femtosekundenlasers, das Umgebungsmedium und das Targetmaterial. Darüber hinaus wurde ein Replikationsverfahren entwickelt, welches auf der Abformung mit Polydimethylsiloxan (PDMS) basiert. Der Prozess ermöglicht die Herstellung einer Master-Form, mit dem identische Kopien der Mikrostrukturen aus anderen Materialien wie Polystyrol und Kupfer fabriziert werden können.

Die hergestellten Targets wurden anschließend in experimentellen Kampagnen am PHELIX-Laser am GSI Helmholtzzentrum für Schwerionenforschung, Darmstadt, Deutschland, und am Omega EP-Laser am Laboratory for Laser Energetics (LLE), Rochester, NY, USA, mit unterschiedlichen Laserkontrasten, -intensitäten und -pulslängen untersucht. Beide Lasersysteme liefern Pulsenergien von über 100 J bei Pulslängen von mehr als 0,5 ps und erfüllen damit eine wichtige Voraussetzung für die Erzeugung leistungsstarker Strahlungs- und Teilchenquellen. Die mikrostrukturierten Targets wurden bezüglich der Erzeugung von Röntgenstrahlung und der Beschleunigung von Ionen mit flachen Folien verglichen. Ergänzend zu den Experimenten wurden 2D Particle-in-Cell (PIC) Simulationen durchgeführt, um den Einfluss der Mikro-Nadeln auf die Elektronenheizprozesse zu untersuchen, die Targetparameter zu optimieren und die experimentellen Ergebnisse zu validieren.

Die mikrostrukturierten Targets zeigten sowohl eine erhöhte Anzahl als auch Maximalenergie der beschleunigten Protonen. Insbesondere durch die Anpassung des Neigungswinkels der Strukturen an den Einfallswinkel des Lasers wurde eine Steigerung der Maximalenergie um 40 % im Vergleich zu Strukturen mit einem relativen Winkel von 30° in den Experimenten und den korrespondierenden Simulationen beobachtet. Darüber hinaus erzeugten die mikrostrukturierten Siliziumtargets bei einer Laserpulslänge von 1 ps eine bis zu 13-mal stärkere He_α-Emission und eine 12-mal stärkere Ly_α-Linie im Vergleich zu einem flachen Target. Mit längeren Pulslängen nimmt der Einfluss der Strukturen ab, aber auch bei der längsten gemessenen Pulslänge von 20 ps zeigte sich eine Intensitätssteigerung beider Linien. Im Gegensatz zu alternativen Targettypen, wie z.B. Schaumtargets oder Targets mit zusätzlichem

Schirm, erzeugen die hier vorgestellten Nadeln einen Röntgenpuls mit definierter Länge und einer kurzen Abklingflanke. Mithilfe der PIC-Simulationen wurde zudem gezeigt, welche Bedeutung die Optimierung der Targetgeometrie für eine weitere Verbesserung des Röntgen- und Teilchenertrags hat. Außerdem wurden die Nadeltargets mit einem anderen typischen Mikrostrukturtyp, den Mikrosäulen, bezüglich ihrer Wirksamkeit für die Protonenbeschleunigung verglichen. Die Ergebnisse, die in dieser Arbeit präsentiert werden, verdeutlichen das Potential mikrostrukturierter Targets für die Verbesserung von laserinduzierten Sekundärquellen.

Contents

Abbreviations

AR	Anti-Reflection	p. 45
ASE	Amplified Spontaneous Emission	p. 4
BSI	Barrier Suppression Ionization	p. 5
CFL	Courant-Friedrich-Lewy	p. 37
CPA	Chirped Pulse Amplification	p. 3
EMP	ElectroMagnetic Pulse	p. 26
FDTD	Finite Difference Time Domain	p. 39
FSS	Front Surface Structure	p. 23
FWHM	Full Width at Half Maximum	p. 43
GSI	Gesellschaft für SchwerIonenforschung (Darmstadt, Germany)	p. v
HED	High Energy Density	p. 1
HPC	High-Performance Computing	p. 75
HSFL	High Spatial Frequency LIPSS	p. 15
ICF	Inertial Confinement Fusion	p. 1
IP	Image Plate	p. 28
KAP	Potassium Hydrogen Phthalate	p. 34
LIPSS	Laser Induced Periodic Surface Structure	p. xiii
LLE	Laboratory for Laser Energetics (Rochester, NY, USA)	p. v
LSFL	Low Spatial Frequency LIPSS	p. 15
LTE	Local Thermal Equilibrium	p. 6
MCP	Multi-Channel-Plate	p. 27
MPI	Multi-Photon Ionization	p. 5
PDMS	PolyDiMethylSiloxane	p. 41
PHELIX	Petawatt High-Energy Laser for Heavy-Ion eXperiments	p. v
PIC	Particle-In-Cell	p. vii
PMMA	PolyMethyl MethAcrylate	p. 54
PS	PolyStyrene	p. 53
PSL	PhotoStimulated Luminescence	p. 28
PU	PolyUrethane	p. 54
RAL	Rutherford Appleton Laboratory (Didcot, UK)	p. 2
RCF	RadioChromic Film	p. 31
SDF	Self-Describing Format	p. 76
SEM	Scanning Electron Microscope	p. 15

TI	Tunnel Ionization	p. 5
TNSA	Target Normal Sheath Acceleration	p. 1
UFXRS	UltraFast X-Ray Spectrometer	p. 61
XRS	X-Ray Spectrometer	p. 61

Symbols and constants

Symbols

A_{spot}	focal spot size	m^2
a_0	laser field amplitude	-
B_0	magnetic field amplitude	T
$\boldsymbol{B}$	magnetic field	T
γ	relativistic Lorentz factor	-
γ_{K}	Keldysh parameter	-
c_s	sound speed	$\mathrm{m\,s^{-1}}$
E_0	electric field amplitude	$\mathrm{V\,m^{-1}}$
$\boldsymbol{E}$	electric field	$\mathrm{V\,m^{-1}}$
$\mathcal{E}_{\mathrm{ion}}$	ionization energy	J or eV
$\mathcal{E}_{\mathrm{p,max}}$	maximum proton (cut-off) energy	J or eV
$\mathcal{E}_{\mathrm{ph}}$	photon energy	J or eV
$\mathcal{E}_{\mathrm{e}}$	electron energy	J or eV
E_{L}	laser electric field strength	$\mathrm{V\,m^{-1}}$
$\mathcal{E}_{\mathrm{L}}$	laser pulse energy	J
$\mathcal{E}_{\mathrm{osc}}$	electron oscillation energy	J or eV
$e_{\mathrm{x}}, e_{\mathrm{y}}, e_{\mathrm{z}}$	cartesian unit vectors	m
$\boldsymbol{F}_{\mathrm{B}}$	magnetic force	$\mathrm{kg\,m\,s^{-2}}$
$\boldsymbol{F}_{\mathrm{E}}$	electric force	$\mathrm{kg\,m\,s^{-2}}$
$\boldsymbol{F}_{\mathrm{L}}$	Lorentz force	$\mathrm{kg\,m\,s^{-2}}$
f_{p}	ponderomotive force	$\mathrm{kg\,m\,s^{-2}}$
I_{L}	laser pulse intensity	$\mathrm{W\,cm^{-2}}$
I_{TI}	tunnel ionization intensity	$\mathrm{W\,cm^{-2}}$
$\boldsymbol{j}$	charge current	$\mathrm{C\,m\,s^{-1}}$
$\boldsymbol{k}$	laser wave vector	$\mathrm{m^{-1}}$
L	plasma scale length	m
Λ	plasma parameter	-
λ_{L}	laser wavelength	m
λ_{γ}	photon wavelength	m
λ_{D}	Debye length	m
λ_{LIPSS}	wavelength of LIPSS	m
l_{s}	skin depth	m

m_i	ion mass	kg
η	plasma refraction index	-
n_c	critical density	m^{-3}
n_e	electron number density	m^{-3}
n_i	ion number density	m^{-3}
ω_L	laser frequency	s^{-1}
ω_p	plasma frequency	s^{-1}
$\boldsymbol{p}$	momentum vector	$\mathrm{kg\,m\,s}^{-1}$
Φ_pond	ponderomotive potential	$\mathrm{C}^2\,\mathrm{V}^2\,\mathrm{s\,kg}^{-1}\,\mathrm{m}^{-2}$
q	particle charge	C
R	crystal reflectivity	-
$\boldsymbol{r}$	position vector	m
ρ_c	charge density	$\mathrm{C\,m}^{-3}$
ρ_m	mass density	$\mathrm{g\,m}^{-3}$
$\boldsymbol{S}$	poynting vector	$\mathrm{W\,m}^{-2}$
t	time	s
θ	laser incidence angle	°
τ_L	laser pulse length	s
t_acc	TNSA acceleration time	s
θ_B	Bragg angle	°
T_e	electron temperature	K or eV
T_i	ion temperature	K or eV
$\boldsymbol{v}_\mathrm{e}$	electron velocity	$\mathrm{m\,s}^{-1}$
v_drift	electron drift velocity	$\mathrm{m\,s}^{-1}$
v_osc	electron quiver velocity	$\mathrm{m\,s}^{-1}$
x, y, z	cartesian coordinates	m
Z	ion charge number	-
z_R	Rayleigh length	m
Z_eff	effective ion charge number	-

Constants

a_B	Bohr radius	$5.292\times10^{-11}\,\mathrm{m}$
$\hbar$	Planck constant	$6.626\times10^{-34}\,\mathrm{m}^2\,\mathrm{kg\,s}^{-1}$
c	speed of light	$2.998\times10^{8}\,\mathrm{m\,s}^{-1}$
e	electron charge	$1.602\times10^{-19}\,\mathrm{C}$
ϵ_0	vacuum permittivity	$8.854\times10^{-12}\,\mathrm{A\,s\,V}^{-1}\,\mathrm{m}^{-1}$
E_a	atomic field strength	$1.602\times10^{-19}\,\mathrm{C}$
I_a	atomic intensity	$5.1\times10^{9}\,\mathrm{V\,m}^{-1}$
k_B	Boltzmann constant	$1.381\times10^{-23}\,\mathrm{m}^2\,\mathrm{kg\,m}^{-2}\,\mathrm{K}^{-1}$
m_e	electron mass	$9.109\times10^{-31}\,\mathrm{kg}$

1. Introduction

The interaction of a high energy, short pulsed laser with matter is a complex field of research, which combines the concepts and methods of several areas, including laser, plasma and atomic physics. The involved processes and outputs resulting from such an interaction depend on the laser parameters and the target properties, which range from electron excitation and relaxation without any permanent changes of the target, to plasma generation, X-ray emission and particle acceleration. Although the underlying mechanisms have been studied thoroughly over the last decades, many of them are still a long way from being fully understood. As lasers are advanced to higher intensities and shorter pulses, new regimes become accessible, which opens up a variety of entirely new questions. In combination with the broad range of realized and potential applications, the field of laser matter interaction attracts a lot of attention up until today.

One particular application of laser-matter interaction is the generation of laser-induced secondary sources. For one thing, the ultrashort, intense bursts of X-rays, that are generated via bremsstrahlung or characteristic inner-shell transitions, are well suited to probe high energy density (HED) states of matter, for example fuel capsules in inertial confinement fusion (ICF) experiments or laboratory produced planetary plasmas. Typical techniques include X-ray radiography (Stoeckl et al., 2017) or X-ray Thomson scattering (Glenzer and Redmer, 2009), which are used to determine the density and temperature of the probed matter. Another type of secondary source are laser particle accelerators, which produce directed, short-pulsed ion beams with a broad energy spectrum in the MeV range and particle numbers in the order of 10^{13} per beam. They were developed in the late 1990s, and first results and models of the proposed target normal sheath acceleration (TNSA) mechanism, which is based on charge separation fields at the target rear side, were presented in the early 2000s by, e.g., Snavely et al. (2000), Wilks et al. (2001), Hatchett et al. (2000) and Mora (2003). Even though several other acceleration mechanisms have been identified since then (Daido et al., 2012), TNSA remains one of the most important due to its great accessibility and stability. Laser-induced, compact particle accelerators are of interest for a number of applications, including proton radiography (Borghesi et al., 2001), isochoric heating of solid samples to create warm dense matter (Patel et al., 2003) and proton fast ignition as an alternative to conventional ICF (Roth et al., 2001). In addition, the produced ion beams can be converted to neutrons via nuclear processes, resulting in a compact neutron source for, e.g., non-destructive imaging (Roth et al., 2013).

For both types of secondary sources, it is of great interest to have a high conversion efficiency from laser energy to secondary output. This can be enhanced by optimizing the laser to target coupling, either by modifying the laser systems or by tailoring the target, specifically its front surface where laser and matter interact primarily. One approach is to control the plasma expansion by influencing the density gradients on the target front, e.g., by modifying the temporal laser pulse profile (Kaluza et al., 2004; McKenna et al., 2008), attaching foams (Nakamura et al., 2010; Passoni et al., 2014), or by modulating the surface with nano- or microstructures. The types of structures studied so far include, for example, nanowires (Hollinger et al., 2017; Kulcsár et al., 2000), micropillars (Bailly-Grandvaux et al., 2020; Sedov et al., 2019), microspheres (Margarone et al., 2012) and triangular structures (Blanco

et al., 2017). Depending on their shape and size, they are fabricated with different methods such as etching, two-photon polymerization, molding and ultrashort laser pulse processing (Liu et al., 2014; van Assenbergh et al., 2018).

In 1998, Her et al. found that irradiating the polished surfaces of silicon wafers in a SF_6 environment with a series of ultrashort pulses creates an irregular array of sharp, spike-like structures of micrometer size. These structured wafers show excellent light absorption properties from the ultraviolet to near-infrared spectral range (Sheehy et al., 2005). This was attributed both to a change of band structure through doping the silicon with ambient atoms, and their characteristic geometry. The microspikes are particularly appealing for high-intensity laser matter experiments for several reasons. To start with, they meet many of the current challenges of target fabrication (Prencipe et al., 2017). The fabrication method is straightforward to implement, allows to tailor the structure properties to the specific needs of the experiments, and can be easily upscaled to produce large quantities of identical targets. Moreover, the sloped surfaces of these microspikes hold potential to substantially enhance the involved coupling mechanisms. Furthermore, lasers with high energies and pulse lengths exceeding 100 fs are desirable to create brilliant X-ray sources and high-flux ion beams (Borghesi, 2014). Therefore, structures that do not immediately dissolve are called for, which sets microstructures apart from the often employed, more fragile nanowires that require ultrahigh contrasts and ultrashort pulse lengths in the order of tens of femtoseconds to obtain optimal results (Andreev et al., 2011).

In a previous proof-of-principle experiment at the VULCAN laser at the Rutherford Appleton Laboratory (RAL), Didcot, UK, conducted in February 2017, the microspikes showed promising results in both terms of X-ray emission and ion beam enhancement (Ebert et al., 2020). This thesis expands these findings by experiments and simulations. Since X-ray generation and particle acceleration require different hot electron spectra, the impact of the structures was studied at varying laser intensities, pulse lengths, and with different structure geometries. In addition to experimental studies at the PHELIX laser at the GSI Helmholtzzentrum für Schwerionenforschung in Darmstadt, Germany, and the Omega EP laser at the Laboratory for Laser Energetics (LLE) in Rochester, NY, USA, particle-in-cell (PIC) simulations were employed to investigate the underlying mechanisms causing the enhanced coupling.

The thesis is structured as follows. Chapter 2 covers the fundamentals of laser matter interaction, both on scales relevant for ultrashort laser pulse processing used for the target fabrication, and for the high-intensity laser matter experiments. It also gives a brief overview of the subsequent applications, namely microstructure fabrication, X-ray generation and ion acceleration and summarizes current findings about the impact of target front surface structures. Consecutively, Chapter 3 summarizes the methods, both experimental and theoretical, that were applied as diagnostic and simulation tools. In Chapter 4, the setup implemented for the fabrication of microstructured targets via ultrashort laser pulse processing is presented, and the different shapes and sizes achievable with this setup are discussed. Also, the replication procedure developed to duplicate the targets for characterization and transferring the geometry to other materials is explained. Last, this chapter discusses the different mounting options that were employed to create targets out of the processed samples.

The results of the thesis are presented in Chapter 5. It starts with the experimental findings, including a description of the experimental campaigns, the recorded ion data and the measured X-ray spectra. The microstructured targets increased the X-ray emission, especially of the He_α and Ly_α line, and improved the proton number and maximum energy. Subsequently, the PIC simulation series are presented, which are employed to study the electron heating, validate the experimental results, identify key parameters to optimize the target geometry and compare the microspikes to other target types. The chapter concludes with a short discussion, combining the results of the two approaches and illustrating their potential to enhance secondary sources. Chapter 6 summarizes the thesis and provides a brief outlook on future developments and applications.

2. Fundamentals of laser plasma interaction

Extensive research over the last decades continuously increased the intensities achievable by short-pulse laser systems by raising the pulse energy, shortening the pulses and minimizing the focal spot size. Along with this, new regimes and applications of laser matter interaction were discovered and studied. Here, the focus lies on irradiating solid samples, which are usually referred to as targets, with intensities of up to $10^{21}\,\mathrm{W\,cm^{-2}}$.

The processes involved in the interaction and the respective outcomes vary depending on the specific laser and target configuration. They range from excitation and relaxation without any permanent changes to irreversible alterations of the target. The latter is often accompanied by the formation of a plasma. During this thesis, two scenarios of laser matter interaction were studied, which are based on two different types of laser systems. On the one hand, surface structuring was investigated using ultrashort pulses with energies in the order of tens of µJ. On the other hand, the behavior of samples irradiated with high energy laser pulses with up to 1 kJ and pulse lengths of 0.5 ps to 20 ps was studied. During the initial stages, the underlying physics is similar, whereas at later times the interaction strongly differs.

Therefore, this chapter summarizes the basic principles involved in the interaction of short laser pulses with solid targets, covers the generation and behavior of plasmas and discusses the subsequent interaction of the laser with such plasmas at high intensities and densities. Furthermore, it gives a short overview of applications relevant for this thesis. As silicon was the main target material employed, exemplary values for this element are given throughout the following sections.

2.1. Laser-induced processes in solids

Since laser development was not part of this work, only a brief introduction to the terminology relevant to the field of high power laser systems is given here. For a detailed introduction and an overview of current petawatt systems, the interested reader is referred to other sources, e.g., Rullière (2005), Eliezer (2002) and Danson et al. (2019).

Nowadays, a typical short pulse laser system consists of an oscillator, a stretcher, an amplifier and a compressor. The oscillator generates low-energy, short pulses in the order of nJ by mode-locking, which is a method that allows to superimpose longitudinal laser modes of the laser resonator with a fixed-phase relationship. The minimal pulse width is inverse proportional to the bandwidth, therefore, short pulses require broad bandwidths.

To reduce the risk of damaging optics with high energy pulses, chirped pulse amplification (CPA) (Strickland and Mourou, 1985) is utilized. Here, the pulse first passes a stretcher, which temporally spreads the broadband pulse and is realized by optical elements such as dispersion gratings or fibers. The resulting pulse has a temporally depending frequency profile, which is referred to as chirp. After stretching, the chirped pulse is amplified in a way that the peak intensity remains below the damage

threshold of the optics before eventually passing a compressor, that compensates the chirp to recompress the pulse.

Especially for high intensity laser systems that exceed $10^{17}\,\mathrm{W\,cm^{-2}}$, another key characteristic is the ratio between the peak signal and the preceding noise level, which is generated by amplified spontaneous emission (ASE) and typically lasts several nanoseconds. This ratio is referred to as ASE contrast, and it can vary between 10^6 and 10^{13}, depending on the amplification system and additional implemented measures such as plasma mirrors (Bagnoud and Wagner, 2016; Dromey et al., 2004; Wagner et al., 2014; Ziener et al., 2003). Its value determines the amount of energy deposited into the target before the main pulse arrives and therefore greatly influences the laser matter interaction.

In all scenarios studied during this thesis, the matter with which the lasers initially interact is at solid state. The timescales as well as the laser and material properties affect the processes at play, which are discussed in the following. Depending on these processes, the intermediate and final state of the sample varies. On short timescales and high energies, at least part of the target becomes a plasma, therefore a brief description of plasma characteristics is given as well.

2.1.1. Electron excitation, plasma generation and relaxation

The processes induced in solids when irradiated with a short pulse laser can be classified into five regimes: (i) electron excitation, (ii) non-thermal structural changes, (iii) thermalization, (iv) free electron removal and (v) thermal and structural effects. The processes occur on different timescales from femtoseconds to microseconds and can overlap in time. In case of femtosecond pulses, most of the processes take place after the pulse as illustrated in Fig. 2.1 (Shugaev et al., 2016; Sundaram and Mazur, 2002). In general, laser pulses are considered to be ultrashort if their pulse length is in the range of femtoseconds to a few picoseconds.

A laser impinging on a solid density sample is absorbed in a thin surface layer with a typical thickness of tens of nanometers (Gamaly and Rode, 2013) and in the initial stages mainly couples to the electrons. In metals, free electrons are available in the conduction band, whereas in semiconductors and dielectrics the electrons need to be excited to energy levels above the bandgap. There are several ways to ionize an atom, and their occurrence depends on the laser's intensity

$$I_\mathrm{L} = \frac{\mathcal{E}_\mathrm{L}}{\tau_\mathrm{L} \cdot A_\mathrm{spot}}\,. \tag{2.1}$$

Here, $\mathcal{E}_\mathrm{L}$ denotes the energy of the laser pulse, τ_L the pulse length and A_spot the focal spot size.

Ionization for any target material is guaranteed when the electric field strength of the laser exceeds the binding strength of the electron. For a hydrogen atom with Bohr radius $a_\mathrm{B} = \hbar/(m_\mathrm{e}e^2) = 5.3{\times}10^{-11}\,\mathrm{m}$, where $\hbar$ is the Planck constant, m_e is the electron mass and e is the electron charge, the binding electric field strength in SI units is given by (Gibbon, 2005, p.18)

$$E_\mathrm{a} = \frac{e}{4\pi\epsilon_0 a_\mathrm{B}^2} \simeq 5.1{\times}10^9\,\mathrm{V\,m^{-1}}\,, \tag{2.2}$$

where ϵ_0 is the vacuum permittivity. This equals a binding energy of 13.6 eV. The corresponding laser intensity, which is also referred to as atomic intensity, is

$$I_\mathrm{a} = \frac{\epsilon_0 c E_\mathrm{a}^2}{2} \simeq 3.5{\times}10^{16}\,\mathrm{W\,cm^{-2}}\,. \tag{2.3}$$

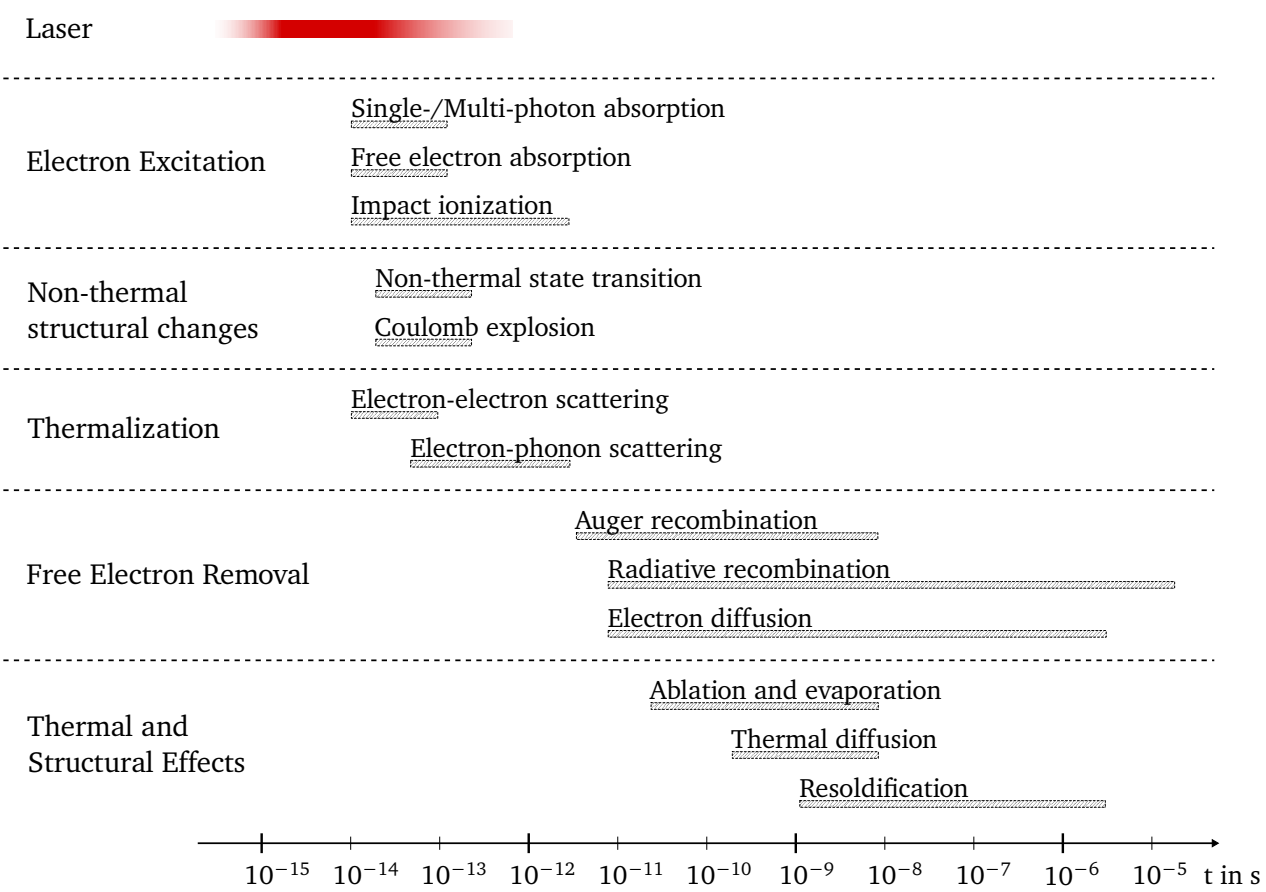

Figure 2.1.: Approximate timescales of regimes and processes that can be involved in the interaction of ultrashort laser pulses with matter (Shugaev et al., 2016; Sundaram and Mazur, 2002). The exact ranges, occurrences and ratios between the processes depend on the properties of the material and the laser.

For target materials other than hydrogen, the ionization energies $\mathcal{E}_{\mathrm{ion}}$ for neutral atoms are between 3 and 25 eV, with 8.2 eV for silicon (Kramida et al., 2021).

Nevertheless, it is also possible to ionize atoms at much lower laser intensities. If high-frequency photons with energies above the binding energy are available, they can ionize atoms via the photoelectric effect. However, typical high energy laser systems generate photons in the infrared range, so the energy of a single photon is insufficient. In this case, the required energy can be exceeded by combining multiple of such lower frequency photons as shown in Fig. 2.2 (a). The rate of this multi-photon ionization (MPI) is proportional to the laser intensity and is observed at intensities exceeding $10^{10}\,\mathrm{W\,cm^{-2}}$ (Gibbon, 2005).

As the laser intensity approaches the atomic intensity I_{a}, it becomes strong enough to distort the binding Coulomb potential and tunnel ionization (TI) becomes the main ionization mechanism. As shown in Fig. 2.2 (b), the Coulomb barrier gets deformed so that the electron can escape the binding potential through the barrier with a finite probability. At even higher intensities, the binding Coulomb potential is so strongly distorted that its maximum drops below the ionization energy, as illustrated in Fig. 2.2 (c). In this case, the electron can pass over the barrier and the mechanism is called barrier suppression ionization (BSI).

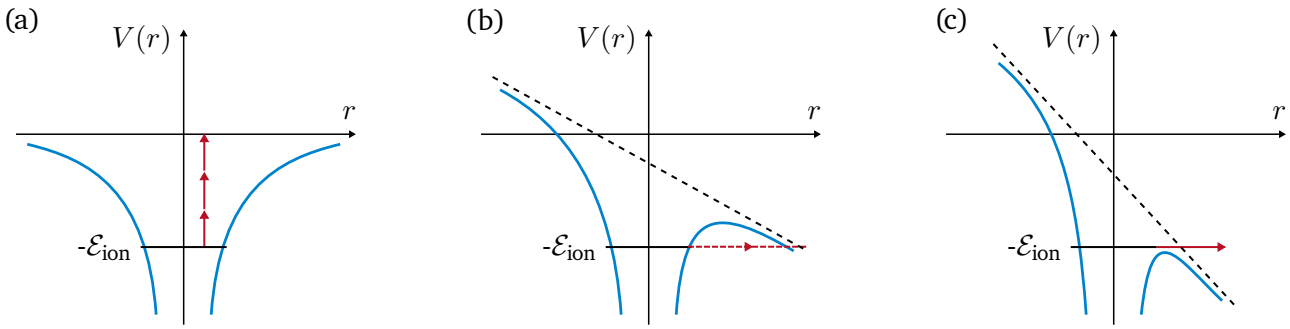

Figure 2.2.: Overview of ionization mechanisms relevant at high laser intensities. An electron that is bound by the ionization energy $\mathcal{E}_{\mathrm{ion}}$ in the Coulomb potential (blue) of an undisturbed ion can be removed by (a) multi-photon ionization, (b) tunneling ionization or (c) barrier suppression ionization. In case of (b) and (c), the laser field (dashed) disturbs the potential $V(r)$ that depends on the radial distance r.

To separate the two regimes of multi-photon ionization and tunnel ionization, the Keldysh parameter

$$\gamma_{\mathrm{K}} = \omega_{\mathrm{L}} \sqrt{\frac{2\mathcal{E}_{\mathrm{ion}}}{I_{\mathrm{L}}}} \sim \sqrt{\frac{\mathcal{E}_{\mathrm{ion}}}{\Phi_{\mathrm{pond}}}} \tag{2.4}$$

with the ponderomotive potential

$$\Phi_{\mathrm{pond}} = \frac{e^2 E_{\mathrm{L}}^2}{4 m_{\mathrm{e}} \omega_{\mathrm{L}}^2}\,, \tag{2.5}$$

is introduced, which depends on the laser electric field strength E_{L} and the angular frequency ω of the laser light (Gibbon, 2005, p. 20). For $\gamma_{\mathrm{K}} > 1$, MPI prevails whereas TI dominates for $\gamma_{\mathrm{K}} < 1$. The intensity above which tunnel ionization for ions with charge Z appears, is given by

$$I_{\mathrm{TI}} \simeq 4{\times}10^{9} \left(\frac{\mathcal{E}_{\mathrm{ion}}}{\mathrm{eV}}\right)^{4} Z^{-2}\,\mathrm{W\,cm^{-2}} \tag{2.6}$$

and is approximately $1.4{\times}10^{14}\,\mathrm{W\,cm^{-2}}$ for hydrogen and $1.8{\times}10^{13}\,\mathrm{W\,cm^{-2}}$ for silicon (Gibbon, 2005, p. 21).

At high densities, the atoms are further ionized by impact ionization if a sufficient amount of free electrons is present. Also, as soon as free electrons are present, which is the case for metals from the beginning, the solid can additionally absorb laser energy via inverse bremsstrahlung.

If more than 10 % of the valence electrons are removed from the bonding orbitals, the lattice of the solid is weakened. This increases the ion mobility although the ions remain cold (Sundaram and Mazur, 2002). The structural changes resulting from this enhanced mobility are therefore non-thermal and are sometimes also called ultrafast phase transitions. Furthermore, especially in wide-bandgap dielectrics or at high laser fluences, a positive charge-up can develop in the surface layers, when the free electrons rapidly migrate to other regions. Here, the repulsive forces between the positively charged ions then can become strong enough to disrupt the surface and a cluster of ions is ejected, which is referred to as Couloumb explosion (Stoian et al., 2002).

Following the excitation of the electrons, the energy, which up to this point was only locally absorbed, is redistributed. Electron-electron scattering, electron-lattice collisions and electron-ion collisions transfer energy to an extended region and to the bulk material. Over time, the electron-electron as well as ion-ion or phonon-phonon collisions result in local thermal equilibria (LTE) of the free electron population

and the ions. It takes tens to hundreds of picoseconds to build up the high-energy tail of each thermal Maxwell distribution (Gamaly and Rode, 2013), but even longer to reach an equilibrium between the two particle species. Therefore, on short timescales it is common to use a two-temperature approximation to describe the state of the solid.

Next, the excess free electrons in the heated region clear away by electron diffusion to outer regions and recombination processes. This includes radiative recombination, during which the electrons are bound again by emitting a luminescence photon, and Auger recombination.

Lastly, structural effects occur, which can be both thermal or non-thermal and arise several nanoseconds after irradiation. If the kinetic energy of individual ions, atoms, molecules or clusters exceeds their bonding energies, they can be ejected before the material is in equilibrium. This process is called ablation. Also, vaporization and melting can take place if the lattice reached an equilibrium and its temperature is above the melting point. Here, the high energy tail of the thermal Maxwell distribution plays an important role, therefore it takes a certain amount of time in the order of picoseconds to nanoseconds before these processes ensue. In addition, thermal diffusion transports the energy away from the heated region, which further aids the achievement of equilibrium. The extent of phase transitions and structural deformation when the solid relaxes depends on the intensity of the laser and the material properties. (Gamaly and Rode, 2013; Sundaram and Mazur, 2002)

The properties and behavior of the intermediate state in which the irradiated sample is partially or fully ionized are of particular interest for this work and will therefore be discussed in more detail in the following.

2.1.2. Plasma properties

A plasma is a state of matter that is at least partially ionized and consequently contains free electrons and ions that interact via electrostatic forces. One essential characteristic of a plasma is that local potentials are effectively screened by the surrounding charged particles. The characteristic shielding length at which the potential of a charge drops to $1/e_{\mathrm{E}}$, with e_{E} being Euler's number, is given by the Debye length (Chen, 2016, p. 9)

$$\lambda_{\mathrm{D}} = \sqrt{\frac{\epsilon_0 k_{\mathrm{B}} T_{\mathrm{e}}}{n_{\mathrm{e}} e^2}}\,. \tag{2.7}$$

Here, n_{e} is the electron number density, e is the electron charge and it is assumed that the electron temperature T_{e} is much larger than the ion temperature T_{i}. With the Debye length, the plasma parameter

$$\Lambda = \frac{4\pi}{3} n_{\mathrm{e}} \lambda_{\mathrm{D}}^3 \tag{2.8}$$

can be defined (Piel, 2010, p. 40). It equals the number of particles contained in an electron Debye sphere. If $\Lambda \gg 1$, the plasma can be treated as quasi-neutral on scales much larger than the Debye length. Since the Coulomb interaction is a long-range force, each particle interacts with a large amount of other particles. This results in plasmas exhibiting collective behavior if the electrostatic interaction dominates over collisions.

Another key characteristic for laser produced plasmas, in particular, is the plasma expansion length. During the laser matter interaction, a plasma is formed in front of the irradiated surface. The plasma

pressure causes a blow-off with sound speed c_s, which translates into a modification of the density profile along the expansion axis z as described by

$$n_{\mathrm{e}}(z) = Z_{\mathrm{eff}}\, n_{\mathrm{i}}(z) = n_{\mathrm{e},0} \exp\left(-\frac{z}{L} - 1\right) , \tag{2.9}$$

where $n_{\mathrm{e},0}$ is the density of the initial step-like profile and Z_{eff} denotes the effective ion charge (Eliezer, 2002, p. 145). The variable L is the pre-plasma scale length and is given by (Gibbon, 2005, p. 129)

$$L = c_s \tau \tag{2.10}$$

$$= \sqrt{\frac{Z_{\mathrm{eff}} k_B T_e}{m_i}} \tau \tag{2.11}$$

$$\simeq 3 \sqrt{\frac{T_e}{\mathrm{keV}}} \sqrt{\frac{Z_{\mathrm{eff}}}{A}}\, \tau_{\mathrm{fs}}\, \text{Å} , \tag{2.12}$$

with A denoting the atomic number. For this equation, isothermal expansion is assumed, which includes quasi-neutrality ($n_{\mathrm{e}} = Z_{\mathrm{eff}}\, n_{\mathrm{i}}$) and a constant electron temperature T_{e} being much greater than the ion temperature. The variable τ is the expansion time and τ_{fs} is this time in femtoseconds.

2.2. Laser absorption in plasmas

As soon as the laser starts to ionize the irradiated material, the laser does not only interact with a cold solid but also with a plasma. In the first instance, the laser couples mainly to the electrons due to their much lower mass compared to ions. Thus, this section provides a description of the single electron motion induced by a plane electromagnetic wave, followed by the interaction of an electron with a more realistic model of the laser, which results in the definition of the ponderomotive force. Continuing with the response of a plasma when exposed to an electromagnetic perturbation, characteristic properties of a plasma including the plasma frequency and critical density are derived. The section closes with a brief summary of electron heating mechanisms relevant for this thesis, including collisional absorption, resonance absorption, Brunel and stochastic heating.

2.2.1. Single electron motion in a plane electromagnetic wave

In one of its simplest approximations, a laser can be described as a linearly polarized electromagnetic wave propagating in z-direction. The electric field $\boldsymbol{E}$ and the magnetic field $\boldsymbol{B}$ are described by

$$\boldsymbol{E}(\boldsymbol{r}, t) = E_0(\boldsymbol{r}) \mathrm{e}^{-i(\omega_{\mathrm{L}} t - kz)} \boldsymbol{e_{\mathrm{x}}} \tag{2.13}$$

$$\boldsymbol{B}(\boldsymbol{r}, t) = B_0(\boldsymbol{r}) \mathrm{e}^{-i(\omega_{\mathrm{L}} t - kz)} \boldsymbol{e_{\mathrm{y}}} , \tag{2.14}$$

with the angular laser frequency ω_{L}, the time t, the position vector $\boldsymbol{r}$, the laser wave vector $\boldsymbol{k} = (\omega_{\mathrm{L}}/c)\boldsymbol{e_{\mathrm{z}}}$ and the unit vectors $\boldsymbol{e_{\mathrm{x}}}$ and $\boldsymbol{e_{\mathrm{y}}}$. In this model, the field amplitudes E_0 and B_0 vary slowly in time compared to the laser frequency. Using the third Maxwell equation (Eliezer, 2002, p. 291)

$$\boldsymbol{\nabla} \times \boldsymbol{E} = -\frac{\partial \boldsymbol{B}}{\partial t} , \tag{2.15}$$

the fields can be expressed by $c\boldsymbol{B} = \boldsymbol{e_{\mathrm{z}}} \times \boldsymbol{E}$ and therefore $E_0 = cB_0$.

A single electron exposed to these fields in a vacuum moves according to the Lorentz equation (Gibbon, 2005, p. 31)

$$\frac{d\boldsymbol{p}}{dt} = -e\left(\boldsymbol{E} + \boldsymbol{v} \times \boldsymbol{B}\right) \tag{2.16}$$

$$= -e\left(\boldsymbol{E} + \frac{\boldsymbol{v}}{c} \times [\boldsymbol{e_z} \times \boldsymbol{E}]\right) . \tag{2.17}$$

Here, $\boldsymbol{v}$ is the electron velocity, $\boldsymbol{p} = \gamma m_\mathrm{e} \boldsymbol{v}$ is the electron momentum and $\gamma = (1 + \boldsymbol{v}^2/c^2)^{-½}$ is the relativistic factor.

At non-relativistic velocities $|\boldsymbol{v}| \ll c$, the electron motion is only influenced by the electric field and the electron acquires the velocity

$$v = \frac{eE_0}{m_\mathrm{e}\omega_\mathrm{L}} \cos(\omega_\mathrm{L} t) = v_\mathrm{osc} \cos(\omega_\mathrm{L} t) , \tag{2.18}$$

where the amplitude v_osc is called quiver velocity. Using this expression, the threshold to the relativistic regime can be described by the dimensionless electric field amplitude (McKenna et al., 2013, p. 94)

$$a_0 = \frac{v_\mathrm{osc}}{c} = \frac{eE_0}{m_\mathrm{e}\omega_\mathrm{L} c} = \sqrt{\frac{I_0\,[\mathrm{W\,cm^{-2}}]}{1.37{\times}10^{18}\,\mathrm{W\,cm^{-2}}}}\,\lambda_\mathrm{L}\,[\mu\mathrm{m}] . \tag{2.19}$$

For $a_0 \ll 1$, non-relativistic treatment is valid, otherwise the electron motion should be regarded as relativistic. The field amplitudes of the experiments conducted during this thesis varied between 0.25 and 17, therefore the particles are treated relativistically.

When the electron motion becomes relativistic, the influence of the magnetic field can no longer be neglected. Taking the magnetic component $e(\boldsymbol{v} \times \boldsymbol{B})$ of the Lorentz force (eqn. 2.16) into account, it can be shown that the electrons move along the direction of the laser propagation with a non-zero drift velocity (Gibbon, 2005, p. 33)

$$\boldsymbol{v}_\mathrm{drift} = c\frac{a_0^2}{4 + a_0^2}\boldsymbol{e_z} . \tag{2.20}$$

However, although the electron position changes, the net energy gain at the end of each laser period is zero, which is known as Lawson-Woodward theorem (Esarey et al., 1995).

2.2.2. Ponderomotive force

In reality, lasers are not well described by plane electromagnetic waves, but feature a spatially and temporally varying amplitude $E_0(\boldsymbol{r}, t)$. Tightly focused and ultrashort laser pulses in particular exhibit strong gradients. In the non-relativistic case ($|\boldsymbol{v}| \ll c$), the equation of motion depends only on the electric field strength as can be seen in eqn. 2.17.

Using $\phi = \omega_\mathrm{L} t - kz$ and $x(t) = x_0 + x_1(t) + x_2(t) + ...$ the field strength, which has only an x-component, can be written as Taylor expansion

$$E_\mathrm{x}(\boldsymbol{r}, t) \simeq E_\mathrm{x}(x_0)\cos\phi + x_1(t)\frac{\partial E_\mathrm{x}(x_0)}{\partial x}\cos\phi + \ ... \tag{2.21}$$

and inserting the first order in eqn. 2.17 gives

$$\iint \frac{\partial v_{\mathrm{x}}^{(1)}}{\partial t} = x_1(t) = \frac{e}{m_{\mathrm{e}}\omega_{\mathrm{L}}^2} E(x_0)\cos\phi\,. \tag{2.22}$$

With this, the second order term can be expressed as

$$\frac{\partial v_{\mathrm{x}}^{(2)}}{\partial t} = -\frac{e}{m_{\mathrm{e}}} x_1(t) \frac{\partial E_{\mathrm{x}}(x_0)}{\partial x}\cos\phi \tag{2.23}$$

$$= -\frac{e^2}{m_{\mathrm{e}}^2\omega_{\mathrm{L}}^2} E_{\mathrm{x}}(x_0) \frac{\partial E_{\mathrm{x}}(x_0)}{\partial x}\cos^2\phi\,. \tag{2.24}$$

Multiplying by the electron mass m_{e}, using $\cos^2\phi = ½(1-\sin 2\phi)$ and averaging over one period gives the ponderomotive force (Piel, 2010, p. 68)

$$f_p = m_{\mathrm{e}}\langle\frac{\partial v_{\mathrm{x}}^{(2)}}{\partial t}\rangle \tag{2.25}$$

$$= -\frac{e^2}{4m_{\mathrm{e}}^2\omega_{\mathrm{L}}^2}\frac{\partial}{\partial x}\left[E_{\mathrm{x}}^2(x_0)\right]\,, \tag{2.26}$$

which is proportional to the negative gradient of the laser intensity $-\nabla I_{\mathrm{L}}$. Accordingly, this time-averaged force pushes electrons away from regions with high intensities since the restoring force is smaller than the displacing force when the electron is driven to lower field regions. Among others, the ponderomotive force plays a role in momentum transfer, changes of the plasma density profile and as a consequence also in self-focusing and filamentation effects (Eliezer, 2002).

2.2.3. Plasma frequency and critical density

When a plasma experiences an electromagnetic perturbation, the displacement of the individual electrons leads to local fluctuations of the electron density n_{e}. Since the ions are much heavier, they can be assumed to be stationary compared to electrons. In combination, this leads to the generation of local charge currents

$$\boldsymbol{j} = -en_{\mathrm{e}}\boldsymbol{v_{\mathrm{e}}} \tag{2.27}$$

and the continuity equation for charge conservation can be written as (Eliezer, 2002)

$$0 = \frac{\partial\rho_{\mathrm{c}}}{\partial t} + \nabla\boldsymbol{j} \tag{2.28}$$

$$= \frac{\partial\rho_{\mathrm{c}}}{\partial t} - e\nabla n_{\mathrm{e}}\boldsymbol{v}\,, \tag{2.29}$$

with ρ_{c} being the charge density. Taking the time derivative and using the equation of motion for a Coulomb force

$$\frac{\partial v}{\partial t} = -\frac{e}{m_{\mathrm{e}}}\boldsymbol{E} \tag{2.30}$$

the equation becomes

$$0 = \frac{\partial^2\rho_{\mathrm{c}}}{\partial t^2} - en_{\mathrm{e}}\frac{\partial\nabla\boldsymbol{v}}{\partial t} \tag{2.31}$$

$$= \frac{\partial^2\rho_{\mathrm{c}}}{\partial t^2} + \frac{e^2 n_{\mathrm{e}}}{m_{\mathrm{e}}}\nabla\boldsymbol{E}\,. \tag{2.32}$$

The electric field field can be expressed by the charge density using Gauss's law $\nabla \boldsymbol{E} = \rho_\mathrm{c}/\epsilon_0$. Substituting this in expression 2.32 results in

$$\frac{\partial^2 \rho_\mathrm{c}}{\partial t^2} + \frac{e^2 n_\mathrm{e}}{m_\mathrm{e}\epsilon_0}\rho_\mathrm{c} = 0\,, \tag{2.33}$$

which has the form of an harmonic oscillator with frequency (Piel, 2010, p. 40)

$$\omega_\mathrm{p} = \sqrt{\frac{e^2 n_\mathrm{e}}{m_\mathrm{e}\epsilon_0}}\,. \tag{2.34}$$

This frequency, which is called plasma frequency, describes the oscillatory motion of electrons around a position of charge equilibrium. In case of the perturbation being caused by a laser, this can be understood as the interplay of the displacement of the electron by the electromagnetic wave and the restoring force induced by the stationary ions. It should be noted that the above presented derivation assumes a non-thermal plasma in which the thermal particle motion can be neglected.

Furthermore, the charge currents $\boldsymbol{j}$ caused by particle motions have an impact on the propagation of electromagnetic waves in a plasma. Solving the relevant Maxwell equations results in the dispersion relation (Chen, 2016, p. 106 ff.)

$$\omega_\mathrm{L}^2 = \omega_\mathrm{p}^2 + c^2 k^2\,, \tag{2.35}$$

which contains the plasma frequency ω_p. Applying the dispersion relation to the plasma refraction index $\eta = ck/\omega_\mathrm{L}$ gives

$$\eta = \sqrt{1 - \frac{\omega_\mathrm{p}^2}{\omega_\mathrm{L}^2}}\,. \tag{2.36}$$

The refraction index becomes imaginary for $\omega_\mathrm{L} < \omega_\mathrm{p}$ and the laser cannot propagate further. Instead, its field decays exponentially behind the boundary layer and reaches up to the skin depth $l_\mathrm{s} = c/\omega_\mathrm{p}$. The critical density, that describes the boundary, is reached when the laser frequency ω_L equals the plasma frequency ω_p and is given by (Gibbon, 2005, p. 128 f.)

$$n_\mathrm{c} = \frac{\omega_\mathrm{L}^2 \epsilon_0 \gamma m_\mathrm{e}}{e^2} \simeq 1.1{\times}10^{21}\gamma \left(\frac{\lambda}{\mu\mathrm{m}}\right)^{-2} \mathrm{cm}^{-3}\,. \tag{2.37}$$

As long as the density is lower than the critical density, $\omega_\mathrm{L} > \omega_\mathrm{p}$ holds and the laser can propagate through the plasma, which in this case is referred to as underdense. However, if the electron density exceeds the critical density, which is the case for $\omega_\mathrm{L} < \omega_\mathrm{p}$, laser propagation is no longer possible and the plasma is called overdense.

In the ultra-relativistic case of $\gamma > 1$, the critical density increases and the laser can propagate in a formerly overdense plasma. This effect, when the relativistic electrons become too inert to follow the laser field, is called relativistic transparency.

2.2.4. Electron heating mechanisms

During the interaction of a high intensity laser with a plasma, part of the energy of the laser pulse is transferred to the plasma via a range of heating mechanisms. The thereby generated high energy

electrons, which are often referred to as *hot electrons*, induce subsequent effects including X-ray generation and ion acceleration (Gibbon, 2005; Roth and Schollmeier, 2017). However, even though some references denote an electron as *hot* when its energy exceeds the oscillation energy $\mathcal{E}_{\mathrm{osc}}$ (Mulser et al., 2012), there exists no common definition. Due to the fluctuations and randomness of the energy transfer, the averaged electron velocity distribution takes on a Maxwellian form (McKenna et al., 2013, p. 94)

$$f(\mathcal{E}_{\mathrm{e,hot}}) = N_{\mathrm{e,hot}} \frac{2}{\sqrt{\pi}} \sqrt{\frac{\mathcal{E}_{\mathrm{e,hot}}}{(k_{\mathrm{B}} T_{\mathrm{e,hot}})^3}} \exp\left(-\frac{\mathcal{E}_{\mathrm{e,hot}}}{k_{\mathrm{B}} T_{\mathrm{e,hot}}}\right), \tag{2.38}$$

where $N_{\mathrm{e,hot}}$ is the total number, $\mathcal{E}_{\mathrm{e,hot}}$ is the energy and $T_{\mathrm{e,hot}}$ is the temperature of the hot electrons. For relativistic electron energies, the generalized Maxwell-Jüttner distribution (Jüttner, 1911) is valid.

Under quasi-steady state conditions, the degree of absorption is generally related to the energy flux density, which is described by the Poynting vector $\boldsymbol{S} = \epsilon_0 c^2 \boldsymbol{E} \times \boldsymbol{B}$. With a laser field of the form $\boldsymbol{E} \sim \sin(\omega_{\mathrm{L}} t)$ and the current density $\boldsymbol{j}$ introduced in eqn. 2.27, Poynting's theorem takes the form (Mulser and Bauer, 2010, p. 378)

$$\overline{\boldsymbol{\nabla} \boldsymbol{S}} = -\overline{\boldsymbol{j} \boldsymbol{E}} \sim -\overline{\cos(\omega_{\mathrm{L}} t + \phi) \sin(\omega_{\mathrm{L}} t)} = -\frac{1}{2} \sin(\phi)\,, \tag{2.39}$$

when averaged over a full laser cycle. The phase shift ϕ, which describes the amount of dephasing between the driver field of the laser and the generated current $\boldsymbol{j}$, is caused by the processes of the heating mechanisms (Liseykina et al., 2015; Mulser and Bauer, 2010).

For high density targets that exceed the critical density n_{c}, the energy transfer occurs either in the undercritical part of the pre-plasma or within the skin depth l_{s} reaching into the overdense part. One of the key parameters to determine which mechanisms are at play is the pre-plasma scale length L (eqn. 2.11), which in reality is always non-zero. Usually, more than one mechanism takes effect since the regimes of the various heating mechanisms overlap. The heating mechanisms described in the following are a selection of the most relevant for the scenario studied during the thesis.

Collisional absorption. At low kinetic temperatures, the absorption is dominated by collisional absorption, which is sometimes also referred to as inverse bremsstrahlung. The laser field causes the electrons to oscillate with their quiver velocity v_{osc} (eqn. 2.18). As they collide with another electron or ion, they experience a phase shift relative to the laser field, and consequently energy is transferred.

Once the kinetic temperature exceeds $10^3 Z^2$ eV, with Z being the ion charge, this mechanism becomes ineffective and non-collisional processes prevail (Liseykina et al., 2015). For these processes, the phase change is caused by the generated space charge fields (Liseykina et al., 2015).

Resonance absorption. If a p-polarized laser hits a target with a rising density gradient with $L \gg \lambda$ under an oblique angle θ, it can propagate up to an electron density of $n_{\mathrm{e}} = n_{\mathrm{c}} \cos^2(\theta)$. There, the laser frequency matches the plasma frequency, so that the laser can resonantly drive a plasma wave, thus this mechanism is called resonance absorption. The excited plasma wave is subsequently damped by collisions or wave breaking (Gibbon, 2005), thereby transferring energy to the plasma. This process takes place at laser intensities of $10^{14}\,\mathrm{W\,cm^{-2}}$ to $10^{17}\,\mathrm{W\,cm^{-2}}$, since in this regime the field strength is strong enough to drive the wave while not yet disturbing the density profile by ponderomotive forces (Arber et al., 2015).

Brunel heating. In 1987, Brunel discussed a mechanism that occurs at discontinuous interfaces between vacuum and an infinitely dense, cold target when irradiated with a p-polarized laser with an oblique incidence angle. This Brunel heating is sometimes also referred to as *vacuum heating*, but this term is ambiguous since some groups also use this term to describe electrons that only circulate in front of the target surface. The heating process can be divided into two parts. During the first half of the laser cycle (0,π), electrons are pulled out of the target by the perpendicular component of the laser field. These electrons are then pushed back into the target during the second half of the cycle (π,2π). Since the electric field of the laser is screened by the infinitely dense target, the evanescent field is not strong enough to reverse their motion and the electrons propagate further into the target having gained kinetic energy from the laser field. The amount of absorbed energy strongly depends on the angle of incidence and it can be shown that at high laser intensities ($a_0 \gg 1$), the absorption curve of this idealized model has a maximum at an incidence angle of 73° (Gibbon, 2005). Detailed discussions about the generated electron spectra and extensions of this model are given by e.g. Liseykina et al. (2015), Mulser et al. (2012) and Gibbon (2005). Experimentally, the Brunel heating mechanism in its pure form can rarely be observed due to the formation of a pre-plasma gradient at the interface. However, if the quivering amplitude of the electrons exceeds the pre-plasma scale length L, the plasma density profile is roughly step-like and Brunel heating becomes a relevant process.

j×B heating. Although the magnetic part of the Lorentz force (eqn. 2.17) is neglected in some of the electron heating models, it has a noteworthy impact at laser intensities exceeding $10^{18}\,\mathrm{W\,cm^{-2}}$ as discussed in Section 2.2.1. The magnetic field exerts a force along the laser axis on the electron, which leads to an oscillatory motion with $2\omega_\mathrm{L}$. Once the electrons are pushed beyond the critical density at the interface of a step-like density profile similar to Brunel's model, the influence of the screened laser field decreases in the overdense region. Thus, the electrons carry the energy gained during the laser interaction into the target bulk. This j×B heating is most efficient for normal incidence (Gibbon, 2005).

Stochastic heating. Another mechanism that plays a role at such ultrahigh laser intensities (exceeding $10^{18}\,\mathrm{W\,cm^{-2}}$) is stochastic heating. In contrast to Brunel and j×B heating, this model requires an underdense plasma region with a scale length in the order of the wavelength ($L \approx \lambda_\mathrm{L}$) in front of an overdense target bulk. Opposed to configurations with low intensities with $a_0 \ll 1$, the interference pattern of two non-colinear beams, e.g., the incident beam and its reflection from the overdense region, prevents the growth of resonant plasma waves in the underdense region. Chopineau et al. (2019) show that the non-uniform electron motion induced in such a chaotic interference leads to significant phase variations, therefore enabling an energy transfer and the generation of high energy electrons. Recently, Williams et al. (2020) presented experimental and simulated evidence that stochastic heating also occurs at lower intensities ($\approx 10^{18}\,\mathrm{W\,cm^{-2}}$), if the focal spot is large enough and the pulse length is long enough, in their case 125 µm (FWHM) and 10 ps (FWHM), respectively, to create filaments in the plasma that last for a significant period of the interaction. The randomness of the filaments results in a reflected beam with strong phase fluctuations and due to the large extent of the coronal plasma, the electrons can gain energy from these inhomogeneous fields along comparatively long trajectories.

Direct laser acceleration. Electrons can gain energy directly from the laser by direct laser acceleration, if their initial position and velocity match the phase of the laser (Jiang et al., 2014a). To achieve a net gain, they need to co-propagate along with the laser for a significant distance during the accelerating half of the pulse and have to be injected into the target bulk before the field reverses.

Scaling laws. The varying combinations of mechanisms involved in the heating of electrons in a specific laser matter experiment make it difficult to determine their precise temperature. However, there exists a variety of scaling laws in literature to estimate the hot electron temperature $k_\mathrm{B}T_\mathrm{e,hot}$. A selection is shown in Fig. 2.3 for comparison.

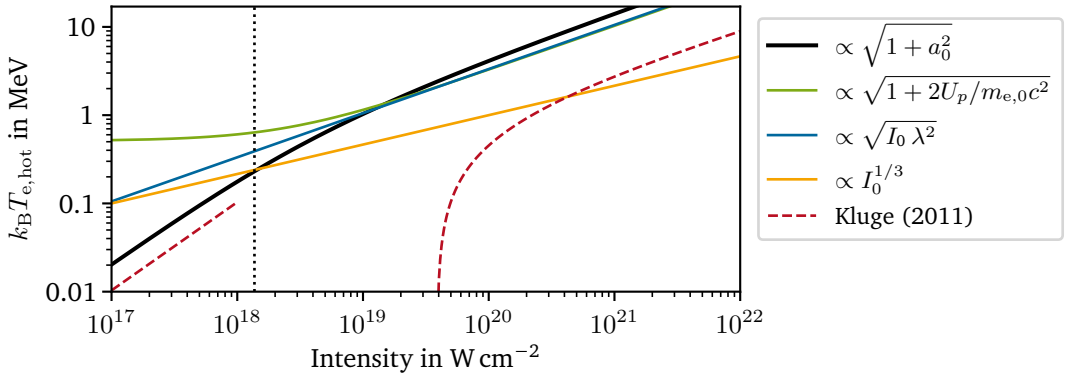

Figure 2.3.: Scaling laws for the hot electron temperature $k_B T_{e,hot}$ plotted for a laser wavelength of 1053 nm. The analytical model by Kluge et al. (2011) is derived for a short pre-plasma scale length. For a detailed description of the expressions see eqn. 2.40 to 2.44.

A common ansatz for models is the ponderomotive potential of the laser, meaning they derive the cycle-averaged kinetic energy of an electron oscillating in laser field. One such ponderomotive scaling law describing the hot electron temperature for a circularly polarized laser is (Daido et al., 2012; Wilks et al., 2001)

$$k_B T_{e,hot} = m_e c^2 \left(\sqrt{1 + a_0^2} - 1 \right) , \tag{2.40}$$

using the electron rest mass m_e and the laser field amplitude a_0 (eqn. 2.19). Another scaling law found in literature, which is valid for the ultra-relativistic case ($a_0 \gg 1$), is given by (Wilks et al., 2001)

$$k_B T_{e,hot} = m_e c^2 \sqrt{1 + \frac{2U_p}{m_e c^2}} \tag{2.41}$$

with $U_p = 9.33 \times 10^{-14}\,\mathrm{eV} \cdot I_0\,[\mathrm{W\,cm^{-2}}] \cdot \lambda^2\,[\mu\mathrm{m}]$. Others also use the expression (Hatchett et al., 2000; Roth and Schollmeier, 2017)

$$k_B T_{e,hot} \approx U_{pond} \approx 1\,\mathrm{MeV} \sqrt{\frac{I_0\,[\mathrm{W\,cm^{-2}}] \cdot \lambda_L^2\,[\mu\mathrm{m}^2]}{10^{19}}} . \tag{2.42}$$

Laser systems with high contrast and intensities exceeding $10^{19}\,\mathrm{W\,cm^{-2}}$, that create short scale pre-plasmas, show significantly lower temperatures than estimated by the ponderomotive scaling. According to Beg et al. (1997), it can be estimated by

$$k_B T_{e,hot} \approx 0.1\,\mathrm{MeV} \left(\frac{I_0\,[\mathrm{W\,cm^{-2}}]}{10^{17}} \right)^{1/3} , \tag{2.43}$$

which is an empirical scaling law for a laser system with a wavelength of 1053 nm. Kluge et al. (2011) propose an analytically derived scaling, that is based on a weighted average of the kinetic energy of an ensemble of electrons. For the extreme cases of very small and very large laser amplitudes, the expressions are

$$k_B T_{e,hot} = \begin{cases} m_e c^2 \dfrac{a_0^2}{4} & \text{if } a_0 \ll 1\,, \\ m_e c^2 \left(\dfrac{\pi a_0}{2 \ln 16 + 2 \ln a_0} - 1 \right) & \text{if } a_0 \gg 1\,. \end{cases} \tag{2.44}$$

The scaling for small field amplitudes converges with the ponderomotive scaling as can be seen in Fig. 2.3.

In all cases, the temperature is determined by the laser intensity and wavelength. M. Schollmeier (2008, p., 15 ff.) compared the different scaling laws to temperature values determined either in experiments or by simulations. He comes to the conclusion, that the expression derived for a circularly polarized laser (eqn. 2.40) gives a valid estimate for intensities in the order of $10^{19}\,\mathrm{W\,cm^{-2}}$. In simple units it can be written as

$$k_\mathrm{B}T_\mathrm{e,hot} = m_\mathrm{e}c^2\left(\sqrt{1+\frac{I_0\,[\mathrm{W\,cm^{-2}}]\cdot\lambda_\mathrm{L}^2\,[\mu\mathrm{m}^2]}{1.37{\times}10^{18}}}-1\right). \tag{2.45}$$

This expression, which will be used in this thesis to estimate electron temperatures, gives an electron temperature of roughly 1 MeV for a laser pulse with a wavelength of 1053 nm and an intensity of $10^{19}\,\mathrm{W\,cm^{-2}}$.

Following this brief introduction to the fundamentals of laser plasma interaction, a description of applications with relevance for this thesis are presented.

2.3. Applications of short laser pulses

The processes and products induced by short laser pulses when interacting with matter have been met with great interest by many fields, which lead to the implementation of an immense number of applications. The two main uses relevant for this thesis are laser processing as a target fabrication method and laser-induced secondary sources, i.e. the generation of intense bursts of X-rays and accelerated ions. After a description of these applications, the influence of target front side modifications on the laser plasma coupling process and the ensuing secondary outputs is discussed.

2.3.1. Laser-induced periodic surface structures

Laser-induced periodic surface structures (LIPSS) were discovered in the 1960s, along with the development of the first laser systems (Birnbaum, 1965), and have been an active field of research ever since. They describe the periodic, permanent surface modulations of a solid with a periodicity from hundreds of nanometers up to several micrometers, that result from irradiating the sample with a laser. Depending on the laser and processing parameters, their periodicity, orientation and depth varies. LIPSS, which are sometimes also referred to as ripples, can be generated on metals, semiconductors and dielectrics (Bonse and Gräf, 2020). They can be divided into two groups. Low spatial frequency LIPSS (LSFL) have a period exceeding half the laser wavelength ($\Lambda_\mathrm{LIPSS} > \lambda_\mathrm{L}/2$), whereas high spatial frequency LIPSS (HSFL) are characterized by much smaller periods ($\Lambda_\mathrm{LIPSS} < \lambda_\mathrm{L}/2$). LSFLs are mostly observed on strongly absorbing materials such as semiconductors or metals, while HSFLs prevail on transparent materials (Bonse et al., 2012). Fig. 2.4 shows an exemplary image of LSFL on Cu, that was taken with a scanning electron microscope (SEM).

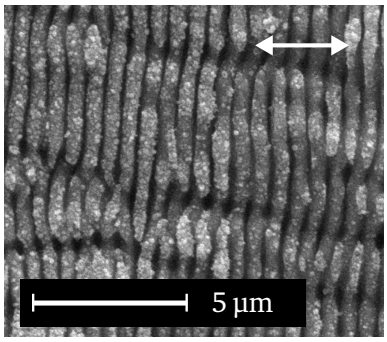

Figure 2.4.: SEM image of LSFL on Cu with a periodicity of roughly 600 nm, created with a laser wavelength of 800 nm. The white arrow shows the laser polarization, which is perpendicular to the ripple orientation.

LIPSS develop when the energy fluence delivered by the laser is close to the ablation threshold of the material (Bonse and Gräf, 2020). The ablation threshold of silicon is approximately $0.2\,\mathrm{J\,cm^{-2}}$, which corresponds to a laser intensity of $2\times10^{12}\,\mathrm{W\,cm^{-2}}$ for a pulse length of 100 fs. However, studies have shown that the ablation threshold decreases with increasing number of pulses irradiating the sample due to incubation effects (Bonse et al., 2002; Mannion et al., 2004).

Over the years, a large number of models describing the formation process of LIPSS were developed, which can be classified into two categories. Electromagnetic models are based on the idea that the incoming light is backscattered at surface imperfections, thereby creating a spatially periodic interference pattern of laser intensity. This pattern is imprinted on the surface by ablation or solidification of capillary waves. The other group of models is centered on matter reorganization. Here, the sample is irradiated homogeneously. The laser-excited material is then transformed by phase transitions, hydrodynamic processes, material instabilities and microscopic accumulation effects, e.g. diffusion, which finally leads to reorganization. The two groups can be differentiated by time-resolved measurements, since the reorganization processes take longer. Currently, the two views are merging, as it is likely that both mechanisms contribute, but the material and laser parameters determine their respective share. An in-depth review of available theories is given by Bonse and Gräf (2020).

When LIPSS are irradiated with further pulses, self-focusing in the rifts occurs, which deepens the structures and eventually leads to the formation of conical structures. This was first reported by Her et al. (1998), who irradiated a Si sample in SF_6 with 500 pulses at a fluence of $1\,\mathrm{J\,cm^{-2}}$ and subsequently observed micron-sized, sharp, conical spikes. Since then, similar structures were also created on metals such as titanium, stainless steel and aluminum (Ahmmed et al., 2015).

The size and shape of the structures is significantly influenced by the sample material, which determines the melting and ablation threshold, the laser parameters and the processing environment. Key parameters controlling the size include the laser wavelength (Maragkaki et al., 2017), the pulse length (Crouch et al., 2004b; Her et al., 2000), the energy fluence (Bonse et al., 2002; Her et al., 2000; Peng et al., 2015) and the number of incident pulses (Bonse et al., 2002; Nayak and Gupta, 2010; Tull et al., 2006). The shape is mainly determined by the laser polarization (Nayak and Gupta, 2010) and the processing medium. Inert, gaseous media such as air, vacuum and N_2 lead to blunt cones, while structuring in atmospheres containing halogens, e.g. SF_6 or Cl_2, results in sharp spikes (Her et al., 1998; Sheehy et al., 2005; Younkin et al., 2003). This is attributed to laser-induced chemical etching by the volatile compounds (Her et al., 2000). Liquid processing media such as water or alcohol greatly impact the thermal transport processes, inducing much smaller structures (Zhang and Sugioka, 2019). Another important parameter is the laser incidence angle as the structures always point in the direction of the incoming light.

Samples with laser-induced, conical surface structures feature two advantageous properties. They are superhydrophobic and highly light absorbing. Incident light gets trapped in the high aspect ratio structures, enforcing multiple interactions with the enlarged surface. This enhances the total absorption and suppresses directed reflection as the escaping light is considerably scattered. Furthermore, processing with ultrashort pulses facilitates doping the surface layers with other elements, thereby adding intermediate energy bands. For silicon, the combination of structuring and simultaneous doping was shown to increase the absorption to near unity from the UV (ultraviolet) to near-IR (infrared) range, which is beyond its bandgap at roughly 1.1 µm (Crouch et al., 2004a; Younkin et al., 2003). The deep black of the initially silver-greyish Si surface after ultrashort laser pulse treatment has led to the name *black silicon*.

If samples larger than the focal spot size are required, scanning the focus over the surface by either moving the sample or the laser itself is a viable option. In this case, the accumulated fluence profile

needs to be as homogeneous as possible to achieve consistent surface structures over the whole area (Ahmmed et al., 2015; Neumann et al., 2018). It should be noted that due to the before mentioned incubation effects, the scan parameters, mainly the velocity in combination with the laser repetition rate, also influence the structure formation. Once the processing system is set up, ultrashort laser pulse processing provides a contactless, time and cost efficient tool with processing rates of up to $\mathrm{m^2\,s^{-1}}$ (Bonse and Gräf, 2020), which aids in the fabrication of targets with highly light absorbing front surface structures.

2.3.2. X-ray generation

When the hot electrons that are produced in the front surface plasma during a high intensity laser matter interaction, see Section 2.2.4, propagate through the initially cold and only barely ionized target bulk, they generate X-ray radiation. The shape of the X-ray spectrum depends on the target material and the plasma conditions, specifically, its temperature, density and ionization state. Therefore, the generated radiation gives a unique diagnostic opportunity to experimentally study plasma conditions and measure the underlying electron distributions (Chen et al., 1993; Neumayer et al., 2010). Furthermore, the ultrashort and bright bursts of X-rays with photon numbers in the order of 10^{11} per Joule of laser energy (Park et al., 2006; Theobald et al., 2006) are an excellent tool to probe matter in subsequent applications (Bouffetier et al., 2020; Glenzer and Redmer, 2009). There are two types of radiation contributing to laser generated X-ray spectra, that is, characteristic line emission and broadband continuum radiation.

Characteristic line emission. Characteristic line emission is caused by a vacancy in a low energy level $\mathcal{E}_f$ of an excited ion, which is subsequently filled by an electron transitioning from a higher energy level with energy $\mathcal{E}_i$. These transitions are accompanied by the emission of either an Auger electron or an X-ray photon with energy $\mathcal{E}_{\mathrm{ph}} = \mathcal{E}_i - \mathcal{E}_f$, and as the energy levels are isotope and ionization state specific, the X-ray energies provide a characteristic signature of the state of matter. Of particular interest is K-shell radiation, which is produced when an electron transitions to the lowest energy level with principal quantum number $n = 1$. If the electron originates from the L-shell ($n = 2$) or the M-shell ($n = 3$), the radiation is called K_α (see Fig. 2.5 (a)) or K_β, respectively. Generally, lower temperatures of the hot electrons are favorable for creating K-shell radiation, as the cross section for inner shell ionization by electron impact peaks in the keV range. For silicon, the cross section has a maximum at roughly 7 keV (Llovet et al., 2014, p. 26 and 47).

Resonance transitions of highly ionized ions are commonly named after the neutral ions with the same isoelectronic sequence, which is exemplified in Table 2.1. As an example, the L- to K-shell transition of a Si atom with only two remaining electrons, as illustrated in Fig. 2.5 (b), is called He-like K_α or, in short, Si He_α. An exception from this naming is the H-like resonance transition, which is more often referred to as Lyman (short: Ly) line. The spectra of these highly ionized ions resemble the ones of the respective neutral atoms, but are shifted to higher energies with increasing nuclear charge.

If more than one excited electron is present, so-called **satellite lines** arise, which is illustrated in Fig. 2.5 (c). Satellite lines have lower energies than the resonance line, because the electric potential of the nucleus is reduced by one or more spectator electrons in the outer shells. This group of additional lines add up to a red wing accompanying the resonance line. Ions with an empty inner shell, meaning both K-electrons are removed, give rise to another subset of characteristic emission lines, which are hypersatellites, i.e., satellites of satellites. Such **hollow ions**, as shown in Fig. 2.5 (d), are most likely produced by photoionization, for which the cross section is proportional to n^{-5}, while for electron impact ionization it goes with n^3 (Skobelev et al., 2012). In highly inhomogeneous plasmas, which are likely produced during the irradiation of targets with ultrashort pulses with ultrahigh contrast

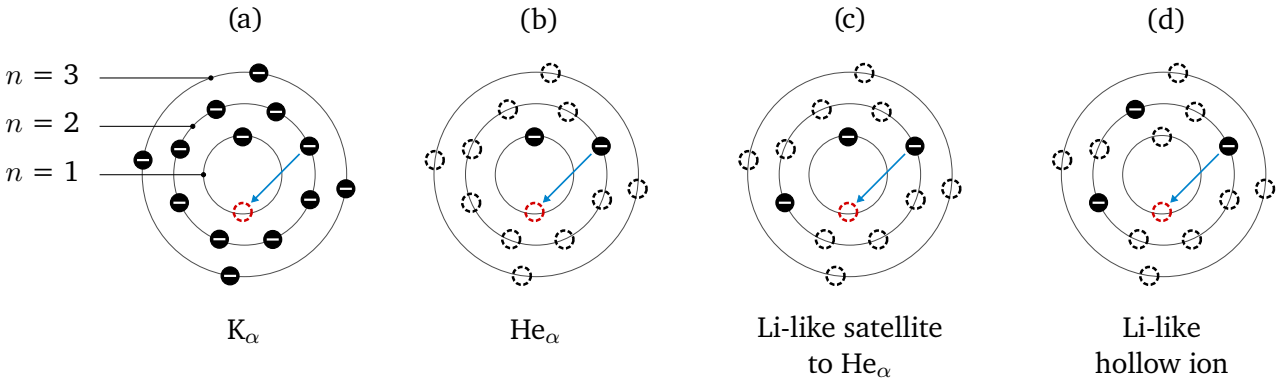

Figure 2.5.: Schematics of exemplary X-ray transitions in a Si atom ($Z = 14$). (a) The Si K_α line is emitted by a singly ionized atom with an electron decaying from the L-shell ($n = 2$) to a vacancy (dotted) in the K-shell ($n = 1$). (b) A 12-times ionized Si atom with two remaining electrons is He-like, therefore the emission line is referred to as Si He_α. (c) With an additional electron in an outer shell (here $n \geq 2$), a Li-like satellite line to the Si He_α is emitted. The transition energy is lowered due to the spectator electron screening the nuclear potential. (d) If more than one vacancy exists in the lowest shells while outer shells are populated, the ion is called hollow. The illustrated Si ion has three remaining electrons and is therefore Li-like.

($> 1{\times}10^{10}$), the photons produced in the hot front part ionize atoms in the cold part, where the outer electrons of the atoms have not been removed by electron impact ionization yet. The resulting spectrum from such an inhomogenous plasma with extreme spatial temperature and density gradients features a highly complex, quasi-continuous structure (Skobelev et al., 2012). As the number of electrons increases for higher Z materials, the number of potential emission lines becomes incredibly large. A very detailed, if not entirely complete, listing of characteristic X-ray energies can be found in the *X-ray Data Booklet* (Thompson et al., 2009) or the *Chianti Database* (ChiantiWeb, 2021).

The X-ray photons emitted by radiative transitions are not monochromatic. The finite life time of the excited states translates to a natural line width, which can be determined by applying Heisenberg's uncertainty principle. In addition, the lines are broadened by the internal plasma pressure, by the temperature distribution and by the surrounding electric field fluctuations (Gigosos, 2014). This, in turn, can be utilized to draw conclusions as to the temperature and density of the plasma by analyzing the line shapes. Furthermore, the line ratios can be included in the analysis as the ionization state distribution is also temperature and density dependent. Fig. 2.6 shows Si spectra at constant density for different temperatures, illustrating the significant changes caused by varying plasma conditions.

Table 2.1.: Overview of ionization states of Si listing the number of remaining electrons, the name, the ground state configuration (Demtröder, 2010), the respective isoelectronic sequence and the energies of the respective K_α radiation (Thompson et al., 2009).

no. of electrons	name	ground state	isoelectronic sequence	K_α in eV
1	Si-XIV	$1s$	H-like	2006
2	Si-XIII	$1s^2$	He-like	1865
3	Si-XII	$1s^2\ 2s$	Li-like	$\sim$ 1840
4	Si-XI	$1s^2\ 2s^2$	Be-like	$\sim$ 1820
⋮	⋮	⋮	⋮	⋮
14	Si-I	$1s^2 2s^2 2p^6 3s^2 3p^2$	-	1740

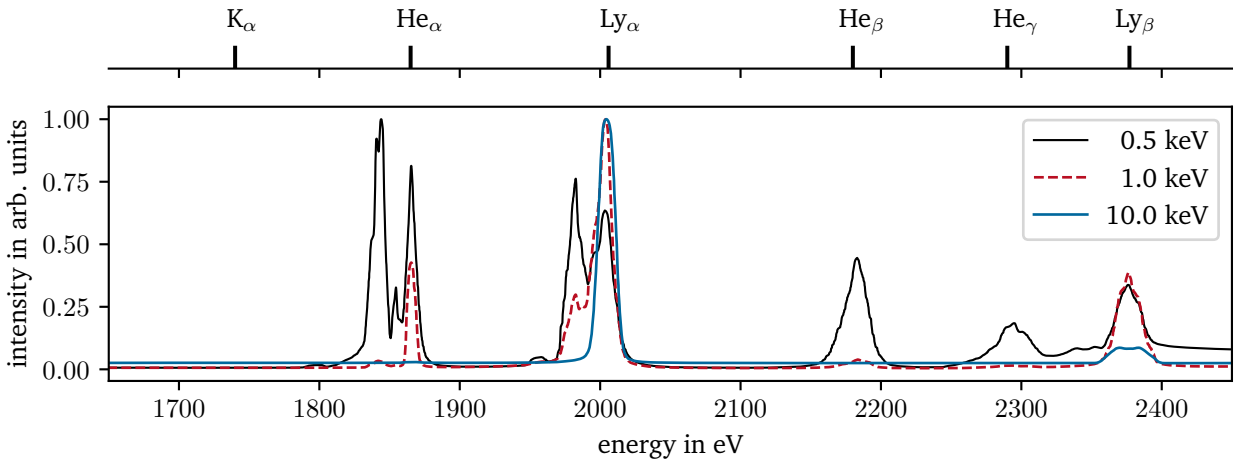

Figure 2.6.: X-ray emission spectra of Si with an electron density of $n_e = 1\times10^{23}\,\mathrm{cm}^{-3}$ for different temperatures. All depicted temperatures are too hot to produce cold K_α emission. With rising temperature, the atoms get increasingly ionized, so that at 10 keV (blue) only Lyman lines are generated. The peaks to the left of the labeled resonance lines are single or summed satellite lines. Usually, experimentally measured spectra are composed of a combined emission of different plasma densities and temperatures. The spectra were calculated by S. Sander with the collisional-radiative code FLYCHK (Chung et al., 2005), convoluted with an instrument function to model the spectral broadening by a diagnostic, and normalized to the most intense emission line.

Continuum emission. The second type of radiation contributing to laser-produced X-ray spectra is broadband continuum emission. The free electrons propagating through the target can interact with the electric field of the ions, thereby generating **bremsstrahlung**. Depending on the laser intensity and plasma parameters, this radiation is in the 100 eV to MeV range (Gibbon, 2005). This mechanism is of particular importance for low-Z plasmas, when most ions are fully stripped, or higher-Z plasmas at high temperatures. Also, free electrons can recombine with ions, thereby emitting **recombination radiation** with the sum of their kinetic and potential energy. This kind of radiation shows an edge structure, which corresponds to the atomic state transitions. Furthermore, the spectrum is broadened by Compton-scattering, which by itself does not generate radiation, but induces a red-shift in monochromatic radiation. However, since this mechanism becomes relevant at X-ray energies in the 100 keV range (Thompson et al., 2009), it can be neglected for Si spectra in the energy range of its resonance transitions.

To apply laser-driven X-ray sources in secondary applications, maximizing the photon yield, minimizing the source size and optimizing the conversion efficiency are essential. Increasing the photon yield is a highly complex topic. It depends on the target density, the electron temperature, and therefore the laser intensity, the K_α emission cross section, the photon mean free path, the photoabsorption cross section, the fluorescence yields, in other words the probability of a vacancy being filled by a radiative process instead of an Auger process, the target thickness and the laser incidence angle (Salzmann et al., 2002). Studies have shown that electron reflux in the target is beneficial for laser intensities exceeding $1\times10^{17}\,\mathrm{W\,cm}^{-2}$ (Neumayer et al., 2010; Theobald et al., 2006), and is more important than the target thickness (Park et al., 2006). In addition, the applications also pose varying constraints on the precise X-ray energy and the bandwidth of the source. For example, cold line radiation is favorable for purposes requiring a narrow bandwidth, since they have fewer to no satellite lines and Doppler broadening is reduced.

2.3.3. Ion acceleration

Another application of high intensity short laser pulses is the generation of ion beams with energies in the tens of MeV range. This was first demonstrated experimentally in the late 1990s by several groups including Hatchett et al. (2000) and Snavely et al. (2000), who observed roughly 10^{13} protons with energies of up to 55 MeV. Theoretical descriptions followed shortly after, e.g., by Wilks et al. (2001) and Mora (2003). After a controversial discussion, the acceleration was attributed to strong quasi-electrostatic fields at the target rear side and it was named *target normal sheath acceleration* (TNSA). Since then, several other mechanisms and models have been demonstrated, but as they are not relevant for this thesis, the interested reader is invited to consult other sources, e.g., by Daido et al. (2012) and Macchi et al. (2013).

The TNSA mechanism occurs when an overdense, thin target of micrometer thickness is irradiated with an ultrashort pulse with intensities exceeding $10^{18}\,\mathrm{W\,cm^{-2}}$. In essence, the process consists of four steps, which are illustrated in Fig. 2.7. First, the laser creates a pre-plasma at the target front and heats the electrons therein (see Section 2.2.4). As the target is overdense, the laser cannot penetrate through. The hot electrons produced at the front then propagate to the target rear side, during which they are spread due to collisions with the target bulk. A small fraction of the hottest electrons escapes on the target rear side, but most are held back by the resulting Coulomb potential. The charge-up at the front induces a compensating current from the target bulk and the electrons start to recirculate, which results in a quasi-static charge-separation field at the target rear side while the target bulk itself remains quasi-neutral. According to the standard self-similar expansion model, the field strength is (Wilks et al., 2001)

$$E = \frac{k_\mathrm{B} T_\mathrm{e,hot}}{eL}\,, \tag{2.46}$$

where $L = c_s t$ is the local plasma scale length (eqn. 2.11). If the target vacuum boundary at the rear side is sharp, the electron sheath has a thickness of roughly a Debye length λ_D (Daido et al., 2012).

The field strength induced by the sheath, which is in the order of $\mathrm{TV\,m^{-1}}$, is strong enough to ionize atoms in the rear side surface layer. Preferred for this ionization are hydrocarbons that originate from the natural contamination layer, which is present at every target handled at normal conditions during its preparation. In the following, these ions are accelerated by the charge separation field normal to the target rear surface, thereby forming a directed beam with electrons traveling along. At last, the target bulk is destroyed by the shock wave originating from the front and random plasma expansion.

In 2003, Mora presented a model to describe the TNSA process based on a 1D, free expanding plasma. Under the assumption that there is a constant hot electron temperature $T_\mathrm{e,hot}$ and a sharp plasma vacuum boundary at the target rear side, the proton energy at the expansion front at time t is given by

$$\mathcal{E}_\mathrm{p,max} \approx 2 k_\mathrm{B} T_\mathrm{e,hot} \ln^2\left(\tau + \sqrt{1+\tau^2}\right) \qquad \text{with} \qquad \tau = \frac{\omega_\mathrm{p,i} t}{\sqrt{2 e_\mathrm{E}}}\,. \tag{2.47}$$

Here, $\omega_\mathrm{p,i} = \sqrt{n_\mathrm{e,0} Z e^2/(m_\mathrm{i}\epsilon_0)}$ denotes the ion plasma frequency and e_E is Euler's number. With this equation, however, the maximum proton energy is not limited, which is in contrast to the observed energy spectra that typically exhibit an exponential energy spectrum with a cut-off at a maximum energy. To overcome this issue, Fuchs et al. (2006; 2007) introduced an acceleration limit based on the energy transfer time, which varies depending on the laser pulse length τ_L. The time t in eqn. 2.47 is replaced with an effective acceleration time

$$t_\mathrm{acc} = \begin{cases} 1.3\,\tau_\mathrm{L} & \text{for } \tau_\mathrm{L} = (0.15 – 10)\,\mathrm{ps} \text{ (Fuchs et al., 2006),} \\ \alpha(\tau_\mathrm{L} + t_\mathrm{transfer}) & \text{for } \tau_\mathrm{L} = (30 – 100)\,\mathrm{fs} \text{ (Fuchs et al., 2007).} \end{cases} \tag{2.48}$$

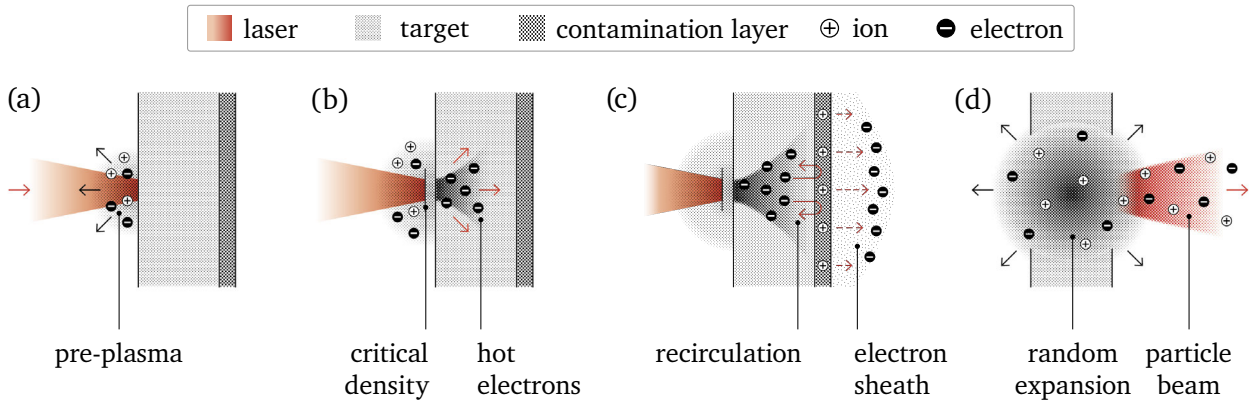

Figure 2.7.: Schematic of the target normal sheath acceleration (TNSA) mechanism. (a) A target is irradiated with a high intensity laser, which leads to the formation of a pre-plasma on the target front side. (b) The expanding pre-plasma shifts the position of the critical density towards the incoming laser, which cannot propagate further into the target. At the same time, the hot electrons generated in the pre-plasma travel to the target rear side. (c) These hot electrons ionize the contamination layer at the target rear side and build an electron sheath, which is constantly replenished by recirculating hot electrons. The charge separation at the rear side results in a strong electric field (dashed arrows). (d) The ions are accelerated normal to the target surface into vacuum and electrons travel along, forming a directed particle beam. Lastly, the target bulk is destroyed by the shock wave and random plasma expansion. *Drawings by Florian Schimanski.*

For short pulse duration, a minimum time $t_{\mathrm{transfer}} = 60\,\mathrm{fs}$ for the energy transfer between electrons and ions as well as an intensity dependent parameter α are added. The latter varies linearly from α=3 at $2\times10^{18}\,\mathrm{W\,cm^{-2}}$ to α=1.3 at $3\times10^{19}\,\mathrm{W\,cm^{-2}}$ and above.

In addition to the fluid expansion based approach by Mora (2003), several other models for TNSA were developed over the years. A selection of these models, which are either quasi-static or hybrid approaches, are compared in Perego et al. (2011). For derivations of the sheath radius, the conversion efficiency, the electron number and the electron density in the sheath, which are input parameters required for some of the theoretical descriptions, see e.g. Daido et al. (2012). In general, it should be noted that such scaling laws often include phenomenological assumptions, are purely empirical or require precise measurements of the input parameters, which are often missing. As a result, the applicability of the scaling laws is only valid in certain parameter ranges.

To achieve TNSA, it is beneficial to have a sharp and unperturbed density gradient at the target rear side. A long plasma scale length would lower the accelerating field strength (compare eqn. 2.46), while perturbations lead to an inhomogeneous accelerating field and in the worst case can prohibit the build-up of a sufficient electron sheath. Such unwanted effects can be caused by shock waves coming from the target front or early plasma formation by the refluxing of hot electrons. Controlling two key components of the experiment can mitigate or even prevent these issues. First, increasing the laser contrast and limiting the laser pulse length is advantageous (Wilks et al., 2001). However, laser systems with longer pulse lengths ($> 0.5\,\mathrm{ps}$) usually provide higher pulse energies, which seems to be a key factor in increasing the maximum proton energies (Zimmer et al., 2021). Also, electron heating can benefit from an increased pre-plasma scale length on the front, which makes choosing the optimal laser contrast challenging. Second, it is important to optimize the target thickness for the respective laser parameters. The minimum target thickness is limited by the shock velocity, since it should be thick enough to prevent the shock wave to break through. However, at the same time the target should be as thin as possible to allow the hot electrons to reach the rear side and reduce the electron spread as they propagate through the target. A lower electron divergence leads to a smaller transverse sheath size with higher charge densities, which in turn results in larger accelerating field strengths (Daido

et al., 2012). Thin targets also increase the overall refluxing and with this the hot electron temperature, which results in higher proton energies (see eqn. 2.47). Typically, TNSA targets are 100 nm to several micrometers thick (Daido et al., 2012).

TNSA favors light ions, protons in particular, as they feature the best charge to mass ratio (Roth and Schollmeier, 2017). Targets that receive no special treatment right before the shot are always coated with a natural contamination layer made of hydrocarbons, which stem from the surrounding air. The ions originating from this layer experience the highest field strengths, which means that the available protons are accelerated first due to their high charge to mass ratio. Other ion species, both from the bulk and the contamination layer, subsequently experience a reduced accelerating field as it is partially screened by the already accelerated protons. In targets made of low-Z materials, less energy is converted to bremsstrahlung when the electrons propagate through the target bulk. Therefore, the electron temperature is higher and the ion cut-off energy is increased. Furthermore, the electron spread is lower than in high-Z target, resulting in a smaller transverse sheath size and therefore higher accelerating field strengths. However, low-Z targets also are more likely to produce density filaments, which results in inhomogeneous accelerating fields and filamented ion beam profiles. If subsequent applications favor smooth beams over high ion energies, high-Z target materials are advisable. An extensive overview of other beam parameters and target dependencies can be found in Roth and Schollmeier (2017).

2.3.4. Influence of target front surface structures

For many experiments and subsequent applications such as the described X-ray generation and particle acceleration, it is crucial to increase the energy deposited into the target. This can be achieved by either modifying the laser systems or by tailoring the interaction region and thereby influencing the heating processes, which in turn can enhance the absorption efficiency. In addition, controlling these processes helps to generate the optimum hot electron spectrum in terms of number and temperature to suit the specific subsequent process or application.

One of the key parameters determining which heating mechanisms prevail is the pre-plasma scale length, as discussed in Section 2.2.4. It can be manipulated by changing the target density, the laser intensity and the laser pulse shape, especially the temporal contrast. Significant effort has been and is spent on creating long gradient pre-plasmas by modifying the ASE contrast level, as well as introducing intentional pre-pulses preceding the main pulse (Kaluza et al., 2004; McKenna et al., 2008). Also, foam targets were employed to reduce the target density in the primary interaction region (Nakamura et al., 2010; Passoni et al., 2014). The near-critical plasmas produced these ways, however, can cause a filamentation of the incoming laser beam, which in turn can limit the energy transfer from the laser pulse into the plasma (McKenna et al., 2008). A different approach is adding structured profiles to the target front surfaces, which has proven to be a very effective option to control the pre-plasma conditions more tightly.

The typical scales describing the interaction between laser and target are to a great extent determined by the laser wavelength λ_L, the density scale length L, the collisionless skin depth l_s and the quiver electron distance. All of these values are usually between 10 nm and 1 µm (Cristoforetti et al., 2017), therefore an obvious approach is to add nano- or microstructures to roughly match these scales. With such structures, the effective target density in the front region is lowered as well, allowing the laser to penetrate further while simultaneously reducing the probability of developing instabilities.

Adding front surface structures (FSS) modifies the interaction in several ways. First, FSS increase the surface area, allowing more electrons to interact with the laser. Second, by increasing the penetration depth, both the volume of the interaction region and the overall interaction time are extended. Third, the geometry of the structures can change the effective laser incidence angle and can lead to a more complex interference of the incident and the scattered light. All these factors alter the efficiency of the different heating mechanisms. Oblique angles between laser and target surface will promote Brunel heating, enlarged volumes of near-critical regions, where the laser can penetrate, will enhance resonance absorption, varying densities across the structures and the gaps between will facilitate stochastic heating, convenient structure spacing relative to the laser wavelength will allow direct laser acceleration and so forth.

Another effect of the structures is their influence onto the electron trajectories. They can both narrow (Jiang et al., 2014a) and widen (Klimo et al., 2011) the angular distribution of the hot electrons. In turn, subsequent X-ray generation (Serebryakov et al., 2019) and ion acceleration (Jiang et al., 2014a; Zhao et al., 2010) is enhanced or diminished.

Over the last years, parallel surface structures were studied intensively. Depending on their diameter, height, spacing and distribution, they are usually classified into two groups. Pillar or tower structures, as depicted in Fig. 2.8 (a), are evenly distributed, have flat tops and are of micron length and height, whereas nanowires or nanobrushes, as shown in Fig. 2.8 (b), typically feature submicron diameters at micron length and are randomly distributed. Experiments and simulations showed that nanowires can increase the number and temperature of hot electrons (Cristoforetti et al., 2017; Jiang et al., 2014a; Zhao et al., 2010), and can therefore enhance X-ray generation (Hollinger et al., 2017; Jiang et al., 2014b; Kulcsár et al., 2000; Sedov et al., 2019; Serebryakov et al., 2019) and ion acceleration (Bailly-Grandvaux et al., 2020; Klimo et al., 2011; Sedov et al., 2019; Vallières et al., 2021). Pillars are particularly suited to narrow the angular distribution of the heated electrons. The electrons are confined by the charge-field of the immobile ions and the B-fields evolving around the hot electron currents in each pillar. This guiding effect at the target front is transferred to the rear side, resulting in smaller and stronger sheaths, thereby enhancing ion acceleration. However, especially pillars with diameters in the order of the focal spot size resemble a flat target with two offset surfaces and target positioning becomes extremely relevant.

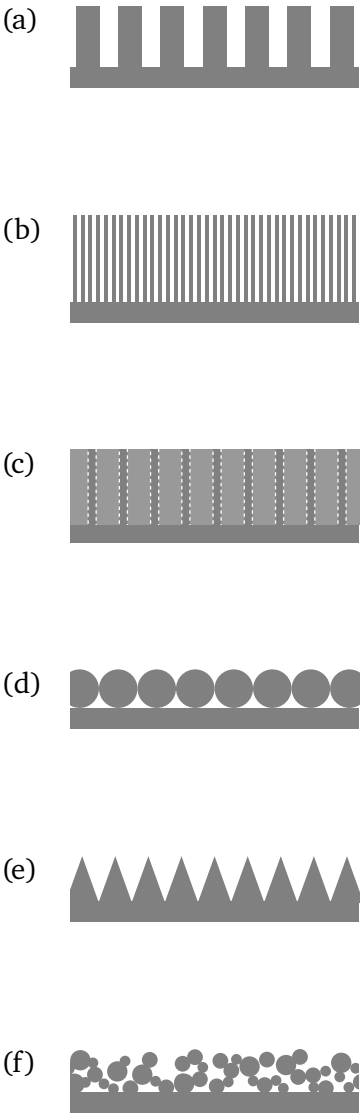

Figure 2.8.: Cross sections of previously investigated front surface structures. (a) Pillars, microwires or towers, (b) nanowires or -brushes, (c) microtubes, (d) nano- or microspheres, (e) triangular structures and (f) nano- or microclusters. The respective references are listed in the text.

Even though nanowires have shown excellent results when used with ultra-high contrast ($> 10^{11}$), short pulse (< 100 fs) laser systems, preplasma expansion and long pulses can significantly reduce their impact. For one thing, the dissolution of the structures can cause a "plasma-shutoff", meaning the critical density boundary is shifted in front of the structures, preventing the laser from interacting with the structured volume. Another effect of dissolving dense nanowire arrays can be a decrease in the energy of accelerated ions. They then resemble thicker targets, the electrons collide more often before reaching the rear and, as a result, less energy is contained in the accelerating sheath (Sedov et al., 2019; Vallières et al., 2021).

Another type of design are waveguiding structures such as microtubes, as shown in Fig. 2.8 (c). They have been investigated regarding their influence on electron, ion and X-ray generation (Bailly-Grandvaux et al., 2020; Ji et al., 2016). The tubes enhance self-focusing of the laser by creating a radial density gradient in the structures, which increases the effective laser intensity. Furthermore, they confine the plasma and cause complex interference patterns of the incoming and reflected light, thereby promoting stochastic heating.

Other microstructure types studied over the years include microspheres (Fig. 2.8 (d)) (Klimo et al., 2011; Margarone et al., 2012), triangular grooves (Fig. 2.8 (e)) (Blanco et al., 2017, 2019) as well as nanoclusters (Fig. 2.8 (f)) (Murnane et al., 1993). In addition, spike-shaped microstructures were studied by our group (Ebert et al., 2020; Neumann, 2018). Their sloped angles and sharp tips provide a unique interaction volume that, due to its micron scale size, is particularly interesting for high energy laser systems with pulses exceeding 0.5 ps, since they retain their shape longer than nanostructures. These microstructures were further investigated during this thesis and will be the focus of the following chapters.

A comprehensive analysis of the key parameters governing this complex field of front surface modifications is challenging. The fabricated microstructures are likely to have imperfections, and often the precise laser parameters on shot are unknown. Pre-plasma formation by pre-pulses or by low ASE contrast complicates this investigation, as it is challenging to measure but was also identified as one of the most influential parameters (Blanco et al., 2019). Often, it is unclear as to which contrast and pulse length the structures "survive" and still have a positive impact. Here, simulations are of limited help, as they usually do not reproduce the complete laser pulse profiles. To add to that, theoretical studies are often two-dimensional, therefore their results offer only partial insights.

For all structure types, the target fabrication process also needs to be considered when evaluating their overall usefulness. The processes should be as cost and time efficient as possible, while also providing high precision and a wide range of shapes and sizes to tailor the exact structure geometry to the needs of the experiment. Furthermore, straightforward alignment is desirable for high repetition rate experiments.

To sum up, modifying target front surfaces with nano- or microstructures has shown great potential to increase the energy conversion between laser and target. They enlarge the target surface area, thus enabling more electrons to interact with the laser, and increase interaction volume and time by confining the electrons. Furthermore, the FSS influence the relevant heating mechanisms, which in turn changes the hot electron temperature. The optimal structure sizes and geometries depend on the subsequent application, e.g., ion acceleration, X-ray or gamma generation, and can strongly vary for each specific laser system. In the following, the methods and setups used to investigate laser-induced ion and X-ray outputs are described.

3. Methodology

Laser matter interactions can be studied using a wide variety of experimental and theoretical methods. The diagnostics chosen to study a particular scenario vary based on the objectives, such as radiation type, respective time scales, required resolution and signal intensities. For the studies conducted as part of this thesis, the experimental characterization of ion beams and X-ray radiation is of interest. Therefore, suitable diagnostics for these quantities are discussed. Since certain parameters of laser matter interactions cannot be measured experimentally, theoretical studies were conducted as well. Thus, a short introduction to the relevant laser-plasma simulation codes is given.

3.1. Experimental diagnostics

Laser-accelerated ion beams typically exhibit a broad, exponentially decaying energy spectrum with an energy dependent divergence angle. They require diagnostic setups with a high-dynamic range as well as good spectral and spatial resolution. Thomson parabolas are well suited for ion species and spectral analysis. Here, they are used in combination with imaging plates, which feature excellent resolution properties as well as a high dynamic range. The second diagnostic employed to characterize the spatial and spectral profiles of the ion beams are radiochromic films. The generated X-ray spectra are analyzed via wavelength dispersive spectroscopy with crystals.

3.1.1. Thomson parabola

The concept of a Thomson parabola spectrometer was first introduced by J. J. Thomson (1907), who proposed this setup as a mass spectrometer. It is based on the deflection of charged particles in electric and magnetic fields and can be used to distinguish the particles according to their charge to mass ratio.

A schematic of a Thomson parabola is shown in Fig. 3.1. First, the incoming particle beam is reduced to a one dimensional source by a pinhole with a typical diameter in the order of 100 µm. After passing the pinhole, the transmitted particles pass a combination of an electric field with field strength E and a magnetic field with strength B, before hitting a two dimensional imaging detector. Due to the Lorentz force

$$\boldsymbol{F}_\mathrm{L} = \boldsymbol{F}_\mathrm{E} + \boldsymbol{F}_\mathrm{B}\,, \tag{3.1}$$

particles moving along the z-direction are deflected in x-direction by the electric force $\boldsymbol{F}_\mathrm{E}$ and in y-direction by the magnetic force $\boldsymbol{F}_\mathrm{B}$. The equation can also be written as

$$\gamma m_\mathrm{i} \frac{\mathrm{d}\boldsymbol{v}}{\mathrm{d}t} = q\,\boldsymbol{E} + q\,(v_\mathrm{z} \times \boldsymbol{B}) \tag{3.2}$$

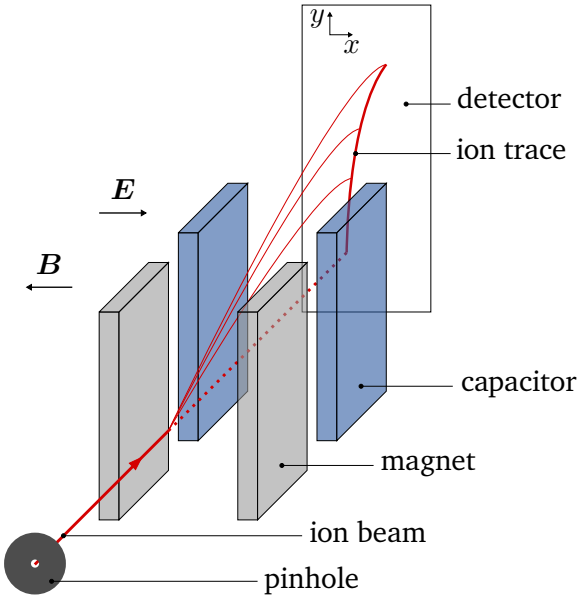

Figure 3.1.: Schematic of a Thomson parabola. The incoming particle beam is reduced to a one-dimensional source by a pinhole (dark gray). Then, the transmitted ions (red) are deflected by the $\boldsymbol{B}$-field of a magnet (light gray) in y-direction and the $\boldsymbol{E}$-field of a capacitor (blue) in x-direction. The deflection depends on the velocity of the ion, hence a beam with a broad energy spectrum is spread along a trace on the detector.

with the relativistic Lorentz factor γ and the particle velocity $\boldsymbol{v}$. From this it becomes clear that the overall deflection of the ion depends on its velocity v_z in the direction of travel, as well as its charge to mass ratio q/m_i. Due to this dependency, a Thomson parabola is able to resolve the energy spectra of ions with different charge to mass ratios, since they hit the detector along different traces as illustrated in Fig. 3.2 (a).

Typically, a permanent magnet is used to create the magnetic field. In contrast to the electric field, which is generated by capacitor plates and therefore susceptible to disturbances by electromagnetic pulses (EMPs) generated during the laser matter interaction, the deflection by the magnetic field can be reliably used to convert the ion traces to spectra. For this, the magnetic field strength B, the length L_B of the magnetic field and the drift length d_B between magnet and detector are required. The deflection is then given by

$$\Delta y = \frac{qBL_\mathrm{B}}{\gamma m_\mathrm{i} v_\mathrm{z}} \left(\frac{L_\mathrm{B}}{2} + d_\mathrm{B} \right), \tag{3.3}$$

and consequently the dispersion function for the particle energy can be written as

$$\mathcal{E}_\mathrm{i}(\Delta y) = \sqrt{\left(\frac{qBc}{\Delta y} \cdot L_\mathrm{B} \cdot \left(\frac{L_\mathrm{B}}{2} + d_\mathrm{B} \right) \right)^2 + (m_\mathrm{i}c^2)^2} - m_\mathrm{i}c^2 \,. \tag{3.4}$$

A detailed derivation can be found in Appendix A.1 and Alejo et al. (2016).

To get an accurate dispersion relation, it is essential to correctly measure all quantities, which is especially challenging for the $\boldsymbol{B}$-field considering its non-uniform behavior. This can be overcome with either simulations of the deflection with programs like *CST* or *GEANT4* or an experimental calibration based on filters (Alejo et al., 2014).

Figure 3.2 (b) shows an image of traces obtained from a laser particle acceleration shot. In brief, the evaluation procedure after acquisition consists of four steps. First, each trace is projected onto the

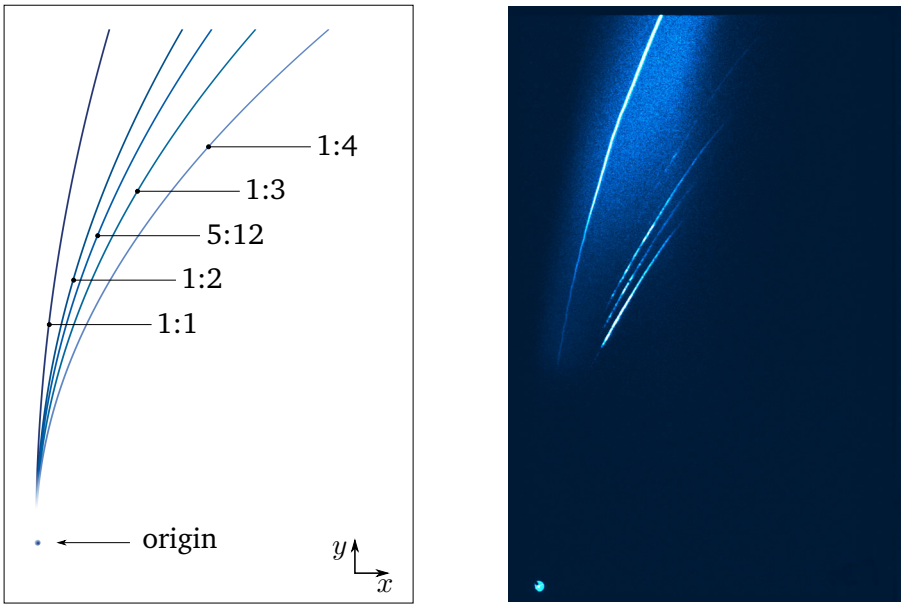

(a) (b)

Figure 3.2.: Illustration of Thomson parabola traces. (a) Theoretical traces for different charge to mass ratios q/m_i. The origin is illuminated by X-rays generated during the laser matter interaction, as they do not get deflected. (b) Exemplary image of ion traces taken during a laser particle acceleration experiment in false color display. The brightness corresponds to the energy deposited by the particles.

y-axis, so that the intensity of the trace is a function of displacement by the $\boldsymbol{B}$-field. Second, the displacement is converted to the corresponding energy using equation 3.4. Due to the non-linearity of this dispersion, the pixel width corresponds to differing energy interval sizes, therefore these need to be normalized in a third step. Last, the intensity is converted to a particle number based on the specific type of imaging detector used. Common options for detectors include fluorescent screens, image plates (see Section 3.1.2), radiochromic films (see Section 3.1.3), solid state nuclear track detectors such as *CR-39* and multi-channel-plates (MCP).

The data obtained using Thomson parabolas in the context of laser-particle acceleration can be subject to some complications. For instance, this diagnostic is prone to perturbations by electromagnetic pulses, which in extreme cases can lead to the crossing of traces. For such data, a decent analysis is almost impossible. Also, due to the utilization of a pinhole, the Thomson parabola only covers a small solid angle and therefore just captures a small fraction of the particle beam. If the Thomson parabola is poorly aligned or the ion beam is filamented, the acquired spectrum might not be representative. Another challenge is choosing the correct pinhole size. A smaller pinhole increases the resolution while also diminishing the intensity of the signal, therefore the pinhole size needs to be matched to each specific experiment.

In summary, Thomson parabolas allow a charge-to-mass specific measurement of continuous energy spectra with high resolution, if they are employed with good EMP shielding, the right pinhole size and in experiments generating a smooth spatial beam profile. The data quality also depends on the chosen imaging detector, which determines the dynamic range, the resolution and the repetition rate with which this diagnostic can be used.

Table 3.1.: Atomic compositions and thicknesses d of all layers of *BAS-SR*, *BAS-MS* and *BAS-TR Fujifilm* image plates (Bonnet et al., 2013). The magnetic layer of all types is made of $ZnMn_2Fe_5NO_{40}H_{15}C_{10}$ (*). For schematics of the structure see Fig. 3.3.

	SR		MS		TR	
layer	composition	d in µm	composition	d in µm	composition	d in µm
protective	C_2H_2O	6	C_2H_2O	9	no layer	0
phosphor	BaFBr	120	$BaFBr_{0.85}I_{0.15}$	115	$BaFBr_{0.85}I_{0.15}$	50
support	C_2H_2O	188	C_2H_2O	190	C_2H_2O	250
magnetic	(*)	160	(*)	160	(*)	160

3.1.2. Image plates

Image plates (IP) are versatile, two dimensional imaging detectors, which are sensitive to ionizing radiation such as X-rays and ions. These plates record signals with a high dynamic range of 10^4 to 10^5 and offer a high spatial resolution of 25 µm to 200 µm. IPs are EMP safe and can be reused, but they need to be read out and erased after each use. Therefore, they have to be exchanged between the shots and can only be employed as an offline diagnostic.

The lightweight, flexible, film like plates consist of several layers, which vary in thickness and composition depending on the specific image plate type. The sensitive component embedded in the phosphor layer is BaF[X]:Eu^{2+} with [X] being Gl, Br or I. This active layer is sandwiched between a protective and a support layer. Furthermore, a magnetic layer is added to the rear side, which allows to place the plate in diagnostic setups. Common IP types are *BAS-SR* (super resolution), *BAS-MS* (multipurpose standard) and *BAS-TR* (tritium) manufactured by *Fujifilm*. Their compositions are listed in Table 3.1 and schematics of the layer configurations are shown in Fig. 3.3. In the scope of this work, *BAS-SR* and *BAS-TR* IPs were employed.

Figure 3.4 shows a simplified level diagram of the active layer. Upon interaction with ionizing radiation, electrons are excited from the valence band to so-called F-centers (from the German word "Farbzentren"), which are inserted during the manufacturing process. After excitation, the electrons are trapped in these meta-stable states until the film is exposed to red light, e.g., during the read-out process with a scanner. In the scope of this work, a *Typhoon FLA7000* (GE Healthcare Life Sciences, 2021) scanner with a He:Ne laser was used. The red light lifts the trapped electrons to the conductive band, from which they rapidly recombine while emitting blue light. This process is referred to as photostimulated luminescence (PSL). The scanner rasters the image plate line by line, recording the location-dependent

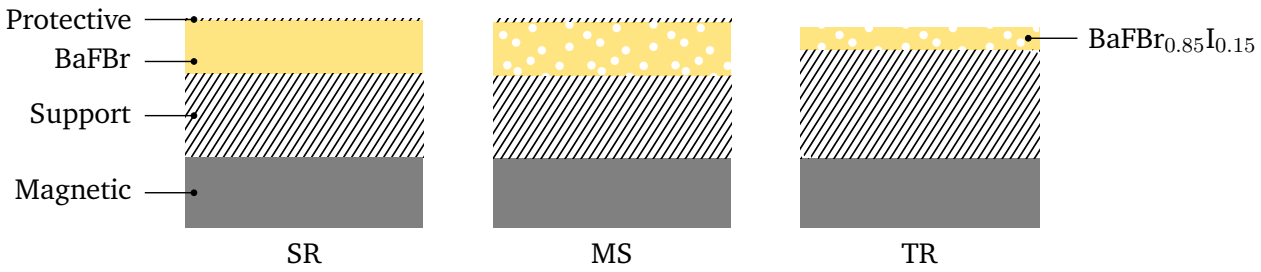

Figure 3.3.: Structures of image plates manufactured by *Fujifilm*. The active BaFBr layer (yellow) of *BAS-MS* and *BAS-TR* plates is doped with iodine (I). *BAS-TR* plates are manufactured without a protective layer. For atomic compositions and layer thicknesses see Table 3.1.

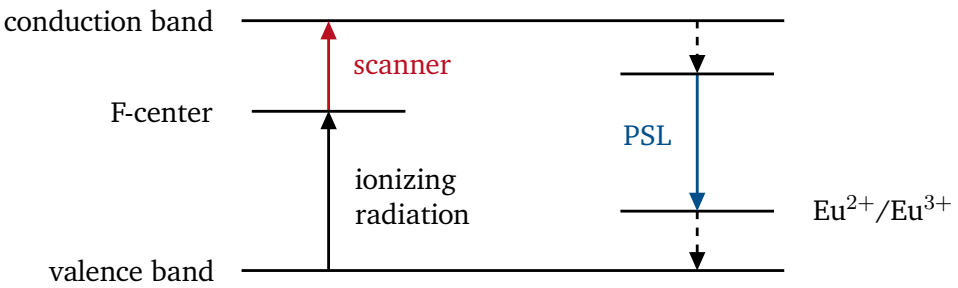

Figure 3.4.: Simplified schematic of the energy levels of an image plate. Electrons of the valence band are lifted to the F-centers via incident radiation. They stay in this meta-stable state until they are lifted to the conduction band by excitation through red light of a scanner. From here, they rapidly decay to an intermediate state, and the following decay to Eu^{2+} and Eu^{3+} levels releases a blue PSL photon. Afterwards, the electron falls back to the valence band.

intensity of the PSL signal. Consequently, a 2D grayscale image showing spatially distributed intensity information is formed. After the read-out process, the image plate can be erased by exposure to a white light source.

The PSL signal read from an IP is correlated to the amount of deposited energy, which is influenced by two factors. First, the particle type and energy determine the ionization processes and the penetration depth. Second, the chemical composition and layer thicknesses of the IP type define the sensitivity and size of the active volume as well as potential attenuation by the protective layer. Ions deposit most of their energy shortly before stopping, so they give rise to very dense regions of excited electrons. Depending on their energy, the depth of these regions in the active layer and the number of excited electrons varies. Unlike ions, X-ray beams deposit their energy uniformly throughout the entire active layer, while being only partially absorbed. IPs of the *BAS-TR* type allow the incident radiation to directly interact with the active volume. In contrast, *BAS-SR* and *BAS-MS* type IPs are better suited to experimental setups where the IPs are likely to be scratched or otherwise damaged, but here the radiation is attenuated by the protective layer before entering the sensitive layer. The energy distribution within the active layer is of interest, because the light of the scanner and the escape probability of the PSL photons are reduced with increasing penetration depth due to absorption and scattering (Stoeckl et al., 2017). Therefore, the signal strength not only depends on the number of excited electrons, but also on the detection probability, which in turn depends on the position of the excited electrons within the active layer.

Furthermore, the measured signal strength depends on the scanner components and the parameters chosen for the scanning process such as resolution, sensitivity of the photomultiplier and bit-depth. For an *FLA7000* scanner with exponential compression, the conversion formula from the bit values b to the PSL signal strength is given by

$$S_{\mathrm{PSL}} = \left(\frac{r}{100}\right)^2 \cdot \frac{4000}{s} \cdot 10^{-0.5L} \cdot 10^{L/G \cdot b} \tag{3.5}$$

with scanning resolution r, sensitivity s, latitude L and gradation G, all of which are stored in respective metadata files for each scan.

The scanner records the PSL signal with a photomultiplier tube, which can saturate if the incident signal is too intense. This can be prevented by inserting a ND (neutral-density) filter that attenuates the detected signal by a known factor during the scanning process. Another way to retrieve the full information is the recovery of the saturated pixels from subsequent scans. For this, a relation between the values of the first unsaturated scan and the initial PSL value needs to be calculated. To establish this relationship, the evolution of a number of unsaturated and non-zero pixels is analyzed over several

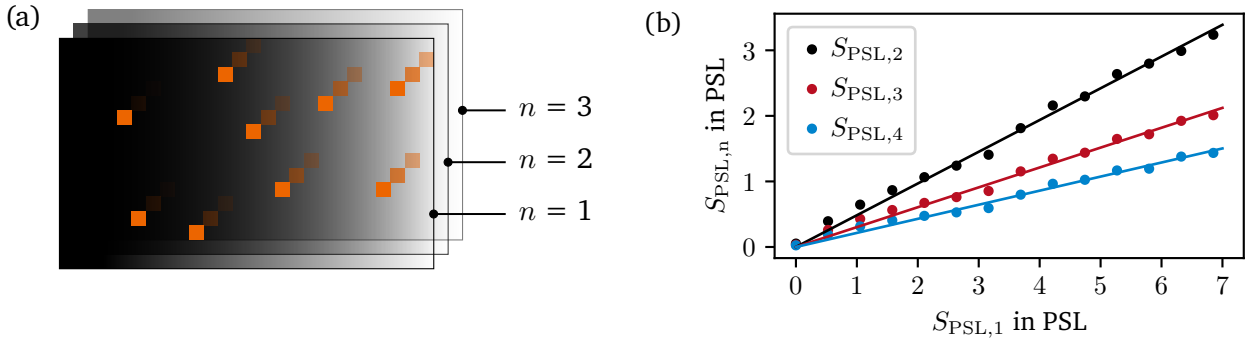

Figure 3.5.: Schematics illustrating the process of IP scan recovery. (a) The IP images are sampled by choosing the same set of random pixels from each of the three subsequent scans n. These pixels are then correlated via a linear relation such as equation 3.6 as shown in (b), where the n-th scan is a function of the 1st scan. With increasing scan number the slope decreases.

scans. With each scan, electrons are deexcited leading to increasingly faint images. For the recovery, a random set of pixels of the scanned image is chosen as illustrated in Fig. 3.5 (a) as first step. Then, a linear function of the form

$$S_{\mathrm{PSL,n}} = m_{\mathrm{n}} \cdot S_{\mathrm{PSL,1}} \tag{3.6}$$

can be fitted to the PSL-values $S_{\mathrm{PSL,n}}$ of the n-th scan as a function of the first scan $S_{\mathrm{PSL,1}}$ to find the gradient m_{n} for each scan as shown in Fig. 3.5 (b). With this, the values of the pixels that were saturated in the first scan can be determined.

Another effect that needs to be compensated is the spontaneous recombination of meta-stable states in the time between IP exposure and scanning. This so-called fading also depends on the IP type, radiation type and scanner as well as the ambient temperature. The functions found in literature differ, as the relevant parameters vary between the underlying data sets. For this reason, a calibration should be performed at the experimental site with the specific IPs if possible. This was not the case for this work, so the functions by Bonnet et al. (2013) and Boutoux et al. (2015), which are shown in Fig. 3.6, were used for ions and X-rays, respectively, since they employed the same *FLA7000* scanner as utilized in this work. An overview of further fading functions found in literature is given in Appendix A.2.

To convert the PSL signal to a particle number, the different sensitivities for the specific IP and radiation type, the fading function, scanning parameters and possibly a respective scan recovery function need to be taken into account. Since all these factors are influenced by experimental and readout conditions, applying calibration functions from literature add uncertainty to the measurement. However, since it was not possible to perform our own calibration in the scope of this work, the conversion functions for protons from Rabhi et al. (2017) were employed due to the use of the same scanner model (*FLA7000*) and the measured response for protons between 1 MeV and 200 MeV. The calibration curves measured by Meadowcroft et al. (2008) were used for X-rays.

In summary, even though image plates are an offline tool and the calibration is very complex, which makes it challenging to acquire decisive results in terms of absolute intensities, their versatility, flexibility, high dynamic range, re-usability and EMP-safety make them a valuable detector for high-intensity laser matter experiments.

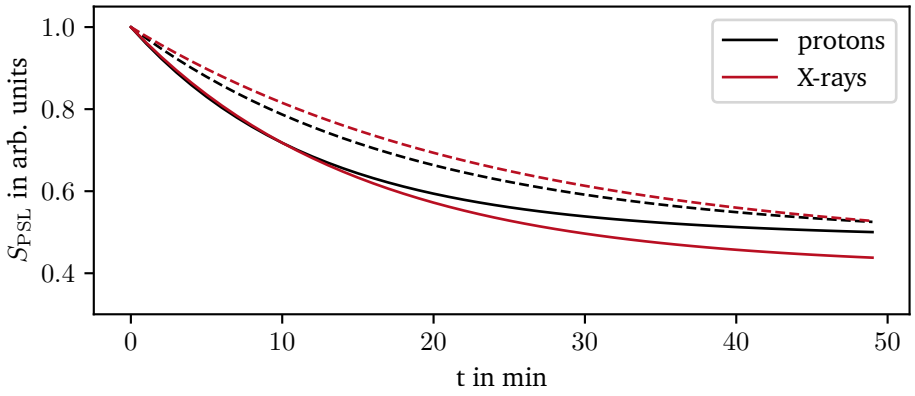

Figure 3.6.: Fading functions used for protons (black) and X-rays (red) as presented by Bonnet et al. (2013) and Boutoux et al. (2015), respectively. The signal S_{PSL} is normalized and plotted as a function of the time t between irradiation and scanning. The continuous lines represent *BAS-SR* and the dashed lines *BAS-TR* type IPs. Both publications employed *FLA7000* scanners. A more extensive comparison of fading functions available in literature is shown in Section A.2.

3.1.3. Radiochromic films

The spatial profile of an ion beam can be measured with radiochromic films (RCF), which when used in a stack configuration can also record the energy spectrum of the ions. These films are sensitive to ionizing radiation and can quantitatively measure the energy deposited by photons, electrons and ions when interacting with the film. The key element of the films is an active layer that contains an active component, marker dye and stabilizers. Upon irradiation, the yellow films turn blue due to the polymerization of the active component. This discolorization is proportional to the absorbed energy dose. The films instantly start to self-develop and most of the discoloration occurs immediately after irradiation, but it can take up to 48 h before the polymerization is complete (McLaughlin et al., 1991). In general, the films can be handled within room light, but their exposure to sun light should be minimized as the films are sensitive to UV rays.

A variety of *GAFchromic*™ films by *Ashland* are available, which differ in structure and sensitivity. The types employed in the scope of this thesis are *HD-V2* (Ashland Advanced Materials, 2021b) and *EBT3* (Ashland Advanced Materials, 2021a), and schematics of their composition are shown in Fig. 3.7. While the *HD-V2* films are asymmetric and have the active layer with a thickness of 12 µm coated onto a clear, 97 µm thick polyester film, the layering of the *EBT3* films is symmetric. Here, the 28 µm thick active

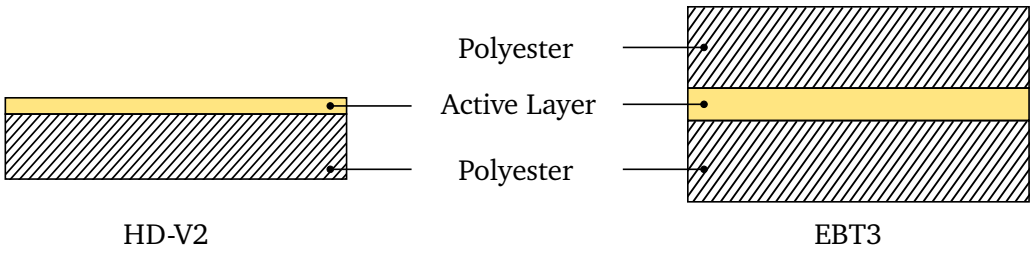

Figure 3.7.: Composition of *GAFchromic*™ radiochromatic films of type *HD-V2* and *EBT3*. *HD-V2* films are asymmetric and consist of an active layer (12 µm) on top of a polyester substrate (97 µm). The symmetric *EBT3* films are made of a 28 µm thick active layer which is sandwiched in between two polyester layers with a thickness of 125 µm each (Ashland Advanced Materials, 2021a,b).

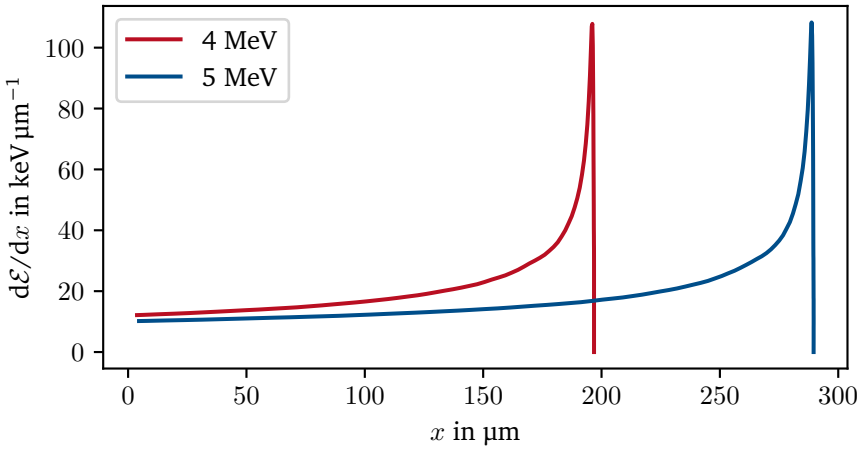

Figure 3.8.: Differential energy loss $\mathrm{d}\mathcal{E}/\mathrm{d}x$ of two protons with different initial energies in polyester as a function of penetration depth x. Shortly before the particles are stopped, the energy loss rapidly increases, which is called Bragg peak. The greater the initial energy, the further the proton can penetrate.

layer is positioned between two matte polyester substrates with a thickness of 125 µm each. The *HD-V2* films are less sensitive and recommended for doses between 10 and 1000 Gray (Gy) whereas the *EBT3* films are better suited for lower doses between 0.2 and 10 Gy.

RCFs are often utilized in a stack composition to simultaneously measure the spatial and spectral profile of an ion beam. For the spectral evaluation, the profile of the differential energy loss function of ions in matter is essential. According to the Bethe equation (Demtröder, 2017, p. 83f.)

$$\frac{\mathrm{d}\mathcal{E}}{\mathrm{d}x} = -\frac{Z^2 e^4 n_\mathrm{e}}{4\pi\epsilon_0^2 v_\mathrm{i}^2 m_\mathrm{e}} \cdot \left[\ln\left(\frac{2m_\mathrm{e}v_\mathrm{i}^2}{\mathcal{E}_\mathrm{ion}(1-(v_\mathrm{i}/c)^2)}\right) - (v_\mathrm{i}/c)^2\right] \propto \rho_\mathrm{m}\frac{Z^2}{\mathcal{E}_\mathrm{i,kin}}\,, \tag{3.7}$$

the differential energy loss, which is sometimes also referred to as stopping power, depends on the mass density ρ_m of the bulk material and the kinetic energy $\mathcal{E}_\mathrm{i,kin}$ of the ion. In the full expression, Z denotes the charge number, v_i the velocity of the ion, $\mathcal{E}_\mathrm{ion}$ the ionization energy, n_e the electron density and m_e the electron mass. While the energy loss is relatively small for high energies, it rapidly increases for low energies. As a consequence, the penetration depth of an ion increases with rising initial energy and most of its energy is deposited shortly before it stops. Figure 3.8 shows the differential energy loss functions of two protons with different initial energies. The characteristic spike in energy deposition shortly before it falls to zero is called Bragg peak. The curves were calculated using the Monte-Carlo based program SRIM (Stopping and Range of Ions in Matter) (Ziegler et al., 2010).

Modeling the energy loss can be used to design the film stack according to the experimental needs. The overall detectable ion energy range of such an RCF stack is determined by the materials of the individual layers and the stack length. By placing absorbers between the films, the energy range can be increased at reasonable stack sizes and costs. Often, the first layer of a stack is aluminum foil to protect the films from debris, block heavy ions and shield the films from light generated during the interaction. By placing the films orthogonal to the direction of beam propagation, the energy-dependent, transverse cross section of the beam is captured. The films of an exemplary RCF stack are depicted in Fig. 3.9. Each film shows the 2D spatial beam profile of ions with a specific energy.

After irradiation and a waiting time of at least 48 h to ensure complete polymerization, the films are scanned with a flat-bed scanner. For the data evaluated in this thesis, the 16-bit RGB *CoolScan 9000ED* scanner was used. During the scan, the alignment of the film is important, because the polymer chains

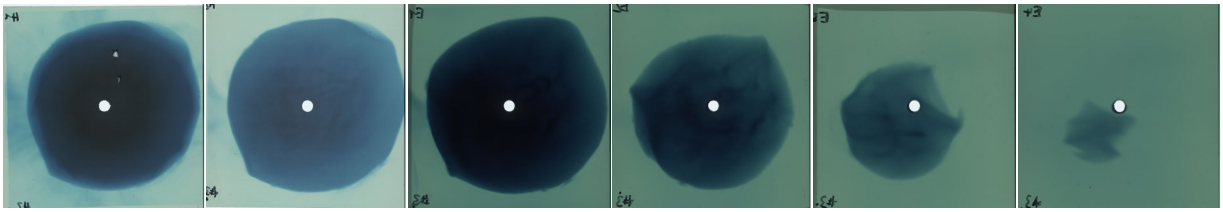

7.4 MeV 13.8 MeV 18.7 MeV 24.2 MeV 30.1 MeV 36.2 MeV

Figure 3.9.: Irradiated films of an exemplary RCF stack with films corresponding to energies between 7.4 MeV and 36.2 MeV, as annotated. The degree of the blue discoloration depends on the amount of absorbed energy, thus, each film shows the transversal profile of protons with a specific energy, as protons with higher energies penetrate further into the stack. The *HD-V2* films used for the first and second layer are slightly lighter than the *EBT3* films of the rest of the stack due to their differing composition and sensitivity. The hole in the middle of each film allows the simultaneous use of further diagnostics.

have a specific direction and the RGB value can drop by approximately 0.05 % per degree if the film is rotated in the scanning plane (Micke and Lewis, 2021).

The particle numbers can be calculated using the RGB values, starting with image preprocessing to remove dust and scratches and subtract the background signal if necessary. Then, a dose to color calibration is required, which is influenced by the scanner, the film type, and the film batch as the composition of the active layer can slightly change during the manufacturing process. For this calibration, a set of films is irradiated with known doses generated by a conventional accelerator, which can then be associated with RGB values (Nürnberg et al., 2009; Schreiber, 2012). During this step, the film detection efficiency is factored into the equation. It depends on the stopping power $\mathrm{d}\mathcal{E}/\mathrm{d}x$, and can increase the determined particle number by up to 25% (Schollmeier et al., 2014). Using the calculated response function, the discoloration can be converted to the corresponding absorbed energy dose, which was integrated for each film presented in this thesis.

The determination of the ion spectrum in terms of particle number per energy is challenging, since each ion deposits fractions of its energy all along its way through the stack. The straightforward method would be to start with the last exposed film, determine the number of particles and recursively subtract their contribution to the previous films. However, due to the composition of the films and potential absorbers in the stack, the deposited energy is only known for a few positions as visualized in Fig. 3.10. Therefore, an interpolation method is required. First, the specific response function of a stack configuration is calculated. The routine employed in this thesis is using energy loss tables computed with SRIM. Then, it is assumed that the ion spectrum follows a specific energy distribution. Here, an exponential function based on a Maxwell-Boltzmann temperature distribution (eqn. 2.38) with the proton temperature $k_\mathrm{B}T_\mathrm{p}$ was chosen. With this and the response function of the stack, the energy dose deposited by a theoretical spectrum can be calculated. By minimizing the root mean square deviation between the theoretical and the experimentally measured doses, a spectrum representing the experimental beam can be determined. A description of the Matlab program and the models used therein to analyze RCF spectra can be found in the PhD thesis of Christian Brabetz (2014) and publications by Nürnberg et al. (2009) and Schollmeier et al. (2014).

Like IPs, RCFs can only be used as an offline diagnostic. Moreover, RCFs are single-use and do not allow to differentiate between different particle types. Also, the number of data points per spectrum is often low and an interpolation is required, thus making the results ambiguous. Nonetheless, their advantageous features such as high spatial resolution, EMP-safety and ease of use make RCF stacks one of the essential diagnostic tools in current laser ion acceleration experiments.

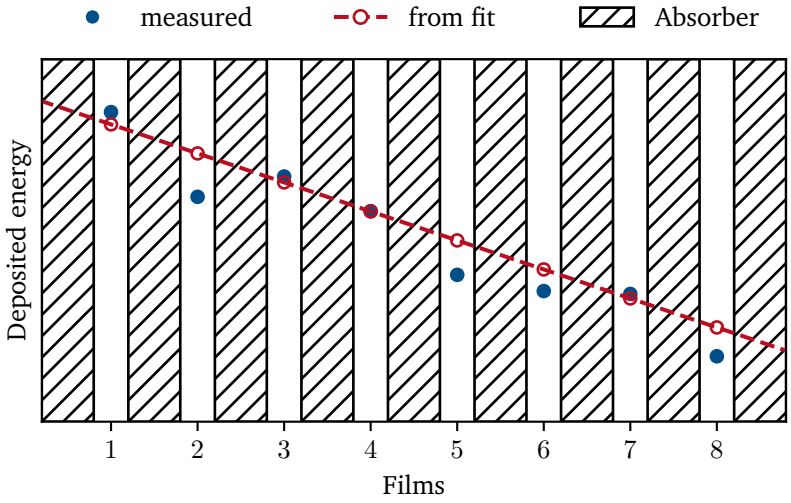

Figure 3.10.: Schematic of an RCF stack consisting of eight films and nine absorbers. The energy deposited by the ion beam (blue) can be obtained from the discoloration of each irradiated film. The experimental ion spectrum can be determined by calculating the energy deposition of a hypothetical ion spectrum (red) and iteratively minimizing the difference to the experimental data by adjusting the respective distribution function.

3.1.4. X-ray spectrometer

In this work, wavelength dispersive spectroscopy based on Bragg reflection was used to measure the generated X-ray spectra. This approach covers an energy range between roughly 250 eV and 100 keV (Renner and Rosmej, 2019) and offers comparatively high collection efficiencies as well as high spectral, temporal and spatial resolution depending on the specific setup.

In its simplest form, such a spectrometer consists of a dispersive element and a detector. Figure 3.11 shows a sketch of the general setup. Here, crystals are chosen to disperse the incident X-rays according to the Bragg condition

$$2d \sin \theta_{\mathrm{B}} = n \cdot \lambda_{\gamma} \tag{3.8}$$

with d denoting the lattice spacing of the crystal, θ_{B} the Bragg angle, n the order of reflection and λ_{γ} the wavelength of the incoming ray. Only if the incidence angle equals θ_B, constructive interference of the beams reflected at the individual crystal layers occurs. The orientation and distances of the source, crystal and detector relative to each other as well as the crystal and detector size determine the measurable energy range and resolution. The dispersion function that relates the position of the signal on the detector to the respective X-ray energy can be determined via two ways. Either, the geometry of the spectrometer is used to analytically derive the function, or, a function with a suitable profile, e.g., a quadratic curve, is fitted to clearly identifiable peaks of a measured spectrum. In this thesis, the latter was chosen, since the first method is very susceptible to uncertainties in the measured distances.

There exists a great number of crystals that are suitable for this diagnostic method. Chapter 4.1 of the X-ray Data Booklet (Thompson et al., 2009) gives a good summary of the relevant properties and overall remarks regarding their usage. It is important to note that it is common to list the crystal lattice spacing as $2d$. Besides single crystals such as Ge or KAP (potassium hydrogen phthalate), mosaic crystals like HOPGs (highly oriented pyrolytic graphite) are among the standard choices as they allow an easier

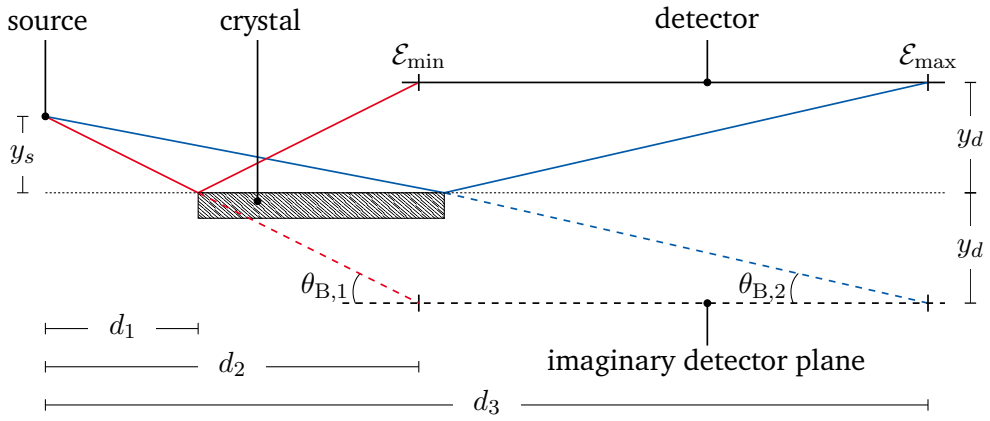

Figure 3.11.: General schematic of an X-ray spectrometer based on Bragg reflection. The X-ray spectrum emitted by a laser plasma source is resolved with the help of a crystal, which acts as a dispersive element. The crystal is distanced to the source by d_1 in horizontal and y_s in vertical direction. X-rays are only reflected if their wavelength and incidence angle meet the Bragg criterion (eqn. 3.8). Therefore, the angle of reflection $\theta_{\mathrm{B},1}$ of a low energetic ray (red) is larger than $\theta_{\mathrm{B},2}$ of a ray with higher energy (blue). The dotted lines show the imaginary extension of the impinging rays and an imaginary detector placed at the same distance y_d from the crystal as the real detector. The intersections of the reflected beams with the detector plane at distances d_2 and d_3 show the outer limits $\mathcal{E}_{\mathrm{min}}$ and $\mathcal{E}_{\mathrm{max}}$ of the measurable energy range.

manufacturing of curved surfaces. This modification in combination with more advanced setups can lead to an enhanced collection efficiency and higher resolutions, both spatial and spectral wise. A short review on different setups is given by Renner and Rosmej (2019).

The experiments performed during this project employed flat KAPs, which are a good general choice for low-Z elements such as Si. Also, KAP crystals offer high quality at reasonable costs and are therefore readily available at many facilities. Table 3.2 summarizes the energies and wavelengths of characteristic Si lines and their respective Bragg angles.

Incoming X-rays of a specific wavelength are not mapped precisely onto one point-like spot on the detector due to a number of reasons. First, the X-ray beam is usually reflected on more than one lattice plane, and even though the Bragg condition is fulfilled at every single one of them, the oblique incidence leads to a shifted position of reflection at each crystal plane, which ultimately results in an expanded beam in the detector plane. Furthermore, crystal inhomogeneities and composition, surface roughness,

Table 3.2.: Energies $\mathcal{E}_\gamma$ and wavelengths λ_γ of characteristic Si emission as well as the respective Bragg angles θ_{B} for a KAP crystal with crystal spacing $2d = 26.634$ Å (Thompson et al., 2009). For the terminology refer to Section 2.3.2.

line	$\mathcal{E}_\gamma$ in eV	λ_γ in Å	θ_{B} in °
$\mathrm{K}_{\alpha 1,2}$	1740	7.13	15.53
K_{β}	1836	6.75	14.68
$\mathrm{He}_{\alpha,2}$	1854	6.69	14.55
$\mathrm{He}_{\alpha,1}$	1865	6.65	14.46
$\mathrm{Ly}_{\alpha,2}$	2004	6.19	13.44
$\mathrm{Ly}_{\alpha,1}$	2006	6.18	13.42
He_{β}	2180	5.69	12.34
He_{γ}	2290	5.41	11.72

dirt, scratches as well as the crystals bending radius and thickness influence the widening of the beam. By rotating the crystal, the reflectivity as a function of the rotation angle is obtained, the so-called rocking curve, which is also influenced by the X-ray wavelength and polarization and can be retrieved both experimentally (Zastrau and Förster, 2014) as well as theoretically with simulations (Hölzer et al., 1998). This curve is then integrated over the relevant interval around the central Bragg-angle θ_{B} to determine the integrated reflectivity

$$R_{\mathrm{int}} = \int_0^{\pi/2} r \, \mathrm{d}\theta_{\mathrm{inc}} \,, \tag{3.9}$$

with r being the reflectivity at the grazing angle θ_{inc} (Chantler, 1992). In 0th-order approximation this simplifies to

$$R_{\mathrm{int}} = R \cdot w_{\mathrm{rc}} \,, \tag{3.10}$$

with R describing the reflectivity of the crystal. For a KAP crystal, the FWHM width w_{rc} of the rocking curve for unpolarized X-rays from a Si K_α source is 130 µrad and the integrated reflectivity is 75.8 µrad (Henke et al., 1993, p. 336). This results in a reflectivity R of approximately 0.58, which was taken into account when converting the measured signal to the number of respective X-ray photons. However, it should be kept in mind that each crystal is unique, thus the measurements found in literature as well as simulated values are approximations for the crystals employed in the scope of this work.

Crystal spectrometers employ imaging detectors such as imaging plates (see Section 3.1.2) or CCD cameras to record the spectra. Depending on the detector type, the measurement can be time integrated or time resolved. Together with the properties of the crystal and the overall geometry of the spectrometer, the detector type also influences the spectral and spatial resolution of the acquired spectra. Moreover, the size of the X-ray source plays an important role. Its influence can be reduced by increasing the distance between the target and the crystal. Furthermore, in some configurations a slit is added before the crystal to reduce the source size, though the total amount of radiation entering the spectrometer is diminished this way. The blurriness of the whole imaging system is described by the point-spread function of the spectrometer, which can be determined by ray-tracing codes. This instrument function is of special interest along the dispersive direction and needs to be deconvolved during the analysis.

Usually, the front of the spectrometer is equipped with a filter to reduce direct or scattered laser light as well as other ambient radiation. It also serves as a blast shield to protect the valuable parts of incoming debris and to prevent over-heating of the crystal and over-exposure of the detector. Filter transmission curves can be found online, for example in the Henke database (Gullikson, 2021; Henke et al., 1993). To shield the diagnostic from accelerated particles, a permanent magnet can be added as well.

3.2. Theoretical modeling

In addition to experimentally investigating the laser plasmas, they can also be studied with simulation codes that are based on models describing the underlying physics. Depending on the specific plasma state, which can be characterized by its temperature, density and temporal evolution, different models are valid. Plasmas that exhibit local thermal equilibria are often described by fluid models whereas plasmas without equilibria and strongly fluctuating particle distributions are frequently studied with kinetic models. The description of the interaction between a high intensity, ultrashort pulse laser and matter is challenging, because the plasma rapidly evolves through different plasma states.

In the following, a short introduction to the kinetic modelling of not strictly Maxwell distributed laser plasmas is given. The plasma code employed during this thesis is the EPOCH code, which is currently maintained and developed by the University of Warwick, UK (Arber et al., 2021). When appropriate, specific details of this code are included in this section. The material presented is mainly based on the book *Short pulse laser interactions with matter* by Paul Gibbon (2005), a publication by Arber et al. (2015) and the EPOCH User Manual (Bennett et al., 2019).

3.2.1. Particle-In-Cell codes

A plasma can be kinetically expressed by a single particle velocity distribution function $f(\boldsymbol{x}, \boldsymbol{v}, t)$, which describes the number of particles at a particular position $\boldsymbol{x}$ with velocity $\boldsymbol{v}$, and therefore with the momentum $\boldsymbol{p}$, at a certain time t. This distribution function evolves according to the Vlasov equation

$$\frac{\partial f}{\partial t} + \boldsymbol{v}\frac{\partial f}{\partial \boldsymbol{x}} + q(\boldsymbol{E} + \boldsymbol{v} \times \boldsymbol{B}) \cdot \frac{\partial f}{\partial \boldsymbol{p}} = 0\,. \tag{3.11}$$

Since the distribution function is 6-dimensional at any given time, finding a general solution can become quite laborious. A more practical approach to solve this problem is utilizing Particle-In-Cell (PIC) codes, where particles are placed and tracked on a grid consisting of cells. This method was first developed in the 1960s and is nowadays among the most commonly used plasma physics codes.

The interaction and movement of each individual particle, which in the following will be denoted by the index i, is given by the Lorentz force

$$\frac{\mathrm{d}\boldsymbol{p}_i}{\mathrm{d}t} = q_i\left(\boldsymbol{E} + \boldsymbol{v}_i \times \boldsymbol{B}\right)\,, \tag{3.12}$$

with the particle velocity $\boldsymbol{v}_i = \mathrm{d}\boldsymbol{x}_i/\mathrm{d}t$ and momentum $\boldsymbol{p}_i = \gamma m \boldsymbol{v}_i$. This form includes the particle charge q_i, the speed of light c, the relativistic Lorentz factor γ and the electric and magnetic fields, which are denoted by $\boldsymbol{E}$ and $\boldsymbol{B}$, respectively. The fields are expressed by the Maxwell equations

$$\frac{\partial \boldsymbol{B}}{\partial t} = -\boldsymbol{\nabla} \times \boldsymbol{E} \quad \text{and} \tag{3.13}$$

$$\frac{\partial \boldsymbol{E}}{\partial t} = c^2 \cdot \boldsymbol{\nabla} \times \boldsymbol{B} - \frac{1}{\epsilon_0}\boldsymbol{j}\,, \tag{3.14}$$

where $\boldsymbol{j}$ denotes the electric current density and ϵ_0 the vacuum permittivity.

To model this system of equations, both space and time need to be discretized. Space is described by a grid with cell size $\Delta\boldsymbol{x}$, while time is divided into time steps Δt. With this, each cell, which will be denoted with the n-dimensional index j, requires only one $\boldsymbol{E}$ and $\boldsymbol{B}$ field vector. In the EPOCH code, a Yee-staggered grid as shown in Fig. 3.12 (a) is employed. Here, the $\boldsymbol{E}$ field vectors are orthogonal to the cell walls whereas the $\boldsymbol{B}$ field vectors are parallel to the cell edges. The grid resolution is fixed and constant in each dimension.

It is crucial to choose the correct cell size to adequately model the plasma behavior. If the cell size is too wide, relevant physical effects might be neglected, whereas very small cell sizes can result in unnecessary computing time. For the description of laser matter interaction, the plasma frequency as well as the Debye length (see Section 2.1.2) should be resolved to account for effects of the laser and the electrons. The cell size directly influences the time resolution, as the Courant-Friedrichs-Lewy (CFL) criterion must be fulfilled to achieve a stable run. In this context, this criterion demands that the time step must be smaller than the time required to cross a cell at the speed of light.

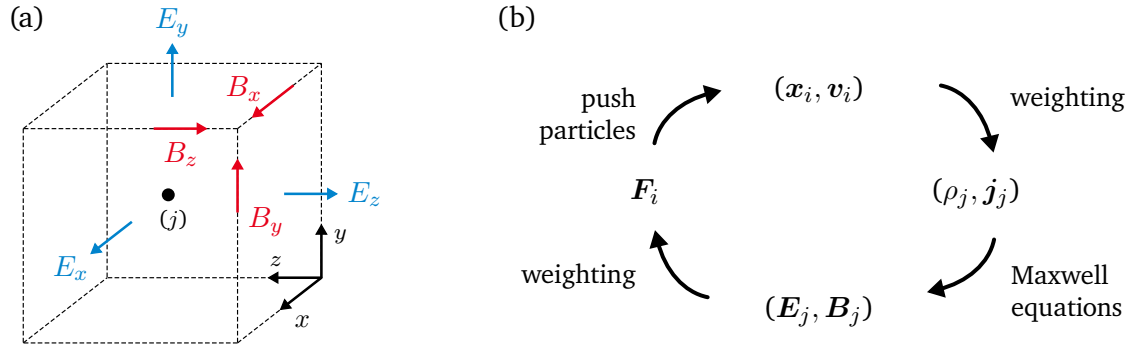

Figure 3.12.: Schematics illustrating essential features of the employed PIC code. Subfigure (a) shows the j-th cell of a Yee staggered grid. The electric field components (blue) are orthogonal to the cell walls while the magnetic field components (red) are parallel to the cell edges. (b) A PIC algorithm consists of four main steps. The density ρ_j and currents $\boldsymbol{j}_j$ on the grid are calculated from the positions $\boldsymbol{x}_i$ and velocities $\boldsymbol{v}_i$ of the particles in a weighting step. These values are then used to determine the electric $\boldsymbol{E}_j$ and magnetic $\boldsymbol{B}_j$ fields by solving the Maxwell equations, which in turn result in the forces $\boldsymbol{F}_i$ that push and accelerate the particles to new positions and velocities.

Laser generated plasmas with near solid state density have electron densities on the order of $10^{22}\,\mathrm{cm}^{-3}$ and the simulated volumes are typically in the order of $10^{-5}\,\mathrm{cm}^3$. In this scenario, the number of particles to be placed and tracked during the simulation is 10^{17}. To deal with this large number, macroparticles are introduced, which treat multiple real particles as one and can contain up to 10^{10} particles. By multiplying the properties of a single particle with the number of particles contained in one macroparticle N_MP, their charge q_MP and mass m_MP are calculated, e.g., by

$$m_\mathrm{MP} = N_\mathrm{MP} \cdot m_\mathrm{single}\,. \tag{3.15}$$

The validity of such a rigorous simplification can only be proven by experiments, and so far the results indicate that this approach is sensible.

Although it is fairly common to treat particles as point-like in other physical models, this is not advisable in PIC schemes. With point-like particles there would be no difference in the calculated $\boldsymbol{E}$ and $\boldsymbol{B}$ fields if the particle gets closer to the cell boundary, but a sudden leap would occur once it moves into an adjacent cell. Also, the particles would only be influenced by the one cell they are currently positioned in. So instead, the particles are represented by a distribution function extending across multiple cells. Although most codes support top-hat distribution functions, which only cover one cell, the particles are typically represented by triangle functions or splines. The charge distribution of a cell at position $\boldsymbol{x}_j$ is then given by

$$\rho_j = \frac{q \cdot N_\mathrm{MP}}{\Delta \boldsymbol{x}} \sum_{i=1}^{N_\mathrm{MP}} W(\boldsymbol{x}_i - \boldsymbol{x}_j)\,, \tag{3.16}$$

with W being the distribution function of choice.

After loading the macroparticles according to the chosen distribution function on the grid, an algorithm consisting of four basic parts is applied. These parts, which are consecutively executed within one time step, are illustrated in Fig. 3.12 (b). First, the positions and velocities of the macroparticles are used to calculate the mass densities and current densities for each grid cell. Then, the Maxwell equations are solved to determine the electric and magnetic fields of the cells. Subsequently, these fields are translated into the forces acting on each macroparticle, which in turn push the particles to their new positions and

velocities. This implicit scheme is repeatedly carried out and since every step only requires the values of the immediately preceding one, the data can be deleted after finishing each step.

To numerically solve the Maxwell equations during the second step, a finite difference time domain (FDTD) method is utilized in the EPOCH code. With this, the y-component of the electric field of the j-th cell, for example, is approximated by the value difference between adjacent cells. It can be calculated by

$$\left(\frac{\partial E_y}{\partial x}\right)_j = \frac{E_{y,j+1} - E_{y,j}}{\Delta x}\,. \tag{3.17}$$

The described algorithm is implemented in EPOCH with a revised leap-frog scheme, which introduces half time steps and updates the fields both at half and full steps, therefore creating a second order approximation. The field solver determines the fields at the half time step $k + 1/2$ using the values of time step k with

$$\boldsymbol{E}^{k+1/2} = \boldsymbol{E} + \frac{\Delta t}{2}(c^2\boldsymbol{\nabla} \times \boldsymbol{B}^k - \frac{\boldsymbol{j}^k}{\epsilon_0}) \tag{3.18}$$

$$\boldsymbol{B}^{k+1/2} = \boldsymbol{B}^k - \frac{\Delta t}{2}(\boldsymbol{\nabla} \times \boldsymbol{E}^{k+1/2})\,. \tag{3.19}$$

Then, the particle pusher updates the particle momentum using

$$\frac{\boldsymbol{p}^{k+1} - \boldsymbol{p}^k}{\Delta t} = q \cdot (\boldsymbol{E}^{k+1/2} + \boldsymbol{v}^{k+1/2} \times \boldsymbol{B}^{k+1/2}) \tag{3.20}$$

$$\boldsymbol{v}^{k+1/2} = \frac{1}{2}(\boldsymbol{v}^{k+1} - \boldsymbol{v}^k) \tag{3.21}$$

$$\boldsymbol{x}^{k+1/2} = \boldsymbol{x}^k + \frac{\Delta t}{2}\boldsymbol{v}^k\,, \tag{3.22}$$

which is subsequently employed to determine the updated current density $\boldsymbol{j}^{k+1}$ as described by Arber et al. (2015). Next, the fields at the full time step $k + 1$ are calculated using

$$\boldsymbol{B}^{k+1} = \boldsymbol{B}^{k+1/2} - \frac{\Delta t}{2}(\boldsymbol{\nabla} \times \boldsymbol{E}^{k+1/2}) \tag{3.23}$$

$$\boldsymbol{E}^{k+1} = \boldsymbol{E}^{k+1/2} + \frac{\Delta t}{2}(c^2\boldsymbol{\nabla} \times \boldsymbol{B}^{k+1} - \frac{\boldsymbol{j}^{k+1}}{\epsilon_0})\,. \tag{3.24}$$

This interleaving set of equations allows all fields to be defined at the same time and incorporates the particle push.

Besides these basic equations, most modern PIC codes include additional physics modules. In the presented form, the particles only interact with each other via the grid. Yet, at high densities and/or low temperatures collisions should be considered. Also, ionization and QED effects such as photon emission and pair production can be relevant. Since the basic equations are only sensitive to the charge to mass ratio but not the mass itself, its role in heating processes is sometimes overlooked. Another important aspect in setting up a specific physical scenario is the correct choosing of the boundaries of the simulation window. EPOCH includes a wide variety of options, including periodic, outflowing or heat bath boundaries.

Especially high contrast laser matter interaction requires a high grid resolution and with this very small time steps to fulfill the CFL criterion. Together with the high particle numbers, this results in high computational costs, which in turn limits the size of the simulation windows and the simulated

timescales. Since PIC is a discretized scheme that is numerically solved, problems such as numerical heating can occur. For the EPOCH code, the change in the temperature T_{eV} in electronvolt over a time t_{ps} in picoseconds can be estimated by (Arber et al., 2015)

$$\frac{\mathrm{d}T_{\mathrm{eV}}}{\mathrm{d}t_{\mathrm{ps}}} = \alpha_{\mathrm{H}} \frac{n_{23}^{3/2} \Delta x_{\mathrm{nm}}^2}{N_{\mathrm{ppc}}} \,. \tag{3.25}$$

Here, the cell size Δx_{nm} is given in nanometer and the electron number density n_{23} is in units of $10^{23}\,\mathrm{cm}^{-3}$. Apart from the grid resolution, the number of particles per cell N_{ppc} as well as the particle shape and current smoothing influence the rate, which are accounted for by the weight factor α_{H}. In addition, unwanted numerical effects can be caused by rounding errors and the applied first or second order approximations, especially at steep gradients in e.g. the particle density that occur in high laser contrast scenarios.

Nonetheless, PIC codes are an invaluable tool in studying high intensity laser plasma physics. If carefully set up, the codes are numerically stable, they parallelize well and the underlying simplifications allow the simulation of 3D problems with reasonable computing cost. Their flexibility makes them applicable to numerous scenarios, but to yield valid results, the user must ensure that the relevant physics is included in the implementation used.

4. Fabrication of microstructured targets

The microstructured targets fabricated and employed during the scope of this thesis were in the first instance produced by ultrashort laser pulse processing. This chapter presents the processing setup and discusses the realized structure characteristics as well as suitable characterization methods. The main focus was on silicon, but the structure formation on titanium, copper and gold was also studied. In addition, a replication procedure was developed to recreate the cone-like microstructures out of materials that cannot be processed directly with ultrashort laser pulses. The procedure is based on casting a mold with PDMS, which is subsequently used as a template to create polystyrene or copper targets.

Besides the fabrication, the preparation, characterization and mounting of the microstructured samples is discussed. These steps are strictly necessary before the samples can be employed as targets in high intensity laser experiments. Furthermore, the manufacturing of layered targets consisting of a microstructured silicon target front and a rear side made out of a different material is addressed.

Parts of the work were published in *High Power Laser Science and Engineering* (Ebert et al., 2017) with a focus on silicon targets and in *Journal of Physics: Conference Series* (Neumann et al., 2018), where a previous version of the experimental setup is described. In addition, the structuring of metals and the replication procedure are presented in a recent publication in *High Power Laser Science and Engineering* (Ebert et al., 2021).

4.1. Ultrashort laser pulse processing

As discussed in Section 2.3.1, ultrashort laser pulses can be used to create surface microstructures. Here, the processing setup as well as the resulting structures are presented and reviewed. Although the emphasis of the developed routines and the parameter studies was on silicon, the setup and procedure can also be applied to generate laser-induced structures on metals such as titanium, copper and gold.

4.1.1. Setup and procedure

The processing setup used to fabricate the laser-induced microstructures consists of four main parts, namely the laser system, the optical setup, the scanning unit and processing chambers for different ambient media. The optical setup was initially developed by Nico W. Neumann (2018) during his PhD thesis, but was advanced and optimized in the scope of this work. In addition to the setup, the substrate preparation, the structuring procedure and the utilized characterization techniques are described in this section.

Laser system and optical setup

The ultrashort pulse laser system is composed of a Ti:sapphire oscillator and a subsequent regenerative amplifier. It is followed by an optical setup which includes a power adjustment system, shutters and the scanning unit. The entire system with its individual components is illustrated in Fig. 4.1.

The oscillator is a *Griffin-3* manufactured by *KMLabs*. It is mode-locked and generates ultrashort pulses with a wavelength λ_L of 795 nm and a bandwidth of 40 nm at a repetition rate of 80 MHz. The pulses are 50 fs to 100 fs long, have an average power of 0.3 W and are horizontally polarized. Following this first stage of the laser system, the laser signal emitted by the oscillator is guided into an *Integra-C.X.* amplifier manufactured by *Quantronix Corporation*. Here, the repetition rate is reduced to 5 kHz and laser pulses with an average power of 1 W, 800 nm wavelength and 20 nm bandwidth are emitted. The beams spatial and temporal profile is Gaussian, and the pulse length can be varied between 50 fs and 2 ps.

Since the laser pulse energy is an important parameter for the structuring process, the power can be adjusted with a combination of a motorized waveplate and a broadband plate polarizer (Laser Components, 2021). The initial polarization is rotated with the waveplate, so that the total amount of reflected light proceeding to the processing setup is set to the desired value. The waveplate can be moved either manually or with a motor controlled by a *LabView* program. With this setup, the average power can be continuously adjusted between 25 mW and 1000 mW with an uncertainty of 1 mW, which equals 5 µJ to 200 µJ per pulse.

Two shutters with different close-activation times are available to block the beam, which can both be used during the structuring process. The mechanical shutter placed immediately after the power

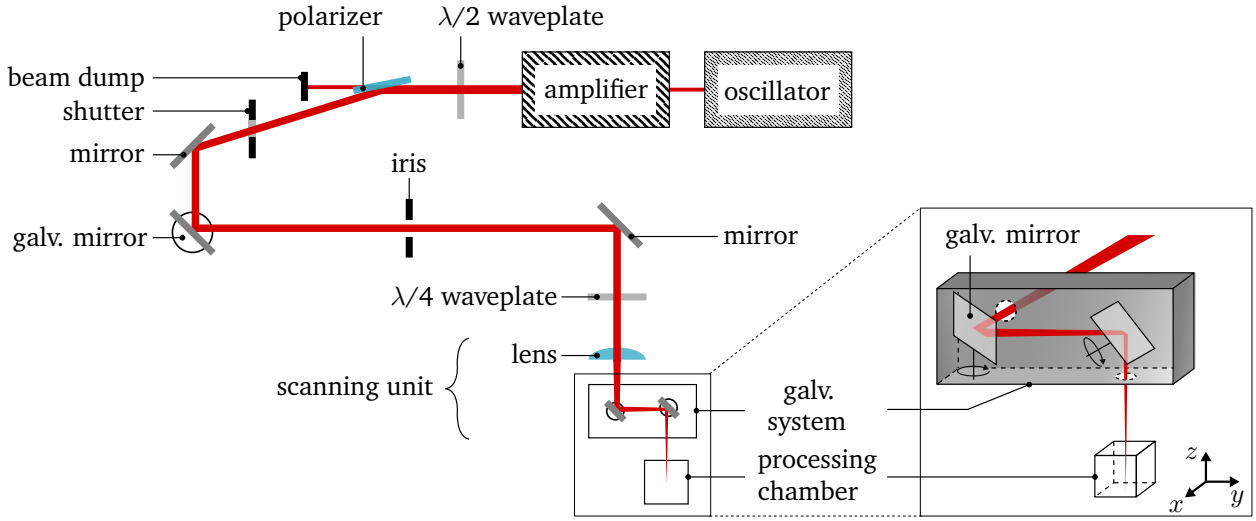

Figure 4.1.: Schematic of the processing setup. The ultrashort laser pulses are generated by a laser system that consists of an oscillator and an amplifier. By combining a $\lambda/2$ waveplate with a polarizer and a beam dump, the pulse energy can be varied. After passing a mechanical shutter, the laser beam is reflected by a mirror onto a galvanometric mirror, which in combination with a subsequent iris serves as an ultrafast shutter. If in open position, the laser beam is then deflected by another mirror before passing through an optional $\lambda/4$ waveplate, which changes the polarization from linear to circular. Then, the beam proceeds into the scanning unit. It passes a plano-convex focal lens and enters a galvanometric system, which is used to move the focal spot in the x-y plane perpendicular to the direction of propagation. At last, the laser beam enters the processing chamber. The box on the right hand side shows the scanning system in a side view.

adjustment system has an opening time of approximately 25 ms and a closing time of approximately 70 ms (Neumann, 2018), which equals 125 and 350 pulses, respectively. It is a *LSTXY* model by *nmLaser Products Inc.* in combination with a *CX2250* controller. The subsequent galvanometric shutter is much faster with a close activation time of approximately 1 ms, which corresponds to 5 pulses. This shutter consists of an IR-coated mirror mounted on a *S10* galvanometer by *SCANLAB AG*, which changes the direction of the reflected beam when rotated. If the shutter is in closed position, the beam is directed onto a beam dump. In the open position, the beam can pass an iris, which is used for alignment. Further on, the beam is deflected by a mirror and passes an optional $\lambda/4$ waveplate, that converts the polarization from linear to circular before entering the scanning unit.

The first component of the scanning unit is a planoconvex focusing lens with a focal length of 300 mm, which can be moved along the direction of laser propagation. With this, the position of the best focus can be set slightly below the substrate surface, so that energy losses by plasma formation in the processing ambient are prevented. The diameter $2w_0$ of the focal spot is 70 µm (FWHM), and the Rayleigh length, which is given by

$$z_{\mathrm{R}} = \frac{n_{\mathrm{r}} \cdot \pi \cdot w_0^2}{\lambda_{\mathrm{L}}} \tag{4.1}$$

with n_{r} being the refractive index, equals 2.5 cm. After the focusing lens, the beam reaches a scanning system consisting of two *S10* galvanometric mirrors by *SCANLAB AG*, which is controlled by a *LabView* program that was written by Nico W. Neumann. This scanning system is used to rapidly move the laser across the substrate surface in the x-y plane to create structured areas larger than the focal spot size. Due to the deflection of the two rotating mirrors, the focal plane is slightly curved, which has an influence on outer regions of large structured areas. However, this can be neglected for the areas created in the scope of this work, which are typically 1 mm^2 to 5 mm^2 large.

For further usage it is of great interest to achieve highly homogeneous structured areas. Therefore, the pattern with which the wafer is scanned by the laser needs to be optimized. In this work, a continuous scanning pattern was developed, which prevents the creation of over-exposed or under-exposed spots during shutter opening and close times. The pattern, which is depicted in Fig. 4.2, features a parallel movement of the beam and results in a structured area of width w and length l. Due to the Gaussian pulse profile, it is crucial to choose the right distance Δd between the lines to create a perfect overlap of the traces. The total trace width is affected by the total laser fluence because the substrate is irreversibly modified only if the ablation threshold is exceeded. Then again, the ablation threshold is influenced by the processing medium so that the parameter Δd can largely vary depending on the specific processing parameter set. Another aspect of the parallel movement is the need to accelerate and decelerate the beam to turn the scanning direction. This is implemented with an overshoot of length o out of the region of interest with a considerably higher scanning velocity.

Additionally, the homogeneity can be increased by scanning the same area multiple times. One option is to rotate the scan pattern with each turn. Another way is slightly changing the starting point by varying the overall width w for each scan. This method also creates smooth slopes in the transitional region between flat and structured surface areas, which increases the stability of the whole substrate.

If necessary, the laser system and optical setup can be complemented with additional diagnostics for measurements of the spectral, temporal and spatial beam profile.

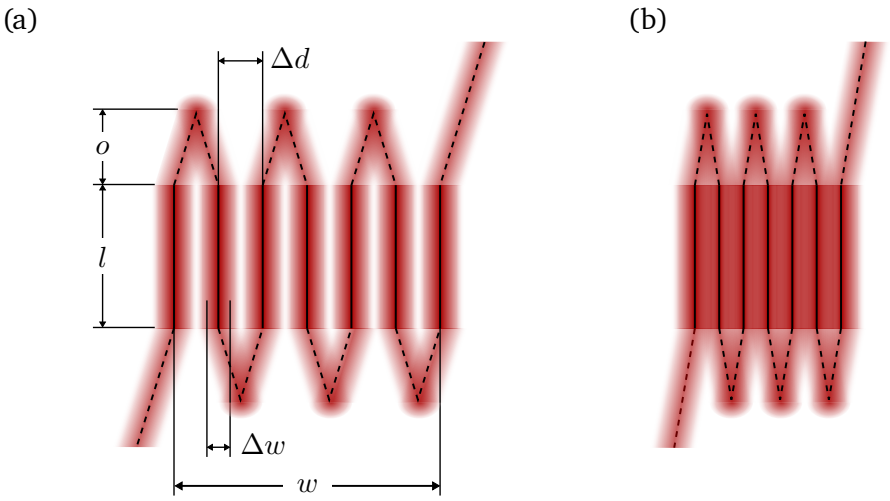

Figure 4.2.: Schematics of the scan pattern. The continuous pattern is defined by four parameters: the width w and length l of the structured area, the overshoot length o and the distance Δd between the scanned lines. The width Δw of the structured trace on the substrate surface depends on the focal spot size, the processing medium and the energy of the pulses. Depending on the scanning velocity v_{scan}, which can differ for the main area and the overshoot, the number of incident pulses varies. To create a homogeneously structured area, the distance Δd has to be selected correctly. In (a) the chosen value is too large, resulting in unstructured gaps, while the traces in (b) overlap perfectly.

Processing chambers

In order to meet the requirements of various processing media, three different processing chambers are implemented, which are depicted in Fig. 4.3. While their features differ, the basic setup is the same for all configurations. The laser enters the chamber from the top (z-direction) and hits the substrate surface (x-y-plane) normal to the incidence direction. All chambers are equipped with mounts for scanning electron microscope (SEM) pins, as the substrates are attached to these pins for easier handling. Also, all designs are mounted via respective adapter plates onto an x-y-stage consisting of two *VT-80* stages manufactured by *PI*. With this stage, the substrate can be precisely positioned relative to the incident laser.

For processing in air, no further add-ons are necessary and a design with an open top is sufficient. In case of liquid media, the fluid level needs to be measured over the course of the structuring process.

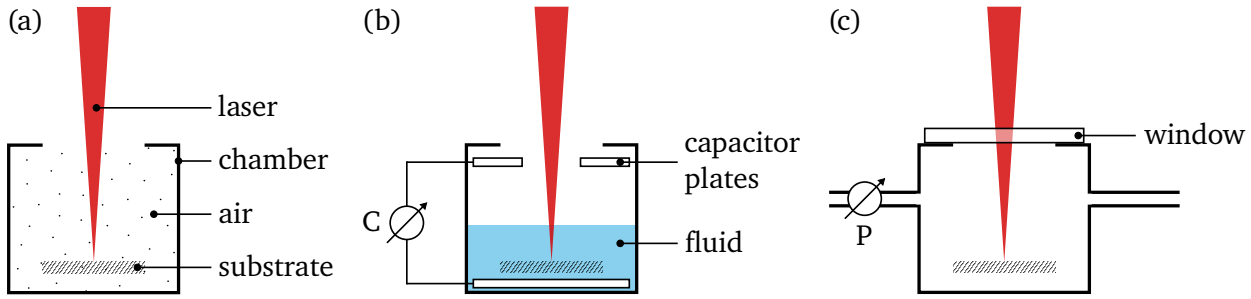

Figure 4.3.: Simplified sketches of implemented processing chambers for different processing media. (a) Structuring in air can be performed in an open chamber without any additional measures. (b) For fluids, a capacitor is added to measure the fluid level. (c) In case of vacuum or gases, the chamber is closed with a window and connected to a pressure sensor as well as a gas supply and filter system.

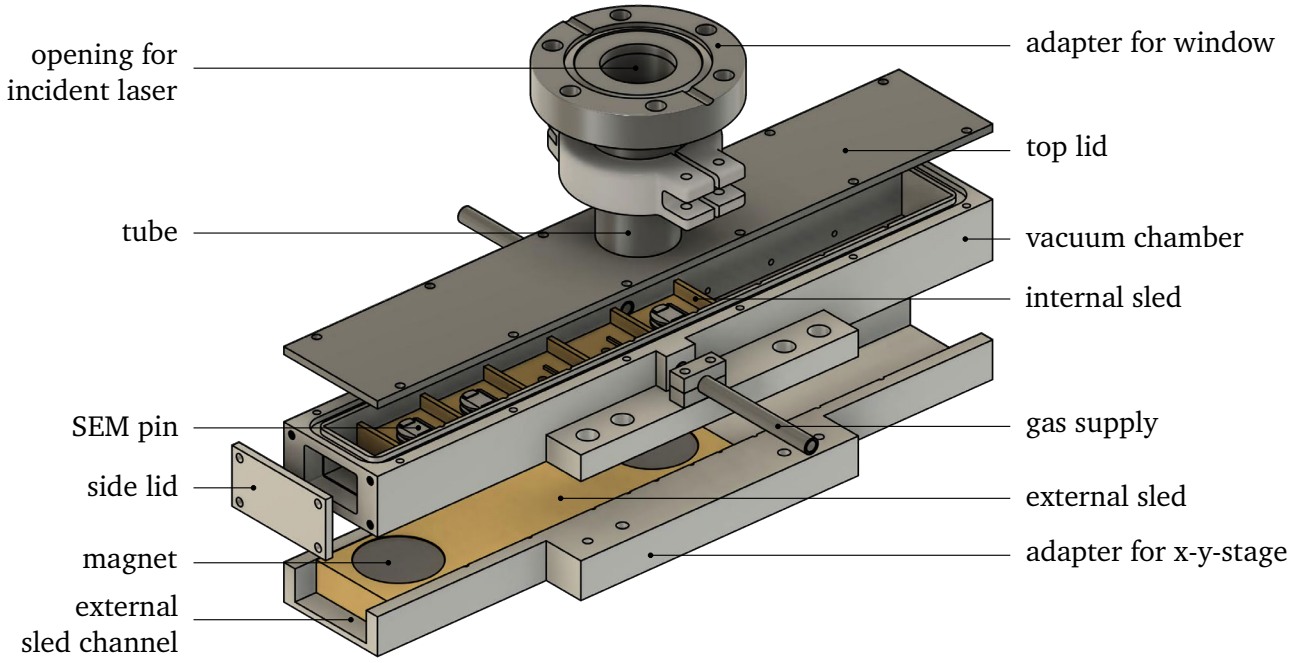

Figure 4.4.: CAD model of the processing chamber for vacuum and gaseous processing media. The laser enters the top vertically through an opening in a KA3525 flange, which serves as an adapter for a window to close the chamber. Using a clamp, the flange can be mounted onto a tube, which is welded to the top lid of the chamber. The vacuum chamber is 27 cm long, and possesses an opening at the side, through which an internal sled can be inserted. The substrates for processing are placed on SEM pins on this sled. Once the whole chamber is closed, the internal sled can be positioned by moving an external sled, which is connected to the internal one by magnets. The external sled channel is part of an adapter plate, which connects the whole setup to an x-y stage. Both sleds are made out of brass, the top lids, tubes and flanges material is stainless steel, while everything else consists of aluminum. The realization of this chamber design was supported by *Torsten Abel*.

Therefore, the chamber is equipped with a parallel plate capacitor. Its capacity changes with varying fluid level, which is monitored with an Arduino Uno microcontroller. The software was originally developed by J. Nethercott (2021), but was adapted for the specific purpose. To avoid electromagnetic interference, this chamber is made out of plastic.

Gaseous processing media require the most advanced chamber, which has to include a vacuum chamber and a gas supply and filter system. The setup that was developed for these specific needs is shown in Fig. 4.4. On top, a vacuum chamber is located, which was designed to process multiple samples consecutively without breaking the gas atmosphere in between. For this, a sled was introduced that can be loaded with up to five SEM pins simultaneously. The pins can only be placed in a specific orientation, thereby yielding a high repositioning accuracy. Also, small dividers protect each substrate from debris caused by structuring one of the neighboring samples. The sled is inserted on the side through a small lid, which allows for easy and quick reloading. Once the chamber is closed, the internal sled is positioned by moving an external sled, which is placed right below the vacuum chamber. The sleds are connected by magnets and are made out of brass, which enhances the sliding capabilities in the respective aluminum channels without requiring any additional lubricants.

The internal sled channel is closed with a top lid, which can be entirely removed for cleaning. During the structuring process, the chamber is sealed with an anti-reflection (AR) coated window. To prevent damages to the window by the converging laser, a tube is added to increase the distance to the substrate,

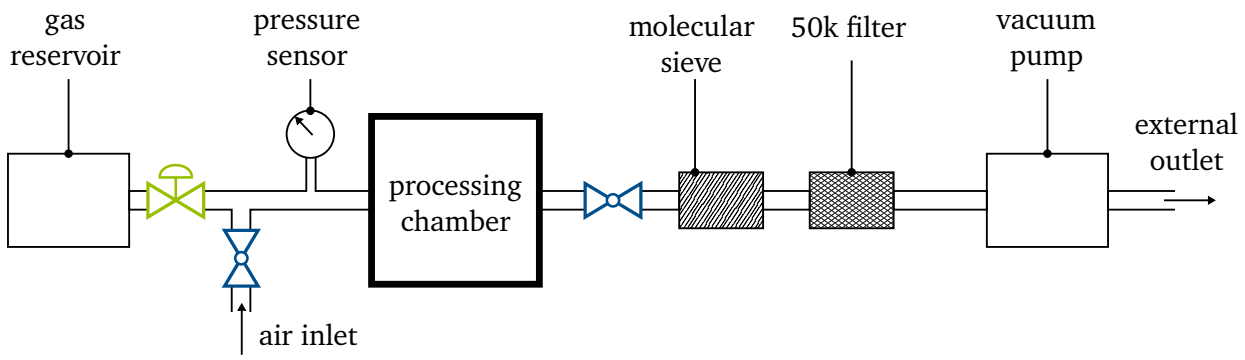

Figure 4.5.: Gas supply and filter system. The left hand side shows the gas supply system. The gas reservoir is connected to the processing chamber and a pressure sensor via a precision control valve (green). An additional air inlet is added for venting, which can be closed with a blocking valve (blue). Another blocking valve can close the outlet through the filter system on the right hand side. The combination of a molecular sieve and a 50k filter reduces toxic byproducts generated during the structuring process. The setup is evacuated through an external outlet with a vacuum pump.

while minimizing the chamber volume at the same time. This is of interest because it decreases the amount of processing gas needed to achieve sufficient pressures. The chamber is designed for pressures below 1 bar.

An inlet and outlet are attached to the chamber sides to connect it to the gas supply and filter system, which is depicted in Fig. 4.5. The process gas is contained in a gas reservoir, e.g., a pressure tank, and is filled into the chamber via a precision control valve. The pressure in the chamber is monitored with a *MS5803-02BA* sensor by *TE Connectivity Corporation* connected to an Arduino. It provides an accuracy of approximately ± 2.5 mbar (TE Connectivity, 2021). Although the gases used so far are non-toxic, toxic side products can be produced during the structuring process. Because of this, the chamber is evacuated by a pump through a combination of a molecular sieve and a 50k microfilter. The whole setup is enclosed in a fume hood to further increase user safety. After structuring the samples, the substrates are prepared to be subsequently mounted as targets.

Substrate preparation

Before the substrate surfaces are structured, they need to be prepared. Depending on the application, the initial substrate thickness varies, so an etching, polishing or grinding step might be necessary. Afterwards, the substrate is cut to the desired size by aid of, e.g., diamond cutters or an ultrashort pulse laser. At this point, it is also possible to implement substrate design features like incisions for deliberate snapping, which is useful for later on characterization. Figure 4.6 shows a substrate with a design including incisions.

Next, the surface is cleaned. In this work, silicon wafers are soaked for 5 min in acetone, which is heated to 40 °C, followed by a methanol bath for another 5 min before being blow-dryed with clean air.

In the following, the substrate pieces are glued to SEM pins to simplify further handling and characterization. The SEM pins are modified with cutouts, so that the region, which is to be processed, is free

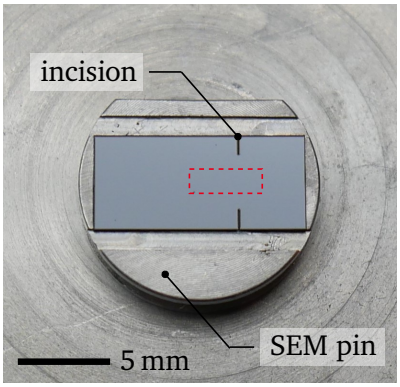

Figure 4.6.: Photo of a substrate piece after laser cutting, which is mounted on an SEM pin for handling. The incisions predetermine the snapping position for ensuing characterization and the red rectangle highlights the designated area for structuring.

standing. In case the substrates need to be tilted during the structuring process, 3D printed wedges are utilized to get precise angles. There is no need to glue the wafers in a specific orientation, because the crystal orientation of the silicon does not affect the formation of the microstructures.

Structuring procedure

The first step of the structuring procedure is checking the parameters of the laser system, which includes the pulse length, the beam profile and the laser alignment. With all safety measures in place, the processing setup is adjusted, starting with the position of the focal lens, which can be determined in an air ambient.

Next, the optimal value for the line distance Δd is identified under the planned processing conditions. For this, the sled is loaded and inserted into the chamber. Then, the chamber, the precision valve and the air inlet valve are closed and the system is evacuated to the minimal pressure, which is about 5 mbar. The gas is filled to the desired pressure through the precision control valve after the valve leading to the filter system has been blocked. Following this, the x-y-stage and the external sled are used to position the substrate, the laser power is set and a number of scan patterns with different Δd are tested. If the target design requires a very thin base, the same area is scanned multiple times until the substrate is perforated. From this, the optimal number of scans is determined.

Once all test structures are done, the chamber is evacuated through the filter system before it is refilled with air through the air inlet. Following this, the sled is removed and the processing parameters are chosen based on the resulting test structures. Afterwards, the sled is loaded with the actual target substrates. The evacuation of the chamber, the filling with the processing gas and the positioning is performed following the same procedure as before. The overall time expenditure for structuring depends on the specific target parameters, but is usually between 1 min and 5 min per sample. In some cases, features like ID numbers for identification of the substrates are also added. After the wafer pieces are structured, they are evaluated with a series of characterization methods.

Characterization of microstructured samples

Since the structured samples are usually intended to be used as targets, they need to be characterized non-destructively. There are several methods available, however, especially techniques based on optical imaging are of limited use due to the highly light absorbing properties of the microstructures. Nonetheless, optical microscopy is applied to evaluate the homogeneity and possible contamination of the structured area. Also, the backlighting mode is used to find potential holes. In addition, optical profiling techniques such as confocal microscopy can be applied to get an impression of the structure geometry, even though recording the 3D topography is not feasible due to the minimimal back reflection.

A suitable way to image the structures is scanning electron microscopy (SEM). It allows the analysis of the geometry and spacing. Also, when viewing the cross section that is produced by dividing the structured area, e.g., by snapping, the structure height and the remaining base thickness can be measured. Silicon is a conductive material, so no additional preparation is necessary to view them with an SEM. A downside of this evaluation method is that it is comparatively time consuming, since the images can only be taken in vacuum. In the scope of this work, a *Phenom XL* microscope (Thermo Fisher Scientific, 2021) with a CeB_6 electron source and a *Philips XL30 FEG* microscope (Materialwissenschaft, Technische Universität Darmstadt, 2021) with a field emission gun were employed.

Even though imaging the cross section with an SEM allows the measurement of the structure height, this method is prone to large uncertainties. Due to the random spatial organization of the structures,

it is not clear whether a minimum in the side view corresponds to the lowest point of a valley or just an intersection between two structures. Therefore, it is of great interest to image the 3D topography. An approach for this is composing the 3D topography out of 2D SEM images with the aid of 3D reconstruction software. Here, one main challenge lies in the self-similarity of the structures. Also, most commercially available software is developed for optical camera systems. Accordingly, they require information such as the focal length of the camera for the reconstruction, which is not available for SEMs. Additionally, SEM images are grayscale only, which further limits the abilities of the software. Although this method is very promising given the right conditions, no reliable procedure could be implemented so far.

Other methods to directly receive information about the structure topography such as atomic force microscopy (AFM) and computer tomography (CT) were also tested, but were found unsuitable. Both techniques are rather time consuming and therefore not convenient for the characterization of large quantities of targets. Furthermore, the high aspect ratio of the silicon spikes makes it difficult to reach the valleys with the AFM tips. It also easily leads to scarring and signal overshooting as well as damage both on the structures and the tips.

The employed measurement and evaluation methods used to characterize the samples are subject to large uncertainties because of the random distribution of the structures, potential inhomogeneities of the structured area, the small field of view at the required high resolution and the viewing angles. Therefore, most of the following results are presented in a qualitative way.

4.1.2. Characteristics of silicon microstructures

The microstructures fabricated with the presented setup feature a wide variety of characteristics, that can be well controlled by adjusting the processing parameters. Since microstructured silicon targets were the main focus of this work, this section summarizes typical properties of these structures, including their height, spacing, shape and tilt. Although another distinguishing characteristic is the resulting electronic band structure, which is linked to the absorptance spectrum at low intensities, it is not discussed in this section due to limited access to the required measurement equipment. However, the interested reader can find information on this topic in supplementary publications, e.g., by Younkin et al. (2003) or Zhao et al. (2020).

The processing parameters studied during this work are the laser fluence and polarization, the pulse number, the processing medium and the tilt angle of the substrate. The parameters that were kept constant include the laser wavelength, repetition rate, pulse length and pressure, but their effect on the formation of microstructures can be found elsewhere (Crouch et al., 2004b; Di Niso et al., 2013; Nivas et al., 2017, 2018). The crystal orientation and doping of the silicon wafer itself do not have an impact, so standard wafers with a (111) orientation and n-type doping sufficed.

Height and spacing

The height and spacing of the structures is influenced by the number of incident pulses and the laser fluence. With the repetition rate f_{rep} of the laser, the focal spot area A_{spot}, the scan velocity v_{scan} and the number of scans n_{scan}, the pulse number can be calculated by

$$N_{\mathrm{p}} = f_{\mathrm{rep}} \cdot \frac{A_{\mathrm{spot}}}{v_{\mathrm{scan}}} \cdot n_{\mathrm{scan}} \ . \tag{4.2}$$

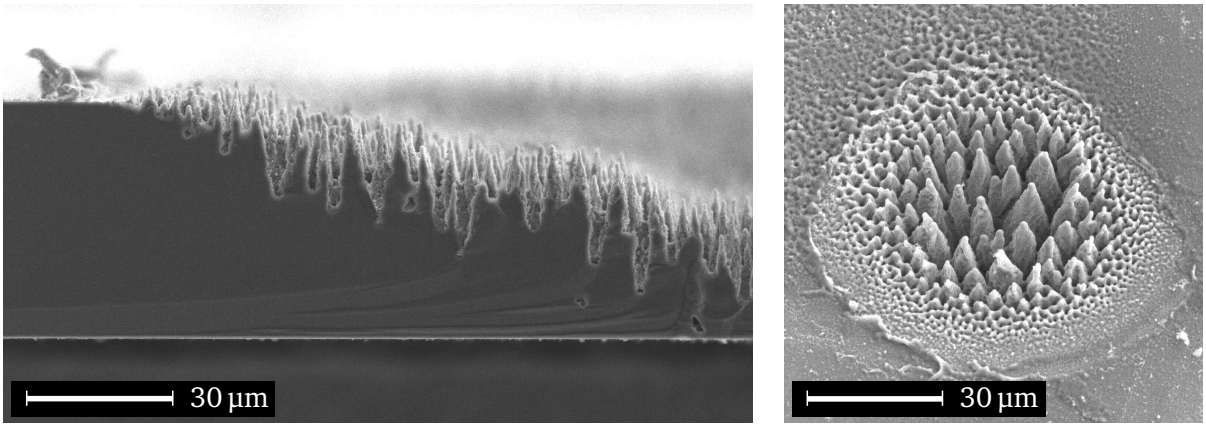

(a) (b)

Figure 4.7.: SEM images of silicon processed in SF_6 showing the influence of (a) pulse number and (b) laser fluence onto height and spacing of the microstructures. For the structured surface shown as cross section in (a), the power was set to 150 mW while the pulse number was increased from 250 to 1250 from left to right. A piece of debris is visible on top of the flat surface on the left side. The spot in (b) was irradiated with 500 pulses with an energy of 25 µJ each. The fluence profile is Gaussian shaped due to the spatial profile of the pulses, which results in structures of different sizes.

Previous works demonstrated that the correlation of pulse number and needle height is non-linear for small pulse numbers (Ebert, 2017; Neumann, 2018). However, Peng et al. (2015) showed that for larger numbers exceeding 500 pulses the correlation becomes linear.

Since ultrashort laser pulse processing is a material removing process, the substrate thickness decreases with increasing structure height. This correlation is depicted in Fig. 4.7 (a). Starting with a flat wafer surface, the valleys deepen towards the left, which coincides with an increasing number of incident pulses.

The laser fluence F is given by the pulse energy $\mathcal{E}_\mathrm{L}$ per spot size A_spot. In the presented setup, fluence is varied by changing the pulse energy. Figure 4.7 (b) shows a single spot irradiated for 100 ms in sulfur hexafluoride (SF_6), which corresponds to 500 pulses. Due to the Gaussian shaped spatial profile of the laser spot, the fluence increases towards the middle. This leads to an increase in structure size. Also, Fig. 4.7 (b) shows that the spacing between the structures becomes wider for larger structures.

Shape

The shape of the microstructures is mostly influenced by the processing medium. As discussed in Section 2.3.1, the material removal during the laser-induced structuring is due to a combination of optical, hydrodynamic and chemical effects. Depending on the state of matter and its chemical composition, the processing ambient changes the samples ablation threshold while also introducing possible chemical reactants.

In this work, a selection of ambients was applied including air at atmospheric pressure, isopropanol and SF_6. Figure 4.8 shows an overview of the generated structures from three different viewing angles with comparable magnification. It should be noted, that the size and distribution of the structures are also influenced by other parameters, as discussed above, so that this section only shows an overall trend.

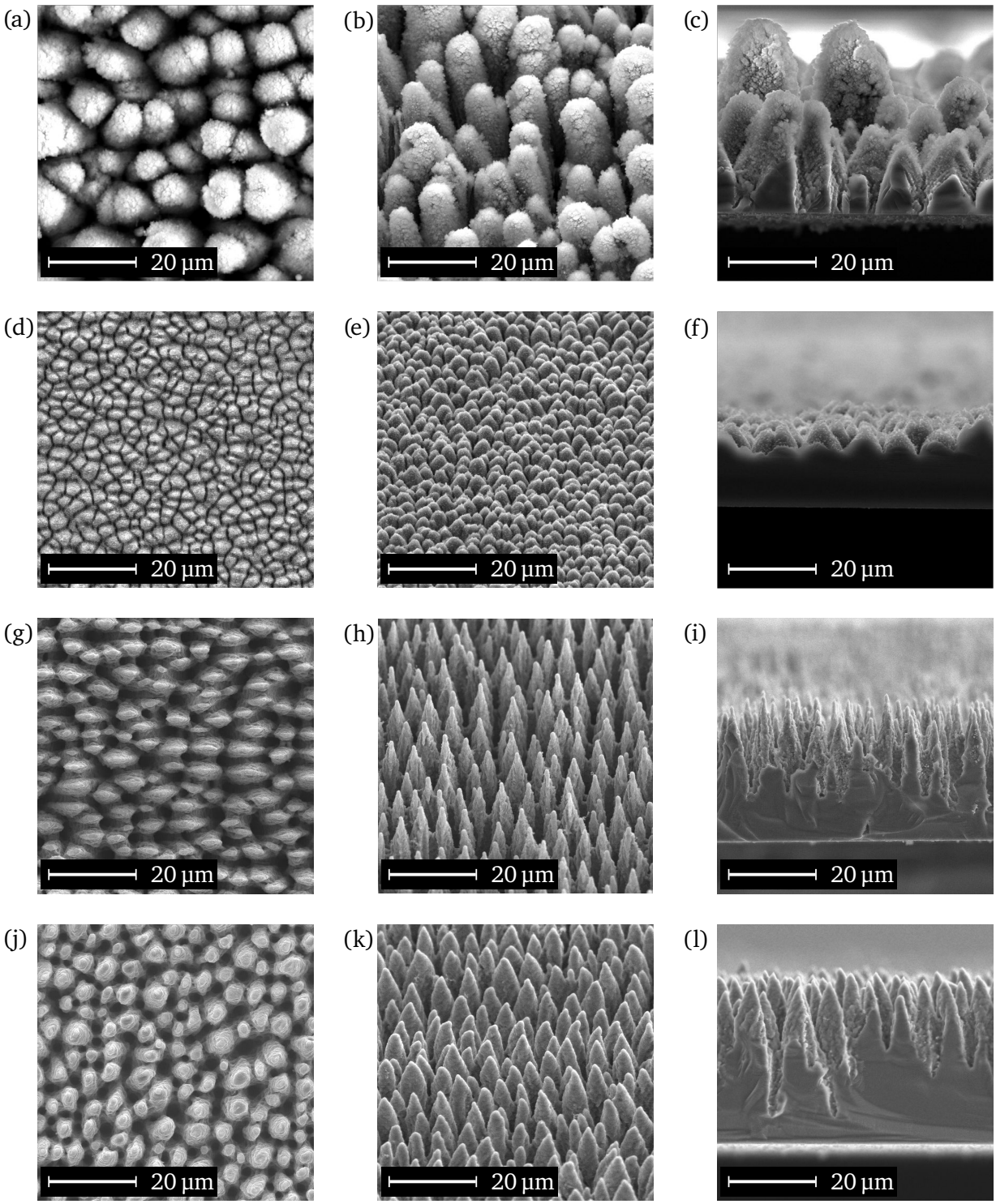

Figure 4.8.: SEM images of silicon microstructures created in different processing media. The top row (a-c) shows closely packed, round structures which result from processing in air. Microstructures generated in isopropanol (d-f) are smaller, exhibit broader slopes and have an angular base. Fabrication in SF_6 (g-i) creates spikes with sharp tips and elliptical bases. Using circularly instead of linearly polarized light (j-l), the bases of microstructures produced in SF_6 become more circular and the tips are less pronounced. The images of the left column (a, d, g, j) were recorded with a top view, the middle column (b, e, h, k) was viewed with a tilt between 30° and 45° and the right column (c, f, i, l) shows cross sections.

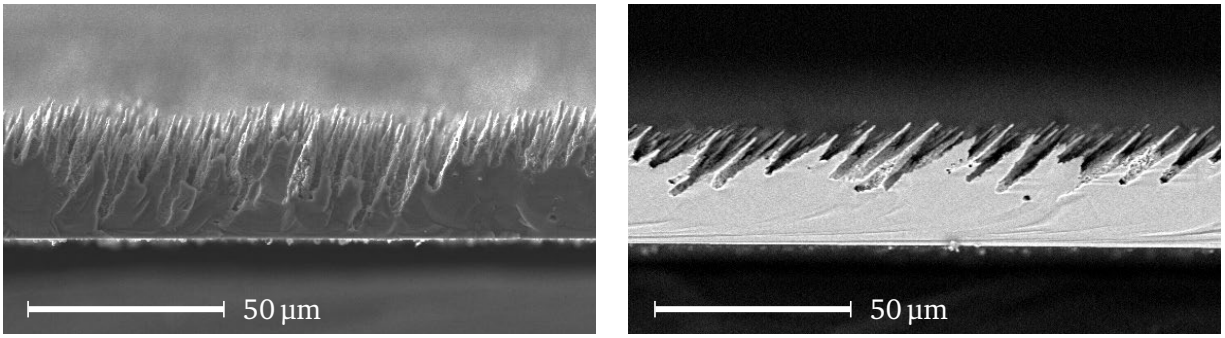

(a) (b)

Figure 4.9.: Slanted silicon spikes with (a) a 15° and (b) a 45° tilt. The SEM images were taken with (a) an secondary electron (SE) and (b) a backscattered electron (BSE) detector. Adapted from Ebert et al. (2021) (Fig. 1), licensed under CC BY 4.0, © The Author(s), 2021. Published by Cambridge University Press in association with Chinese Laser Press.

Microstructures generated in air at atmospheric pressure, which are shown in Fig. 4.8 (a-c), exhibit round tops and bases while being covered with a fluffy coat. They are separated by narrow, straight gaps and are rather inhomogeneous in terms of height and width. When the silicon wafer is immersed in isopropanol during processing, the fabricated structures are cones with broad slopes that are covered with bead-like nanostructures as depicted in Fig. 4.8 (d-f). The structures are separated by almost straight rifts of similar width, so that the bases become angular. Gaseous SF_6 leads to the formation of quasi-periodic spikes with a high-aspect ratio, which in some cases feature small droplets on their tip as can be seen in Fig. 4.8 (g-i). The needles have a consistent height and are separated by craters and bridges of varying depth. The influence of other gaseous processing media onto the structure shape is discussed by, e.g., Sheehy et al. (2005).

Besides the processing medium, the microstructure shape is also influenced by the polarization of the laser light. The samples shown in Fig. 4.8 (a-i) were created with linearly polarized light. For the structures created in SF_6 the influence is most obvious, as can be seen in the top view image (Fig. 4.8 (g)). Their bases are oval with the short axis of the elliptic base perpendicular to the laser polarization. Circularly polarized light, on the other hand, leads to round bases, as shown in Fig. 4.8 (j-l). However, in this case the needles feature larger tip radii. This phenomenon can be explained by the polarization dependence of Fresnel-refraction (Zhu et al., 2006).

Tilt

So far, the presented structures are all perpendicular to the wafer rear side. However, for some high energy matter experiments it is of interest to orient the structures along or against the incoming laser, which usually hits the target under an oblique angle. During the structuring process, the microstructures develop parallel to the direction of the incident laser. By tilting the sample, slanted spikes can be produced with an angle that exactly corresponds to the tilt angle.

Figure 4.9 shows two samples processed with a 15° and a 45° tilt angle, respectively. Especially for the 45° tilt, a reduced spacing between the spikes is noticeable. For spikes with an oval base, the microstructure shape becomes leaf like.

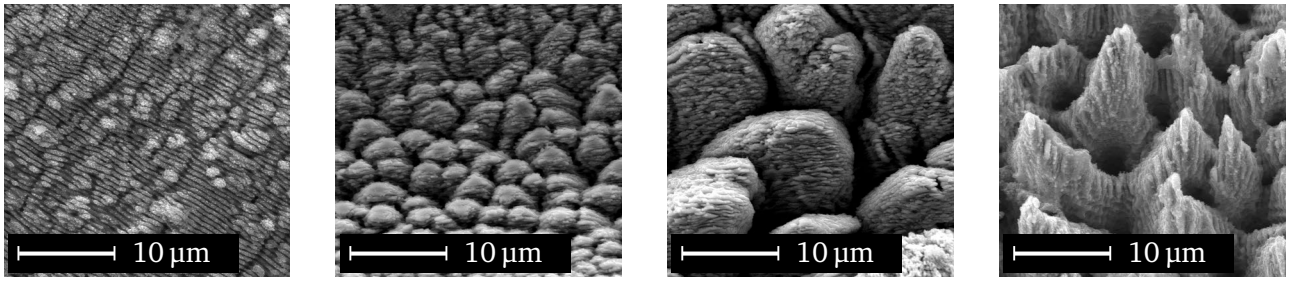

(a) (b) (c) (d)

Figure 4.10.: SEM images of microstructures on metals generated by ultrafast pulse laser processing. (a) Cu sample processed in air with 75 mW and a scanning speed of 1 mm s^{-1}. The Ti samples were structured in vacuum of roughly 5 mbar with (b) 35 mW at 0.5 mm s^{-1}, (c) 205 mW at 0.5 mm s^{-1} and (d) 496 mW at 2.5 mm s^{-1}.

4.1.3. Microstructured metal surfaces

In the scope of this work, not only silicon, but also metals such as titanium (Ti), copper (Cu) and gold (Au) were structured. Copper and gold surfaces show only the formation of ripples after being irradiated with ultrashort pulses. Figure 4.10 (a) shows a Cu surface that was processed in air with a laser power of 75 mW and a scanning speed of 1 mm s^{-1}. The ripples are covered with tiny beads and have a wavelength of approximately 600 nm, therefore falling in the category of LSFLs (see Section 2.3.1).

Irradiated titanium surfaces exhibit microstructures similar to the ones generated on silicon. They are, however, more susceptible to changes in power as the energy distribution and incubation in metals differs from dielectrics (Mannion et al., 2004). The irradiation with low laser power pulses around 35 mW leads to very regular structures with a width of only 2 to 3 µm (Fig. 4.10 (b)), while an irradiation with higher power around 200 mW generates structures with diameters exceeding 10 µm (Fig. 4.10 (c)). Both the diameter and the height of these bumpy structures are subject to large variances. In case of even higher power around 500 mW, the microstructures become more cone-like with sharper tips (Fig. 4.10 (d)). The base of titanium microstructures also becomes more circular with circularly polarized pulses. Parameter studies of the influence of the laser power and the number of incident pulses are shown in Appendix A.3. For further information refer to Ahmmed et al. (2015), who present another detailed parameter study on the evolution of titanium structures.

4.2. Replication

There exists a number of materials that are of interest for high power laser matter experiments that cannot be structured directly via ultrashort laser pulse processing. Furthermore, the experiments carried out with recently built laser systems require increasingly large quantities of targets. Both of these issues can be addressed by employing a replication procedure based on molding. The molds can be used repeatedly, which lowers the production effort in terms of costs and time. Also, replicas can be characterized using destructive methods, which is not an option for the master targets themselves.

The implemented process chain consists of three steps. First, a master needs to be produced, e.g., by ultrashort laser pulse processing as described in Section 4.1. Second, a mold of this master is fabricated via a molding procedure using polydimethylsiloxane (PDMS). The implementation of this step was greatly supported by René Heber (2019) in the scope of his master's thesis. Lastly, the mold, which is a

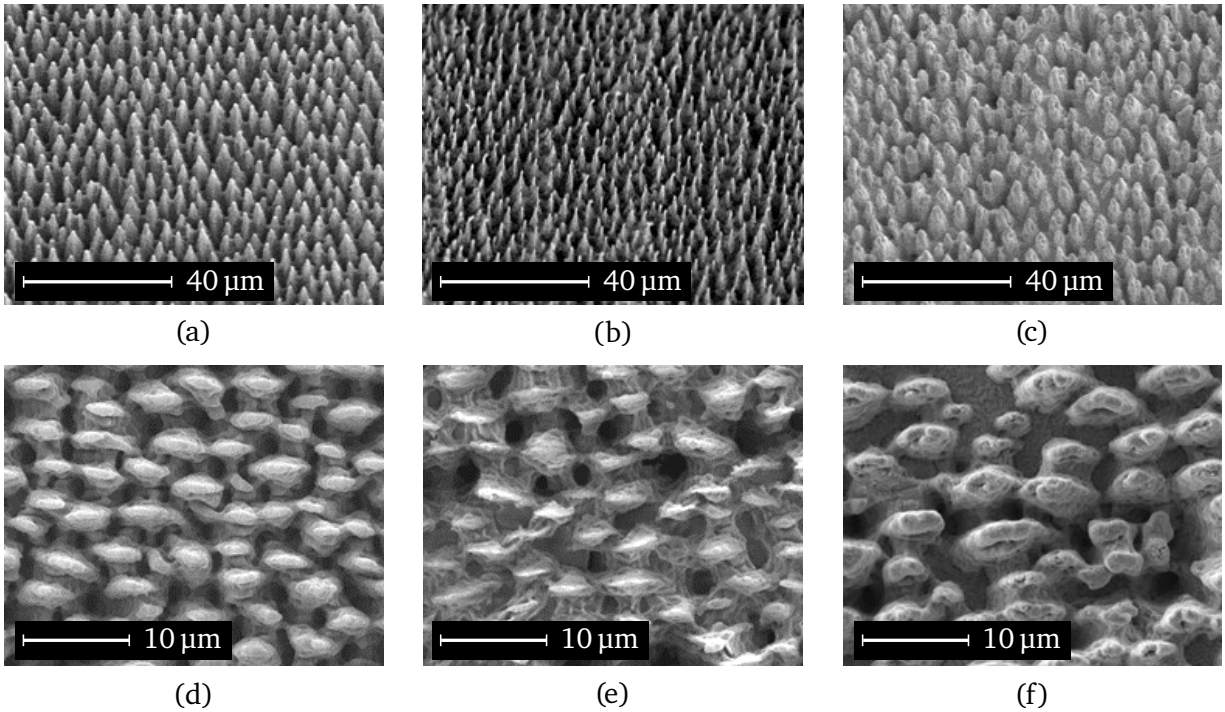

Figure 4.11.: SEM images of a silicon master (a, d), a PS replicate (b, e) and a Cu replicate (c, f). The top row is viewed with an approximate tilt angle of 25°, while the bottom row shows a top view with a higher magnification. Adapted from Ebert et al. (2021) (Fig. 4), licensed under CC BY 4.0, © The Author(s), 2021. Published by Cambridge University Press in association with Chinese Laser Press.

negative impression of the master, is used to create replicas out of the desired material. One possibility is creating microstructured polymer foils by spin coating. Another way is employing electroplating to realize metal targets. Although the main motivation for this part of this work was developing and implementing a replication procedure for microstructures in particular, the procedure can easily be applied to all sorts of masters.

A silicon master, a polystyrene (PS) replicate and a Cu replicate are depicted in Fig. 4.11. Even though the substructures differ slightly, which is most likely caused by shrinking and swelling of the mold, the shapes show a great similarity. In the following sections, the fabrication is described in detail, starting with the molding procedure and followed by the replication processes for polymers and metals.

4.2.1. Molding procedure

Over the years, a vast variety of micro molding procedures were developed to create thermoplastic objects with at least micrometer resolution. These procedures range from simple impression techniques, e.g., for dental applications, to soft and nanoimprint lithography processes such as hot embossing or UV imprint lithography (Pimpin and Srituravanich, 2012; van Assenbergh et al., 2018). For this work, the chosen technique is casting, where a fluid polymer is poured onto the master before it polymerizes due to a mixed-in linker. This method can be performed with a comparatively simple setup, and the materials are easily available and cost friendly.

For the application at hand, the material used for casting needs to meet several requirements. Its viscosity has to be adequate to fill all microscale voids of the structures, it should be easily removable from the master as well as the replica and it should show minimal shrinkage and distortion. A material

that suits these requirements is PDMS. Studies showed a resolution down to a few nanometers (Hua et al., 2004), and due to its outstanding properties it is a commonly used material in other fields like nano- and microfluidics (Friend and Yeo, 2010).

Essentially, the molding procedure consists of five steps, that are illustrated in Fig. 4.12 (a)-(e). First, the master is placed in a container. Next, an anti-sticking coating is applied to improve the detachment of the mold later on. For this, the container is placed in a desiccator together with a small amount of chlorotrimethylsilane in the order of 100 µL. Once the desiccator is evacuated, the silane evaporates due to the low pressure and coats the master.

In the mean time, the PDMS is mixed with a 10:1 ratio of base to cross-linker according to the manufacturers recommendation (The Dow Chemical Company, 2021). After being thoroughly mixed, the PDMS is placed in another desiccator to remove remaining air bubbles for 60 min.

Afterwards, both components are removed from the desiccators and the PDMS is slowly poured onto the master. Then, the polymer is degassed for another 60 min at room temperature, so that trapped air is extracted and a precise impression is achieved. Following this, the container is placed on a hot plate at 100° for 30 min to accelerate the curing process. At last, the solidified mold is carefully peeled off. This step can be challenging, especially if the master features small overhangs or undercuts. To remove crooked edges, the mold is then cut to a typical size of roughly 2 cm × 2 cm.

The whole procedure is executed in a setup specifically designed for this purpose. It is an enclosed box connected to a fume hood, that increases user safety when handling the toxic silane. Furthermore, contamination of other workplaces with PDMS can be prevented and the heating plate is less likely to be brushed by accident. For more detailed information on the setup, the material properties and the procedure refer to the master's thesis by R. Heber (2019).

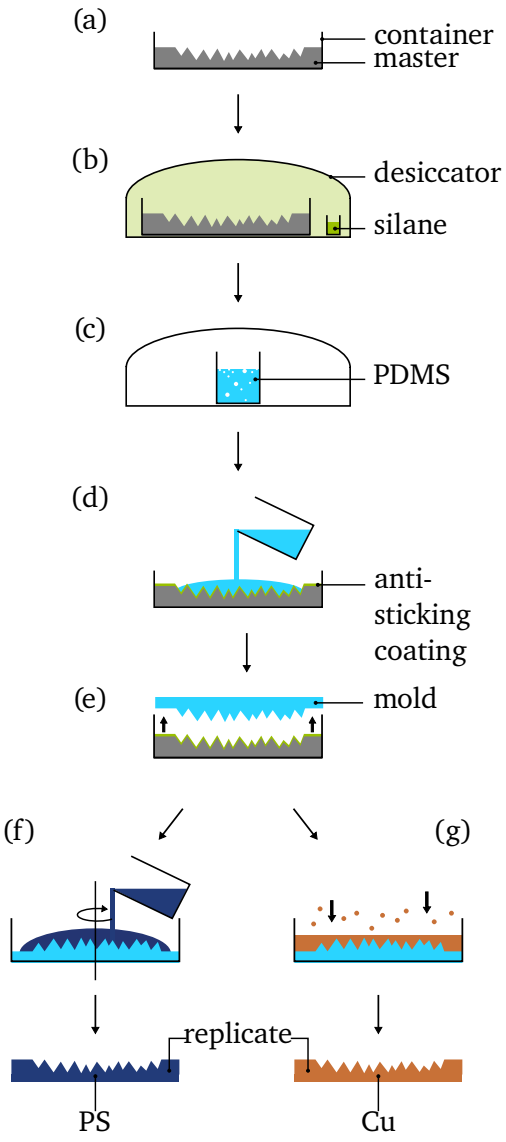

Figure 4.12.: Replication procedure. (a) The master is placed in a container before (b) both are positioned in a desiccator together with silane to apply an anti-sticking coating. (c) After mixing the PDMS it is degassed prior to (d) being poured onto the master. (e) Once solidified, the PDMS mold is detached and can then be employed to either create (f) a PS replicate by spin coating or (g) a Cu replicate by thermal evaporation. Based on Heber (2019) and adapted from Ebert et al. (2021) (Fig. 2), licensed under CC BY 4.0, © The Author(s), 2021. Published by Cambridge University Press in association with Chinese Laser Press.

4.2.2. Polymer replicas

The PDMS mold can be employed to manufacture thin, microstructured polymer foils as illustrated in Fig. 4.12 (f). Of particular interest for current applications such as proton and neutron acceleration, is the polymer PS, which is used either deuterated (C_8D_8) or non-deuterated (C_8H_8) depending on the experiment. Other polymers like polyurethane (PU) and polymethyl methacrylate (PMMA) also work with this replication procedure (Heber, 2019).

For thin foils, so-called spin coating has proven to be a suitable fabrication method. Herefore, a substrate, in our case the mold, is fixed on a vacuum chuck that can be rotated with up to 10.000 rpm. Then, a solution of the polymer in a solvent, e.g., toluol, is poured onto the substrate, which is at rest and subsequently accelerated or already spinning. The fluid solution is spread outwards by the centrifugal force leading to a smooth and thin foil once the solvent is evaporated.

So far, targets were created with a PS solution of 0.104 g PS per 1 ml toluol. To prevent the foil from irregular solidification, a toluol atmosphere is created in the spin coater. Spinning the mold at 3000 rpm for 60 s results in an approximately 15 µm thick foil with indented microstructures. Because the PDMS mold is slightly swelling in toluol, the microstructures are marginally thinner, as can be seen in Fig. 4.11 (b) and (e). However, this effect can be reduced by fabricating a thicker mold.

4.2.3. Metal replicas

For some metals, like Cu or Au, directly irradiating the surfaces with ultrashort laser pulses does not lead to the generation of high aspect ratio microstructures. However, electroplating in PDMS molds can be applied to fabricate these kind of structures. In this work, the microstructures are replicated with copper. For this, the small PDMS molds are placed on standard 4-inch Si wafers to simplify handling during the procedure.

To prepare the mold for electroplating, it needs to be covered with a conductive seed layer. Here, thermal evaporation is used to deposit a 10 nm thin layer of chrome before adding another 90 nm layer of copper. The chrome enhances the adhesion between seed layer and polymer, which prevents it from detaching during the subsequent procedure. It is common to heat the substrates during the thermal evaporation process to create a smoother and more homogeneous layer. However, tests showed that thin cracks develop in the seed layer covering the PDMS mold during the cool down due to shrinking, consequently, the mold is kept cold. An alternative to thermal evaporation would be sputtering.

After the mold is coated, everything except the region featuring the microstructures is covered with capton tape to limit the deposition to this area only. Further on, two strips of copper tape are stuck onto opposite mold edges, which extend beyond the Si wafers edge. Figure 4.13 shows the electroplating setup used during this project. It is part of the clean room equipment of the *Integrated Micro- and Nanosystems Lab* at TU Darmstadt, who kindly gave their permission for usage. The electrolytic cell is made out of stainless steel with a teflon inlet, which is resistant to chemicals. To set up the cell for usage, the prepared wafer with mold and copper tape is positioned on the base plate of the cell and clamped in place with the side enclosure. With the aid of teflon spacers, a flat copper electrode is placed about 1 cm above the mold.

Next, the cell is filled with the electrolyte *Tifoo Bright Copper Plating Solution* (Tifoo Shop - Electroplating & Surface Technology, 2021), and the electrode and copper tape are connected to a voltage supply. It is crucial to immediately start the deposition, because otherwise the seed layer dissolves in the electrolyte. The copper deposition is carried out for 60 min at room temperature with a current density of approximately 6 A dm^{-2} in potentiostatic mode. During the entire time, an agitator stirs the electrolyte to prevent inhomogeneities in the deposited layer due to the formation of H_2 bubbles or local depletion of the electrolyte.

Following this, the wafer is removed from the electrolytic cell and thoroughly rinsed with distilled water to wash away any electrolyte residues. Last, the approximately 25 µm thick Cu foil is carefully lifted of with a scalpel. The resulting microstructures are shown in Fig. 4.11 (c) and (f). So far, the tips are slightly blunder than the masters. One issue could be insufficient coating of the valleys of the

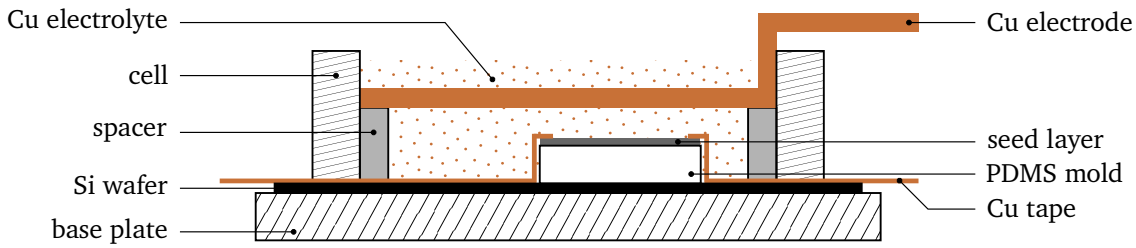

Figure 4.13.: Cross section of the setup for replicating microstructures with Cu. The PDMS mold, which is coated with a seed layer and attached to Cu tape, is placed on top of a 4-inch Si wafer. It is then positioned in an electrolytic cell made out of stainless steel with a teflon inlet, which is filled with a Cu electrolyte. By the means of teflon spacers, a flat electrode with a diameter of 6 cm is placed above. This electrode as well as the Cu tape are connected to a voltage supply to carry out the Cu deposition. The mold is placed slightly to the edge of the cell to leave room for an agitator (not shown).

mold when creating the seed layer, which might be solved by switching to sputtering instead of thermal evaporation.

Regardless of the method used to fabricate the structured samples, they are then prepared as targets for experimental campaigns, as described in the following.

4.3. Target fabrication

Before the structured samples can be shot in experimental campaigns, they need to be characterized and mounted to become targets. Additionally, in some cases it might be necessary to add another material as second layer. This section gives a short summary of the methods used to prepare the microstructured targets for experiments.

4.3.1. Preparation and characterization

In order to be able to draw any conclusions from the experiments, the experimenter must have precise knowledge of the properties of the target. This means that the microstructured samples need to be characterized prior to being shot. The relevant information includes the homogeneity of the structured area, the structure geometry and spacing, the remaining base thickness and in some cases the material composition. Also, the samples need to be free of contamination. To keep the structures intact, the targets are characterized with non-destructive methods as described in Section 4.1.1.

For the Si samples or directly structured metal foils, analysis with an SEM is straightforward. The samples are already glued to SEM pins for processing and are vacuum ready. This is particularly advantageous for intermittent inspection during the processing. However, before the final characterization, the samples usually need to be removed from the pin for two reasons. First, cleaning in an ultrasonic bath or rinsing with distilled water is necessary to remove any residues of ablated material. Second, the samples are divided into two parts with the breaking edge crossing the structured area. This way, one part can be employed as target while the other can be stored or used for destructive characterization methods.

The structured samples can be divided either by laser cutting, which is preferable for metal foils, or by snapping. Snapping works very well for silicon samples due to their crystal structure. By introducing predetermined breaking points with a diamond cutter or an ultrashort pulse laser, the position of the break is defined. Using a laser to insert the incisions is more precise, and the incisions can already be

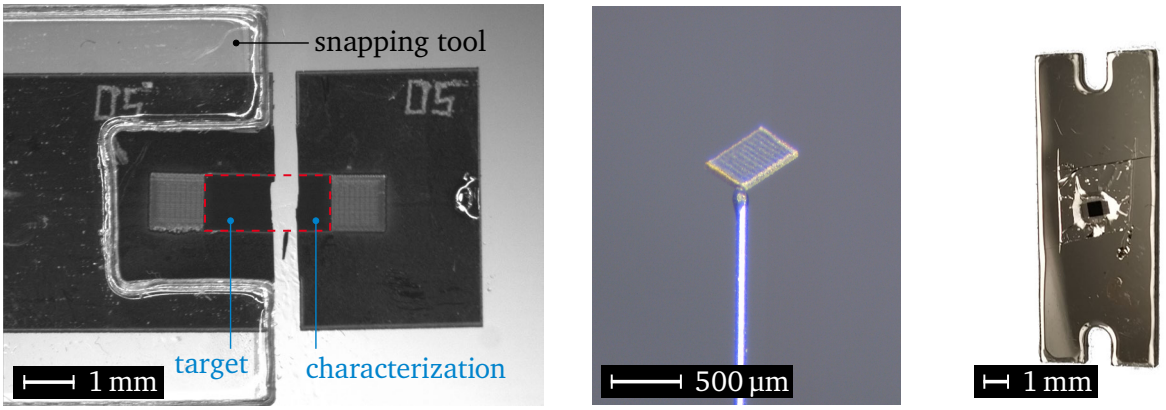

(a) (b) (c)

Figure 4.14.: Further processed microstructured samples. (a) Photo of a snapped silicon substrate showing the two pieces that will be used as target (left) and for characterization (right). Both parts are labeled with a two-digit ID number. Also visible is the snapping tool with a notch to keep the structured area intact. (b) Microstructured silicon cut to a 500 × 500 µm^2 square mounted on a SiC stalk with a 45° tilt. Image and mounting by *Dayna Peterson* at *LLE, Rochester, USA*. (c) Structured PS foil placed on a plastic target holder. The target was sputtered with a thin coat of Ag for characterization, which shows off the strong light absorption in the structured area in the middle.

made when the wafer is cut to pieces for the structuring procedure (see Section 4.1.1). In both cases, the structured area is left intact and the breaking points are only marked on the wafer edges. This way, the broken edge can be used to examine the cross section of the microstructures.

The snapping is performed with the aid of a snapping tool as shown in Fig. 4.14 (a). It features a notch to keep the structured area intact. The wafer is placed on a microscope slide with the tool on top of the wafer such that the edge of the tool, the incision marks and the edge of the slide align. By applying slight pressure uniformly along the free hanging wafer edge, the substrate snaps into two separate pieces.

The piece meant for characterization or, if this step was omitted, the target itself are then viewed with an SEM for the final analysis. With the exception of polymers, all materials processed so far are conductive, so that no additional coating is necessary. For the polymer foils, a thin coating of silver or gold enables imaging. Last, the target parts are mounted to suitable frames or holders that can be employed in the respective experiments.

4.3.2. Mounting

There is an infinite number of ways to mount microstructured targets to suitable holders. Therefore, this section only points out a few possibilities that were implemented for the experimental campaigns relevant for this thesis.

Perhaps the simplest approach to create targets from the structured silicon samples is using the entire wafer pieces. Here, the non-structured area, which typically has a thickness of 50 µm, gives support and can be directly glued to a stalk or holder. In case smaller targets are required, the structured area is cut down to smaller pieces, e.g., 500×500 µm^2, with an ultrashort pulse laser. These pieces are then glued to thin stalks, as shown in Fig. 4.14 (b), with the desired orientation. This method is more delicate and the mounting process requires more time, but the time effort for structuring can be lowered because one structured area is used to fabricate multiple targets.

One option to prepare the thin, structured polymer foils as targets is placing them over frames with a hole in the middle through which the laser or the particle beam pass. Figure 4.14 (c) shows a microstructured foil fabricated by replication on such a holder. The foil stays in place by electrostatic force, so no glue is necessary. The main challenge is to position the foil without wrinkles, which would influence, e.g., the particle acceleration.

4.3.3. Layered targets

Sometimes it is not strictly necessary or desired to have the whole target made out of the same material. In this case, layered targets are useful. They enable the experiment to benefit from the microstructures in terms of laser matter coupling, while also having the opportunity to choose from a wider range of materials for the specific application. As discussed in the previous sections, the generation of microstructures on silicon is well known and a large variety of shapes and sizes can be realized. For this reason, silicon is used as the target front component. Depending on the second component, it is structured either before or after the rear layer is added.

For laser ion acceleration and subsequent neutron generation, proton or deuteron rich rear side layers are of great interest to boost the number of available ions. With this in mind, thin polymer foils are manufactured via spin coating on glass wafers. Figure 4.15 (a)-(c) shows the procedure by which the polymer foils are attached to the silicon pieces. First, the foils are separated from the substrate by submerging the glass wafer into distilled water, leaving the foils floating on the water surface. The Si piece, which is structured beforehand and attached to a plastic frame, is then dipped into the water and used to lift the foils off of the surface. If speed and angle are chosen correctly, the foils cling to the Si piece without any further adhesives. A photo of such a layered target is shown in Fig. 4.15 (d).

Experiments focusing on the generation of X-rays often call for high-Z materials. These materials can be added to the silicon targets by techniques like thermal evaporation, sputtering or electroplating. All of these methods can be executed with or without masks, so that either full layers or spatially restricted layers are added. Furthermore, grains or precut dots can be glued to the rear side. For experimental campaigns connected to this thesis, silicon targets with copper grains and dots via masked thermal evaporation were built (Ebert et al., 2021; Sander et al., 2021). The former used silicon pieces that were already structured. The latter started with adding the rear side layer before creating the microstructures on the target front.

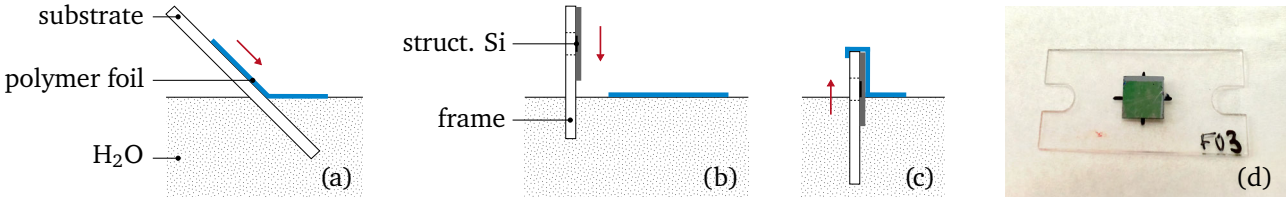

Figure 4.15.: Fabrication of a layered target consisting of a microstructured Si target front and a polymer rear side. (a) The substrate, on which the polymer foil was produced via spincoating, is submerged in water (H_2O). The foil separates itself and is left floating on the surface. (b) The target frame, to which the structured Si wafer piece is glued, is submerged into the water. (c) An edge of the foil is caught with the frame. Then, the foil is lifted out of the water, clinging to the rear side of the wafer. Subfigure (d) shows a photo of the rear side of such a layered target with the polymer foil appearing greenish. The Si wafer, which has a size of $5 \times 5\,\mathrm{mm}^2$, is glued to a plastic holder with F03 denoting its identification number.

5. Interaction of high intensity lasers with microstructured surfaces

Target front side modifications can significantly enhance the transfer of the energy delivered by a high intensity laser to the target, as discussed in Section 2.3.4. The exact amount of the carryover depends on the respective experimental parameters, because the properties of the produced front surface plasma determine the relevant electron heating mechanisms and their efficiency. Depending on the laser intensity, pulse length, pulse energy, structure size, geometry, orientation, etc., the front surface structures dissolve on different timescales, giving rise to varying plasma temperatures and density gradients.

Here, the interaction of microstructured targets with petawatt laser systems with pulse lengths of more than 0.5 ps was studied experimentally. For this, a variety of Si targets were produced via laser-induced periodic surface structuring, as described in Chapter 4. Starting with a description of the experimental setups, the measured ion beams and X-ray spectra are subsequently evaluated. The results give insights into the influence of the ASE contrast, the laser pulse length as well as the structure size and orientation on the laser target coupling.

Furthermore, PIC simulations were conducted to study the interaction theoretically. In such simulations, the parameters that can be observed are not limited to products leaving the target. Instead, the evolution of the electric and magnetic fields as well as the particle behavior are analyzed in different laser target configurations. First, the influence of the characteristic spike geometry on electron heating is studied, followed by a simulation series validating the results of the experimentally studied tilted microstructures. Afterwards, a study on target optimization is presented and the spike-like structures are compared to the often employed pillar structures.

The chapter concludes by summarizing and discussing the findings of both perspectives. In particular, their significance for current research is highlighted and references to other work in this field are established.

5.1. Experimental investigation

Over the course of this project, the interaction between high intensity lasers and microstructured targets was studied in two main experimental campaigns, which took place at the PHELIX (Petawatt High-Energy Laser for Heavy-Ion eXperiments) laser at the GSI Helmholtzzentrum für Schwerionenforschung in Darmstadt, Germany (Bagnoud et al., 2010), and the Omega EP laser at the Laboratory for Laser Energetics (LLE) in Rochester, NY, USA (Stoeckl et al., 2006). Furthermore, a few targets were investigated during two contributing campaigns at the PHELIX facility, with the focus of these experiments being on neutron generation. The parameters of the two laser systems employed for all main and contributing campaigns are summarized in Table 5.1. Both the PHELIX laser at GSI and

Table 5.1.: Overview of the employed laser systems. The Omega EP laser is situated at the LLE in Rochester, NY, USA, and the PHELIX laser at the GSI in Darmstadt, Germany. For both laser systems, the pulse length τ_L, the pulse energy $\mathcal{E}_L$, the focal spot diameter d_f and the intensity I as well as the ASE contrast and the laser incidence angle are listed. The central wavelength λ_L is 1053 nm for both systems. In case of the experiments at LLE, the pulse length was varied. At GSI, the ASE contrast was varied. All intensity and contrast values are approximations.

laser system	τ_L in ps	$\mathcal{E}_L$ in J	d_f in µm	I in W cm^{-2}	ASE contrast	incidence angle
Omega EP	1 – 20	250 – 1000	300	10^{17}	10^{10}	45°
PHELIX	0.5	120 – 220	6	10^{20}	10^{7} – 10^{13}	15°

the Omega EP laser at LLE are CPA based systems with a central wavelength of 1053 nm. They have relatively low repetition rates of 1 shot per 90 min (PHELIX) and 45 min (Omega EP), so the number of shots was limited. Since secondary applications were studied at the same time, an extensive number of target and laser configurations was shot, which lead to a data set with very low statistics.

5.1.1. Experimental campaigns

PHELIX campaign. The campaign at the PHELIX laser at GSI was conducted in February 2019. Here, the influence of the laser contrast was studied, which was realized by varying the ASE contrast of the laser system between 10^7 (3 shots), 10^{10} (3 shots) and 10^{13} (19 shots). Figure 5.1 shows the temporal profiles of all contrast configurations. The focal spot size was (6.4±1.2) µm (FWHM), but only 40 % of the energy was inside the focal spot area due to coma-like aberrations. These aberrations were probably caused by the Cu parabola used for focusing and have also been documented by others (Hornung et al., 2020). With a pulse length of 0.5 ps, the mean peak intensity on target was $(3.4\pm1.2)\times10^{20}$ W cm^{-2}.

Figure 5.2 (a) shows the experimental setup, in which the s-polarized laser hit the target with an incidence angle of 15°. Three diagnostics were employed to collect the data relevant for this thesis. The Si X-ray emission on the front side was studied with an energy dispersive crystal spectrometer

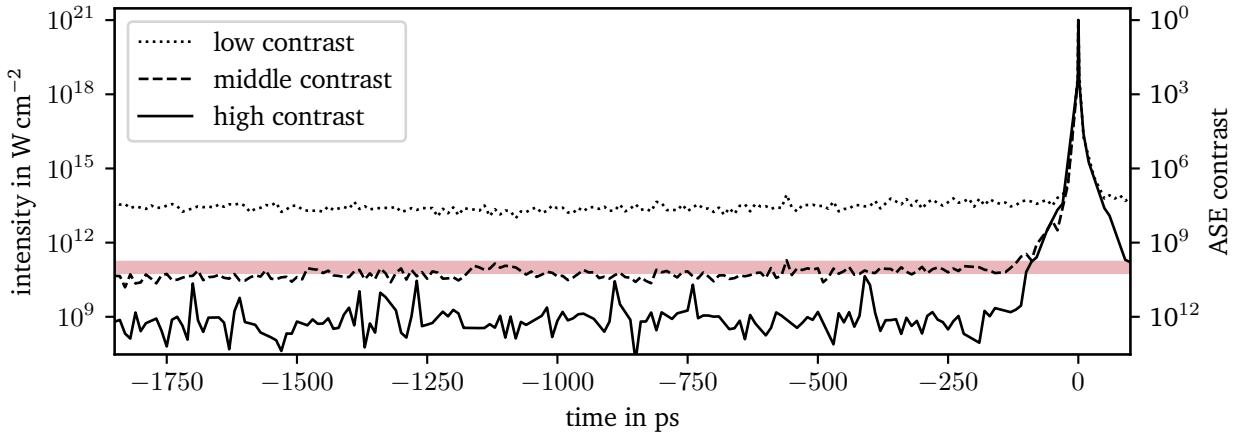

Figure 5.1.: Pulse profiles of the PHELIX laser system with low (dotted), middle (dashed) and high (solid) ASE contrast. The ASE level of the high contrast is in the order of or below the diagnostic limit. The semi-transparent red line at 1×10^{11} W cm^{-2} shows the ionization threshold of silicon (Martynenko et al., 2021).

(XRS), which covered an energy range from roughly 1700 eV to 2100 eV and had a viewing angle of 76°. The IP of type *BAS-SR* (Section 3.1.2) was placed parallel to a flat, $50 \times 15\,\mathrm{mm}^2$ large KAP crystal. A 12 µm polycarbonat filter was placed in front of the 15 mm entrance slit to protect the spectrometer from debris and background radiation. Potentially interfering electrons were deflected by a permanent magnet in front of the XRS. For the working principle of such X-ray spectrometers see Section 3.1.4.

The accelerated ions were observed with an RCF stack and a Thomson parabola, the working principles of which are described in Section 3.1.3 and 3.1.1, respectively. The stack covered an energy range from 7 MeV to 74 MeV and used Mylar and PMMA plates between the active layers. It was positioned with a distance of 54 mm from the target in target normal direction. A fraction of the beam passed the stack through a hole in the middle without being absorbed. This fraction was recorded with a Thomson parabola, which was also placed in target normal direction with a distance of 299 mm between target and parabola. A 200 µm pinhole was used to limit the source size and a voltage of 10 kV was applied. The geometry and magnetic field strength of the TP can be found in the master's thesis of N. Schroeter (2017). Both *BAS-SR* and *BAS-TR* IPs were used as detector. Since the available IPs were too small to cover the whole trace, two IPs with a small overlap were used. This required an additional stitching step during the analysis. To distinguish deuterons from other ion species with the same charge to mass ratio, a Cu filter was placed in front of the IP, which only transmits deuterons. The thickness was increased from 30 µm at the low energy end to 3000 µm at the high energy end of the trace.

All image plates were scanned roughly 20 min after the shot with an *FLA7000* scanner. The resolution was set to 25 µm, the sensitivity to 10,000, the latitude to 5, the scan depth was 16-bit and the compression was exponential. The IPs used in the Thomson parabola had to be scanned multiple times in almost all cases due to a saturation of the scanned signal.

A total of eight target types was investigated, which are shown in Fig. 5.3 (a) to (h). Their parameters are summarized in Table 5.2. As reference target, blank, flat Si foils (Fig. 5.3 (a)) with a thickness of 15 µm were shot. The other targets can be assigned to two subsets. One has copper rear sides (Fig. 5.3 (b) to (e)), which was motivated by studying the Cu X-ray emission of so-called layered targets.

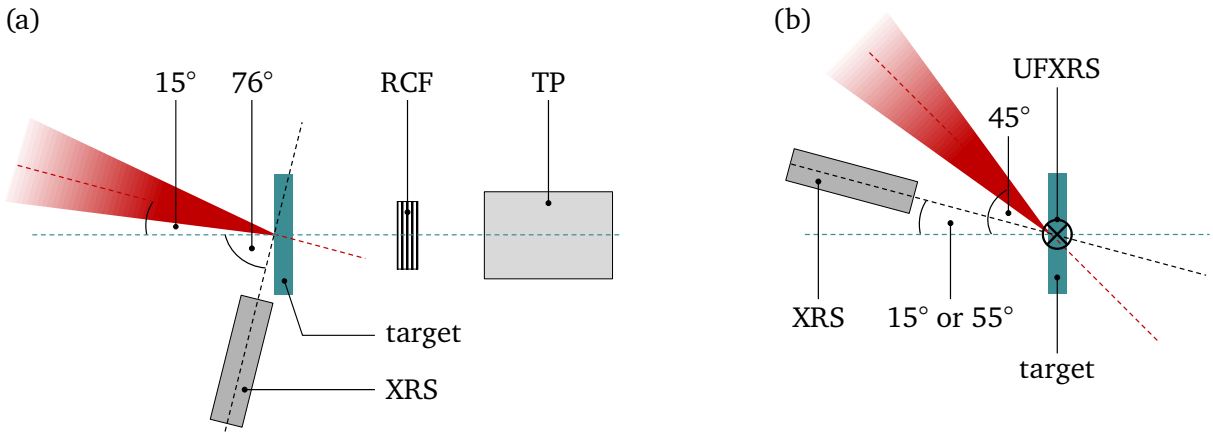

Figure 5.2.: Schematics of the experimental setups used during the main campaigns viewed from above. (a) During the PHELIX campaign the laser (red) had an incidence angle of 15° relative to target normal (turquoise). As diagnostics, an XRS, an RCF stack and a Thomson parabola (TP) were employed. Both ion diagnostics were aligned along the target normal direction, while the XRS had a viewing angle of 76° on the front side. (b) The laser incidence angle during the Omega EP campaign was 45° relative to target normal. The interaction was studied with an XRS, which was observing the target front side under either 15° or 55° depending on the configuration, and an ultrafast XRS (UFXRS), which was looking along the target.

Table 5.2.: Summary of target parameters and place of usage. The target type refers to the geometries shown in Fig. 5.3, which also illustrates the definitions of the target height h, the distance between the spikes d, the tilt angle α, the base thickness b and the back layer l. Structures that are parallel to target normal or the laser incidence direction are denoted by (TN) or (||), respectively. In case of flat targets, the base thickness is equivalent to the thickness of the foils, which is given as provided by the manufacturer. The characterization methods are described in Section 4.3.1. The small structures (h) and PS structures (j) could not be evaluated from the target side, therefore approximations are given. Besides the laser system, at which the targets were shot, the angle of laser incidence is listed.

type	label	h in µm	d in µm	α	b in µm	l in µm	laser	angle
(a)	flat	-	-	-	15	-	PHELIX	15°
(b)	flat + Cu	-	-	-	15	5.0 (Cu)	PHELIX	15°
(d)	0° (‖) + Cu	26.1±2.9	6.3±1.7	15°	5.5±3.7	5.0 (Cu)	PHELIX	15°
(c)	15° (TN) + Cu	23.0±3.2	6.5±1.6	0°	5.4±3.4	5.0 (Cu)	PHELIX	15°
(e)	30° + Cu	26.1±2.9	6.3±1.7	-15°	5.5±3.7	5.0 (Cu)	PHELIX	15°
(f)	flat + PS	-	-	-	15	1.2 (CHD)	PHELIX	6.5°, 15°
(g)	15° (TN) + PS	23.0±3.2	6.5±1.6	0°	5.4±3.4	1.2 (CHD)	PHELIX	6.5°, 15°
(h)	small (TN) + PS	4.0±0.7	3.4±0.8	0°	8.0±2.0	1.2 (CHD)	PHELIX	15°
(i)	PS foil	-	-	-	0.4−1.1	-	PHELIX	5°
(j)	15° (TN) PS	15.0±2.5	4.1±0.9	0°	5.0±2.0	-	PHELIX	5°
(k)	flat	-	-	-	10	-	Omega EP	45°
(l)	flat + shield	-	-	-	10	-	Omega EP	45°
(n)	0° (‖)	18.1±1.8	7.6±2.0	45°	8.9±1.8	-	Omega EP	45°
(m)	45° (TN)	21.6±2.2	5.9±1.5	0°	6.9±2.0	-	Omega EP	45°
(o)	struct. + shield	21.6±2.2	5.9±1.5	0°	6.9±2.0	-	Omega EP	45°

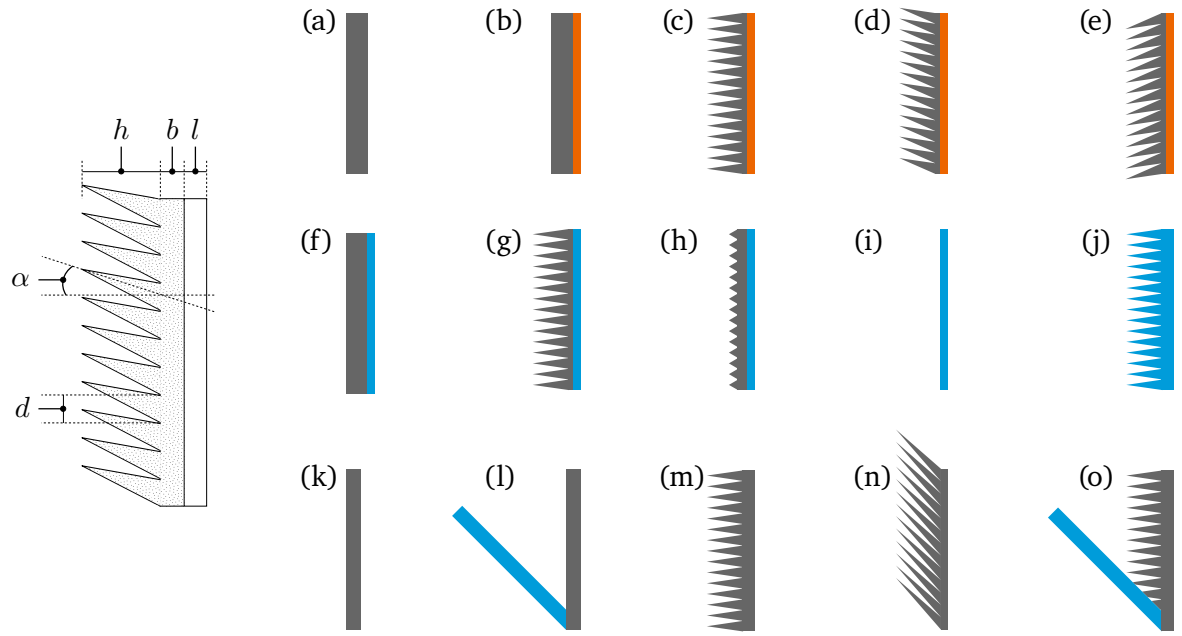

Figure 5.3.: Definitions of the characteristic target dimensions (left) and schematics of the employed target types (right). The targets can be described by the microstructure height h, the tilt angle α, the distance between the spikes d, the base thickness b, and the back layer l. For the experiments, the flat and structured silicon foils (gray) are backed up with Cu foils (orange) or PS foils (blue) to suit the development of secondary sources and subsequent applications such as Cu X-ray backlighters and neutron production. The parameters of each design are listed in Table 5.2.

The behaviour of these layered targets in regards to Cu X-ray emission will not be discussed here, as they are analyzed by *Steffen Sander* in the scope of his PhD thesis. The results are currently under review at *Physical Review E* (Sander et al., 2021). However, the Si X-ray yield as well as the ion acceleration of these targets will be discussed in the following sections.

The other subset (Fig. 5.3 (f) to (h)) featured a rear layer out of a mixture of deuterated and non-deuterated polystyrene (CHD). The CHD foils were produced with a ratio of 0.1505 g deuterated and 0.2531 g non-deuterated polystyrene to 5 ml toluol, which served as solvent and evaporated during the solidification of the polymer foils. In a previous campaign at the VULCAN laser system at the Rutherford Appleton Laboratory (RAL), Didcot, UK, the number of accelerated protons was presumably limited by the number of available protons in the contamination layer (Ebert et al., 2020; Neumann, 2018). The CHD mixture therefore served two purposes. The non-deuterated part increased the number of available protons while the appearance of deuterons in the accelerated spectrum would indicate a depletion of the contamination layer, because these ions must have come from the target foil itself.

Both subsets include targets with flat front surfaces (Fig. 5.3 (b) and (f)) as reference. The thickness of these Si foils was chosen to roughly match the amount of material of the microstructured targets. Four different microstructured fronts were employed. One set of structures was pointing along target normal (Fig. 5.3 (c) and (g)), another pointing along the direction of the incoming laser (Fig. 5.3 (d)) and a third opposed (Fig. 5.3 (e)) to the laser incidence direction, which results in an effective incidence angle of 30°. Since one of the open questions regarded the durability of the microstructures, smaller structures (Fig. 5.3 (h)) were also investigated. The targets were mounted on PS posts as illustrated in Fig. 5.4 (a), with the structured area still being part of a larger, unstructured wafer piece with a size of $7.5 \times 5.0\,\mathrm{mm}^2$. As described in Section 4.3.1, the processed wafer pieces were broken across the microstructured area to allow for characterization. The structured area thus extends to the upper edge.

The highly light absorbing properties of the microstructured Si challenged the target alignment process. Illuminating the front of the target to choose the right position did not work. Instead, alignment holes marking the corners of the structured area with a diameter of roughly 70 µm were added during the fabrication process, which were used in combination with a light source on the rear side to determine the final position. The fabrication procedure discussed in Section 4.1.1 allows to create particularly homogeneous microstructured areas, which is essential to produce reliable results with this alignment method.

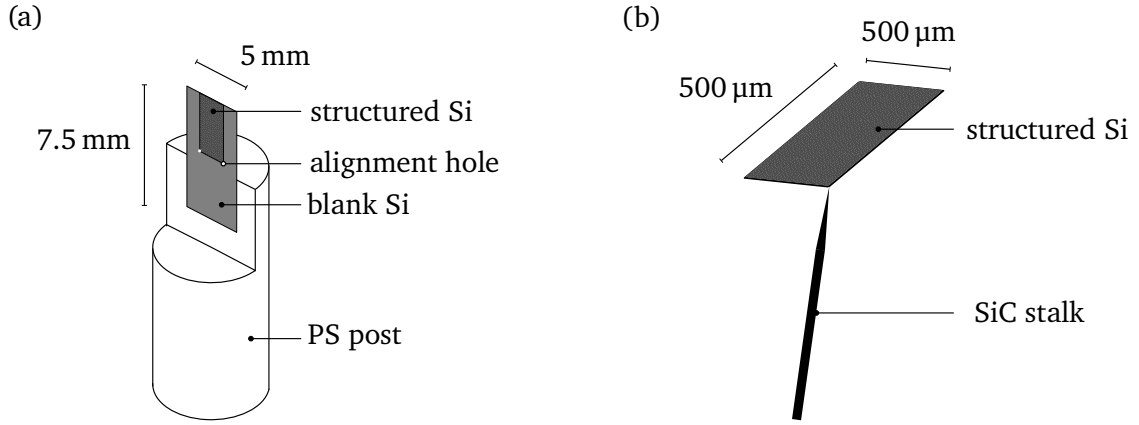

Figure 5.4.: Target mounts for the (a) PHELIX and (b) Omega EP campaign. (a) The microstructured region is in the upper middle area of a blank Si wafer piece, with two alignment holes marking the corners. The piece is glued to a polystyrene (PS) post. (b) The structured Si wafer is cut to square pieces, which are then glued at a corner to a SiC stalk.

Omega EP campaign. The setup used during the Omega EP campaign at LLE, in which the targets were shot with a 45° incidence angle, is illustrated in Fig. 5.2 (b). This campaign consisted of four separate shot days over the course of three years (September 2018, January 2019, October 2019 and September 2020). It was part of the *SiBLDev* campaign, which primarily focuses on the development of a Si He_α X-ray backlighter for ICF implosions and is lead by *Christian Stoeckl* (Stoeckl et al., 2021). The Omega EP facility uses standardized diagnostics and setups, therefore the recorded data is well comparable between the different shot days and can be analyzed with the same routines.

The main objective of the shots performed within this project was to evaluate the influence of the laser pulse length on the Si X-ray output. Since the Omega EP laser can deliver up to 1 kJ of laser energy, an intensity of $10^{17}\,\mathrm{W\,cm^{-2}}$ at a pulse length of 20 ps is reached, even with the relatively large focal spot size of (292±13) µm. This large spot size results in the simultaneous irradiation of multiple structures. To get similar intensities for all shots, the energy was reduced for the 10 ps and 1 ps shots. A summary of the shot configurations is given in Table 5.3.

The Si X-rays emitted from the target front side were recorded with two different diagnostics. A time-integrated X-ray spectrometer (XRS) was placed under 15° (September 2018, January 2019 and October 2019) or 55° (September 2020) relative to target normal. The dispersive element was a flat, 120 mm×20 mm large KAP crystal. Because the lowest energy range accessible with the designated crystal positions would not have covered the Si K_α line at 1740 eV, the crystal had to be manually tilted, which resulted in slight differences of the measured energy range on the different shot days. The front of the XRS was equipped with a 200 µm slit, a 50.8 µm thick Be blast shield and a 25.4 µm thick Be filter. As detector, *BAS-TR* image plates were used, which were scanned with an *FLA7000* scanner with 50 µm resolution, a latitude of 5, a sensitivity of 1000 and 16-bit depth approximately 20 min after the shot. The solid angle Ω_{sr} per detector pixel covered by this spectrometer, which is defined as the pixel size divided by the squared distance, was approximately 2.78×10^{-8} sr. For the values used for the filter transmission, the reflectivity of the crystal, the IP fading and IP sensitivity see Section 3.1.2 and 3.1.4.

The second diagnostic was a time-resolved detector based on a streak camera (UFXRS). It has a time resolution of approximately 3 ps. Here, a combination of differential filters was used to separate the Si radiation from other X-ray emission, in particular, the transmitted signal through a CH(Cl) filter was analyzed. More information about these spectrometers can be found in Thorn et al. (2018) and Stoeckl et al. (2021).

During this campaign, five different target types were investigated, which are schematically shown in Fig. 5.3 (k) to (o). As reference, flat, 10 µm thin Si foils were employed (Fig. 5.3 (k)). In addition, targets with microstructures pointing along target normal (Fig. 5.3 (m)) and parallel to the laser incidence direction (Fig. 5.3 (n)) were shot. Furthermore, targets with both flat and microstructured surfaces were equipped with shields (Fig. 5.3 (l) and (o)) made out of plastic (CH). These shields were glued to the Si part with a 45° angle, thereby forming a cavity into which the laser enters during the

Table 5.3.: Shot configurations of the nominal pulse lengths at Omega EP. The 'x' marks the target types that were shot in the respective configuration.

nominal pulse length	τ_p in ps	E_L in J	I in $\mathrm{W\,cm^{-2}}$	target flat	45° (TN)	0° (‖)
1 ps	0.7±0.3	290±1	$6.3\pm2.8\times10^{17}$	x	x	x
10 ps	10.8±0.8	906±11	$1.3\pm0.2\times10^{17}$	x	-	x
20 ps	19.8±0.5	980±26	$7.5\pm1.0\times10^{16}$	x	x	-

irradiation. All targets had a size of $500 \times 500\,\mu m^2$, and they were mounted to SiC stalks as shown in Fig. 5.4 (b). A photo of a mounted target of type Fig. 5.3 (m) is depicted in Fig. 4.14 (b). The target parameters are also given in Table 5.2.

In addition to the main campaigns, a few individual targets were investigated in two beam times with a focus on neutron beam production. Both of these campaigns took place at the PHELIX laser at GSI and were lead by *Marc Zimmer*. For these campaigns, targets made out of deuterated polystyrene (CD) were of interest, because the accelerated deuterons are favorable for the subsequent generation of neutrons. Therefore, all target types either featured a CD back layer (Fig. 5.3 (g), August 2018) or were manufactured entirely out of CD (Fig. 5.3 (i) and (j), May 2020). The respective target parameters are also listed in Table 5.2. During these campaigns, the accelerated ion beams were measured with a Thomson parabola (2018) and RCFs (2018 and 2020). The distance between target and RCF was 123 mm and 51 mm in 2018 and 2020, respectively. The laser pulse length was 0.5 ps, the focal spot size approximately 5 µm and the energy varied between 20 J and 164 J due to problems with the laser system. In case of the CD targets, the limited number of shots combined with the widely varying laser parameters unfortunately resulted in a data set with too large uncertainties. The targets were successfully employed to generate neutrons, but will not be further discussed.

5.1.2. Ion generation

The experimental parameters of the **PHELIX campaigns** are within the TNSA regime. The ions, which are accelerated in target normal direction (see Section 2.3.3), were recorded with RCF stacks and a Thomson parabola. Figure 5.5 shows the RCFs of five different target configurations that were shot with high contrast in the 2019 beam time. The stack is shown up to the last irradiated film, which gives the cut-off energy $\mathcal{E}_{p,max}$ of each spectrum.

The beam shape of all targets is almost round at low energies, but shows increasing asymmetry with higher energies. Except for the flat target with Cu backing, the beam profiles on the first film (7.4 MeV) exhibit a straight upwards component, which could have been caused by the electric fields formed in the vicinity of the target post. The hole in the middle of each film was aligned with the target normal direction and the pinhole of the Thomson parabola. Clearly, the fraction of the beam that passes this hole is often not a good representation of the beam. Either the beam is off-center or exhibits filamentation. In particular, the profile of the 0° ($\parallel$) target shows a star-like structure, which might be an imprint of a valley between three structures. In this configuration, the laser hits the target parallel to the structures axis and can therefore ideally propagate into the valley. The focal spot size of (6.4 ± 1.2) µm matches the average structure spacing of (5.8 ± 1.6) µm. Therefore, a 1:1 imprint of the structure formation in the electron sheath at the target rear side and with this in the ion beam itself is conceivable, especially if the target base is very thin.

The cut-off energies that are acquired from the last irradiated RCF are plotted in Fig. 5.6. They are sorted by contrast and target front, and are normalized to the average laser energy of 170 J using $\mathcal{E}_{p,max} \propto \sqrt{\mathcal{E}_L}$. This follows from eqn. 2.42 and eqn. 2.47 under the assumption that the focal spot size, the laser wavelength and the laser pulse length are constant. Even though the data set is relatively noisy, a trend for the tilt angle at high contrast is visible. The structures that are parallel to the laser incidence direction (0°) provide the highest cut-off energy, and this value decreases with an increasing angle between structures and laser. At middle and low contrast, the tilt does not seem to have an impact, which also applies to varying the rear side material. The small microstructures also show enhanced cut-off energies at high contrast, while performing similar to the larger microstructures at middle contrast.

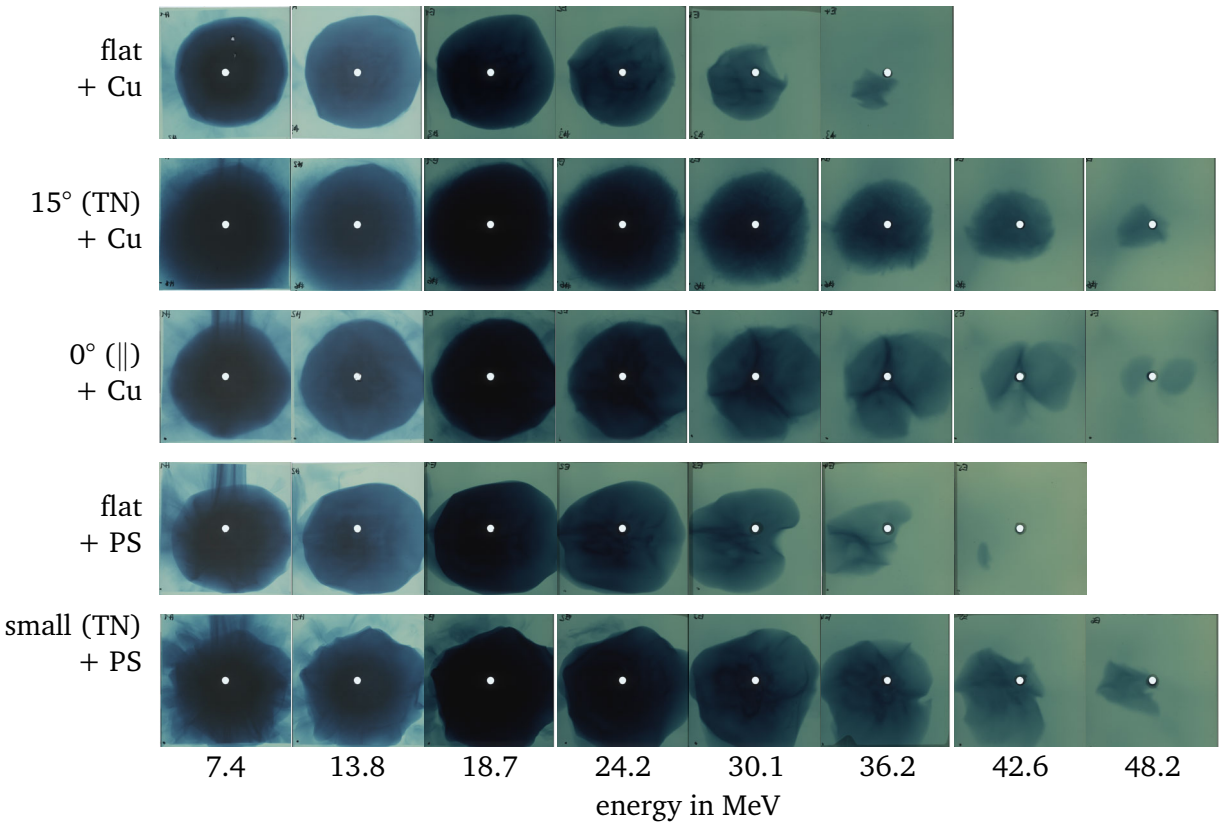

Figure 5.5.: RCF stacks of different target types irradiated during the PHELIX campaign (2019) with high contrast. All films showing a signal are displayed with the respective proton energies noted below each column. The first two films of each stack are *HD-V2* films, while the others are *EBT-3* films. All films are centered and cropped to the same size.

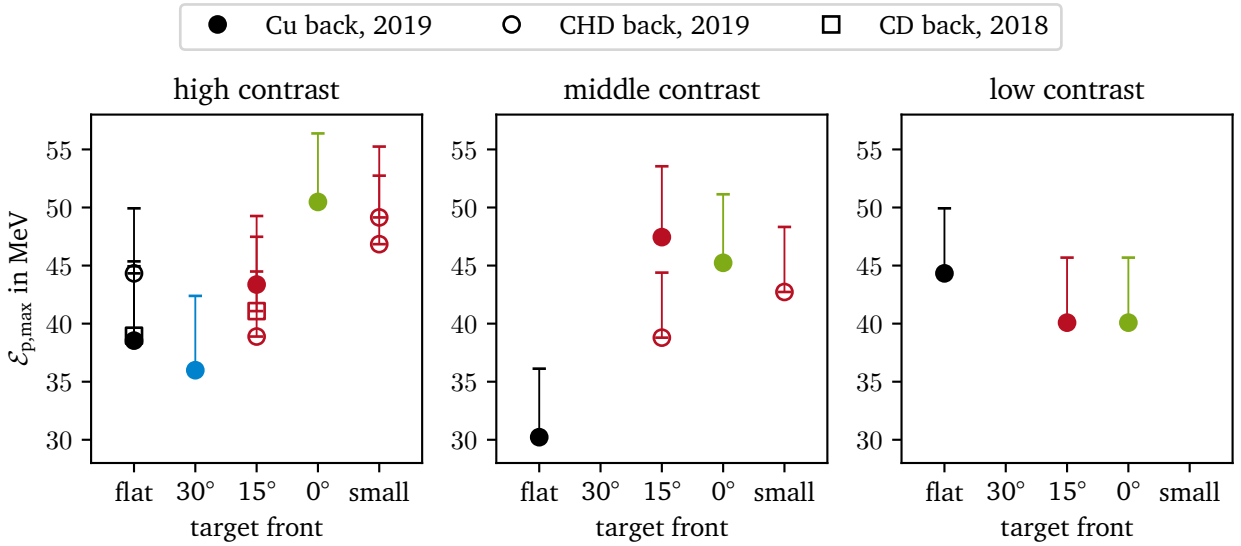

Figure 5.6.: Proton cut-off energies $\mathcal{E}_{p,max}$ normalized to 170 J of targets with different front sides sorted by laser contrast. The flat (black) and microstructured targets (colored by tilt angle) feature either Cu (filled markers) or plastic back sides (empty markers). The plot includes shots from the 2019 PHELIX campaign (circles) and the 2018 PHELIX neutron beam time (squares), which agree well. The values correspond to the energy of the last discolorized RCF, and the error bar shows the energy range covered by the following absorber.

The measured maximum proton energies of 40 MeV to 50 MeV are below the peak value of 93 MeV that was recently achieved at the PHELIX laser facility (Hornung et al., 2020). However, in contrast to the 1.5 µm thin CH foil used for this shot, the Si targets studied here are roughly ten times thicker. As discussed in Section 2.3.3, the electron sheath at the target rear side gets larger with increasing target thickness, which results in lower accelerating field strengths and therefore lower cut-off energies. The observed energy range of the experiments presented here matches proton energies that were recorded at the Trident laser at the Los Alamos National Laboratory, USA, with diamond targets of similar thickness (Jung et al., 2013).

As described in Section 3.1.3, the RCF stacks can be used to determine the proton spectra by fitting an exponential model to the energy doses deposited in the films. Figure 5.7 shows RCF spectra of microstructured targets with different tilt angles in comparison to flat targets, sorted by laser contrast. Unlike the cut-off energies, the spectra can not be easily normalized to the varying laser energy, therefore the respective values are included in the figure.

At high contrast (Fig. 5.7 (top)), the proton spectrum emitted from the flat target yields the lowest particle numbers. This is slightly improved by microstructures with a 30° angle relative to the laser incidence. Tilting the microstructures closer to the laser incidence direction improves both particle numbers and maximum energy. Even though the structures parallel to the laser incidence (0°) were shot with only 155 J, the spectrum is comparable to 15° structures shot with 210 J. This indicates an enhanced laser target coupling for structures pointing along the incoming axis of the laser. In case of middle and low contrast (Fig. 5.7 (middle) and (bottom)), the targets with structured surfaces show similar outputs. The flat target irradiated at low contrast yields the lowest particle numbers.

On a side note, a few points should be kept in mind when interpreting this data. First, the number of discolorized films, and therefore the number of doses to which the model is fitted, is very limited. For the displayed shots, the number varies between six and nine, which corresponds to cut-off energies of 36.2 MeV and 54.1 MeV, respectively. The fewer films are ex-

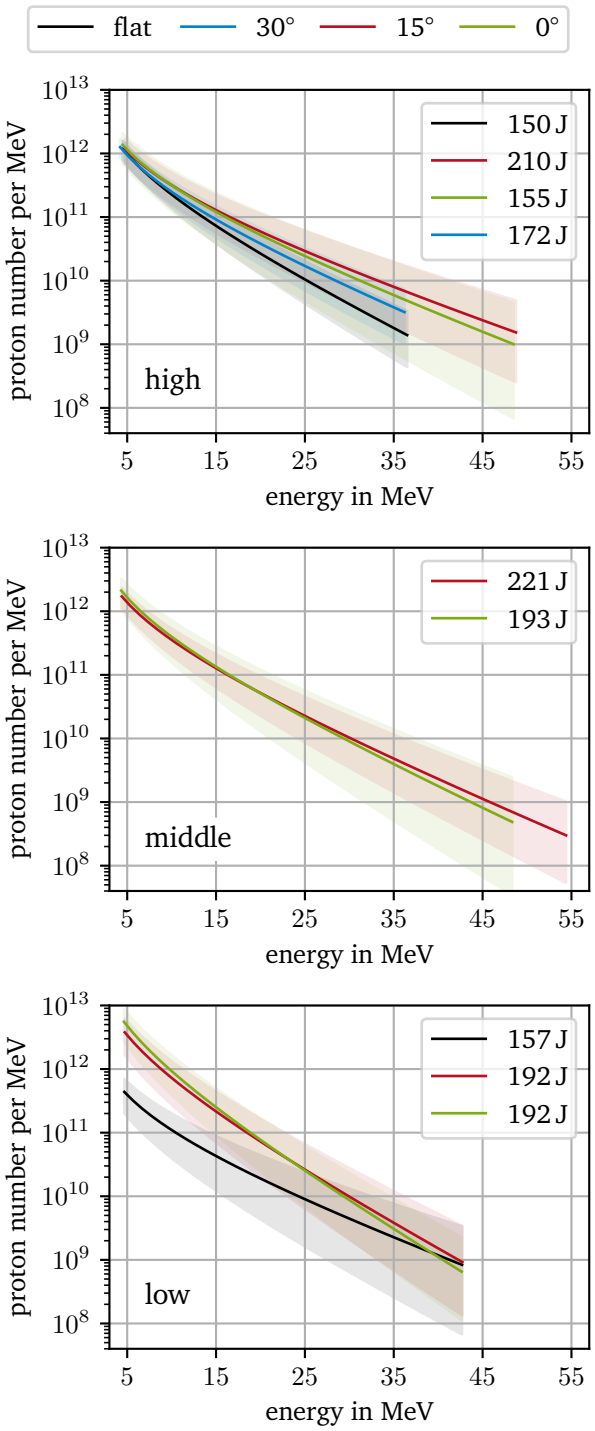

Figure 5.7.: RCF spectra of 0°, 15° and 30° microstructured as well as flat targets with Cu backing sorted by high (top, solid), middle (middle, dashed) and low (bottom, dotted) laser contrast. The transparent bands show the uncertainty of the fit. As the laser energy significantly varied between the shots, the respective energies are annotated.

posed, the more unstable the fit can become. Second, especially the front films tended to be a little bit too small, thereby cutting the beam edges off, which can be seen in Fig. 5.5. As a result, the measured doses are too low, which can lead to a distortion of the fit and an underestimation of the particle numbers. Third, an underestimation can also be caused by saturated films, especially in the front layers, since all information above the saturation threshold is lost. Fourth, although TNSA spectra often include a second or even third temperature, which is caused by the underlying multi-temperature electron distributions (see Section 2.2.4), the model employed in the fit routine described in Section 3.1.3 includes only one temperature.

The Thomson parabola data shows that in addition to protons, deuterons were accelerated in case of the CHD-backed targets. Figure 5.8 shows the stitched traces of 15° (TN) targets with (a) a Cu and (b) a CHD rear side (compare Fig. 5.3 (c) and (g)). The Cu filter combination blocks all ion species except for protons and deuterons from reaching the IP, which is confirmed in the traces of the Cu target. Here, a signal on the 1:2 charge to mass ratio trace is only visible in the areas without filter as no deuterons are present. The measured signal is probably generated by C^{6+} ions that stem from the natural contamination layer. In case of the CHD target, the signal on the 1:2 trace must therefore be caused by deuterons.

Accelerated deuterons indicate that the natural contamination layer at the target rear side, which consists of hydrocarbons, is at least partially depleted and ions from the target bulk are accelerated. This is an important result in that the conversion efficiency from laser energy to protons is likely limited in case of bare Si or Cu backed targets. Here, the only proton source is the contamination layer, so once this layer is depleted, no more energy can be transferred to protons. Previous experiments at the VULCAN laser at RAL, UK, suggested such a limitation (Ebert et al., 2020). Thus, it is favorable to add a proton rich layer such as CH or CHD when high proton numbers are of interest.

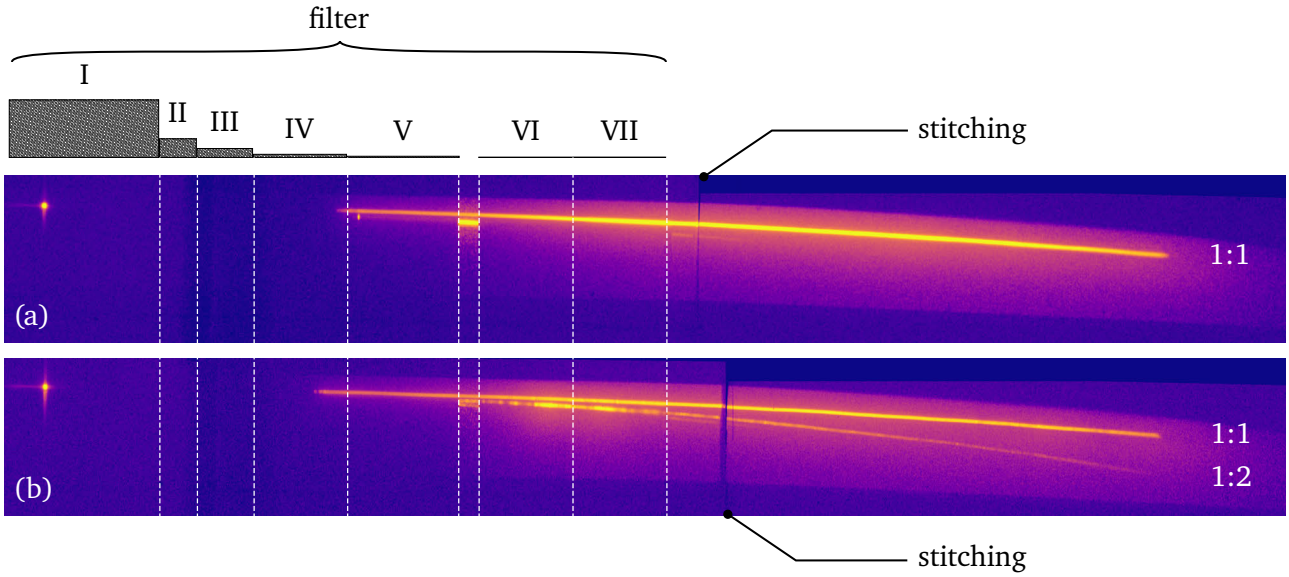

Figure 5.8.: IPs with Thomson parabola traces acquired during the PHELIX campaign with a microstructured target with (a) Cu and (b) CHD backing in false colors. A filter combination of seven Cu foils with 3000 µm (I), 1000 µm (II), 500 µm (III), 200 µm (IV), 100 µm (V), 50 µm (VI) and 30 µm (VII) thickness was used to stop all ion species except protons (1:1 charge to mass ratio) and deuterons (1:2 ratio). As expected, a continuous trace of the latter is only visible in (b). In the gap between the filter pieces V and VI as well as in the region without filters, a signal on the 1:2 trace is observed in both cases. This is is probably produced by C^{6+}, which is present in the contamination layer on the target rear side. The images of the two IP pieces were stitched as indicated.

Since the particles entering the Thomson parabola were an inadequate representation of the accelerated ion beam, as can be seen on the RCFs in Fig. 5.5, the spectra were not analyzed quantitatively. Because of this, the influence of the additional CHD layer on the actual number of accelerated protons could not be evaluated. Without knowledge of the ratio of protons to deuterons in the ion beam, the discolorization of the RCFs can also not be converted to particle numbers in the case of CHD rear sides.

In short, the recorded beam profiles show imprints of the valleys between the microstructures, which is most pronounced for the structures that are parallel to the laser incidence direction. Tilting the structures towards the laser enhances both the maximum energy and the number of accelerated protons, if the ASE contrast of the laser is high (10^{13}). With decreasing contrast, the impact of the structures is reduced. Furthermore, the acceleration of deuterons from the target bulk proves that the natural contamination layer at the target rear side is at least partially depleted. This indicates that without adding an artificial proton source the number of accelerated protons might be at its limit.

5.1.3. X-ray generation

The X-ray spectra measured during the **PHELIX campaign** using the flat foils, the normal (TN, 23 µm) and small (TN, 4 µm) microstructures pointing along target normal, and the structures parallel to the laser incidence (||) are shown in Fig. 5.9, sorted by the respective laser contrast.

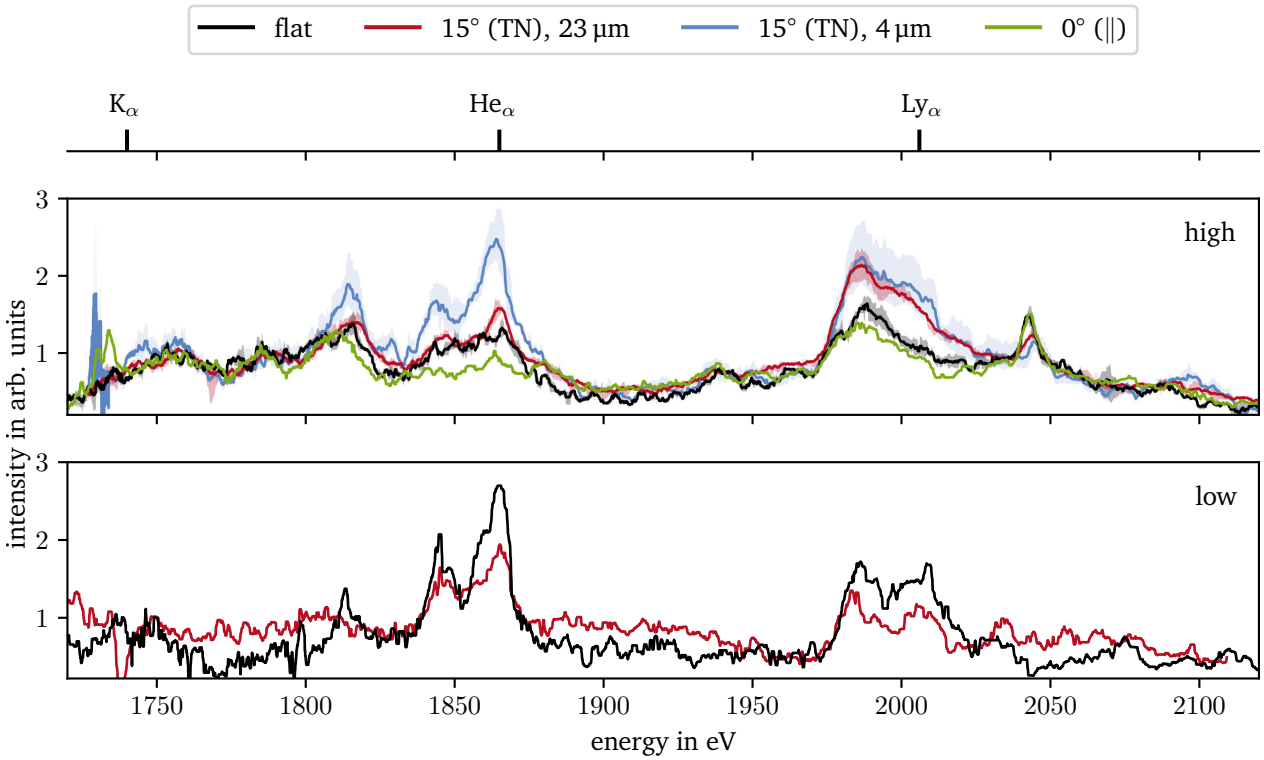

Figure 5.9.: X-ray spectra of flat and microstructured targets shot with the PHELIX laser system with an ASE contrast of roughly 10^{13} (top, solid) and 10^{8} (bottom, dotted). The structures parallel to target normal (15° (TN)) were evaluated for two different heights (for target parameters see Table 5.2). For comparison, the spectra are normalized. Multiple shots of the same laser target configuration were averaged and the minimum and maximum value of each bin is shown by the semi-transparent bands. The energies of the most relevant characteristic lines are annotated above.

The error bands (semi-transparent) show that the shape of the spectra agrees well for the respective configurations. However, as the shot to shot variance of the signal intensity is very large, the spectra were normalized at 1755 eV and a conversion to photon numbers was skipped. The variations might have been caused by a combination of the large viewing angle of 76° of the spectrometer, the substantial shot to shot differences of laser energy of 170±50 J and slight rotations of the target during alignment.

In the spectra attained with low contrast (Fig. 5.9 (bottom)), the characteristic He_α and Ly_α as well as their respective satellite lines are well distinguishable from the background, especially in case of the flat target. However, due to the high noise level, the necessity of normalization and only one shot per configuration each, no clear conclusion can be drawn about the impact of the microstructured target onto the generated X-ray spectra. When comparing the high and low contrast shots, the high contrast shots (Fig. 5.9 (top)) feature more and broader peaks. As discussed by Skobelev et al. (2012), this is likely caused by the strongly changed plasma conditions. A higher contrast reduces the amount of generated pre-plasma before the main pulse arrives. In turn, the gradients of electron density and temperature increase, and hollow ions are generated (see Section 2.3.2). This adds additional transitions that overlap and lead to broader peaks as well as an almost continuous substructure. With a well-calibrated, high resolution X-ray spectrometer with a high signal to noise ratio, the spectral changes could be used to gain valuable insights about the complex atomic shell structure. Furthermore, Martynenko et al. (2021) propose to use this spectral change to diagnose the laser pulse itself. Unfortunately, neither of the two approaches is viable with the current data set.

Another observation is the likeliness of the flat and parallel (0° (∥)) target performance at high contrast. Although it is expected that the laser target coupling is highest with these structures, as will be discussed in Section 5.2.3, some spaces between the structures are very confined due to the high aspect ratios of 5:1. The gaps are further narrowed by the tilt of the structures and the coarse substructures, as illustrated in Fig. 5.10. The plasma confined in these structures might have had similar properties as the one generated on the flat targets, therefore generating a comparable X-ray output for the fully ionized Ly_α state. However, the two target types differ in the generated K_α emission in particular, which is much more intense for the structured target. This indicates that in the case of the 0° target, the interaction of the hot electrons with a cold part of the target takes place over a longer period of time or in a larger volume.

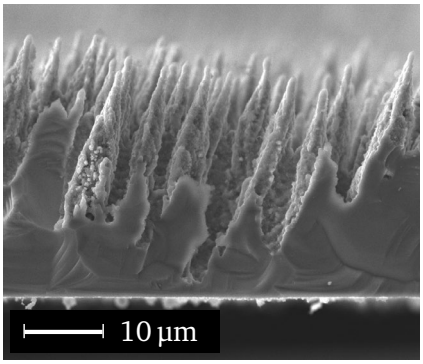

Figure 5.10.: SEM image of a 0° (∥) target of the PHELIX campaign (Fig. 5.3 (d)), viewed from the side.

The small, 4 µm high microstructures with a 15° angle relative to the laser axis show the best signal to noise ratio at high contrast. The generated Ly_α emission matches the signal generated by the larger structures with a height of 23 µm and the same orientation, however, the He_α is most intense for the small structures. It is likely that the geometry of the smaller structures better suited the laser parameters to produce the optimal energy distribution of hot electrons for X-ray generation, showing the potential of tailoring the microstructure shape and size to the respective laser configuration.

Other studies indicate that lower intensities in the order of $10^{17}\,\mathrm{W\,cm^{-2}}$ might be better suited for X-ray generation (Neumayer et al., 2010). Therefore, it would be useful to repeat these experiments with varying contrast at a lower intensity. With a better viewing angle of the XRS and increased shielding, the signal to noise ratio might be improved so that the almost continuous substructure of the spectrum could be directly attributed to the increased number of transitions without being confused with noise.

Figure 5.11 shows the X-ray emission spectra of the **Omega EP campaign** sorted by the laser pulse length. Due to the limited number of shots available at this low repetition rate system, it was not possible to shoot all target types in all pulse configurations, but for each configuration there is at least one flat (black) and one structured (red or orange) shot. The manual alignment of the crystal of the XRS unfortunately lead to a clipping of the spectrum below 1850 eV for the 20 ps shots taken with a 15° viewing angle.

The dispersion relation, that converts the position of the X-ray signal on the IP to an energy, was determined with a quadratic fit to the clearly assignable He_α, Ly_α and He_β lines. The peak with the lowest energy, that is observed somewhere between 1700 eV and 1800 eV, was not used during that

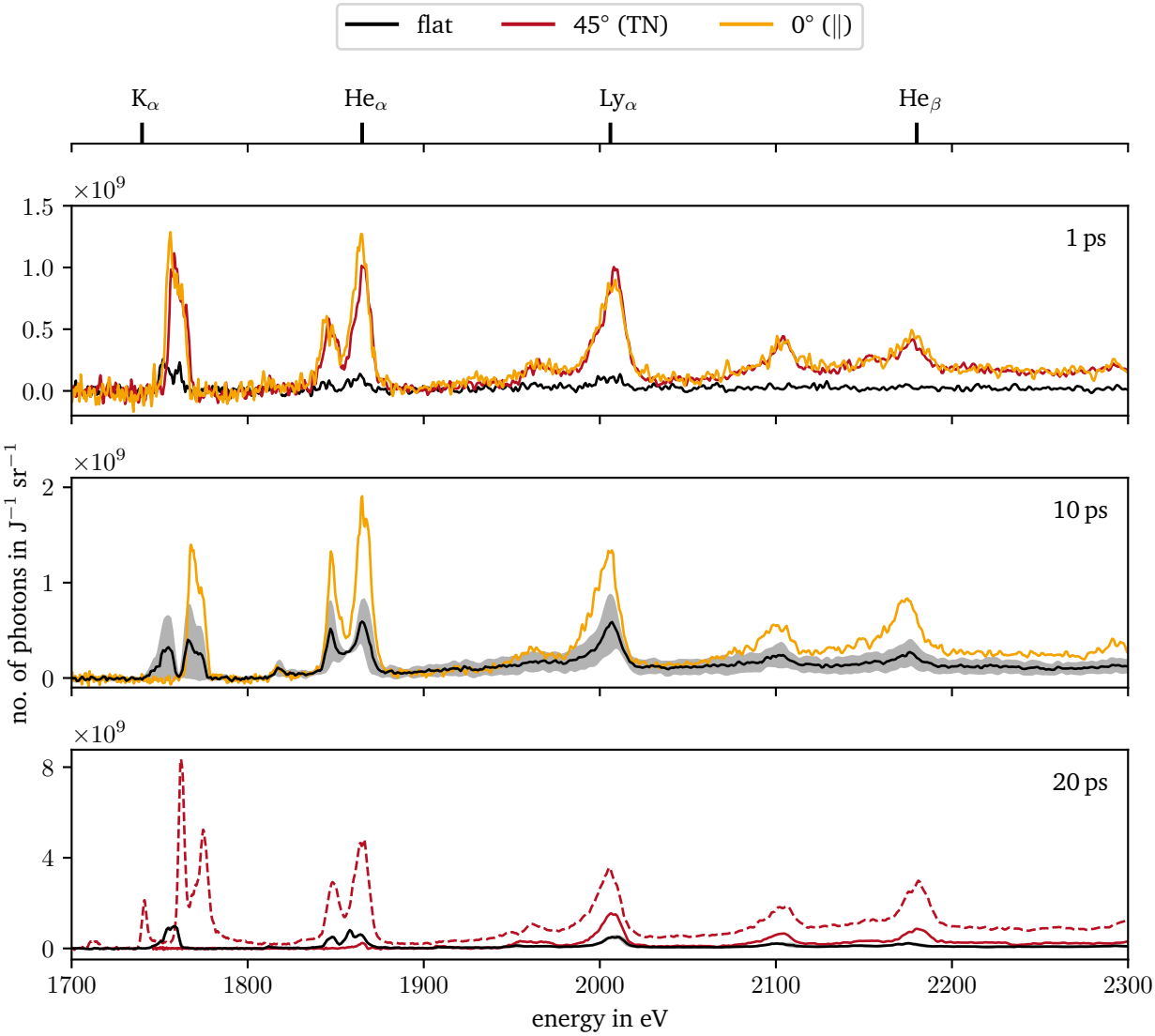

Figure 5.11.: X-ray spectra of flat (black), 45° (TN) (red) and 0° (||) (orange) microstructured Si targets observed during the Omega EP campaign. The spectra are sorted by the laser pulse length, which was 1 ps, 10 ps and 20 ps from top to bottom. Above the plots the theoretical values for the characteristic emission lines of Si are indicated. As there were two shots with a flat target at 10 ps, the spectra are averaged and the gray band shows the minimum and maximum value of each energy bin. The XRS was observing the emission under 15° (solid) or 55° (dashed) relative to target normal.

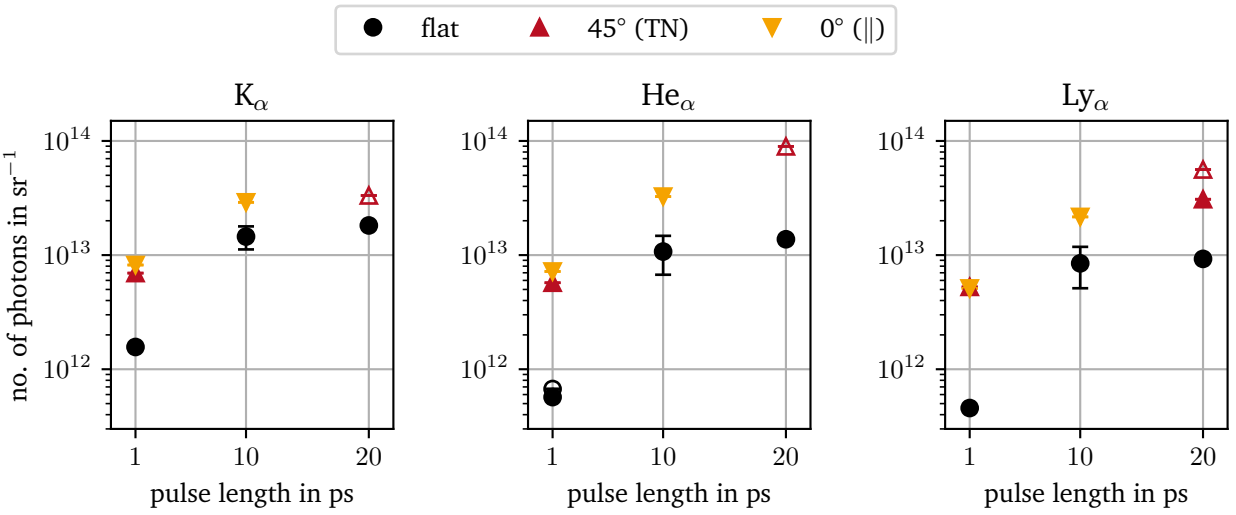

Figure 5.12.: Characteristic line emission observed during the Omega EP campaign in logarithmic display as a function of pulse length. The K_α (left), He_α (middle) and Ly_α (right) emission increase for longer pulse lengths for all target types. For all lines and pulse lengths the structured targets (red and orange) show a greater emission than the flat targets (black). Values with filled markers were measured under 15° while values with blank markers were observed under 55°. When available, shots of the same type were averaged and their standard deviation displayed as errorbars. The integral width was 0.7 % bandwidth for the K_α emission and 0.5 % bandwidth for the He_α and Ly_α lines.

fit, because it could not be clearly identified. It could be Si K_α radiation from the colder bulk material, but since this line shifts depending on the temperature and density of the plasma it cannot be used as reference. Other causes could be an artifact of the edge of the crystal or some kind of contamination in or around the target, which could not be verified yet. In the following analysis, the peak is treated as K_α radiation. The peak around 2100 eV is most likely a Li-like satellite to the He_β line, which has a literature value of 2132 eV (Dere et al., 1997; Landi et al., 2011).

The spectra show that the microstructured targets enhance the X-ray generation for all pulse lengths. To further illustrate this, Fig. 5.12 shows the line intensities of the K_α, He_α and Ly_α lines. They are calculated by integrating the signal around the central peak energy in a 0.7 %, 0.5 % and 0.5 % bandwidth interval for the K_α, He_α and Ly_α line, respectively. As expected, the overall yield increases with increasing pulse length, even though the energy of the 10 ps and 20 ps shots was almost the same with (906±11) J and (980±26) J, respectively. According to eqn. 2.45, the electron temperature roughly scales with $\sqrt{I_L}$, which gives an estimate of 26 keV for the 10 ps pulses and 15 keV for the 20 ps pulses. The cross section for electron impact K-shell ionization of the Si, He and H states does not significantly change between the two temperature values (Llovet et al., 2014, p. 47-48), but the increased pulse length increases the overall interaction time, leading to an increased signal. In this representation, the enhancement by the structures is clearly visible for all lines at all pulse lengths. The 0° (‖) structures seem to perform slightly better than the 45° (TN) structures, but the data set is too small to be certain.

The highest X-ray yield is reached with a 0° microstructured target at 20 ps. However, this is the only evaluable shot of this series with the XRS pointing at the target under 55° relative to target normal, so it is possible that the signal is increased due to an extended line of sight of the spectrometer. This only applies, though, if the plasma is optically thin, which means that the radiation can escape the plasma without being absorbed. The angular dependence of X-ray emission has been discussed by others (Arora et al., 2014; Hu et al., 2008), but strongly depends on the exact experimental parameters and can

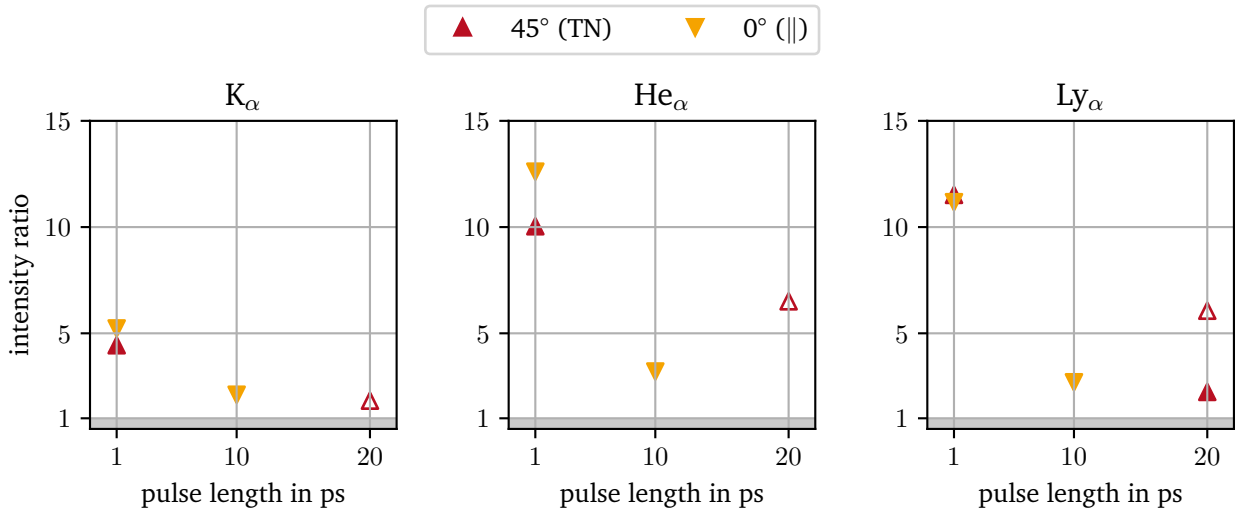

Figure 5.13.: Line intensity ratios of structured to flat targets. All values are greater than one, therefore showing an overall enhancement by the structured surfaces. For all three lines (K_α (left), He_α (middle) and Ly_α (right)) the influence is greatest for the shortest pulse length of 1 ps. Filled markers denote values measured under 15°, while blank markers represent an XRS viewing angle of 55°.

therefore only give an indication of possible influences. A second reason for an increased signal, not counting the laser-matter interaction itself, is based on the spectrometer configuration. This shot is the only one acquired during the 4th shot day in 2020 and differences in, e.g., the reflectivity of the crystal could also cause an increased signal, which is not comparable on a one-to-one basis. Nonetheless, although the other recorded 20 ps spectra are clipped right below the He_α, their Ly_α can be evaluated and this yield is also greater than all other values.

To quantitatively assess the improvement by using microstructured front surfaces, Fig. 5.13 shows the line emission ratios of structured to flat targets. All values are greater than one. The greatest enhancement for all lines is achieved at the shortest pulse length of 1 ps, with a 13× increase of the He_α and a 12× increase of the Ly_α emission. This agrees well with the structures dissolving over time, so that their relative impact is higher on shorter time scales. A rough approximation using eqn. 2.45 for the electron temperature and eqn. 2.11 for the plasma scale length gives a closing time of the gaps between the structures of 3 ps as lower limit in case of full ionization. At least up until then, the microstructures change the interaction between laser and target. The increased surface area allows more electrons to be heated and the structures trap the laser light and plasma, thereby further enhancing the energy deposition. All of these factors are favorable for X-ray generation, but once the gaps are closed and the critical density boundary lies before the structured volume, the target probably behaves similar to a flat target. As a result, the relative fraction of enhanced X-ray generation by the structures becomes smaller for longer pulses and therefore their overall impact is reduced.

Also studied during this campaign were targets with attached shields (Fig. 5.3 (l) and (o)). As shown in Fig. 5.14 (left), there is almost no difference in the spectra of flat and structured front surfaces in this target configuration. In both cases, the yield is much higher than with bare microstructured targets. However, the UFXRS data, which is shown in Fig. 5.14 (right), reveals that a large portion of this signal is caused during an afterglow, which is clearly distinguishable from the main X-ray pulse centered at 0 ps. In case of the flat targets with shield, the emission drops after the main pulse around 20 ps before having a second maximum around 75 ps, which then decays over more than 250 ps. The structured targets do not exhibit such a minimum, but emit an almost constant amount of radiation over more than 250 ps after dropping to approximately 40% of the peak value.

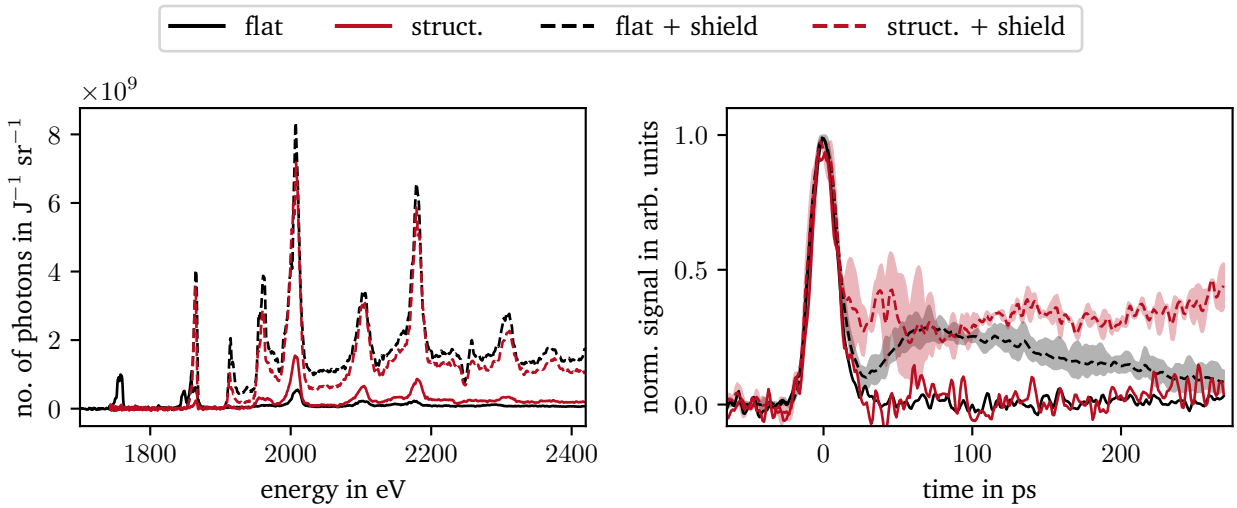

Figure 5.14.: Comparison of X-ray emission from structured (solid) and shielded targets (dashed) with flat (black) and structured (red) front surfaces irradiated with a laser pulse length of 20 ps. The spectra (left) show the increased emission of shielded targets. The normalized, spectral profiles measured with the UFXRS (right) agree for the rising edge of the X-ray pulse, but clearly differ after the main pulse. Both shielded target types exhibit an afterglow, in contrast to the other types. In case of the shielded targets two shots each were available for evaluation, which were averaged. The transparent band shows the minimum and maximum of each bin.

For a possible explanation of this afterglow, Fig. 5.15 shows a schematic of a flat shield target. The laser hits the Si part of the target under 45°, is reflected towards the CH shield, and is subsequently reflected back onto the Si target. In the process, it generates two plasmas, which expand from the target surfaces. Under the assumption that the focal spot with a size of approximately 300 µm (FWHM) hits the 500 µm large Si part in the center, the minimum distance between the two target parts is 70 µm. Using the same equations as above (eqn. 2.45 and eqn. 2.11), the expansion range of the plasmas after 30 ps, which is when the signal of the flat shield target starts to rise again, is roughly 30 µm for fully ionized Si and 40 µm for protons originating from the CH shield. The sum of both ranges matches the minimum distance of 70 µm that needs to be covered before the plasmas collide. Once they join, collisional heating of the two colliding plasmas leads to rising X-ray emission, which is recorded as afterglow. In case of the structured shield targets, the absence of a minimum might be due to a messier joint between shield and target, which would possibly shorten the distance the plasmas need to cover before colliding.

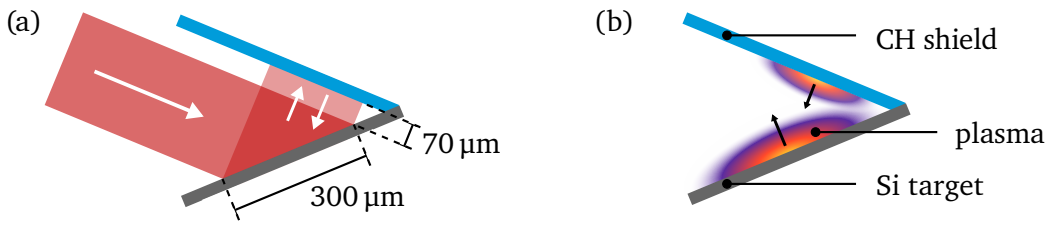

Figure 5.15.: Schematic of the laser interaction with a shield target with approximated dimensions. (a) The laser hits the Si target (gray) under a 45° incidence angle with a 300 µm large focal spot. It is reflected towards the CH shield (blue), which reflects it back to the Si target. (b) The interaction of the laser with the two parts of the target leads to the generation of two plasmas (color gradients), which expand away from the surfaces. For a discussion of the resulting X-ray signal see text.

In contrast, the targets without shield exhibit a well defined pulse profile with a FWHM of (19.7±0.4) ps, which matches the laser pulse length of (19.8±0.5) ps. Especially for secondary applications that use integrated detectors or cameras with longer exposure times, this is a great advantage. The front surface structures enhance the signal without prolonging the temporal profile of the X-ray pulse.

In brief, even though the large variances in the X-ray data measured during the PHELIX campaign only allowed for a qualitative analysis, the comparison of the low and high contrast shots at an intensity of $10^{20}\,\mathrm{W\,cm^{-2}}$ showed that for the latter the number of transitions is increased, which is likely caused by hollow ions. The Omega EP data, that was generated at lower intensities around $10^{17}\,\mathrm{W\,cm^{-2}}$, revealed that the X-ray yield increases with increasing pulse length. In addition, it showed that the microstructures enhance the K_α, He_α and Ly_α line emission for all studied pulse lengths, but have the highest impact at 1 ps. An even higher X-ray yield was achieved with shield targets, however, a large fraction of this signal is generated during an afterglow. This is not the case for the microstructured targets, which makes them favorable for applications that require short X-ray pulse lengths.

5.2. Simulations

After discussing the experimental findings, three series of PIC simulations are presented, which are used to theoretically investigate the interaction of a high intensity laser with microstructured targets. Starting with a description of the overall simulation setup, the influence of the spike characteristics on the evolution of the electric fields and the electron temperature is discussed. This gives insights into effects causing the enhanced absorption efficiency. Then, the tilted microstructured targets investigated during the PHELIX campaign are modeled and the simulation outputs are related to the experimental results. Last, a simulation series for optimizing the microstructure geometry is presented, and the optimal spikes are compared to the often employed pillar structures.

The simulation setup, the implementation of the analysis scripts and the target optimization study was greatly supported by *Sarah Grimm* in the scope of her bachelor's thesis (Grimm, 2020) and during her work as research assistant.

5.2.1. Simulation setup

In the following, the fundamental setup parameters that apply to all simulation configurations are summarized. This includes an overview of the employed software and hardware, the mutual simulation window and grid properties as well as a short discussion on the target initialization. A detailed description of the respective input parameters is given in, e.g., the EPOCH User Manual (Bennett et al., 2019). An exemplary input file, in which all these parameters are set, can be found in Appendix A.4.

Software and hardware. The simulations were performed using the PIC code EPOCH (Arber et al., 2015) with the latest available version at the time, which are either versions 4.17.9 or 4.17.15. EPOCH is an open-source, CPU based, MPI (message passing interface) parallelized code for high energy density physics, which is based on the older PSC code written by Hartmut Ruhl. EPOCH is currently hosted on a GitHub repository (Arber et al., 2021) and maintained by the University of Warwick. For a description of PIC codes in general and the underlying equations of EPOCH see Section 3.2.1.

Due to the high computational costs of several thousand CPU hours per simulation, the simulations were run on the High-Performance Computing (HPC) infrastructure at GSI, Darmstadt. Until December 2020, the Kronos cluster, which provided 532 nodes with 13.5k CPU cores with a GNU/Linux Debian 8

operating system, was employed. In the following, the new Virgo cluster was utilized. Its "long" partition features 349 nodes with 66.3k CPU cores and runs on the operating system CentOS 7.

The simulation data was analyzed with the visualization software VisIt (version 3.1.0) (Childs et al., 2012) and a series of python scripts. EPOCH writes the field and particle properties at a requested frequency to files in a self describing format (SDF). These files, which can be as large as hundreds of gigabytes, are then either visualized with VisIt, which can directly handle such SDF files, or read via python utilizing the library *sdf helper* provided by the developers to handle the large files. For further analysis, such as binning into energy spectra, the data is subsequently compressed by choosing every 10th particle at random. Then, it is saved in separate files for each grid or particle property. Depending on the desired output, these files are then further analyzed and plotted with python scripts.

Simulation window and boundaries. All simulations are two-dimensional, but the size of the simulation window varies depending on the particular aspect of laser matter interaction studied. In general, the window needs to be large enough to contain the target as well as empty space in front of and behind the target to allow for laser propagation, plasma expansion and particle acceleration. Also, the FWHM diameter of the laser focal spot needs to fit in the window. At the same time, an oversized window results in unnecessary computational costs, therefore its size must be chosen carefully. The width w and height h of the simulation window is determined by the outmost grid positions $x_{\min}$, $x_{\max}$, $y_{\min}$ and $y_{\max}$ as illustrated in Fig. 5.16. Table 5.4 summarizes the window sizes of all investigated configurations.

EPOCH offers different options for the boundaries of the simulation window, that can be defined individually for each side. The boundary type determines the form of transmission, reflection or replacement of particles as well as the handling of in- and outflowing electromagnetic fields. For the simulations of this thesis, open boundaries of the type *simple_outflow*, which absorb fields and particles reaching the edge, were chosen for the $x_{\max}$, $y_{\min}$ and $y_{\max}$ sides. For the $x_{\min}$ edge, a *simple_laser* boundary was selected, which has the same absorbing properties for particles but allows the attachment

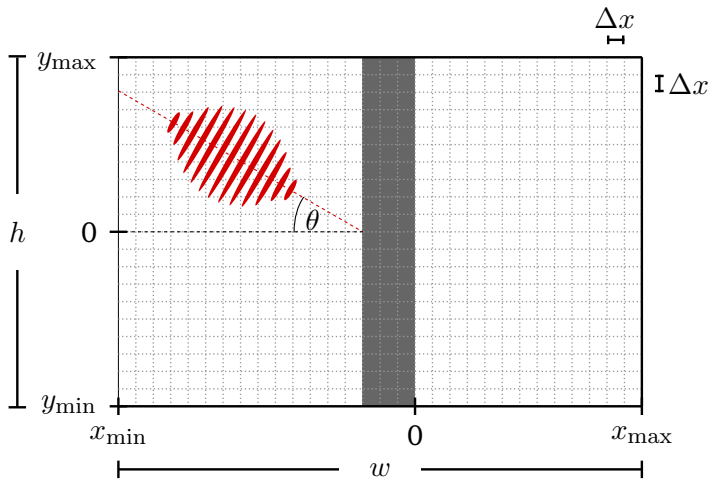

Figure 5.16.: Schematic of the 2D simulation window with the outer limits $x_{\min}$, $x_{\max}$, $y_{\min}$ and $y_{\max}$, which determine its width w and height h. The target is placed in the middle to leave space for any pre-plasma expansion on the front (left section) and particle acceleration on the rear (right section). The laser (red) enters the window from the left and hits the target under an incidence angle θ. The width and height Δx of the square cells are not shown to scale. The top, bottom and right boundaries (bold) are absorbing both fields and particles, while the left boundary (thin) is of a radiating type and can therefore have an electromagnetic field source attached.

Table 5.4.: Overview of simulation setup parameters. All simulations were run on a 2D grid with width w and height h with outflowing boundaries on all sides. The cell size and number of particles per cell are denoted by Δx and N_{ppc}, respectively. The pulse duration τ_{L} of the laser is defined as FWHM, which also applies to the focal spot size d_{fs}, which was set to 10 µm for all simulations. The intensity I and the incidence angle θ, which is illustrated in Fig. 5.16, were varied. All ions were modeled as fully ionized with an initial temperature T_{i}. Also, the electron temperature T_{e} and density n_{e} are listed. Configurations A, B, and C are discussed in Sections 5.2.2, 5.2.3 and 5.2.4, respectively.

	grid				laser			particles			
config.	$w \times h$ in µm^2	Δx in nm	Δx in λ_{D}	N_{ppc}	τ_{L} in fs	I in W cm^{-2}	θ	ion species	T_{i} in eV	T_{e} in eV	n_{e} in n_{c}
A	40×20	4.0	5.4	20	100	2×10^{20}	0°	H	10	100	10
B	90×80	8.4	3.0	20	500	1×10^{20}	15°	Si, Cu, H	100	7000	50
C	80×80	31.0	5.0	30	50	1×10^{20}	0°	Si, H	100	7000	10

of an electromagnetic source, namely the laser. Choosing such absorbing boundaries means that, over time, particles are "lost" to the simulation, but their positions and energies when leaving the window are saved to output files so that they can be included in the later on analysis. Other boundary types that would preserve the particle number, such as periodical boundaries or a surrounding thermal heat bath, where tested, but they either created non-physical effects or are not suited for the rapidly changing temperatures of the heated target. In general, choosing a larger simulation window reduces boundary effects in the region of interest, however, this can also significantly increase the computational cost.

Grid resolution and number of particles per cell. A very important parameter that can greatly influence the simulation results is the grid resolution Δx, which here denotes both width and height of the square cells as shown in Fig. 5.16. In laser plasma interaction scenarios, the smallest length of interest is usually the Debye length λ_{D}, which plays a crucial role in the relevant physics (see Section 2.1.2). Failure to resolve this length can not only affect the modeled physics, but can also introduce an effect that is referred to as self-heating. As discussed in Section 3.2.1, eqn. 3.25, it can be minimized by decreasing the cell size, increasing the number of particles per cell or choosing a higher order particle shape function.

Usually, convergence tests are performed to find the best values for resolution and particle number at reasonable computational cost, i.e., computing time and power. However, the simulation window size necessary to model the laser and target parameters of interest severely constrain the feasible parameter range. Table 5.5 lists the computational costs for the three implemented simulation configurations together with the total number of cells and particles. With an average of 74,500 CPU hours, configuration B, which is discussed in detail in Section 5.2.3, is the most expensive simulation setup. Still, its resolution is only as low as three times the Debye length, but convergence studies with even finer grids were not practicable. Another drawback of highly resolved grids with large particle numbers is the size of the output files, which are also listed in Table 5.5. Even though the employed python library was developed to handle such large files, the time and memory required to analyze the data comes to a limit. As a consequence, sensible values for grid resolution and particle number were chosen as to keep the required resources within reasonable amounts. They are listed in Table 5.4 for all simulation setups.

Target and laser initialization. The target is initialized by distributing a specified number of macroparticles in the desired regions, and adjusting their weight so that the specified number density is achieved. As macroparticle shape, a first order b-spline, i.e., a triangle distribution function is chosen. The rest of the window is left empty, modeling perfect vacuum. To minimize numerical problems, the sharp

Table 5.5.: Overview of the total number of cells and particles, the computational expense, namely run time and average file size of each full output dump, the HPC machine and the EPOCH version for the different simulation configurations. All simulations were run on 1024 CPU cores. The results of configurations A, B, and C are presented in Sections 5.2.2, 5.2.3 and 5.2.4, respectively.

config.	no. of cells	no. of particles	run time in CPU hours	file size in GB	machine	version
A	5.0×10^7	1.0×10^9	9200	65	virgo	4.17.15
B	1.0×10^8	2.0×10^9	74,500	190	virgo	4.17.15
C	6.6×10^7	2.0×10^8	12,500	18	kronos	4.17.9

boundaries of the target are smoothed with an exponentially decaying density profile with a scale length of 0.8 µm in all simulations.

Choosing valid initialization temperatures and densities is rather tricky. Typically, PIC simulations are covering timescales of a few picoseconds at most, therefore modeling the initial heating and plasma expansion induced by the laser pre-pulse is not practical. As a result, the target state at the time of the arrival of the main pulse needs to be estimated, either by hydrodynamic simulations or educated guesses. In the presented simulations, the particles are initialized using a Maxwell-Boltzmann distribution with temperatures in the electronvolt to kiloelectronvolt range to model preheating in a very simplified manner. Because lasers primarily couple to the electrons, the initial ion temperatures are set to lower values than the electron temperatures. The initial density in all setups is higher than the critical density, but lower than the solid density of the target material. The reason for that is the previously discussed desire to resolve the Debye length, which decreases with increasing density. As long as the target is overdense, reducing the density does not significantly change the overall physics, but influences the absolute particle energies resulting from these simulations. Also, any temperature or density gradients in the target bulk at the time of initialization are neglected, which can further increase the deviation from the actual experimental results.

Another aspect is the ionization state of the target. All particles are loaded as fully ionized, which is likely true for the ions at the target front, but with increasing Z the probability of the target bulk being in that state decreases. Modeling ionization is, in principle, possible, but significantly increases the computation time and is therefore deactivated.

The surface of any real target handled under normal laboratory conditions, meaning atmospheric pressure at room temperature, is covered with a natural contamination layer which mainly consists of hydrocarbons. In case of target materials that do not contain any hydrogen, accelerated protons stem from this layer only. Therefore, a thin layer of pure hydrogen is added to the back of the simulated targets to model this proton source. According to G. Hoffmeister (2014), the areal density of the contaminants on a metal surface is $(4.27\pm1.28)\times10^{16}\,\mathrm{cm}^{-2}$, with a fraction of $(40\pm10)\,\%$ being hydrogen. This leads to a layer thickness of roughly a few nanometers. To resolve the layer to at least some degree, the proton layer was initialized as exponentially decaying density profile with a scale length of five cells. This results in an approximately tenfold increase in the available proton number compared to experimental conditions.

The laser is modeled with a Gaussian profile in both space and time without including focusing effects. Such an ideal pulse shape is rarely achieved experimentally, which can cause deviations between the modeled and experimental results. In all simulation setups, the laser enters the simulation window from the left (see Fig. 5.16) at the start of the simulation. For some configurations, the incidence angle θ is varied by changing its phase. The laser always hits the target in the center at y=0.

Even though the discretization of the grid, the limited resolution, the uncertainty regarding the target conditions at the time of initialization and the short simulation times require a series of simplifications and educated guesses, PIC simulations have proven to be a valid tool to study laser matter interaction. Their results should not be considered as absolute, but are rather useful to study specific aspects of the highly complex scenarios of interest. Thus, the simulation results presented in the following sections are only compared within their own simulation series.

5.2.2. Influence of spike characteristics on electron heating

To investigate the impact of the general microstructure shape on electron heating, simulations with a simplified geometry were carried out. Especially in experimental setups where the focal spot size is in the order of a few micrometers, this simplification is a suitable description of the interaction. Nevertheless, the general insights can also be applied to configurations with larger focii. The three basic geometries, which are depicted in Fig. 5.17 in gray, are a flat target as reference (top row), a tilted surface (middle row) and a trough (bottom row), which resembles the region between two microstructures and has the same angle of inclination as the tilt target. As only the interaction on the target front side is of interest, all targets are infinitely thick.

The simulation window has a size of $40 \times 20\,\mu m^2$ with a resolution of 4 nm in both x and y direction, which corresponds to $5.4\,\lambda_D$. The target is made out of pure, fully ionized hydrogen with an electron

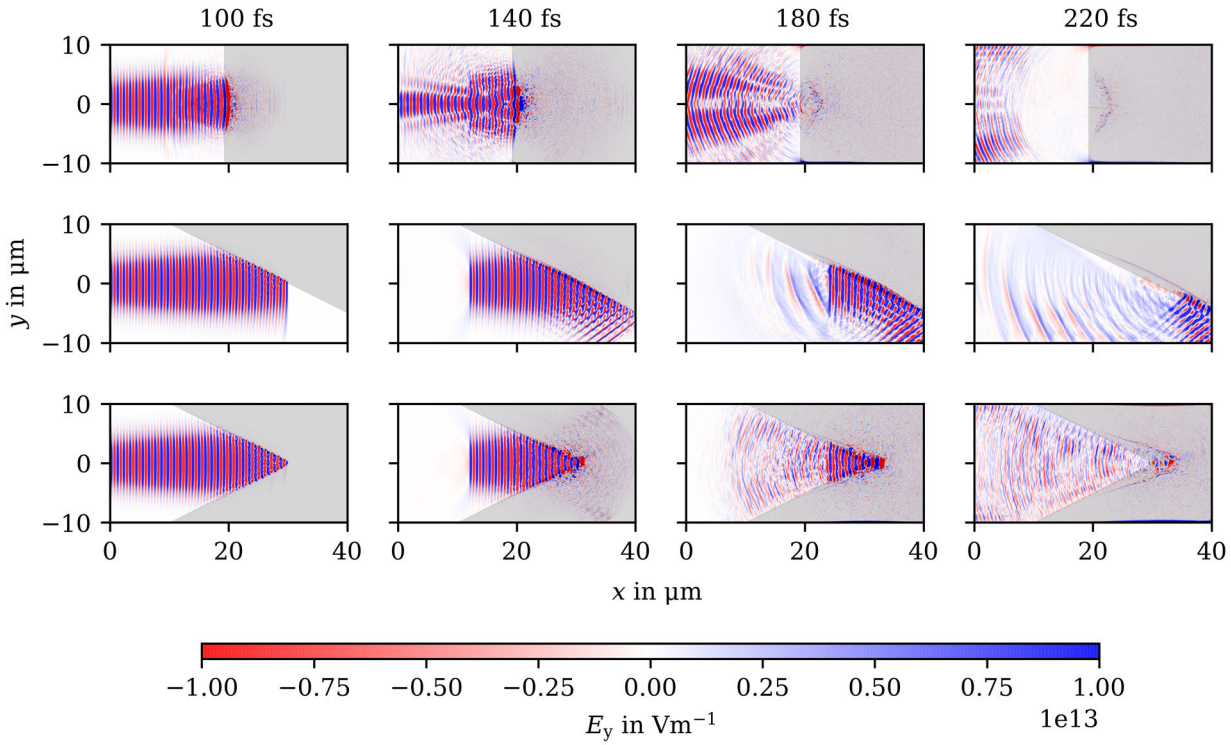

Figure 5.17.: Evolution of the E_y component of simulated electric fields for three different target geometries at 100 fs, 140 fs, 180 fs and 220 fs (from left to right) after simulation start. The top row shows a flat target front, the middle row a tilted surface and the bottom row represents a trough between two microstructures. The laser enters the simulation window from the left and is reflected from the overcritical target depending on the surface geometry. At all time steps, the initial form of the target geometries is plotted in gray for orientation.

density of 10 n_c, and the protons and electrons are initialized with a temperature of 10 eV (1.2×10^5 K) and 100 eV (1.2×10^6 K), respectively. These temperatures, being well above room temperature, partially account for slight preheating of the target by the laser pre-pulse, while the expansion of a low density pre-plasma is not included in this simulation. The laser main pulse has a pulse length of 100 fs (FWHM), a lateral spot size of 10 µm (FWHM) and an intensity of 2×10^{20} W cm^{-2}. It enters the simulation window from the left with an incidence angle of 0°. All initialization parameters are summarized in Table 5.4 as configuration A.

Figure 5.17 shows the evolution of the electric field component E_y with snapshots t_i at 100 fs, 140 fs, 180 fs and 220 fs after the start of the simulation. The periodic blue and red stripes show the laser with its wavelength of 1053 nm. Due to positioning the flat target in the middle of the window, it interacts with the laser peak intensity slightly earlier than the other two configurations. At t_1=100 fs, the counter-propagating, directed reflection of the laser at the flat surface is clearly visible, while the laser reaches the bottom of the trough not until this time step. The reflection at the tilted surface becomes more clear in the next snapshot at t_2=140 fs, and is evidently also directed. In case of the trough, such a directed reflection is not discernible. Here, the laser is reflected back and forth between the two slopes instead, which retains the laser energy in a region where it can be absorbed. Furthermore, the complex field pattern resulting from this is likely beneficial for stochastic electron heating, promoting an absorption mechanism that is less viable in the other two configurations.

The impact of these varying interactions on the induced electron temperatures is illustrated in Fig. 5.18. The composition of the figure is the same as for the electric fields in Fig. 5.17. Each row depicts one of

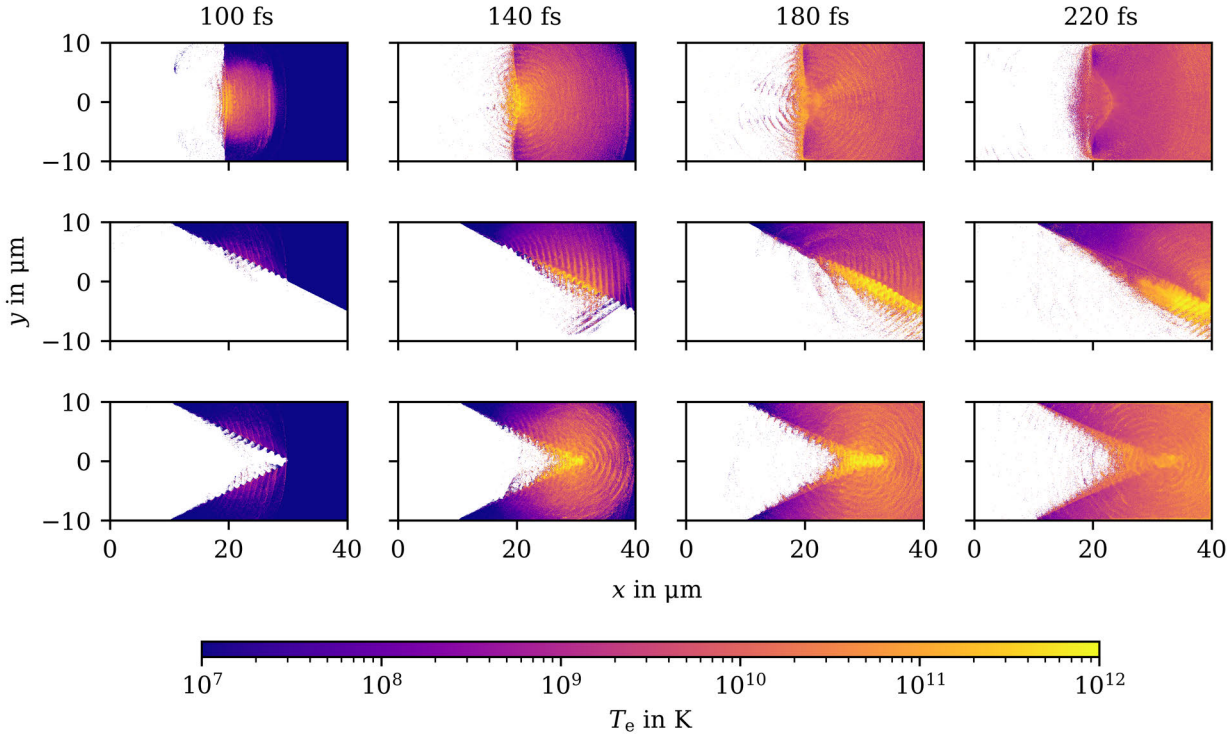

Figure 5.18.: Evolution of the electron temperature of a flat (top), tilt (middle) and trough (bottom) target at 100 fs, 140 fs, 180 fs and 220 fs (from left to right) after simulation start. The electrons of the flat target are heated earlier since the laser reaches the surface sooner than in the other two geometries. For the oblique surfaces, periodic bundles of electrons along the vacuum target interface are visible, which are probably caused by Brunel heating. The trough target produces a point-like hot electron source in the bottom of the valley.

the three target configurations while the columns show snapshots at four time steps. As discussed for the fields, the electron heating on the flat surface starts slightly earlier, resulting in a higher temperature at the first snapshot at $t_1 = 100$ fs. At this time, the significance of tilting the target surface is visible. The tilt changes the effective incidence angle, here, from 0° to 63°, thereby enabling Brunel heating. Both for the tilt and the trough geometry, the electrons are periodically accelerated at the vacuum target interface, which remains visible for the subsequent time steps. For the trough target, on the other hand, the increasing complexity of the fields as well as the underdense plasma filling the gap soon reduce this heating mechanism.

Another aspect that can be observed in these plots is the spatial distribution of the hot electrons. In case of the flat target, the Gaussian profile of the 10 µm wide laser focal spot is cast onto the electron distribution at the vacuum target interface. While the location of the hottest electrons for the tilt target continuously shifts as the laser slides along the surface, the trough creates a point-like source with its origin in the bottom of the valley, resulting in a wide angular spread of the electrons propagating through the target.

For better comparison, Fig. 5.19 (a) shows the hot electron temperature as it evolves over the simulation time. The values were derived by fitting a two-temperature Maxwell-Boltzmann distribution to the energy spectrum of all simulated electrons, with the depicted $T_{\mathrm{e,hot}}$ being the hotter component. Since the spectra are often more complex than the selected distribution, the temperatures obtained this way are only rough approximations. The time span of the laser irradiation is indicated by the gray, shaded area, which slightly varies for the different target geometries as can be seen in the previous Figures 5.17 and 5.18.

As discussed before, the heating of the flat target starts the earliest. Shortly after, the temperatures of the electrons of the tilt and trough targets begin to rise and at first follow a similar curve. Even though the interaction area is twice as large in the trough, the heating mechanism is the same in both geometries, therefore, the hot temperature is comparable. After 120 fs, the values begin to differ. The trough target reaches its hottest temperature at roughly 170 fs whereas the heating continues for additional 40 fs in case of the tilt target. This can be explained by the laser continuously interacting with a comparatively

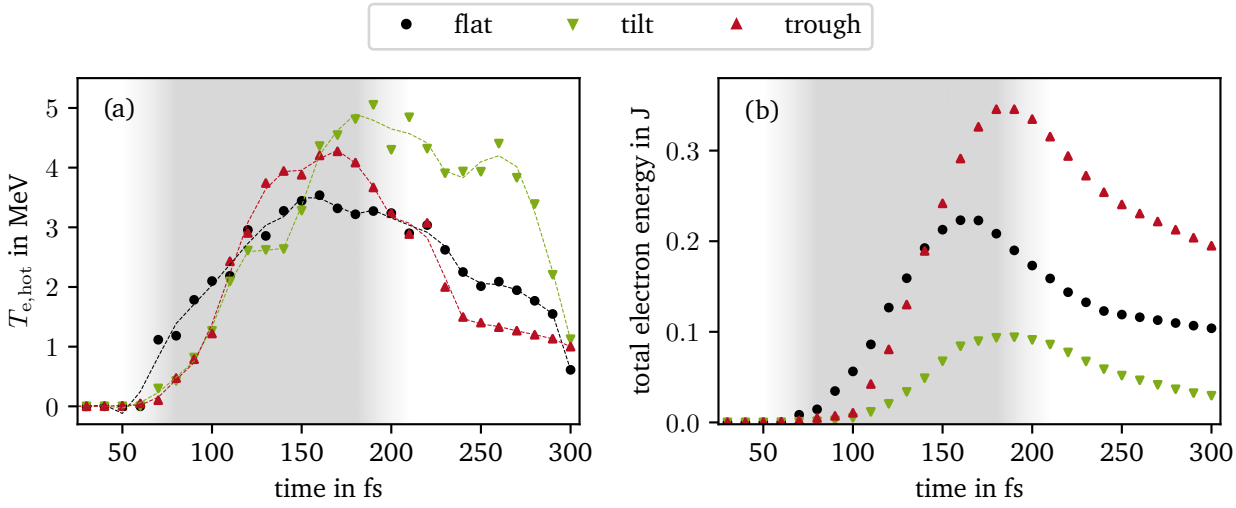

Figure 5.19.: Evolution of (a) the hot electron temperature $T_{\mathrm{e,hot}}$ and (b) the total electron energy for the simulated flat, tilt and trough targets over the simulation time. The tilt target induces a hotter temperature, but the deposited energy is higher for the trough target. The shaded area indicates the time span of the laser irradiation. The dashed lines in (a) are shown to guide the eye.

sharp interface, from which it can directly access cold electrons with its full intensity. However, in terms of overall energy transfer, the trough target exceeds both flat and tilt target as illustrated in Fig. 5.19 (b). The tilt target facilitates the lowest energy transfer.

Several effects need to be considered when finding an explanation for the differing energy absorption behavior. First, both advanced geometries feature an enlarged interaction area compared to the flat target. This increases the number of electrons interacting with the laser, but also decreases the effective intensity by a factor of 2.2 for the tilt and the trough target. However, this might be compensated by enabling Brunel heating, which requires an electric field component perpendicular to the surface. In the flat target configuration, the laser field is perfectly parallel to the surface, which can explain the lower temperatures.

Another aspect is the energy loss by laser reflection. In case of the tilt target, the deflected laser energy is simply lost. This is slightly improved in case of the flat target, since the counter-propagating light interacts with the underdense plasma expanding normal to the target front. The trough target provides the best conditions. Here, the underdense plasma is trapped in the trough, creating a region where collisionless heating mechanisms are dominant. In addition, the reflected laser immediately interacts with the opposite surface, going back and forth through the trapped plasma, which significantly enhances the energy transfer. This behavior is likely further enhanced in 3D, as the trough encloses the plasma from all sides while the tilted surface remains open to the sides.

In short, sloped surfaces increase the number of heated electrons, while also facilitating additional heating mechanisms that are able to counteract the decrease in laser intensity. Furthermore, geometries that enforce multiple interactions between laser and target surface while enabling energy deposition throughout the whole time can significantly increase laser absorption.

5.2.3. Tilted microstructures

To gain insight as to why the microstructures tilted in the direction of the incoming laser enhance the measured proton cut-off energies, four target configurations shot during the 2019 PHELIX campaign are simulated. The target types of interest are the Si foils backed with Cu (Fig. 5.3 (b)-(e)), including a flat target as reference and microstructures with a 0°, 15° and 30° tilt relative to the incident laser axis.

The simulation window has a size of $90 \times 80\,\mu\text{m}^2$, which gives enough space to accomodate the micrometer sized structures as well as propagation regions on the target front and rear side. The grid resolution is Δx=8.4 nm, and the PHELIX laser is modeled according to the experimental parameters with a pulse length of 500 fs (FWHM), an intensity of $1\times10^{20}\,\text{W cm}^{-2}$ and an incidence angle of 15°. Matching the experimental parameters, the flat foil has a thickness of 15 µm, and the microstructured targets feature a 5 µm base topped with 25 µm high, and 6 µm wide triangles with a tilt angle that varies between 0°, 15° and 30°. All targets are backed with a 5 µm thick Cu layer, and the further attached hydrogen layer modeling the natural contamination (see Section 5.2.1) has a thickness of 42 nm. Similar to the previous simulation setup, the target is preheated but initialized without a pre-plasma. The ion temperature is set to 100 eV and the electron temperature to 7 keV, which results from a hydrodynamic simulation performed for the PHELIX pulse profile by Theo Schlegel (Bagnoud et al., 2017). All materials are assumed to be fully ionized with an electron density of $50\,n_\text{c}$, which results in mass densities of $0.17\,\text{g cm}^{-3}$ (7 % ρ_solid) for Si and $0.18\,\text{g cm}^{-3}$ (2 % ρ_solid) for Cu, with ρ_solid denoting the respective solid densities. As discussed in Section 5.2.1, these low densities yield a "cold" Debye length that can be sufficiently resolved by the grid. All initialization parameters are summarized in Table 5.4 as configuration B, and the EPOCH input file for the 0° structures can be found in Appendix A.4.

Figure 5.20 shows the electric field in x-direction for the four targets at 0.5 ps, 0.7 ps, 0.9 ps and 1.1 ps after the start of the simulation. It should be kept in mind that this plot of E_x makes the laser field appear weaker, since the laser enters the window from the left and its main electric field component oscillates in the y-direction. In this laser-matter interaction scenario, the influence of the microstructures

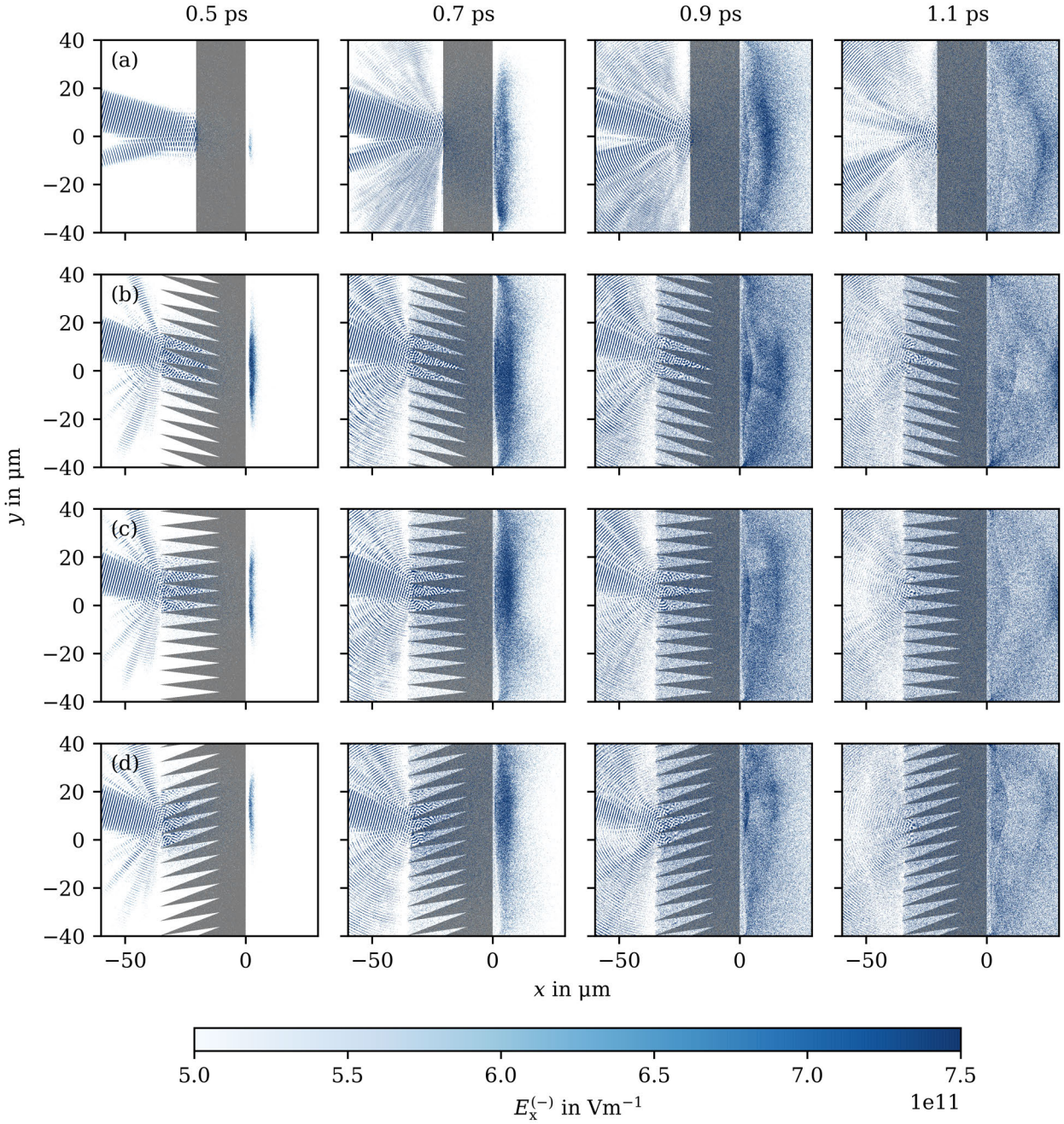

Figure 5.20.: Negative component of the electric field in x-direction $E_\mathrm{x}^{(-)}$ of targets with (a) a flat surface, (b) 0° tilted, (c) 15° tilted and (d) 30° tilted microstructures at four time steps, namely 0.5 ps, 0.7 ps, 0.9 ps and 1.1 ps (from left to right), after simulation start. The peak of the laser pulse reaches the flat target at 0.80 ps and the spike tips at 0.73 ps. The main component of the laser, which enters from the left, is in the y-direction, therefore its field seems rather weak compared to the sheath field at the target rear side. The positive $E_\mathrm{x}^{(+)}$ component is omitted to show the accelerating fields more clearly. For orientation, the target geometries (gray) are plotted in their initial form without evolving.

on the backreflected laser light can be seen clearly. Instead of a directed beam, as it is the case for the flat surface, the light is widely scattered by the structures, which in experiments reduces the risk of damaging optics in the beam path. In this figure, the positive component of the field is omitted to enhance the visibility of the accelerating sheath field, which develops over time. For all configurations, the sheath is already evident after 0.5 ps as a thin blue stripe at the target rear side. It is most intense and widest for the 0° tilt target (Fig. 5.20 (b)) and weakest for the flat target (Fig. 5.20 (a)), and its vertical position slightly changes depending on the target front surface structure.

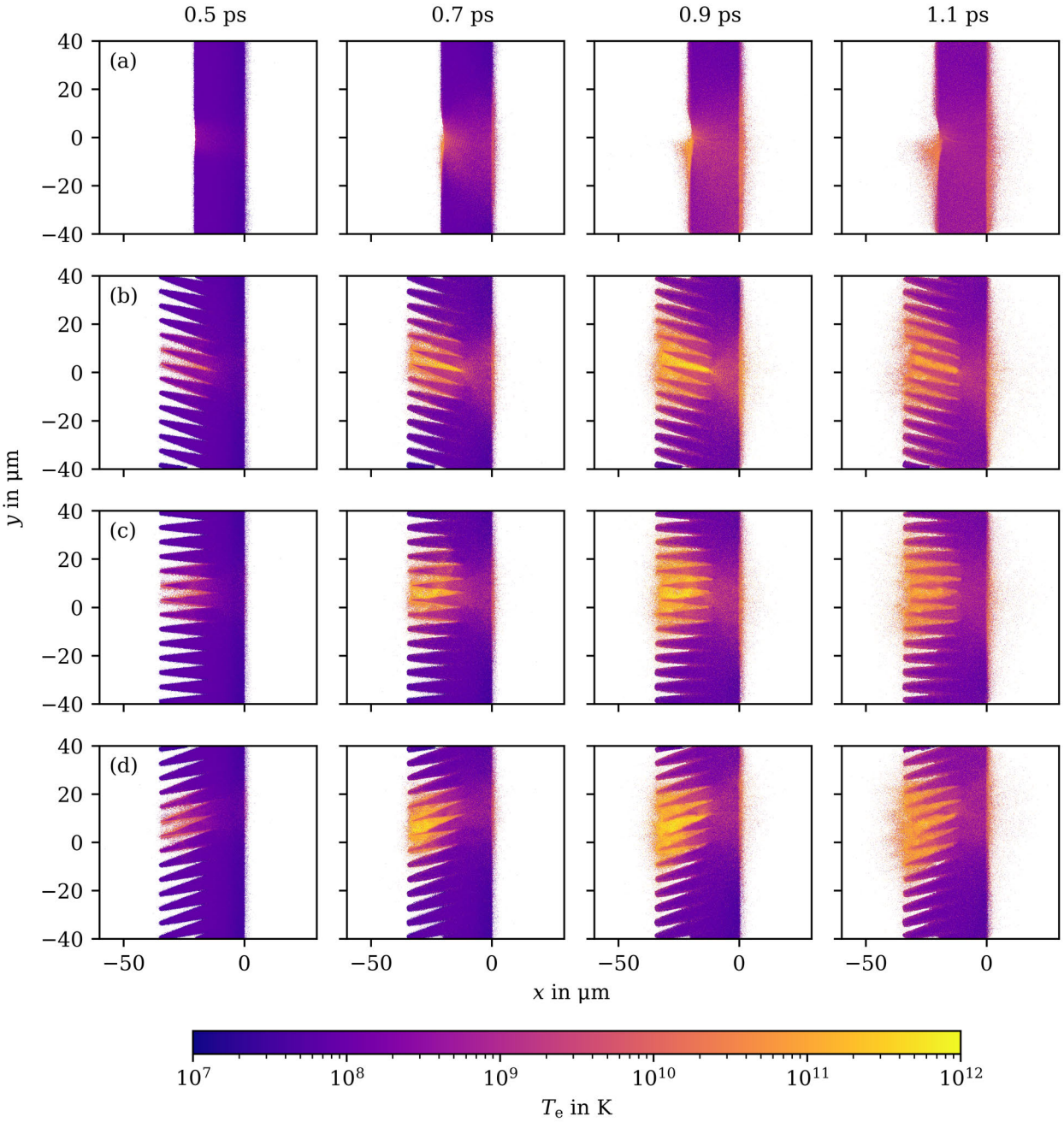

Figure 5.21.: Electron temperature of targets with (a) a flat front, (b) 0° tilted, (c) 15° tilted and (d) 30° tilted microstructures at 0.5 ps, 0.7 ps, 0.9 ps and 1.1 ps (from left to right) after simulation start. The microstructured targets generate higher temperatures than the flat target. The tilt angle of the structures affects the vertical position and shape of the hot electron sheath at the target rear side.

A reason for this shift of the sheath field position can be observed in the plots of the electron temperature in Fig. 5.21. In case of the flat target, the direction of motion of the heated electrons is mainly influenced by the oblique incidence angle of the laser, which causes a momentum component in the negative y-direction, thereby shifting the middle of the sheath slightly below the horizontal middle axis. For the microstructured targets, the tilt of the triangles is more influential. At a 0° tilt, the structures are per definition parallel to the laser axis. Here, the laser can reach the bottom of the troughs almost undisturbed, creating the hottest electrons in the tip of the middle trough, as can be seen in Fig. 5.21 (b)

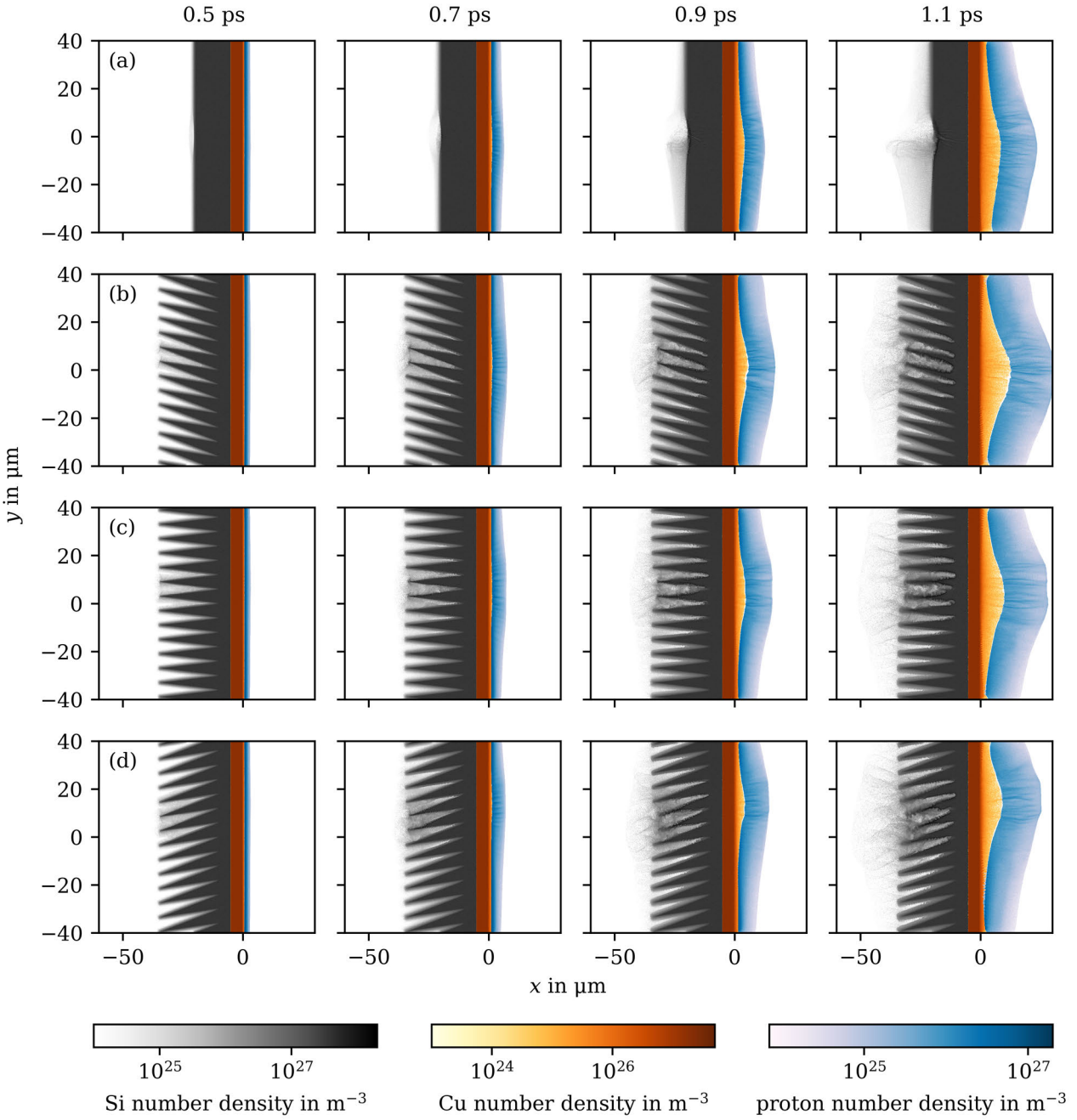

Figure 5.22.: Number densities of Si ions (grays), Cu ions (oranges) and protons (blues) of (a) a flat , (b) 0°, (c) 15° and (d) 30° tilt targets at 0.5 ps, 0.7 ps, 0.9 ps and 1.1 ps (from left to right) after simulation start. The proton layer at the target rear is accelerated first, followed by Cu ions from the underlying layer. The profile of the the accelerated particles matches the electron sheath shape.

at 0.7 ps and 0.9 ps. This effect was also seen in the simulations focusing on the basic trough shape in the previous Section 5.2.2. As a result, a small, compact electron source with a wide opening angle develops at the bottom of the trough at y=0, which creates a strong, extended sheath field centered at the horizontal axis. With increasing angle between laser axis and structure tilt, the sheath moves upwards. This is due to guiding effects in the structures that direct the electrons to the valley bottoms, which in this geometry lie at increasing y positions. Furthermore, the region of the hottest electrons moves towards the tips of the structures with increasing tilt angle, which is likely due to the decreasing penetration depth and a change of the dominant heating mechanisms from Brunel to stochastic heating and resonance absorption. The drawback of heating the electrons at the tips of the structures is that they undergo more collisions on their way to the rear side, which reduces their energy and as a result weakens the sheath (compare Fig. 5.20 (c) and (d)).

The impact of these varying sheath strengths can be observed in Fig. 5.22, which shows the number densities of the Si ions, the Cu ions and the protons. At 0.7 ps, the proton layer of all target types has expanded with a shape matching the accelerating sheath field, as expected from the TNSA mechanism (Section 2.3.3). The protons, as outermost layer and with the best charge to mass ratio, are accelerated first, with some Cu ions following after. The separation of the two species is also visible in the structure of the E_x-field in Fig. 5.20. At 0.9 ps and 1.1 ps, two distinct transversal profiles are observable, which coincide with the snapshots at which the density profiles show a clear expansion of both ion species as well.

Furthermore, the density plots show a filamentation of the accelerated ion beams, however, since the simulation is only two-dimensional, a comparison with the experimental beam profiles discussed in Section 5.1.2 is not practical. It can be noted, though, that opposed to the flat target, the filamentation in case of the structured targets seems to be mostly restricted to the center of the beam, which might be explained by guiding effects in the structures.

The final proton energy spectra that developed over a run time of 3 ps, are displayed in Fig. 5.23. These spectra include all protons, both those remaining in the simulation window and those that were ejected. All structured targets show higher proton numbers in the middle energy range between 10 MeV and

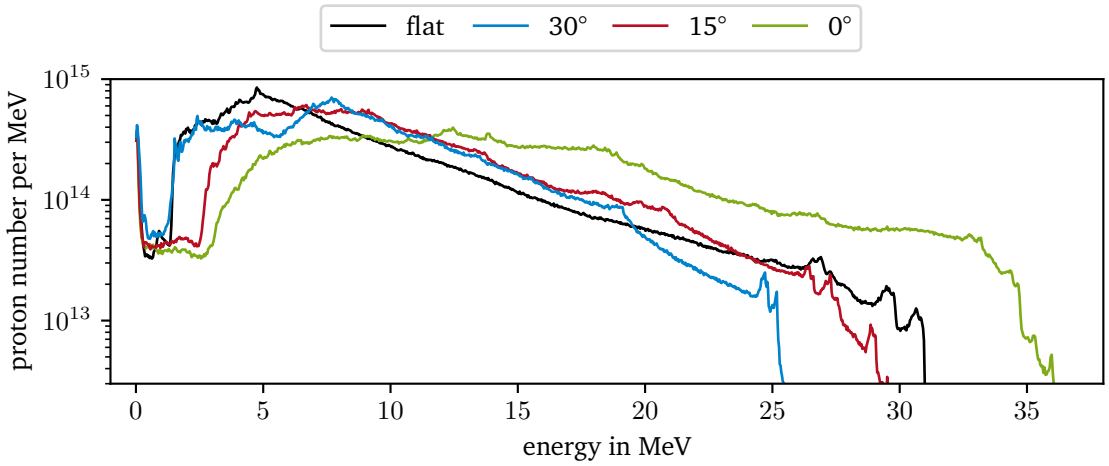

Figure 5.23.: Simulated proton spectra of targets with varying tilt angles of the microstructures relative to the incident laser axis in comparison to a flat reference target. The highest number of high energy protons as well as the maximum proton energy are generated with microstructures that are parallel to the laser axis, in other words, with a 0° tilt. The drop in proton numbers in the low energy range could be caused by the simulation window being too small or the limited amount of available protons.

20 MeV, with the 0° tilt target showing the overall highest numbers of high energy protons as well as the maximum cut-off energy. In the low energy range between 1 MeV and 3 MeV, all spectra show a considerably lower number than expected from a roughly Maxwellian energy distribution. This could be the effect of two different causes. First, if the proton layer is too thin, it can be depleted before the accelerating sheath decreases in strength, which is consistent with the fact that a significant amount of Cu ions is accelerated in the following, as can be seen in the number density plots in Fig. 5.22. Second, the simulation window is too small to contain the outer edges of the sheath, where the strength is decreasing and a considerable amount of low energy particles would be generated.

The proton cut-off energies are summarized in Fig. 5.24 and compared to the experimental results of the 2019 PHELIX campaign. Apart from a slight offset, the simulated and experimental values agree. With decreasing angle between the laser and microstructure axis, the maximum energy increases. The best performance is observed for the 0° structures pointing along the direction of the incoming laser, with an enhancement of roughly 40% compared to the 30° microstructures. The offset between the two data sets is expected, as 2D simulations typically overestimate cut-off energies, because the sheath decays slower due to omitting one spatial dimension (Blanco et al., 2019; Xiao et al., 2018).

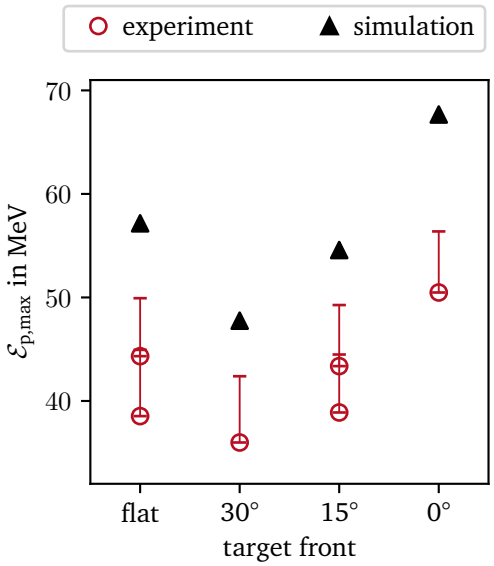

Figure 5.24.: Proton cut-off energies $\mathcal{E}_{\mathrm{p,max}}$ from the PHELIX campaign in 2019 (compare Fig. 5.6) in comparison to corresponding simulations for microstructures with different tilt angles. All values, both simulated and experimental, were normalized to a laser energy of 170 J. The experimental results were measured with RCFs and thus have only an upper uncertainty.

In summary, the simulations demonstrate the ability of the microstructures to suppress directly reflected laser light and the significant impact of their tilt angle relative to the laser axis on the accelerated proton spectrum. In excellent agreement with the experimental results, the highest cut-off energies are achieved with microstructures that are parallel to the incoming laser. As described in Section 4.1.2, manufacturing such tilted microstructures requires only a simple adjustment during the fabrication process, therefore it is highly recommended to match the tilt angle of the structures to each specific experimental setup.

5.2.4. Target optimization and comparison to pillar structures

The number of feasible microspike shapes and sizes is countless due to the flexibility of the fabrication process, as was discussed in Section 4.1.2. This offers the great opportunity to freely design the microstructures, but in order to maximize the output in a specific experiment, the optimal geometry needs to be determined in advance. For this optimization, simulations can be employed. Parameters that can be easily varied are the target base thickness b, the slope angle β and the height h of the structures, all of which are illustrated in Fig. 5.25 (a). In the following, a series of parameter studies based on S. Grimm's work during her bachelor's thesis are presented, which help to identify the most relevant characteristic to optimize the maximum and arithmetic mean energy of protons accelerated by TNSA. Furthermore, it exemplifies the enhancement that can be reached by optimizing the target geometry.

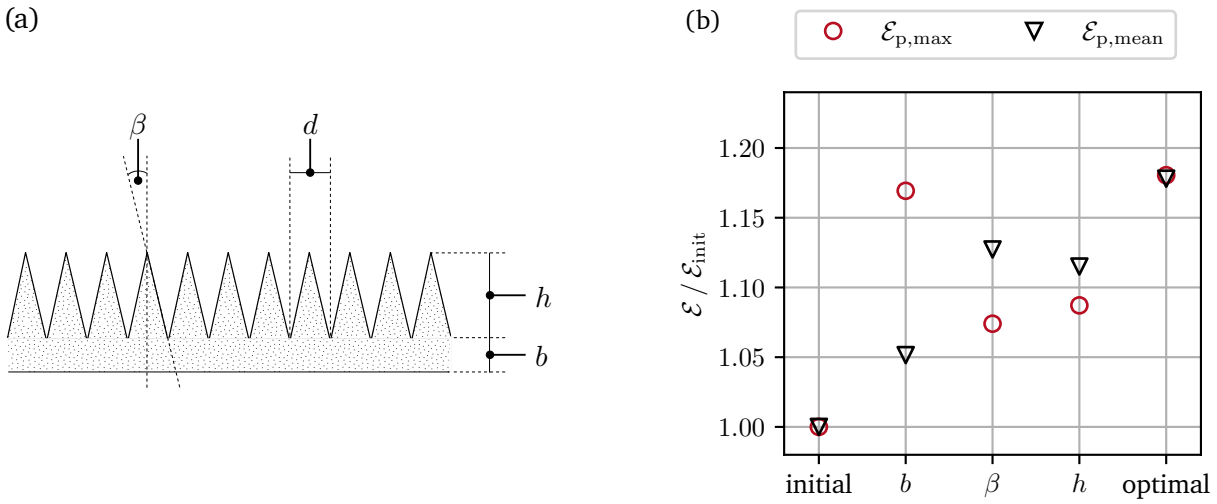

Figure 5.25.: Target geometry optimization. (a) Schematic of a microstructured target with base thickness b, structure height h, slope angle β and the diameter d of a single spike, which is equivalent to the distance between two microstructures. (b) Comparison of the maximum (circle) and mean (triangle) proton energies for optimal base, slope and height of the microstructures in units of the initial target geometry energies $\mathcal{E}_{\mathrm{p,max,init}}$ and $\mathcal{E}_{\mathrm{p,mean,init}}$. Combining the optimized parameters in an optimal target results in the highest maximum and mean energy. Adapted from Grimm (2020) (Fig. 5.18) with kind permission from Sarah Grimm.

The simulations are run in a square window with a width and height of 80 µm. The cell size is set to 31 nm, which equals five times the Debye length at an electron temperature of 7 keV and an electron density of $10\,n_{\mathrm{c}}$. Due to the large number of 27 simulations required for the optimization, the laser pulse length is shortened to 50 fs, while the focal spot size of 10 µm and the intensity of $1\times10^{20}\,\mathrm{W\,cm^{-2}}$ are similar to the laser parameters of the PHELIX campaign. The laser incidence angle is set to 0°. The initial target geometry was chosen based on a typically fabricated shape, i.e., spikes with a height of 15 µm and a diameter of 5 µm, which equals a slope angle of 9.5°, on a base with a remaining thickness of 5 µm. The target material was Si and a proton layer with a scale length of 5 cells, which equals 150 nm, was added to the rear side of all targets to imitate the natural contamination layer. The ions were initialized with a temperature of 100 eV, and a summary of all simulation parameters is provided in Table 5.4 as configuration C.

The next paragraphs summarize the values identified as optima. For a complete overview of both maximum and mean energies for the complete parameter series refer to Appendix A.5. First, the target base was optimized by varying its thickness between 0.0 µm and 5.0 µm in 0.5 µm steps, which gives a total of eleven simulations. The maximum proton energy was achieved without any remaining base and decreased slightly with increasing thickness. However, the highest mean energies were reached with thicknesses between 0.5 µm and 1.5 µm, thus, 0.5 µm was identified as the optimal value. This thickness is also easier to fabricate, since the structures, which are also connected to each other by slim ridges, can in principle indeed be manufactured without a base, but this increases the likelihood of larger holes and jeopardizes the overall stability of the target.

The optimal slope angle was determined in a series of five simulations, during which the spike height was kept constant while the diameter was varied. Both the maximum and mean proton energy were realized with a slope angle of 18.5°. This value results in an effective laser incidence angle of 71.5° relative to the target surface, which coincides well with the optimal angle of 73° for Brunel heating (see

Section 2.2.4). Consequently, this value is likely to change substantially with increasing pre-plasma scale length, which is not considered in these simulations.

By shrinking the microstructures while keeping the aspect ratio constant, the optimal height is attained. For this, another series of eleven simulations was conducted, varying the height between 1.5 µm and 15 µm in 1.5 µm steps. This series showed an optimum for both cut-off and mean energy at a height of 6 µm.

Figure 5.25 (b) shows the enhancement achieved by optimizing each parameter in comparison. The greatest enhancement of the mean proton energy is observed for the optimized slope angle. Regarding the maximum proton energy, the base thickness has the highest impact. This might be attributed to lowering the energy loss of the electrons on their way to the target rear side by reducing the number of collisions inside the target bulk. Lastly, an optimal target combining all optimized values was simulated. It has a 0.5 µm thick base, the spikes are 6 µm high and the diameter is reduced to 4 µm to match the ideal slope angle. This target shows by far the best improvement of roughly 22 % in mean energy compared to the initial target design. The cut-off energy is also significantly enhanced by approximately 18 %. It should be noted, that the parameters were optimized independently. Possibly, even greater improvements can be achieved through a correlated optimization.

As discussed in the fundamentals (Section 2.3.4), the topic of microstructured targets has been widely explored over the last two decades. An evergreen are pillar or wire targets, that feature parallel structures with their length exceeding their diameter. It is therefore of interest to compare this type of microstructure to the spikes investigated during this thesis.

The simulation setups for the different target geometries are illustrated in Fig. 5.26. It shows the initial spike target (Fig. 5.26 (a)), as well as the optimized geometry (Fig. 5.26 (b) and (c)). A flat foil serves as reference (Fig. 5.26 (d)). It has a thickness of 0.45 µm, which was identified in a separate parameter study as the optimal thickness for the modeled scenario. The simulated pillars (Fig. 5.26 (e) and (f)) are made of the same amount of material as the initial spike target and were not optimized further. They have a 5 µm thick base, which is the same as for the initial spike geometry. Each pillar is 15 µm tall and 2.5 µm wide. The gap width between two adjacent pillars is 2.5 µm. To study the pointing stability, the laser is focused once in the gap and once on the top, which was also applied to the spike geometry. All other simulation parameters are identical to the setup used to optimize the target geometry.

The proton spectra generated by the six different target types are shown in Fig. 5.27. The optimal flat target is outperformed by all microstructured targets, which allows the reliable conclusion that the microstructures indeed improve the proton acceleration. Clearly, the spike targets enhance the middle energy range the most of all three target types, both in the initial and optimized geometry.

Pointing the laser on or between the microstructures primarily affects the maximum proton energy, while the low and middle energy range of the spectrum remain comparable. When focused on top of a pillar or on a spike tip, the effective target thickness is increased, causing the electrons to lose more energy in the target bulk. This, in turn, reduces the cut-off energies. In contrast, focusing in a gap results in the shortest distance between target front and rear, therefore the electrons retain more of their energy. For experiments in which the focal spot diameter and the microstructure spacing are of a similar size, the relative positioning between laser and target is therefore of importance. This effect will likely decrease, though, for focal spot sizes that are significantly larger than the microstructure spacing, as in this case multiple gaps and tips are averaged.

Besides the energy distribution, the profile and opening angle of the proton beam can be of interest for further applications. Hence, the angular distributions of the accelerated protons of a flat, spike and pillar target are compared in Fig. 5.28. All target types generate the highest energies along the target

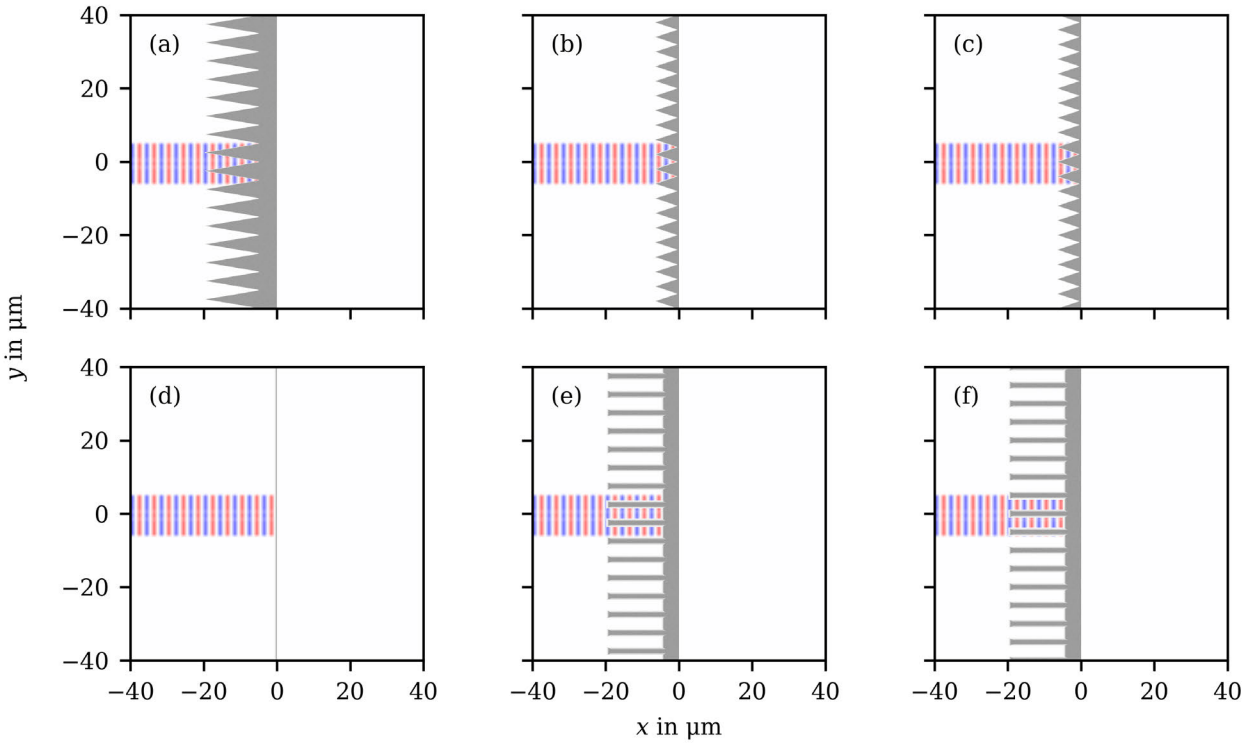

Figure 5.26.: Simulation setups for different target types in a $80 \times 80\,\mu m^2$ simulation window. The initial target geometry of the spike target (a) is compared to the optimized spikes ((b) and (c)), a flat reference target with a thickness of 0.45 µm (d) and pillars ((e) and (f)). The laser, which enters the window from the left with a 0° incidence angle, is stylized to show the difference between hitting the gaps ((b) and (c)) and the tips ((e) and (f)) of the microstructures.

normal direction. With decreasing energy, the opening angle gets wider. This agrees with the shape of the electron sheath causing the acceleration, which is strongest in the center and weakens towards the edges. The thin, flat target produces the narrowest beam, while the spike target creates the widest. Comparing the two microstructured targets, the pillar target induces stronger guiding effects along its structures than the conical microspikes, which translates to a more compact beam.

To sum up, optimizing the microstructure geometry in terms of base thickness, slope angle and height can significantly enhance the mean and maximum proton energies. Minimizing the base has the greatest impact on the cut-off energy, while the slope angle affects the mean energy most. In comparison to an optimized flat reference target, both spike and pillar microstructures improve the accelerated proton numbers and energies. For small laser spots, focusing in the gap between two adjacent structures can further increase the maximum proton energy.

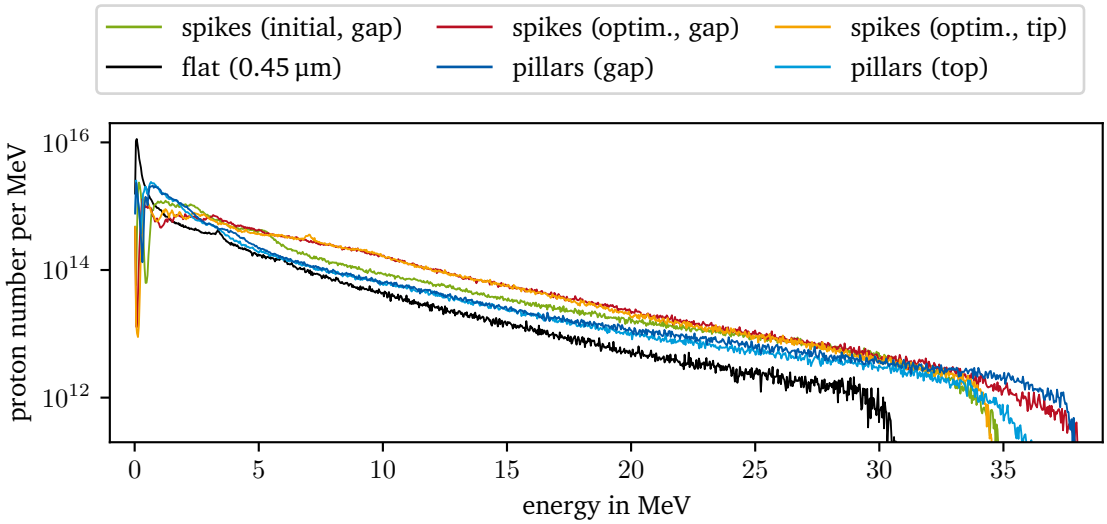

Figure 5.27.: Proton spectra of different target types after a simulation run time of 3 ps. The thin, flat target shows the lowest performance. It is surpassed by the two types of microstructured targets, which generate similar cut-off energies. The optimized spikes enhance both proton numbers and the cut-off energy compared to the initial design. Centering the laser focus on a tip of a microstructure results in lower cut-off energies than focusing in the gap. The spiked targets create the highest proton numbers in the middle energy range between 3 MeV and 30 MeV, even with an suboptimal design.

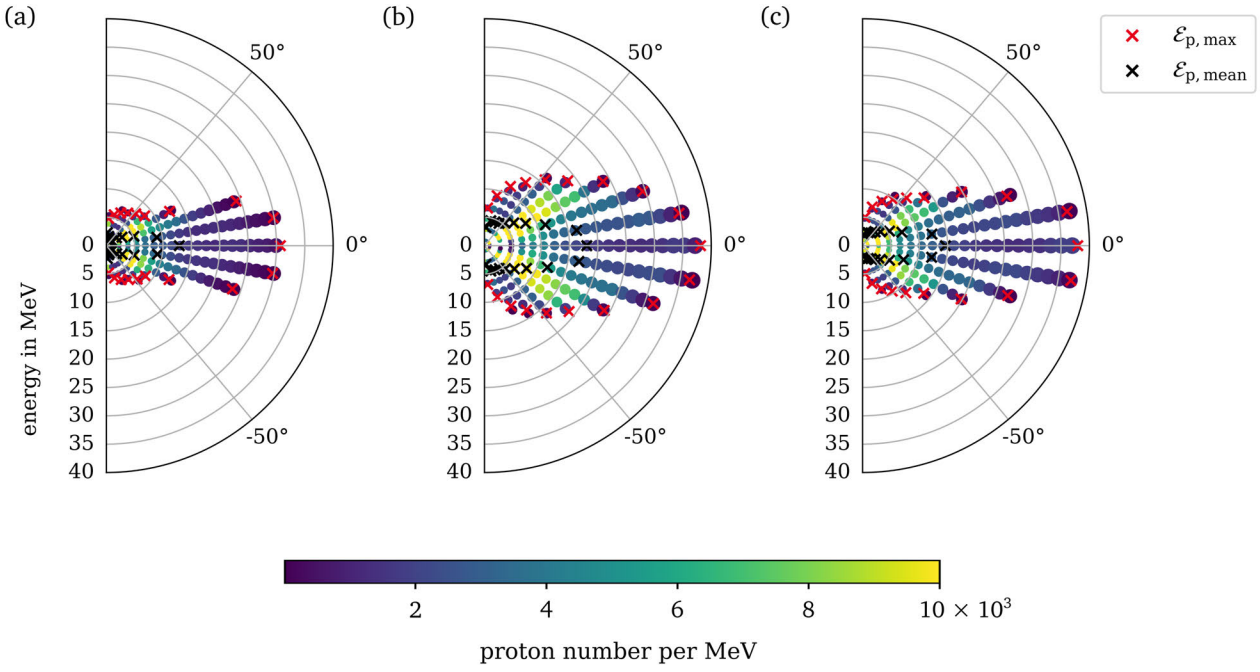

Figure 5.28.: Angular distributions of the accelerated protons generated by (a) a 0.45 µm thin flat foil, (b) an optimized spike target and (c) a pillar target. The target normal direction corresponds to 0°. The laser was focused into the gap between two microstructures in both cases. The colorbar shows the number of protons per MeV and the red and black cross markers show the maximum $\mathcal{E}_{\mathrm{p,max}}$ and mean $\mathcal{E}_{\mathrm{p,mean}}$ proton energy for each angle, respectively. All target types produce the highest energy protons in target normal direction and the opening angle gets wider for decreasing energy.

5.3. Discussion

The main objective of this thesis was to enhance the coupling between lasers and matter by modifying the front surfaces of targets. Ideally, the modifications would allow to tailor the electron spectrum to suit the subsequent processes of X-ray generation and ion acceleration, and thereby improve the respective yields. In contrast to many other studies involving micro- and nanostructures for enhanced coupling, high energy laser systems with fairly long pulses exceeding 0.5 ps were employed in this thesis. These systems are indispensable for brilliant X-ray emission and high particle numbers, because the yield of these secondary, laser-induced sources is ultimately limited by the input energy. Since the spike-shaped microstructures under investigation have only recently gained attention by proof-of-principle experiments by our group (Ebert et al., 2020; Neumann, 2018), the interaction was studied both experimentally and theoretical over a large parameter space. This kind of exploratory research entails very low statistics due to the limited number of shots provided by the high energy laser systems of interest. Moreover, the number of PIC simulations was limited by the available computing power and the necessary approximations allowed for qualitative assessment only. Nonetheless, a number of guiding trends could be identified, underlying phenomena were analyzed and the X-ray and ion yields were improved.

A key to creating powerful secondary sources is improving the laser to target energy transfer, specifically by manipulating the involved electron heating processes to their greatest advantage. The simulations revealed that the presented microspikes improve the energy transfer by multiple effects (Section 5.2.2). First, the increased surface area increases the number of electrons interacting with the laser. Second, the sloped geometry changes the incidence angle, which enables Brunel heating in addition to resonance absorption and stochastic heating. Third, the high aspect troughs trap the laser light by enforcing multiple reflections, which, fourth, prolongs the interaction time and volume since the expanding plasma is also trapped in these gaps. In addition, compared to parallel structures such as pillars or wires, the increasing distance between the adjacent structures towards the front delays a plasma-shutoff.

Although Blanco et al. (2017) showed that an optimal energy transfer in triangular structures is achieved when crossing the gap takes half a laser period, the significantly smaller structures fulfilling this condition might be too small to be employed with high energy laser systems. Even if they outlast the pre-pulse, they are expected to dissolve quickly and their impact becomes negligible for irradiation times in the order of several hundred femtoseconds. The considerably larger structures studied here are more durable, yet, the amount of energy deposited before the main pulse still plays an important role. The measured proton cut-off energies (Fig. 5.6) show that the structured targets have no impact at low ASE contrast (10^7). This is not surprising, considering that the respective ASE intensity is above the Si ionization threshold of $1\times10^{11}\,\mathrm{W\,cm^{-2}}$ (Martynenko et al., 2021) and therefore the target front is fundamentally modified by the generated pre-plasma. Even if the ASE level is below the ionization threshold, as it is the case for the high (10^{13}) contrast shots, Wharton et al. (2001) discussed that thermal heating can lead to the formation of vapor clouds on the target front. These are easily ionized in the rising edge of the pulse, thus also creating a non-negligible pre-plasma. In all cases, the scale length of the pre-plasma strongly affects the actual geometry of the front surface when the main pulse arrives and consequently influences the laser target coupling efficiency. Ideally, simulations take this into account, but the high complexity of the pre-plasma formation process calls for supplementary investigation, e.g., with hydrodynamic codes.

Previous experiments, e.g., at the VULCAN laser at RAL, UK, and the PIC simulations discussed in Section 5.2.3 show the remarkable capabilities of microstructured targets to suppress directly back reflected light (Ebert et al., 2020; Jarrett et al., 2019; Neumann, 2018). For one thing, this is caused by

the increased absorption, but they also widely scatter the remaining light. In case of pillar targets, the scattered light is imprinted with an interference pattern that is caused by the equidistant array, which can be used to diagnose the front surface plasma (Jarrett et al., 2019). The VULCAN data showed, that a smoother distribution of the backscattered light is reached by the spike-like structures, since they are randomly distributed due to the fabrication process (Section 2.3.1). Especially for high energy laser facilities this is a highly appreciated target property, as directly back reflected light can damage the valuable optics.

Typically, the hazard of backreflected light entering the laser system is mitigated by shooting the targets under an oblique incidence angle, which is usually between 5° and 45°. Apart from the work of our group, so far only two experimental studies on proton acceleration with microstructured targets using lasers with pulse lengths $> 0.5\,\mathrm{ps}$ and intensities $> 10^{20}\,\mathrm{W\,cm^{-2}}$ were published. Both Sedov et al. (2019) and Bailly-Grandvaux et al. (2020) investigated parallel microstructures, that is, pillars and microtubes. Their incidence angles were 45° and 15°, respectively, and while Bailly-Grandvaux et al. at least observed a considerable enhancement of the proton number and conversion efficiency, Sedov et al. did not record any enhancement by their structures in terms of proton yield. Neither of the two observed any improvement of the proton cut-off energy. The experiments conducted in this thesis, however, showed that matching the microstructure tilt angle to the laser incidence direction can increase the maximum proton energy. The results are in very good agreement with the simulations, which coincides with the results obtained by Blanco et al. (2017) for smaller triangular structures. This finding indicates that modifying the tilt angle is necessary to fully exploit the potential of the structures, the guiding effects in particular.

Of course, the modest results reported so far might also have been caused by a suboptimal target geometry. For the microspike targets, the simulation series performed in this thesis showed that thin bases are favorable, and both height and slope have a great impact on the proton yield. The latter two parameters were not optimized for the targets shot during this work, because the simulations have not yet provided any quantitative results due to their dimensionality and the unavoidable approximations. Nevertheless, the targets were fabricated with the thinnest feasible base and as homogeneously as possible. In order to optimize the microstructure geometry for future experiments, it is of great importance to include the pre-plasma formation in the modeling to account for its significance for the heating processes.

The simulations for the geometry optimization as well as the comparison to pillar targets illustrated the substantial increase of accelerated protons achieved with microstructured targets (Fig. 5.27). When employing such targets in experiments, it is essential to provide a sufficient amount of protons in the first place to maximize the yield. For targets made of materials containing no hydrogen, the protons originate exclusively from the natural contamination layer. The available numbers determined by, e.g., Hoffmeister (2014) and Jiang et al. (2018), are in the order of the proton numbers in typical TNSA beams, therefore they might preset an upper particle number limit. The experiments conducted with Si targets with an additional CHD layer on the rear side proved, that the contamination layer is at least partially depleted since deuterons were detected in the Thomson parabola traces (Section 5.1.2). Based on these results, it is therefore highly recommended to either use target materials containing hydrogen or provide an additional proton source at the target rear sides. Both can be implemented for the presented spikes as described in Chapter 4.

Shortly after TNSA was discovered in 1999, reports on imprints of the target rear side structure on the proton beam profile were published, e.g., by Roth et al. (2006) and Nürnberg et al. (2009). Among other inferences, they used these imprints to determine the virtual source size of the proton beam. The RCF data collected during this thesis showed an imprint of the structure arrangement, which is different to the other studies in that the initial pattern stems from the target front. Still, this could be

used to diagnose, e.g., guiding effects or beam propagation. For this, a series of 3D simulations would be helpful to study the imprinting process in detail.

Another achievement of the conducted experiments is the improved X-ray yield by the presented microstructures, as this forms one of the cornerstones for powerful backlighters. Here, the process of X-ray generation profits from the increased penetration depth, the trapped plasma and the increased number of hot electrons. As expected, the impact is highest for short pulses as demonstrated with the Omega EP experiments, but even at long pulse lengths of 20 ps the structured targets enhance the performance (Fig. 5.13). This is excellent news since the experiments also showed that the highest total X-ray yield is achieved with the longest laser pulses.

Besides a high yield, another crucial property of a bright X-ray backlighter is a short pulse length. In the past, nanowire targets also showed very promising results in terms of X-ray yield, but they also increased the duration of emission by an additional afterglow (e.g. Kulcsár et al. (2000)). Similar behavior was found for targets treated with intentional pre-pulses to extend the pre-plasma scale length as well as for shield targets (Stoeckl et al., 2021). The falling edge of the X-ray pulse depends mainly on the kinetic transport of the absorbed energy. Since solid targets are likely to develop steeper temperature gradients and feature shorter mean free paths, cooling occurs more rapidly than for low density targets (Kulcsár et al., 2000). The discussed spike structures seem to offer a great compromise, combining an increased interaction volume by trapping both light and plasma with steep temperature gradients and high density regions that are needed to rapidly distribute the absorbed energy. Especially for setups that require diagnostics with a high temporal resolution, and which are not equipped with ultrashort exposure cameras, employing the proposed microstructures might be an ideal solution. Without increasing the pulse duration and thereby the capture time, they still enhance the X-ray intensity. Also, using them in a layered configuration with the structures providing enhanced laser absorption and an additional rear layer of the desired X-ray material, both the variety of feasible materials can be extended and unwanted heating lines can be suppressed (Sander et al., 2021).

All things considered, the experiments and simulations presented in this thesis demonstrate the potential of equipping targets with microstructured front surfaces. Even though the microspikes were not optimized for either of the two employed laser systems, they improved both proton acceleration and X-ray generation. The proposed targets are relatively straightforward to align and feature the additional benefit of suppressing directly back reflected light.

6. Summary and Conclusion

In this work, the energy transfer between high intensity lasers and matter is optimized to enhance laser based secondary sources. This is accomplished by equipping the target front sides, where the primary interaction with the laser occurs, with microstructures. One essential requirement for the structures is to be beneficial for high energy laser pulses with lengths exceeding 0.5 ps, as these lasers ultimately produce the highest X-ray and ion yields. In this work, a target fabrication process for spike-like microstructures was developed and the interaction between microstructured targets and high energy lasers was investigated, both experimentally and in simulations.

The target fabrication process, which is described in Chapter 4, is based on ultrashort laser pulse processing. The implemented setup enables the production of large, structured samples with high homogeneity due to an optimized scanning pattern. The microstructures can be generated in different processing atmospheres, including air, sulfur hexafluoride and isopropanol, and with varying laser parameters, such as pulse energy, pulse number and polarization. This allows for a wide variety of shapes and geometries, which is further extended by optionally tilting the structures. Most processing parameters can be easily adjusted, which allows to tailor the target sets to the specific experimental needs. In addition, the laser processing was applied to different substrate materials, namely silicon and titanium, to directly generate the spike-like microstructures. The structured samples were characterized mainly with SEMs, as other tested methods proved to be unsuitable for the highly light absorbing, high aspect structures that need to be characterized non-destructively to be of further use as targets. A special design of the substrate allows the sample to be snapped along a premeditated line to evaluate the cross sections of the microstructures.

Furthermore, a process chain for subsequent replication based on molding with polydimethylsiloxane (PDMS) was developed, which can be used to produce targets with the same front surface geometry out of a larger variety of materials. Here, the mold was used to fabricate copper microstructures by electroplating as well as polystyrene structures, both deuterated and non-deuterated, by spincoating. The presented micro-replication procedure can be applied to other target types without major changes. Targets fabricated with the two described methods can either be made completely of the same material, or can be equipped with a rear layer of a different material, e.g., copper or polystyrene. Such layered targets are of great interest for applications requiring a proton or deuteron-rich backside for ion acceleration or for X-ray backlighters with a specific characteristic emission line. Both single material and layered targets were produced from the structured samples.

The manufactured targets were employed in two main experimental campaigns at the PHELIX laser system at GSI, Darmstadt, Germany and the Omega EP system at LLE, Rochester, NY, USA, which are described in Chapter 5.1. Both laser systems provide petawatt pulses with energies exceeding 100 J and pulse lengths greater than 0.5 ps, and are therefore well suited for the generation of high intensity ion and X-ray sources. During the experiments with the PHELIX laser, the focus was on ion acceleration and X-ray generation at $10^{20}\,\mathrm{W\,cm^{-2}}$ for three different ASE laser contrasts, namely 10^{7}, 10^{10} and 10^{13}. The experiments at the Omega EP facility, on the other hand, investigated the influence of the laser pulse length on the X-ray emission at lower intensities on the order of $10^{17}\,\mathrm{W\,cm^{-2}}$. In these

campaigns, a total of 12 target configurations was studied, which were mainly made of silicon and featured different microstructure sizes, tilts and back layers. Flat, polished foils were used as reference targets. As described in Chapter 5.2, the experiments were supplemented by a series of PIC simulations, which provided insights into the microstructure-induced changes in the underlying energy transfer mechanisms. The simulations were run on the high power computing clusters Kronos and Virgo at GSI with computational costs of up to 74,500 CPU hours per simulation.

One of the main findings of this work regards the tilt angle of the microstructures relative to the laser incidence direction. In typical high intensity laser matter experiments, the targets are shot with an oblique incidence angle to protect the laser system from unwanted back reflections. The experimental data, validated by simulations, showed that matching the tilt of the structures to the laser incidence angle enhances the maximum proton energy and the number of accelerated protons. Compared to structures with an angle of 30° relative to the laser axis, the parallel oriented structures showed a roughly 40% higher maximum energy. This result is also applicable to other types of microstructures and a mismatch between the angles might be one of the reasons why neither Sedov et al. (2019) nor Bailly-Grandvaux et al. (2020) saw an enhanced cut-off energy in their proton acceleration experiments. Based on the presented results, it is highly recommended to adjust the tilt of the structures to match the laser incidence angle during the target fabrication process, which in case of ultrashort laser pulse processing requires no additional effort.

Another result confirms a theory that was raised during VULCAN experiments in 2017 with the same type of microstructured targets. The data suggested that the accelerated proton number may be limited by the amount of available protons in the natural contamination layer on the target surface. The experiments conducted in the scope of this work, that had a deuterated plastic foil attached to the target rear side, showed accelerated deuterons. Since the protons that are present in the natural contamination layer are accelerated first, this is a strong indication that after at least partially depleting this depot, the sheath field is still strong enough to accelerate further particles out of the target itself. Therefore, higher proton numbers might be possible if the microstructured targets are equipped with an artificial proton source at the rear side, e.g., a plastic foil with a high proton content. The experiments also confirmed that the structures have a higher impact at high contrast, where their geometry is mostly preserved until the main pulse arrives.

In terms of X-ray emission, the experiments with high intensity and high contrast at the PHELIX facility showed an increased number of X-ray transitions. This can be attributed to the strong temperature and density gradients in the target, which lead to the generation of hollow ions. The X-ray yield can be significantly increased by using longer pulses, as was shown by the Omega EP experiments. Even though the impact of the structures is higher at shorter pulse lengths, an enhancement of the X-ray intensity was recorded for all pulse lengths up to 20 ps. The highest impact was observed for the He_α line at 1 ps pulse length, which was increased by a factor of 13, closely followed by the Ly_α line, which was 12 times stronger with microstructured targets. Another target type tested during the campaign were shield targets that had a plastic foil attached to the silicon target at a 45° angle, thereby forming a cavity. This target type further increased the emission without any significant difference between flat and microstructured silicon surfaces. However, these targets also increased the length of the produced X-ray pulse due to an afterglow. For applications requiring high intensity, short X-ray pulses, the presented microstructures are well suited, as they increase the signal intensity without broadening the pulse length.

The conducted PIC simulations helped to identify key parameters leading to the enhanced performance of the microspike targets. For one thing, the sloped surfaces increase the surface area and thus the number of electrons interacting with the laser. In addition, they promote Brunel heating, which compensates the decrease of effective laser intensity on the enlarged target surface. Furthermore, the pointed troughs

between the spikes trap both laser light and plasma, which increases the interaction volume and time. In contrast to parallel structures, such as wires or micropillars, the gaps between the microspikes become wider toward the front, which delays a plasma shut-off that prevents the laser from further interacting with the main target volume. To add to that, the microstructures suppress directly back-reflected laser light, both by increasing the absorption and by widely scattering the remaining light. This is a desirable target property to reduce the risk of damaging the laser optics or diagnostics in the reflected beam path. The importance of the findings in light of recent studies is discussed in Chapter 5.3 in detail.

Building on these results, further experiments with more statistics should be conducted. The wide parameter space covered during this thesis was vital to identify guiding trends, however, it also lead to relatively low statistics due to the limited shot rates of 1 shot per 90 min (PHELIX) and 1 per 45 min (Omega EP). One focus of extended experiments should be on optimizing the microstructure geometry for a specific laser system, as the simulations performed during this thesis showed that this aspect is crucial to further enhance ion acceleration. Furthermore, experiments with a high resolution XRS would give insights into the production of hollow ions and their complex atomic structure in high contrast experiments. As suggested by Martynenko et al. (2021), this could even be applied to diagnose the laser pulse itself. Also, during this thesis, proof-of-principle experiments with microstructured targets made out of pure deuterated plastic for neutron production were conducted. Expanding this investigation holds the potential to enhance laser-based neutron sources as well.

So far, the pre-plasma scale length, which profoundly influences the laser matter interaction, was neglected in the simulations, since its properties strongly depend on the laser pulse profile and the target parameters. Here, it would be interesting to perform a series of simulations with different pre-plasma scale lengths to optimize the target properties. Ideally, the pre-plasma conditions would be determined by suitable simulations, e.g., with radiation hydrodynamic codes, to better match the experimental conditions. Another option to further expand the insights of this thesis would be a simulation series with particle tracking to study the electron motion during the heating processes, and as a result achieve a better understanding of the actual heating mechanisms involved. With this knowledge, it might be possible to derive general scaling relations for the optimal target parameters and tailor the hot electron spectrum to the desired subsequent processes.

Based on the developed target fabrication procedures, it is straightforward to extend the range of materials from which the targets can be produced. In particular, the electroplating step can be easily performed with other materials such as silver, nickel or gold, which is of interest for laser-based X-ray sources. Mixing nano-powders of the desired material into the base material used during the molding procedure would further broaden the range of available materials. The flexible PDMS molds might also be used to add microstructures to other target geometries such as hemispheres, thereby allowing other experimental configurations to profit from the enhanced laser target coupling. Moreover, the molds can be used for comprehensive characterization, since the replicas can be measured destructively. One option would be slicing the replica, image each layer and create a genuine 3D model of the target, which could be used, for example, as input parameter in simulations. Furthermore, it is crucial to efficiently fabricate large quantities of targets to advance the current laser based secondary sources to industrial standards. Using the same mold to produce multiple targets can considerably expedite the fabrication process. Another way to increase the manufacturing efficiency is to create larger samples and subsequently cut them to the required target shape. In high-repetition rate experiments with shot rates in the Hz range, another challenge of solid state targets that are built beforehand, off site is the pre-shot alignment. Although the field of robotics for target alignment advances rapidly, creating the targets in-situ would be advantageous. For this, the discussed method of ultrafast laser pulse processing is a prime candidate as, e.g., structuring with multi-kHz systems in a vacuum environment is a viable option to create the desired microstructures.

In conclusion, the thesis at hand presents process chains to create spike-like microstructures based on ultrashort laser pulse processing and molding. The microstructured targets created out of the processed samples were studied using both experiments and PIC simulations, and their impact on laser matter coupling was investigated. The front surface modifications significantly enhanced the X-ray emission and proton acceleration, and the simulations showed that optimizing the microstructure shape and size for the employed high energy laser systems can further improve the yields. The presented results emphasize both the current value and the outstanding potential of target front surface modifications for high-performance laser based secondary sources.

Bibliography

K. M. T. Ahmmed, E. J. Y. Ling, P. Servio, and A.-M. Kietzig. Introducing a new optimization tool for femtosecond laser-induced surface texturing on titanium, stainless steel, aluminum and copper. *Optics and Lasers in Engineering*, 66:258–268, 2015. doi: 10.1016/j.optlaseng.2014.09.017.

A. Alejo, S. Kar, H. Ahmed, A. G. Krygier, D. Doria, R. Clarke, J. Fernandez, R. R. Freeman, J. Fuchs, A. Green, J. S. Green, D. Jung, A. Kleinschmidt, C. L. S. Lewis, J. T. Morrison, Z. Najmudin, H. Nakamura, G. Nersisyan, P. Norreys, M. Notley, M. Oliver, M. Roth, J. A. Ruiz, L. Vassura, M. Zepf, and M. Borghesi. Characterisation of deuterium spectra from laser driven multi-species sources by employing differentially filtered image plate detectors in Thomson spectrometers. *Review of Scientific Instruments*, 85(9):093303, 2014. doi: 10.1063/1.4893780.

A. Alejo, S. Kar, A. Tebartz, H. Ahmed, S. Astbury, D. C. Carroll, J. Ding, D. Doria, A. Higginson, P. McKenna, N. W. Neumann, G. G. Scott, F. Wagner, M. Roth, and M. Borghesi. High resolution Thomson Parabola Spectrometer for full spectral capture of multi-species ion beams. *Review of Scientific Instruments*, 87(8):083304, 2016. doi: 10.1063/1.4961028.

A. Andreev, N. Kumar, K. Platonov, and A. Pukhov. Efficient generation of fast ions from surface modulated nanostructure targets irradiated by high intensity short-pulse lasers. *Physics of Plasmas*, 18(10):103103, 2011. doi: 10.1063/1.3641965.

T. Arber, K. Bennett, and T. Goffrey. Github - warwick-plasma/epoch: Particle-in-cell code for plasma physics simulations, 2021. URL `https://github.com/Warwick-Plasma/epoch`. date of access: 2021/03/31.

T. D. Arber, K. Bennett, C. S. Brady, A. Lawrence-Douglas, M. G. Ramsay, N. J. Sircombe, P. Gillies, R. G. Evans, H. Schmitz, A. R. Bell, and C. P. Ridgers. Contemporary particle-in-cell approach to laser-plasma modelling. *Plasma Physics and Controlled Fusion*, 57(11):113001, 2015. doi: 10.1088/0741-3335/57/11/113001.

V. Arora, P. A. Naik, U. Chakravarty, H. Singhal, B. S. Rao, J. A. Chakera, M. P. Singh, and P. D. Gupta. A comparative study of the inner-shell and the ionic line radiation from ultra-short laser-produced magnesium plasma. *Physica Scripta*, 89(11):115601, 2014. doi: 10.1088/0031-8949/89/11/115601.

Ashland Advanced Materials. GAFCHROMIC™ Dosimetry Media, Type EBT-3, 2021a. URL `http://www.gafchromic.com/documents/EBT3_Specifications.pdf`. date of access: 2021/01/19.

Ashland Advanced Materials. GAFCHROMIC™ Dosimetry Media, Type HD-V2, 2021b. URL `http://www.gafchromic.com/documents/gafchromic-hdv2.pdf`. date of access: 2021/01/19.

V. Bagnoud and F. Wagner. Ultrahigh temporal contrast performance of the PHELIX petawatt facility. *High Power Laser Science and Engineering*, 4:e39, 2016. doi: 10.1017/hpl.2016.38.

V. Bagnoud, B. Aurand, A. Blazevic, S. Borneis, C. Bruske, B. Ecker, U. Eisenbarth, J. Fils, A. Frank, E. Gaul, S. Goette, C. Haefner, T. Hahn, K. Harres, H.-M. Heuck, D. Hochhaus, D. H. H. Hoffmann, D. Javorková, H.-J. Kluge, T. Kuehl, S. Kunzer, M. Kreutz, T. Merz-Mantwill, P. Neumayer, E. Onkels, D. Reemts, O. Rosmej, M. Roth, T. Stoehlker, A. Tauschwitz, B. Zielbauer, D. Zimmer, and K. Witte. Commissioning and early experiments of the PHELIX facility. *Applied Physics B*, 100(1):137–150, 2010. doi: 10.1007/s00340-009-3855-7.

V. Bagnoud, J. Hornung, T. Schlegel, B. Zielbauer, C. Brabetz, M. Roth, P. Hilz, M. Haug, J. Schreiber, and F. Wagner. Studying the dynamics of relativistic laser-plasma interaction on thin foils by means of Fourier-transform spectral interferometry. *Physical Review Letters*, 118(25):255003, 2017. doi: 10.1103/PhysRevLett.118.255003.

M. Bailly-Grandvaux, D. Kawahito, C. McGuffey, J. Strehlow, B. Edghill, M. S. Wei, N. Alexander, A. Haid, C. Brabetz, V. Bagnoud, R. Hollinger, M. G. Capeluto, J. J. Rocca, and F. N. Beg. Ion acceleration from microstructured targets irradiated by high-intensity picosecond laser pulses. *Physical Review E*, 102 (2):021201, 2020. doi: 10.1103/PhysRevE.102.021201.

F. N. Beg, A. R. Bell, A. E. Dangor, C. N. Danson, A. P. Fews, M. E. Glinsky, B. A. Hammel, P. Lee, P. A. Norreys, and M. Tatarakis. A study of picosecond laser–solid interactions up to $1\times10^{19}\,\mathrm{W\,cm^{-2}}$. *Physics of Plasmas*, 4(2):447–457, 1997. doi: 10.1063/1.872103.

K. Bennett, C. Brady, H. Schmitz, C. Ridgers, T. Arber, R. Evans, and T. Bell. EPOCH - University of Warwick - Users Manual for the EPOCH PIC codes, 2019. Version 4.17.0.

M. Birnbaum. Semiconductor surface damage produced by ruby lasers. *Journal of Applied Physics*, 36 (11):3688–3689, 1965. doi: 10.1063/1.1703071.

M. Blanco, M. T. Flores-Arias, C. Ruiz, and M. Vranic. Table-top laser-based proton acceleration in nanostructured targets. *New Journal of Physics*, 19(3):033004, 2017. doi: 10.1088/1367-2630/aa5f7e.

M. Blanco, M. T. Flores-Arias, and M. Vranic. Suitability and robustness of triangular nanostructured targets for proton acceleration. *arXiv preprint*, 2019. arXiv:1902.05641, URL `https://arxiv.org/abs/1902.05641`.

T. Bonnet, M. Comet, D. Denis-Petit, F. Gobet, F. Hannachi, M. Tarisien, M. Versteegen, and M. M. Aléonard. Response functions of Fuji imaging plates to monoenergetic protons in the energy range 0.6–3.2 MeV. *Review of Scientific Instruments*, 84(1):013508, 2013. doi: 10.1063/1.4775719.

J. Bonse and S. Gräf. Maxwell meets Marangoni—a review of theories on laser-induced periodic surface structures. *Laser & Photonics Reviews*, 14(10):2000215, 2020. doi: 10.1002/lpor.202000215.

J. Bonse, S. Baudach, J. Krüger, W. Kautek, and M. Lenzner. Femtosecond laser ablation of silicon–modification thresholds and morphology. *Applied Physics A*, 74(1):19–25, 2002. doi: 10.1007/s003390100893.

J. Bonse, J. Krüger, S. Höhm, and A. Rosenfeld. Femtosecond laser-induced periodic surface structures. *Journal of Laser Applications*, 24(4):042006, 2012. doi: 10.2351/1.4712658.

M. Borghesi. Laser-driven ion acceleration: State of the art and emerging mechanisms. *Nuclear Instruments and Methods in Physics Research Section A*, 740:6–9, 2014. doi: 10.1016/j.nima.2013.11.098.

M. Borghesi, A. Schiavi, D. H. Campbell, M. G. Haines, O. Willi, A. J. MacKinnon, L. A. Gizzi, M. Galimberti, R. J. Clarke, and H. Ruhl. Proton imaging: a diagnostic for inertial confinement fusion/fast ignitor studies. *Plasma Physics and Controlled Fusion*, 43(12A):A267–A276, 2001. doi: 10.1088/0741-3335/43/12a/320.

V. Bouffetier, L. Ceurvorst, M. P. Valdivia, F. Dorchies, S. Hulin, T. Goudal, D. Stutman, and A. Casner. Proof-of-concept Talbot–Lau x-ray interferometry with a high-intensity, high-repetition-rate, laser-driven K-alpha source. *Applied Optics*, 59(27):8380–8387, 2020. doi: 10.1364/AO.398839.

G. Boutoux, N. Rabhi, D. Batani, A. Binet, J.-E. Ducret, K. Jakubowska, J.-P. Nègre, C. Reverdin, and I. Thfoin. Study of imaging plate detector sensitivity to 5-18 MeV electrons. *Review of Scientific Instruments*, 86(11):113304, 2015. doi: 10.1063/1.4936141.

C. Brabetz. *Development of specially shaped laser beams for the optimized acceleration of particles*. PhD thesis, Johann Wolfgang Goethe-Universität Frankfurt am Main, 2014. URL `http://nbn-resolving.de/urn/resolver.pl?urn:nbn:de:hebis:30:3-355087`.

F. Brunel. Not-so-resonant, resonant absorption. *Physical Review Letters*, 59(1):52–55, 1987. doi: 10.1103/PhysRevLett.59.52.

C. T. Chantler. X-ray diffraction of bent crystals in Bragg geometry. I. Perfect-crystal modelling. *Journal of Applied Crystallography*, 25(6):674–693, 1992. doi: 10.1107/S0021889892005053.

F. F. Chen. *Introduction to Plasma Physics and Controlled Fusion*. Springer International Publishing Switzerland, 3rd edition edition, 2016. doi: 10.1007/978-3-319-22309-4.

H. Chen, B. Soom, B. Yaakobi, S. Uchida, and D. D. Meyerhofer. Hot-electron characterization from Kα measurements in high-contrast, p-polarized, picosecond laser-plasma interactions. *Physical Review Letters*, 70(22):3431–3434, 1993. doi: 10.1103/PhysRevLett.70.3431.

ChiantiWeb. The CHIANTI atomic database, 2021. URL `http://www.chiantidatabase.org/`. date of access: 2021/03/09.

H. Childs, E. Brugger, B. Whitlock, J. Meredith, S. Ahern, D. Pugmire, K. Biagas, M. Miller, C. Harrison, G. H. Weber, H. Krishnan, T. Fogal, A. Sanderson, C. Garth, E. W. Bethel, D. Camp, O. Rübel, M. Durant, J. M. Favre, and P. Navrátil. VisIt: An end-user tool for visualizing and analyzing very large data. In E. W. Bethel, H. Childs, and C. Hansen, editors, *High Performance Visualization–Enabling Extreme-Scale Scientific Insight*, pages 357–372. CRC Press, 2012. URL `https://visit-dav.github.io/visit-website/`.

L. Chopineau, A. Leblanc, G. Blaclard, A. Denoeud, M. Thévenet, J.-L. Vay, G. Bonnaud, P. Martin, H. Vincenti, and F. Quéré. Identification of coupling mechanisms between ultraintense laser light and dense plasmas. *Physical Review X*, 9(1):011050, 2019. doi: 10.1103/PhysRevX.9.011050.

H.-K. Chung, M. Chen, W. Morgan, Y. Ralchenko, and R. Lee. FLYCHK: Generalized population kinetics and spectral model for rapid spectroscopic analysis for all elements. *High Energy Density Physics*, 1 (1):3–12, 2005. doi: 10.1016/j.hedp.2005.07.001.

G. Cristoforetti, P. Londrillo, P. K. Singh, F. Baffigi, G. D'Arrigo, A. D. Lad, R. G. Milazzo, A. Adak, M. Shaikh, D. Sarkar, G. Chatterjee, J. Jha, M. Krishnamurthy, G. R. Kumar, and L. A. Gizzi. Transition from coherent to stochastic electron heating in ultrashort relativistic laser interaction with structured targets. *Scientific Reports*, 7(1):1–8, 2017. doi: 10.1038/s41598-017-01677-5.

C. H. Crouch, J. E. Carey, M. Shen, E. Mazur, and F. Y. Génin. Infrared absorption by sulfur-doped silicon formed by femtosecond laser irradiation. *Applied Physics A*, 79(7):1635–1641, 2004a. doi: 10.1007/s00339-004-2676-0.

C. H. Crouch, J. E. Carey, J. M. Warrender, M. J. Aziz, E. Mazur, and F. Y. Génin. Comparison of structure and properties of femtosecond and nanosecond laser-structured silicon. *Applied Physics Letters*, 84 (11):1850–1852, 2004b. doi: 10.1063/1.1667004.

H. Daido, M. Nishiuchi, and A. S. Pirozhkov. Review of laser-driven ion sources and their applications. *Reports on Progress in Physics*, 75(5):056401, 2012. doi: 10.1088/0034-4885/75/5/056401.

C. N. Danson, C. Haefner, J. Bromage, T. Butcher, J.-C. F. Chanteloup, E. A. Chowdhury, A. Galvanauskas, L. A. Gizzi, J. Hein, D. I. Hillier, N. W. Hopps, Y. Kato, E. A. Khazanov, R. Kodama, G. Korn, R. Li, L. Y., J. Limpert, J. Ma, C. H. Nam, D. Neely, D. Papadopoulos, R. R. Penman, L. Qian, J. J. Rocca, A. A. Shaykin, C. W. Siders, C. Spindloe, S. Szatmári, R. M. G. M. Trines, J. Zhu, P. Zhu, and J. D. Zuegel. Petawatt and exawatt class lasers worldwide. *High Power Laser Science and Engineering*, 7:e54, 2019. doi: 10.1017/hpl.2019.36.

W. Demtröder. *Experimentalphysik 3 - Atome, Moleküle und Festkörper*. Springer, Berlin, Heidelberg, 4th edition, 2010. doi: 10.1007/978-3-642-03911-9.

W. Demtröder. *Experimentalphysik 4 - Kern-, Teilchen und Astrophysik*. Springer Spektrum, 5th edition, 2017. doi: 10.1007/978-3-662-52884-6.

K. P. Dere, E. Landi, H. E. Mason, B. C. Monsignori Fossi, and P. R. Young. CHIANTI - an atomic database for emission lines* - I. Wavelengths greater than 50 Å. *Astronomy and Astrophysics Supplement Series*, 125(1):149–173, 1997. doi: 10.1051/aas:1997368.

F. Di Niso, C. Gaudiuso, T. Sibillano, F. Mezzapesa, A. Ancona, and P. Lugarà. Influence of the repetition rate and pulse duration on the incubation effect in multiple-shots ultrafast laser ablation of steel. *Physics Procedia*, 41:698–707, 2013. doi: 10.1016/j.phpro.2013.03.136.

B. Dromey, S. Kar, M. Zepf, and P. Foster. The plasma mirror — A subpicosecond optical switch for ultra-high power lasers. *Review of Scientific Instruments*, 75(3):645–649, 2004. doi: 10.1063/1.1646737.

T. Ebert. Homogeneous surface structuring of silicon with ultashort laser pulses. Master's thesis, Technische Universität Darmstadt, 2017.

T. Ebert, N. W. Neumann, T. Abel, G. Schaumann, and M. Roth. Laser-induced microstructures on silicon for laser-driven acceleration experiments. *High Power Laser Science and Engineering*, 5:e13, 2017. doi: 10.1017/hpl.2017.13.

T. Ebert, N. W. Neumann, L. N. K. Döhl, J. Jarrett, C. Baird, R. Heathcote, M. Hesse, A. Hughes, P. McKenna, D. Neely, D. Rusby, G. Schaumann, C. Spindloe, A. Tebartz, N. Woolsey, and M. Roth. Enhanced brightness of a laser-driven x-ray and particle source by microstructured surfaces of silicon targets. *Physics of Plasmas*, 27(4):043106, 2020. doi: 10.1063/1.5125775.

T. Ebert, R. Heber, T. Abel, J. Bieker, G. Schaumann, and M. Roth. Targets with cone-shaped microstructures from various materials for enhanced high-intensity laser–matter interaction. *High Power Laser Science and Engineering*, 9:e24, 2021. doi: 10.1017/hpl.2021.10.

S. Eliezer. *The Interaction of High-Power Lasers with Plasmas*. IOP Publishing Ltd, CRC Press, 2002.

E. Esarey, P. Sprangle, and J. Krall. Laser acceleration of electrons in vacuum. *Physical Review E*, 52(5): 5443–5453, 1995. doi: 10.1103/PhysRevE.52.5443.

J. Friend and L. Yeo. Fabrication of microfluidic devices using polydimethylsiloxane. *Biomicrofluidics*, 4 (2):026502, 2010. doi: 10.1063/1.3259624.

J. Fuchs, P. Antici, E. d'Humières, E. Lefebvre, M. Borghesi, E. Brambrink, C. A. Cecchetti, M. Kaluza, V. Malka, M. Manclossi, S. Meyroneinc, P. Mora, J. Schreiber, T. Toncian, H. Pèpin, and P. Audebert. Laser-driven proton scaling laws and new paths towards energy increase. *Nature Physics*, 2(1):48–54, 2006. doi: 10.1038/nphys199.

J. Fuchs, Y. Sentoku, E. d'Humières, T. E. Cowan, J. Cobble, P. Audebert, A. Kemp, A. Nikroo, P. Antici, E. Brambrink, A. Blazevic, E. M. Campbell, J. C. Fernández, J.-C. Gauthier, M. Geissel, M. Hegelich, S. Karsch, H. Popescu, N. Renard-LeGalloudec, M. Roth, J. Schreiber, R. Stephens, and H. Pépin. Comparative spectra and efficiencies of ions laser-accelerated forward from the front and rear surfaces of thin solid foils. *Physics of Plasmas*, 14(5):053105, 2007. doi: 10.1063/1.2720373.

E. G. Gamaly and A. V. Rode. Physics of ultra-short laser interaction with matter: From phonon excitation to ultimate transformations. *Progress in Quantum Electronics*, 37(5):215–323, 2013. doi: 10.1016/j.pquantelec.2013.05.001.

GE Healthcare Life Sciences. Typhoon™ FLA 7000 and 7000 IP biomolecular imager, 2021. URL `https://cdn.cytivalifesciences.com/dmm3bwsv3/AssetStream.aspx?mediaformatid=10061&destinationid=10016&assetid=15539`. Data file 28-9610-73 AC, date of access: 2021/01/11.

P. Gibbon. *Short Pulse Laser Interactions with Matter*. Imperial College Press, 2005. doi: 10.1142/p116.

M. A. Gigosos. Stark broadening models for plasma diagnostics. *Journal of Physics D: Applied Physics*, 47(34):343001, 2014. doi: 10.1088/0022-3727/47/34/343001.

S. H. Glenzer and R. Redmer. X-ray Thomson scattering in high energy density plasmas. *Reviews of Modern Physics*, 81(4):1625–1663, 2009. doi: 10.1103/RevModPhys.81.1625.

S. J. Grimm. Modelling target front structures for enhanced laser-particle acceleration. Bachelor's thesis, Technische Universität Darmstadt, 2020.

E. Gullikson. Filter transmission, 2021. URL `https://henke.lbl.gov/optical_constants/filter2.html`. The Center for X-Ray Optics, date of access: 2021/01/07.

S. P. Hatchett, C. G. Brown, T. E. Cowan, E. A. Henry, J. S. Johnson, M. H. Key, J. A. Koch, A. B. Langdon, B. F. Lasinski, R. W. Lee, A. J. Mackinnon, D. M. Pennington, M. D. Perry, T. W. Phillips, M. Roth, T. C. Sangster, M. S. Singh, R. A. Snavely, M. A. Stoyer, S. C. Wilks, and K. Yasuike. Electron, photon, and ion beams from the relativistic interaction of petawatt laser pulses with solid targets. *Physics of Plasmas*, 7(5):2076–2082, 2000. doi: 10.1063/1.874030.

R. Heber. Target fabrication for laser ion acceleration by micro molding. Master's thesis, Technische Universität Darmstadt, 2019.

B. L. Henke, E. M. Gullikson, and J. C. Davis. X-ray interactions: photoabsorption, scattering, transmission and reflection E = 50–30,000 eV, Z = 1–92. *Atomic Data and Nuclear Data Tables*, 54(2):181–342, 1993. doi: 10.1006/adnd.1993.1013.

T.-H. Her, R. J. Finlay, C. Wu, S. Deliwala, and E. Mazur. Microstructuring of silicon with femtosecond laser pulses. *Applied Physics Letters*, 73(12):1673–1675, 1998. doi: 10.1063/1.122241.

T.-H. Her, R. J. Finlay, C. Wu, and E. Mazur. Femtosecond laser-induced formation of spikes on silicon. *Applied Physics A*, 70(4):383–385, 2000. doi: 10.1007/s003390051052.

G. Hölzer, O. Wehrhan, and E. Förster. Characterization of flat and bent crystals for x-ray spectroscopy and imaging. *Crystal Research and Technology: Journal of Experimental and Industrial Crystallography*, 33(4):555–567, 1998. doi: 10.1002/(SICI)1521-4079(1998)33:4<555::AID-CRAT555>3.0.CO;2-Q.

G. Hoffmeister. *Influencing laser-accelerated ions by femtosecond-laser desorption*. PhD thesis, Technische Universität Darmstadt, 2014. URL `https://tuprints.ulb.tu-darmstadt.de/id/eprint/4113`.

R. Hollinger, C. Bargsten, V. N. Shlyaptsev, V. Kaymak, A. Pukhov, M. G. Capeluto, S. Wang, A. Rockwood, Y. Wang, A. Townsend, A. Prieto, P. Stockton, A. Curtis, and J. J. Rocca. Efficient picosecond x-ray pulse generation from plasmas in the radiation dominated regime. *Optica*, 4(11):1344–1349, 2017. doi: 10.1364/OPTICA.4.001344.

J. Hornung, Y. Zobus, P. Boller, C. Brabetz, U. Eisenbarth, T. Kühl, Z. Major, J. B. Ohland, M. Zepf, B. Zielbauer, and V. Bagnoud. Enhancement of the laser-driven proton source at PHELIX. *High Power Laser Science and Engineering*, 8:e24, 2020. doi: 10.1017/hpl.2020.23.

G.-Y. Hu, J.-Y. Zhang, J. Zheng, B.-F. Shen, S.-Y. Liu, J.-M. Yang, Y.-K. Ding, X. Hu, Y.-X. Huang, H.-B. Du, R.-Q. Yi, A.-L. Lei, and Z.-Z. Xu. Angular distribution and conversion of multi-keV L-shell x-ray sources produced from nanosecond laser irradiated thick-foil targets. *Laser and Particle Beams*, 26(4): 661–670, 2008. doi: 10.1017/S0263034608000682.

F. Hua, Y. Sun, A. Gaur, M. A. Meitl, L. Bilhaut, L. Rotkina, J. Wang, P. Geil, M. Shim, J. A. Rogers, and A. Shim. Polymer imprint lithography with molecular-scale resolution. *Nano Letters*, 4(12): 2467–2471, 2004. doi: 10.1021/nl048355u.

J. Jarrett, M. King, R. J. Gray, N. W. Neumann, L. Döhl, C. D. Baird, T. Ebert, M. Hesse, A. Tebartz, D. R. Rusby, N. C. Woolsey, D. Neely, M. Roth, and P. McKenna. Reflection of intense laser light from microstructured targets as a potential diagnostic of laser focus and plasma temperature. *High Power Laser Science and Engineering*, 7:e2, 2019. doi: 10.1017/hpl.2018.63.

L. L. Ji, J. Snyder, A. Pukhov, R. R. Freeman, and K. U. Akli. Towards manipulating relativistic laser pulses with micro-tube plasma lenses. *Scientific Reports*, 6(1):1–7, 2016. doi: 10.1038/srep23256.

L. Jiang, Q.-S. Huang, I. V. Kozhevnikov, Y.-Y. Yao, J.-T. Feng, Y.-F. Feng, B. Ma, H.-F. Jiao, H. Chen, Z. Zhang, and Z.-S. Wang. Investigation of natural contamination layer growth on optical substrates. *Chinese Physics C*, 42(11):115001, 2018. doi: 10.1088/1674-1137/42/11/115001.

S. Jiang, A. G. Krygier, D. W. Schumacher, K. U. Akli, and R. R. Freeman. Effects of front-surface target structures on properties of relativistic laser-plasma electrons. *Physical Review E*, 89(1):013106, 2014a. doi: 10.1103/PhysRevE.89.013106.

S. Jiang, A. G. Krygier, D. W. Schumacher, K. U. Akli, and R. R. Freeman. Enhancing bremsstrahlung production from ultraintense laser-solid interactions with front surface structures. *The European Physical Journal D*, 68(10):1–8, 2014b. doi: 10.1140/epjd/e2014-50339-4.

D. Jung, B. J. Albright, L. Yin, D. C. Gautier, R. Shah, S. Palaniyappan, S. Letzring, B. Dromey, H.-C. Wu, T. Shimada, R. P. Johnson, M. Roth, J. C. Fernandez, D. Habs, and B. M. Hegelich. Beam profiles of proton and carbon ions in the relativistic transparency regime. *New Journal of Physics*, 15(12): 123035, 2013. doi: 10.1088/1367-2630/15/12/123035.

F. Jüttner. Das Maxwellsche Gesetz der Geschwindigkeitsverteilung in der Relativtheorie. *Annalen der Physik*, 339(5):856–882, 1911. doi: 10.1002/andp.19113390503.

M. Kaluza, J. Schreiber, M. I. K. Santala, G. D. Tsakiris, K. Eidmann, J. Meyer-ter Vehn, and K. J. Witte. Influence of the laser prepulse on proton acceleration in thin-foil experiments. *Physical Review Letters*, 93(4):045003, 2004. doi: 10.1103/PhysRevLett.93.045003.

O. Klimo, J. Psikal, J. Limpouch, J. Proska, F. Novotny, T. Ceccotti, V. Floquet, and S. Kawata. Short pulse laser interaction with micro-structured targets: simulations of laser absorption and ion acceleration. *New Journal of Physics*, 13(5):053028, 2011. doi: 10.1088/1367-2630/13/5/053028.

T. Kluge, T. Cowan, A. Debus, U. Schramm, K. Zeil, and M. Bussmann. Electron temperature scaling in laser interaction with solids. *Physical Review Letters*, 107(20):205003, 2011. doi: 10.1103/PhysRevLett.107.205003.

A. Kramida, Y. Ralchenko, J. Reader, and N. A. Team. NIST Atomic Spectra Database (version 5.8), 2021. URL `https://physics.nist.gov/asd`. date of access: 2021/04/23.

G. Kulcsár, D. AlMawlawi, F. W. Budnik, P. R. Herman, M. Moskovits, L. Zhao, and R. S. Marjoribanks. Intense picosecond x-ray pulses from laser plasmas by use of nanostructured "velvet" targets. *Physical Review Letters*, 84(22):5149–5152, 2000. doi: 10.1103/PhysRevLett.84.5149.

E. Landi, G. Del Zanna, P. R. Young, K. P. Dere, and H. E. Mason. CHIANTI - An atomic database for emission lines. XII. Version 7 of the database. *The Astrophysical Journal*, 744(2):99, 2011. doi: 10.1088/0004-637X/744/2/99.

Laser Components. Thin film polarizers - high power polarizers, 2021. URL `https://www.lasercomponents.com/de-en/product/thin-film-polarizers/`. date of access: 2021/09/02.

T. Liseykina, P. Mulser, and M. Murakami. Collisionless absorption, hot electron generation, and energy scaling in intense laser-target interaction. *Physics of Plasmas*, 22(3):033302, 2015. doi: 10.1063/1.4914837.

X. Liu, P. R. Coxon, M. Peters, B. Hoex, J. M. Cole, and D. J. Fray. Black silicon: fabrication methods, properties and solar energy applications. *Energy & Environmental Science*, 7(10):3223–3263, 2014. doi: 10.1039/C4EE01152J.

X. Llovet, C. J. Powell, F. Salvat, and A. Jablonski. Cross sections for inner-shell ionization by electron impact. *Journal of Physical and Chemical Reference Data*, 43(1):013102, 2014. doi: 10.1063/1.4832851.

A. Macchi, M. Borghesi, and M. Passoni. Ion acceleration by superintense laser-plasma interaction. *Reviews of Modern Physics*, 85(2):751–793, 2013. doi: 10.1103/RevModPhys.85.751.

A. Mančić, J. Fuchs, P. Antici, S. A. Gaillard, and P. Audebert. Absolute calibration of photostimulable image plate detectors used as (0.5–20 MeV) high-energy proton detectors. *Review of Scientific Instruments*, 79(7):073301, 2008. doi: 10.1063/1.2949388.

P. Mannion, J. Magee, E. Coyne, G. O'Connor, and T. Glynn. The effect of damage accumulation behaviour on ablation thresholds and damage morphology in ultrafast laser micro-machining of common metals in air. *Applied Surface Science*, 233(1):275–287, 2004. doi: 10.1016/j.apsusc.2004.03.229.

S. Maragkaki, T. J.-Y. Derrien, Y. Levy, N. M. Bulgakova, A. Ostendorf, and E. L. Gurevich. Wavelength dependence of picosecond laser-induced periodic surface structures on copper. *Applied Surface Science*, 417:88–92, 2017. doi: 10.1016/j.apsusc.2017.02.068.

D. Margarone, O. Klimo, I. J. Kim, J. Prokůpek, J. Limpouch, T. M. Jeong, T. Mocek, J. Pšikal, H. T. Kim, J. Proška, K. H. Nam, L. Štolcová, I. W. Choi, S. K. Lee, J. H. Sung, T. J. Yu, and G. Korn. Laser-driven proton acceleration enhancement by nanostructured foils. *Physical Review Letters*, 109(23):234801, 2012. doi: 10.1103/PhysRevLett.109.234801.

A. S. Martynenko, I. Y. Skobelev, S. A. Pikuz, S. N. Ryazantsev, C. Baird, N. Booth, L. Doehl, P. Durey, D. Farley, R. Kodama, K. Lancaster, P. McKenna, C. Murphy, C. Spindloe, T. A. Pikuz, and N. Woolsey. Determining the short laser pulse contrast based on x-ray emission spectroscopy. *High Energy Density Physics*, 38:100924, 2021. doi: 10.1016/j.hedp.2021.100924.

Materialwissenschaft, Technische Universität Darmstadt. HREM – Advanced Thin Film Technology, 2021. URL https://www.mawi.tu-darmstadt.de/kompetenzzentrum/kompetenzzentrum_details_1536.de.jsp. date of access: 2021/09/02.

P. McKenna, D. C. Carroll, O. Lundh, F. Nürnberg, K. Markey, S. Bandyopadhyay, D. Batani, R. G. Evans, R. Jafer, S. Kar, D. Neely, D. Pepler, M. N. Quinn, R. Redaelli, M. Roth, C.-G. Wahlström, X. H. Yuan, and M. Zepf. Effects of front surface plasma expansion on proton acceleration in ultraintense laser irradiation of foil targets. *Laser and Particle Beams*, 26(4):591–596, 2008. doi: 10.1017/S0263034608000657.

P. McKenna, D. Neely, R. Bingham, and D. Jaroszynski (*Editors*). *Laser-Plasma Interactions and Applications*. Springer, Heidelberg, 2013. doi: 10.1007/978-3-319-00038-1. Scottish Graduate Series.

W. McLaughlin, C. Yun-Dong, C. G. Soares, A. Miller, G. Van Dyk, and D. F. Lewis. Sensitometry of the response of a new radiochromic film dosimeter to gamma radiation and electron beams. *Nuclear Instruments and Methods in Physics Research Section A: Accelerators, Spectrometers, Detectors and Associated Equipment*, 302(1):165–176, 1991. doi: 10.1016/0168-9002(91)90506-L.

A. L. Meadowcroft, C. D. Bentley, and E. N. Stott. Evaluation of the sensitivity and fading characteristics of an image plate system for x-ray diagnostics. *Review of Scientific Instruments*, 79(11):113102, 2008. doi: 10.1063/1.3013123.

A. Micke and D. Lewis. State of the art film dosimetry, 2021. URL http://www.gafchromic.com/documents/Micke_Lewis_State_of_the_Art_Film_Dosimetry_Oregon_201211.pdf. Ashland Inc. - Advanced Materials, Presentation, November 2012, date of access: 2021/01/19.

P. Mora. Plasma expansion into a vacuum. *Physical Review Letters*, 90(18):185002, 2003. doi: 10.1103/PhysRevLett.90.185002.

P. Mulser and D. Bauer. *High Power Laser-Matter Interaction*. Springer, Berlin Heidelberg, 2010. doi: 10.1007/978-3-540-46065-7. Springer Tracts in Modern Physics 238.

P. Mulser, S. M. Weng, and T. Liseykina. Analysis of the Brunel model and resulting hot electron spectra. *Physics of Plasmas*, 19(4):043301, 2012. doi: 10.1063/1.3696034.

M. M. Murnane, H. C. Kapteyn, S. P. Gordon, J. Bokor, E. N. Glytsis, and R. W. Falcone. Efficient coupling of high-intensity subpicosecond laser pulses into solids. *Applied Physics Letters*, 62(10):1068–1070, 1993. doi: 10.1063/1.108797.

T. Nakamura, M. Tampo, R. Kodama, S. V. Bulanov, and M. Kando. Interaction of high contrast laser pulse with foam-attached target. *Physics of Plasmas*, 17(11):113107, 2010. doi: 10.1063/1.3507294.

B. K. Nayak and M. C. Gupta. Ultrafast laser-induced self-organized conical micro/nano surface structures and their origin. *Optics and Lasers in Engineering*, 48(10):966–973, 2010. doi: 10.1016/j.optlaseng.2010.05.009.

J. Nethercott. Capacitance measurement with the Arduino Uno | PIC Tutorials, 2021. URL https://wordpress.codewrite.co.uk/pic/2014/01/21/cap-meter-with-arduino-uno/index.html. date of access: 2021/09/02.

N. W. Neumann. *Fabrication of micro-structured surfaces with increased light absorption and their influence on intense laser-plasma experiments*. PhD thesis, Technische Universität Darmstadt, 2018. URL https://tuprints.ulb.tu-darmstadt.de/id/eprint/7480.

N. W. Neumann, T. Ebert, G. Schaumann, and M. Roth. A setup for micro-structured silicon targets by femtosecond laser irradiation. *Journal of Physics: Conference Series*, 1079(1):012011, 2018. doi: 10.1088/1742-6596/1079/1/012011.

P. Neumayer, B. Aurand, M. Basko, B. Ecker, P. Gibbon, D. C. Hochhaus, A. Karmakar, E. Kazakov, T. Kühl, C. Labaune, O. Rosmej, A. Tauschwitz, B. Zielbauer, and D. Zimmer. The role of hot electron refluxing in laser-generated K-alpha sources. *Physics of Plasmas*, 17(10):103103, 2010. doi: 10.1063/1.3486520.

J. J. Nivas, F. Gesuele, E. Allahyari, S. L. Oscurato, R. Fittipaldi, A. Vecchione, R. Bruzzese, and S. Amoruso. Effects of ambient air pressure on surface structures produced by ultrashort laser pulse irradiation. *Optics Letters*, 42(14):2710–2713, 2017. doi: 10.1364/OL.42.002710.

J. J. Nivas, K. K. Anoop, R. Bruzzese, R. Philip, and S. Amoruso. Direct femtosecond laser surface structuring of crystalline silicon at 400 nm. *Applied Physics Letters*, 112(12):121601, 2018. doi: 10.1063/1.5011134.

F. Nürnberg, M. Schollmeier, E. Brambrink, A. Blažević, D. C. Carroll, K. Flippo, D. C. Gautier, M. Geißel, K. Harres, B. M. Hegelich, O. Lundh, K. Markey, P. McKenna, D. Neely, J. Schreiber, and M. Roth. Radiochromic film imaging spectroscopy of laser-accelerated proton beams. *Review of Scientific Instruments*, 80(3):033301, 2009. doi: 10.1063/1.3086424.

H. Ohuchi and A. Yamadera. Dependence of fading patterns of photo-stimulated luminescence from imaging plates on radiation, energy, and image reader. *Nuclear Instruments and Methods in Physics Research Section A: Accelerators, Spectrometers, Detectors and Associated Equipment*, 490(3):573–582, 2002. doi: 10.1016/S0168-9002(02)01074-4.

H.-S. Park, D. M. Chambers, H.-K. Chung, R. J. Clarke, R. Eagleton, E. Giraldez, T. Goldsack, R. Heathcote, N. Izumi, M. H. Key, J. A. King, J. A. Koch, O. L. Landen, A. Nikroo, P. K. Patel, D. F. Price, B. A. Remington, H. F. Robey, R. A. Snavely, D. A. Steinman, R. B. Stephens, C. Stoeckl, M. Storm, M. Tabak, W. Theobald, R. P. J. Town, J. E. Wickersham, and B. B. Zhang. High-energy K_α radiography using high-intensity, short-pulse lasers. *Physics of Plasmas*, 13(5):056309, 2006. doi: 10.1063/1.2178775.

M. Passoni, A. Zani, A. Sgattoni, D. Dellasega, A. Macchi, I. Prencipe, V. Floquet, P. Martin, T. V. Liseykina, and T. Ceccotti. Energetic ions at moderate laser intensities using foam-based multi-layered targets. *Plasma Physics and Controlled Fusion*, 56(4):045001, 2014. doi: 10.1088/0741-3335/56/4/045001.

P. K. Patel, A. J. Mackinnon, M. H. Key, T. E. Cowan, M. E. Foord, M. Allen, D. F. Price, H. Ruhl, P. T. Springer, and R. Stephens. Isochoric heating of solid-density matter with an ultrafast proton beam. *Physical Review Letters*, 91(12):125004, 2003. doi: 10.1103/PhysRevLett.91.125004.

I. J. Paterson, R. J. Clarke, N. C. Woolsey, and G. Gregori. Image plate response for conditions relevant to laser–plasma interaction experiments. *Measurement Science and Technology*, 19(9):095301, 2008. doi: 10.1088/0957-0233/19/9/095301.

Y. Peng, Y. Zhou, X. Chen, and Y. Zhu. The fabrication and characteristic investigation of microstructured silicon with different spike heights. *Optics Communications*, 334:122–128, 2015. doi: 10.1016/j.optcom.2014.08.034.

C. Perego, A. Zani, D. Batani, and M. Passoni. Extensive comparison among target normal sheath acceleration theoretical models. *Nuclear Instruments and Methods in Physics Research Section A: Accelerators, Spectrometers, Detectors and Associated Equipment*, 653(1):89–93, 2011. doi: 10.1016/j.nima.2011.01.100.

A. Piel. *Plasma Physics*. Springer, Berlin, Heidelberg, 1st edition, 2010. doi: 10.1007/978-3-642-10491-6.

A. Pimpin and W. Srituravanich. Review on micro-and nanolithography techniques and their applications. *Engineering Journal*, 16(1):37–56, 2012. doi: 10.4186/ej.2012.16.1.37.

I. Prencipe, J. Fuchs, S. Pascarelli, D. W. Schumacher, R. B. Stephens, N. B. Alexander, R. Briggs, M. Büscher, M. O. Cernaianu, A. Choukourov, M. De Marco, A. Erbe, J. Fassbender, G. Fiquet, P. Fitzsimmons, C. Gheorghiu, J. Hund, L. G. Huang, M. Harmand, N. J. Hartley, A. Irman, T. Kluge, Z. Konopkova, S. Kraft, D. Kraus, V. Leca, D. Margarone, J. Metzkes, K. Nagai, W. Nazarov, P. Lutoslawski, D. Papp, M. Passoni, A. Pelka, J. P. Perin, J. Schulz, M. Smid, C. Spindloe, S. Steinke, R. Torchio, C. Vass, T. Wiste, R. Zaffino, K. Zeil, T. Tschentscher, U. Schramm, and T. E. Cowan. Targets for high repetition rate laser facilities: needs, challenges and perspectives. *High Power Laser Science and Engineering*, 5:e17, 2017. doi: 10.1017/hpl.2017.18.

N. Rabhi, D. Batani, G. Boutoux, J.-E. Ducret, K. Jakubowska, I. Lantuejoul-Thfoin, C. Nauraye, A. Patriarca, A. Saïd, A. Semsoum, L. Serani, B. Thomas, and B. Vauzour. Calibration of imaging plate detectors to mono-energetic protons in the range 1-200 MeV. *Review of Scientific Instruments*, 88(11): 113301, 2017. doi: 10.1063/1.5009472.

O. Renner and F. B. Rosmej. Challenges of x-ray spectroscopy in investigations of matter under extreme conditions. *Matter and Radiation at Extremes*, 4(2):024201, 2019. doi: 10.1063/1.5086344.

M. Roth and M. Schollmeier. Ion acceleration - target normal sheath acceleration. *arXiv preprint*, 2017. doi: 10.5170/CERN-2016-001.231. arXiv:1705.10569, URL `https://arxiv.org/abs/1705.10569`.

M. Roth, T. E. Cowan, M. H. Key, S. P. Hatchett, C. Brown, W. Fountain, J. Johnson, D. M. Pennington, R. A. Snavely, S. C. Wilks, K. Yasuike, H. Ruhl, F. Pegoraro, S. V. Bulanov, E. M. Campbell, M. D. Perry, and H. Powell. Fast ignition by intense laser-accelerated proton beams. *Physical Review Letters*, 86(3): 436–439, 2001. doi: 10.1103/PhysRevLett.86.436.

M. Roth, P. Audebert, A. Blazevic, E. Brambrink, J. Cobble, T. Cowan, J. Fernandez, J. Fuchs, M. Geissel, M. Hegelich, S. Karsch, H. Ruhl, M. Schollmeier, and R. Stephens. Laser accelerated heavy particles – tailoring of ion beams on a nano-scale. *Optics Communications*, 264(2):519–524, 2006. doi: 10.1016/j.optcom.2005.12.085.

M. Roth, D. Jung, K. Falk, N. Guler, O. Deppert, M. Devlin, A. Favalli, J. Fernandez, D. Gautier, M. Geissel, R. Haight, C. E. Hamilton, B. M. Hegelich, R. P. Johnson, F. Merrill, G. Schaumann, K. Schoenberg, M. Schollmeier, T. Shimada, T. Taddeucci, J. L. Tybo, F. Wagner, S. A. Wender, C. H. Wilde, and G. A. Wurden. Bright laser-driven neutron source based on the relativistic transparency of solids. *Physical Review Letters*, 110(4):044802, 2013. doi: 10.1103/PhysRevLett.110.044802.

C. Rullière. *Femtosecond Laser Pulses - Principles and Experiments*. Springer-Verlag New York, 2nd edition, 2005. doi: 10.1007/b137908.

D. Salzmann, C. Reich, I. Uschmann, E. Förster, and P. Gibbon. Theory of Kα generation by femtosecond laser-produced hot electrons in thin foils. *Physical Review E*, 65(3):036402, 2002. doi: 10.1103/PhysRevE.65.036402.

S. Sander, T. Ebert, D. Hartnagel, M. Hesse, X. Pan, G. Schaumann, M. Šmíd, K. Falk, and M. Roth. Microstructured layered targets to improve laser-induced x-ray backlighters. *Physical Review E*, 2021. *under review*.

M. Schollmeier, M. Geißel, A. B. Sefkow, and K. A. Flippo. Improved spectral data unfolding for radiochromic film imaging spectroscopy of laser-accelerated proton beams. *Review of Scientific Instruments*, 85(4):043305, 2014. doi: 10.1063/1.4870895.

M. S. Schollmeier. *Optimization and control of laser-accelerated proton beams*. PhD thesis, Technische Universität Darmstadt, 2008. URL https://tuprints.ulb.tu-darmstadt.de/id/eprint/1232.

A. Schreiber. RGB-Farbkalibrierung von radiochromatischen Filmen. Bachelor's thesis, Technische Universität Darmstadt, 2012.

N. Schroeter. Development and calibration of a high-dispersive Thomson parabola for laser-accelerated ion beams. Master's thesis, Technische Universität Darmstadt, 2017. URL http://dx.doi.org/10.15120/GSI-2020-00608.

M. V. Sedov, A. Y. Faenov, A. A. Andreev, I. Y. Skobelev, S. N. Ryazantsev, T. A. Pikuz, P. Durey, L. Doehl, D. Farley, C. Baird, K. L. Lancaster, C. D. Murphy, N. Booth, C. Spindloe, K. Y. Platonov, P. McKenna, R. Kodama, N. Woolsey, and S. A. Pikuz. Features of the generation of fast particles from microstructured targets irradiated by high intensity, picosecond laser pulses. *Laser and Particle Beams*, 37(2): 176–183, 2019. doi: 10.1017/S0263034619000351.

D. A. Serebryakov, T. M. Volkova, E. N. Nerush, and I. Y. Kostyukov. Efficient gamma-ray source from solid-state microstructures irradiated by relativistic laser pulses. *Plasma Physics and Controlled Fusion*, 61(7):074007, 2019. doi: 10.1088/1361-6587/ab209b.

M. A. Sheehy, L. Winston, J. E. Carey, C. M. Friend, and E. Mazur. Role of the background gas in the morphology and optical properties of laser-microstructured silicon. *Chemistry of Materials*, 17(14): 3582–3586, 2005. doi: 10.1021/cm049029i.

M. V. Shugaev, C. Wu, O. Armbruster, A. Naghilou, N. Brouwer, D. S. Ivanov, T. J.-Y. Derrien, N. M. Bulgakova, W. Kautek, B. Rethfeld, and L. V. Zhigilei. Fundamentals of ultrafast laser–material interaction. *MRS Bulletin*, 41(12):960–968, 2016. doi: 10.1557/mrs.2016.274.

I. Y. Skobelev, A. Y. Faenov, T. A. Pikuz, and V. E. Fortov. Spectra of hollow ions in an ultradense laser plasma. *Physics-Uspekhi*, 55(1):47, 2012. doi: 10.3367/UFNe.0182.201201c.0049.

R. A. Snavely, M. H. Key, S. P. Hatchett, T. E. Cowan, M. Roth, T. W. Phillips, M. A. Stoyer, E. A. Henry, T. C. Sangster, M. S. Singh, S. C. Wilks, A. MacKinnon, A. Offenberger, D. M. Pennington, K. Yasuike, A. B. Langdon, B. F. Lasinski, J. Johnson, M. D. Perry, and E. M. Campbell. Intense high-energy proton beams from petawatt-laser irradiation of solids. *Physical Review Letters*, 85(14):2945–2948, 2000. doi: 10.1103/PhysRevLett.85.2945.

C. Stoeckl, J. A. Delettrez, J. H. Kelly, T. J. Kessler, B. E. Kruschwitz, S. J. Loucks, R. L. McCrory, D. D. Meyerhofer, D. N. Maywar, S. F. B. Morse, J. Myatt, A. L. Rigatti, L. J. Waxer, J. D. Zuegel, and R. B. Stephens. High-energy petawatt project at the University of Rochester's Laboratory for Laser Energetics. *Fusion Science and Technology*, 49(3):367–373, 2006. doi: 10.13182/FST06-A1155.

C. Stoeckl, R. Epstein, R. Betti, W. Bittle, J. A. Delettrez, C. J. Forrest, V. Y. Glebov, V. N. Goncharov, D. R. Harding, I. V. Igumenshchev, D. W. Jacobs-Perkins, R. T. Janezic, J. H. Kelly, T. Z. Kosc, R. L. McCrory, D. T. Michel, C. Mileham, P. W. McKenty, F. J. Marshall, S. F. B. Morse, S. P. Regan, P. B. Radha, B. Rice, T. C. Sangster, M. J. Shoup, W. T. Shmayda, C. Sorce, W. Theobald, J. Ulreich, M. D. Wittman, D. D. Meyerhofer, J. A. Frenje, M. Gatu Johnson, and R. D. Petrasso. Monochromatic backlighting of direct-drive cryogenic DT implosions on OMEGA. *Physics of Plasmas*, 24(5):056304, 2017. doi: 10.1063/1.4977918.

C. Stoeckl, M. J. Bonino, C. Mileham, S. P. Regan, W. Theobald, T. Ebert, and S. Sander. Optimization of a short-pulse-driven Si He_α soft x-ray backlighter. *High Energy Density Physics*, 2021. *under review*.

R. Stoian, A. Rosenfeld, D. Ashkenasi, I. V. Hertel, N. M. Bulgakova, and E. E. B. Campbell. Surface charging and impulsive ion ejection during ultrashort pulsed laser ablation. *Physical Review Letters*, 88(9):097603, 2002. doi: 10.1103/PhysRevLett.88.097603.

D. Strickland and G. Mourou. Compression of amplified chirped optical pulses. *Optics Communications*, 55(6):447–449, 1985. doi: 10.1016/0030-4018(85)90151-8.

S. Sundaram and E. Mazur. Inducing and probing non-thermal transitions in semiconductors using femtosecond laser pulses. *Nature Materials*, 1(4):217–224, 2002. doi: 10.1038/nmat767.

TE Connectivity. Digitaler 0-2 bar-Drucksensor, 2021. URL `https://www.te.com/deu-de/product-CAT-BLPS0010.html?q=&type=products&samples=N&inStoreWithoutPL=false&instock=N&q2=02BA`. date of access: 2021/01/15.

The Dow Chemical Company. SYLGARD™ 184 Silicone Elastomer, 2021. URL `https://www.dow.com/en-us/pdp.sylgard-184-silicone-elastomer-kit.01064291z.html`. date of access: 2021/09/09.

W. Theobald, K. Akli, R. Clarke, J. A. Delettrez, R. R. Freeman, S. Glenzer, J. Green, G. Gregori, R. Heathcote, N. Izumi, J. A. King, J. A. Koch, J. Kuba, K. Lancaster, A. J. MacKinnon, M. Key, C. Mileham, J. Myatt, D. Neely, P. A. Norreys, H.-S. Park, J. Pasley, P. Patel, S. P. Regan, H. Sawada, R. Shepherd, R. Snavely, R. B. Stephens, C. Stoeckl, M. Storm, B. Zhang, and T. C. Sangster. Hot surface ionic line emission and cold K-inner shell emission from petawatt-laser-irradiated Cu foil targets. *Physics of Plasmas*, 13(4):043102, 2006. doi: 10.1063/1.2188912.

Thermo Fisher Scientific. Phenom XL Desktop SEM for automation, 2021. URL `https://www.phenom-world.com/it/desktop-scanning-electron-microscopes/phenom-xl`. date of access: 2021/01/04.

A. Thompson, D. Attwood, E. Gullikson, M. Howells, K.-J. Kim, J. Kirz, J. Kortright, I. Lindau, Y. Liu, P. Pianetta, A. Robinson, J. Scofield, J. Underwood, G. Williams, and H. Winick. *X-ray Data Booklet*. Lawrence Berkeley National Laboratory, University of California, Berkeley, 3rd edition, 2009.

J. J. Thomson. XLVII. On rays of positive electricity. *The London, Edinburgh, and Dublin Philosophical Magazine and Journal of Science*, 13(77):561–575, 1907. doi: 10.1080/14786440709463633.

D. B. Thorn, F. Coppari, T. Döppner, M. J. MacDonald, S. P. Regan, and M. B. Schneider. X-ray spectrometer throughput model for (selected) flat bragg crystal spectrometers on laser plasma facilities. *Review of Scientific Instruments*, 89(10):10F119, 2018. doi: 10.1063/1.5039423.

Tifoo Shop - Electroplating & Surface Technology. Acidic bright copper plating solution, 2021. URL `https://www.tifoo.de/en-uk/acidic-bright-copper-plating-solution`. date of access: 2021/09/02.

B. R. Tull, J. E. Carey, E. Mazur, J. P. McDonald, and S. M. Yalisove. Silicon surface morphologies after femtosecond laser irradiation. *MRS Bulletin*, 31(8):626–633, 2006. doi: 10.1557/mrs2006.160.

S. Vallières, M. Salvadori, A. Permogorov, G. Cantono, K. Svendsen, Z. Chen, S. Sun, F. Consoli, E. d'Humières, C.-G. Wahlström, and P. Antici. Enhanced laser-driven proton acceleration using nanowire targets. *Scientific Reports*, 11(1):1–11, 2021. doi: 10.1038/s41598-020-80392-0.

P. van Assenbergh, E. Meinders, J. Geraedts, and D. Dodou. Nanostructure and microstructure fabrication: From desired properties to suitable processes. *Small*, 14(20):1703401, 2018. doi: 10.1002/smll.201703401.

F. Wagner, C. P. João, J. Fils, T. Gottschall, J. Hein, J. Körner, J. Limpert, M. Roth, T. Stöhlker, and V. Bagnoud. Temporal contrast control at the PHELIX petawatt laser facility by means of tunable sub-picosecond optical parametric amplification. *Applied Physics B*, 116(2):429–435, 2014. doi: 10.1007/s00340-013-5714-9.

K. B. Wharton, C. D. Boley, A. M. Komashko, A. M. Rubenchik, J. Zweiback, J. Crane, G. Hays, T. E. Cowan, and T. Ditmire. Effects of nonionizing prepulses in high-intensity laser-solid interactions. *Physical Review E*, 64(2):025401, 2001. doi: 10.1103/PhysRevE.64.025401.

S. C. Wilks, A. B. Langdon, T. E. Cowan, M. Roth, M. Singh, S. Hatchett, M. H. Key, D. Pennington, A. MacKinnon, and R. A. Snavely. Energetic proton generation in ultra-intense laser–solid interactions. *Physics of Plasmas*, 8(2):542–549, 2001. doi: 10.1063/1.1333697.

G. J. Williams, A. Link, M. Sherlock, D. A. Alessi, M. Bowers, A. Conder, P. Di Nicola, G. Fiksel, F. Fiuza, M. Hamamoto, M. R. Hermann, S. Herriot, D. Homoelle, W. Hsing, E. d'Humières, D. Kalantar, A. Kemp, S. Kerr, J. Kim, K. N. LaFortune, J. Lawson, R. Lowe-Webb, T. Ma, D. A. Mariscal, D. Martinez, M. J.-E. Manuel, M. Nakai, L. Pelz, M. Prantil, B. Remington, R. Sigurdsson, C. Widmayer, W. Williams, L. Willingale, R. Zacharias, K. Youngblood, and H. Chen. Production of relativistic electrons at subrelativistic laser intensities. *Physical Review E*, 101(3):031201, 2020. doi: 10.1103/PhysRevE.101.031201.

K. D. Xiao, C. T. Zhou, K. Jiang, Y. C. Yang, R. Li, H. Zhang, B. Qiao, T. W. Huang, J. M. Cao, T. X. Cai, M. Y. Yu, S. C. Ruan, and X. T. He. Multidimensional effects on proton acceleration using high-power intense laser pulses. *Physics of Plasmas*, 25(2):023103, 2018. doi: 10.1063/1.5003619.

R. Younkin, J. E. Carey, E. Mazur, J. A. Levinson, and C. M. Friend. Infrared absorption by conical silicon microstructures made in a variety of background gases using femtosecond-laser pulses. *Journal of Applied Physics*, 93(5):2626–2629, 2003. doi: 10.1063/1.1545159.

U. Zastrau and E. Förster. Integrated reflectivity measurements of hydrogen phthalate crystals for high-resolution soft x-ray spectroscopy. *Journal of Instrumentation*, 9:P09008, 2014. doi: 10.1088/1748-0221/9/09/P09008.

K. Zeil, S. D. Kraft, A. Jochmann, F. Kroll, W. Jahr, U. Schramm, L. Karsch, J. Pawelke, B. Hidding, and G. Pretzler. Absolute response of Fuji imaging plate detectors to picosecond-electron bunches. *Review of Scientific Instruments*, 81(1):013307, 2010. doi: 10.1063/1.3284524.

D. Zhang and K. Sugioka. Hierarchical microstructures with high spatial frequency laser induced periodic surface structures possessing different orientations created by femtosecond laser ablation of silicon in liquids. *Opto-Electronic Advances*, 2(3):190002, 2019. doi: 10.29026/oea.2019.190002.

J.-H. Zhao, X.-B. Li, Q.-D. Chen, Z.-G. Chen, and H.-B. Sun. Ultrafast laser-induced black silicon, from micro-nanostructuring, infrared absorption mechanism, to high performance detecting devices. *Materials Today Nano*, 11:100078, 2020. doi: 10.1016/j.mtnano.2020.100078.

Z. Zhao, L. Cao, L. Cao, J. Wang, W. Huang, W. Jiang, Y. He, Y. Wu, B. Zhu, K. Dong, Y. Ding, B. Zhang, Y. Gu, M. Y. Yu, and X. T. He. Acceleration and guiding of fast electrons by a nanobrush target. *Physics of Plasmas*, 17(12):123108, 2010. doi: 10.1063/1.3507292.

J.-T. Zhu, Y.-F. Shen, W. Li, X. Chen, G. Yin, D.-Y. Chen, and L. Zhao. Effect of polarization on femtosecond laser pulses structuring silicon surface. *Applied Surface Science*, 252(8):2752–2756, 2006. doi: 10.1016/j.apsusc.2005.04.048.

J. F. Ziegler, M. D. Ziegler, and J. P. Biersack. SRIM – The stopping and range of ions in matter. *Nuclear Instruments and Methods in Physics Research Section B: Beam Interactions with Materials and Atoms*, 268(11-12):1818–1823, 2010. doi: 10.1016/j.nimb.2010.02.091.

C. Ziener, P. S. Foster, E. J. Divall, C. J. Hooker, M. H. R. Hutchinson, A. J. Langley, and D. Neely. Specular reflectivity of plasma mirrors as a function of intensity, pulse duration, and angle of incidence. *Journal of Applied Physics*, 93(1):768–770, 2003. doi: 10.1063/1.1525062.

M. Zimmer, S. Scheuren, T. Ebert, G. Schaumann, B. Schmitz, J. Hornung, V. Bagnoud, C. Rödel, and M. Roth. Analysis of laser-proton acceleration experiments for development of empirical scaling laws. *Physical Review E*, 104(4):045210, 2021. doi: 10.1103/PhysRevE.104.045210.

Acknowledgments

Abschließend möchte ich all den geschätzten Menschen danken, die mich während meiner Promotion begleitet und unterstützt haben. Ohne sie wäre meine Arbeit in dieser Form nicht möglich und mein Alltag wesentlich anstrengender gewesen.

Meinem Doktorvater, Prof. Markus Roth, möchte ich für das Ermöglichen dieser Arbeit danken. Die vermittelte Begeisterung für unser Forschungsfeld sowie die Vielfältigkeit des Projekts, von täglicher Laborarbeit, zu Simulationen, zu experimentellen Kampagnen in aller Welt bei stets ermunterter Gestaltungsfreiheit haben die vergangenen Jahre spannend und interessant gemacht.

Des Weiteren möchte ich mich bei Herrn Prof. Oliver Boine-Frankenheim für seine Unterstützung des Projekts sowie seine Bereitschaft, meine Dissertation als Korreferent zu begutachten, bedanken. Ebenso danke ich den Professoren Robert Roth und Thomas Walther für ihr Mitwirken an meinem Promotionsverfahren als Prüfer.

Ein nicht minder großer Dank geht an Gabriel Schaumann und Torsten Abel, ohne die ich in technischen Fragen, von Targetbau zu Lasersystemen, deutlich häufiger an meine Grenzen gestoßen wäre. Die damit einhergehenden Gespräche, Kaffeepausen sowie die tägliche Zusammenarbeit haben euch zu einem nicht wegzudenkenden Teil meines Alltags gemacht.

Desweiteren möchte ich meinen beiden Weggefährten Markus Hesse und Steffen Sander herzlich danken. In euch habe ich nicht nur zuverlässige Kollegen, sondern auch gute Freunde gefunden. Dienstreisen nach England, Spanien und in die USA wären ohne euch nur halb so schön, die mittäglichen Kaffeepausen nur halb so unterhaltsam und die motivierenden morgendlichen Calls überhaupt nicht vorhanden gewesen.

Ein weiterer Dank geht an „meine“ Studenten Christoph Bläser, René Heber, Sarah Grimm und Matthias Brönner, die meine Vorstellungen an die von Ihnen bearbeiteten Projekte nicht nur erfüllt, sondern in allen Fällen übertroffen haben. Außerdem danken möchte ich Nico Neumann, der mir mit seiner Arbeit und durch die Betreuung meiner Masterarbeit die idealen Startbedingungen für dieses Projekt bereitet hat. Auch Alexandra Tebartz sei an dieser Stelle herzlich gedankt, die mich als Bachelor-Küken mit der Gruppe vertraut gemacht und meine Arbeit bis zuletzt durch Anmerkungen unterstützt hat. Einer weiteren Kollegin und Freundin, Franziska Treffert, möchte ich an dieser Stelle ebenfalls für Ihre Zeit und Unterstützung aus der Ferne danken. Allen anderen Kollegen meiner Arbeitsgruppe gebührt auch ein großes Dankeschön. Ihr habt stets dafür gesorgt, dass die gemeinsame Zeit im Büro, im Labor und in anderen Ländern in guter Erinnerung bleiben wird.

Ebenso möchte ich Johannes Hornung, Marc Zimmer, Anna Tauschwitz, Benedikt Schmitz und Johannes Bieker danken, die für Simulationen, Experimente und Reinraumarbeiten durchgehend wertvolle Ansprechpartner gewesen sind. Ihr habt meine Arbeit nicht nur fachlich, sondern auch menschlich wesentlich bereichert.

Eine experimentelle Arbeit in diesem Umfang wäre ohne die Teams der beteiligten Werkstätten und Laser-Einrichtungen nicht möglich gewesen. Daher möchte ich sowohl den elektrischen und feinmechanischen

Werkstätten des IKP, sowie dem PHELIX-Team danken. Hier sei insbesondere Diana Lang ein Dankeschön ausgesprochen, die sich während meiner gesamten Promotionszeit wie selbstverständlich um sämtliche GSI-bezogenen Formalien gekümmert hat. Des Weiteren danke ich unseren Partnern am LLE in Rochester. Ohne das gesamte OmegaEP Team sowie das dortige Targetlabor wären die in dieser Arbeit präsentierten Experimente nicht möglich gewesen. Persönlich danken möchte ich hier Christian Stöckl, der uns nicht nur Teil seiner Kampagne hat werden lassen, sondern auch fachlich stets mit Zeit und Rat zur Verfügung stand.

Sowohl die Darmstädter Exzellenz-Graduiertenschule für Energiewissenschaft und Energietechnik als auch der LOEWE-Schwerpunkt Nukleare Photonik haben mein Projekt finanziell ermöglicht. Beide Bereiche haben mich durch ihre Mitglieder aber auch fachlich unterstützt und insbesondere Tanja Drobek möchte ich herzlich für den Austausch und ihre Zeit danken.

Ohne Vincent, Flo, Flo, Verena, und Katha wären die letzten Jahre nur halb so schön gewesen. Ob Freitags-, Samstags- oder Sonntagsfrühstück, Grillabende, Spaziergänge, Laufrunden, Rückentraining oder Nordseeluft, ihr habt stets für einen unbedingt notwendigen Ausgleich gesorgt. Dass wir uns im ersten Semester gefunden haben, war eine der glücklichsten Darmstädter Begebenheiten.

Nicht weniger herzlich möchte ich meiner Familie danken, die durchgehend für mich da war. Ob durch Besuche, Telefonate oder Päckchen, ich weiß, dass ich mich immer auf euch verlassen kann. Vielen Dank für diese Rückendeckung.

Der letzte und größte Dank geht an Sebastian Dehe, der seit über einem Jahrzehnt an meiner Seite steht und ohne den die letzten Jahre in dieser Art nicht möglich gewesen wären. Manche Dinge lassen sich nicht angemessen in Worte fassen, und so sei hier nur gesagt, dass du jeden Tag zu etwas Besonderem für mich machst.

A. Appendix

A.1. Thomson parabola

The energy dispersion relation in the magnetic field of a Thomson parabola can be determined using the ion charge q, the magnetic field strength B, the length of the magnetic field L_B, the drift length d_B between magnet and detector, the velocity of the ion in the direction of travel v_z and the ion mass m_ion. Using the following relations (Alejo et al., 2016)

$$b = L_\mathrm{B} \cdot \left(\frac{L_\mathrm{B}}{2} + d_\mathrm{B} \right), \tag{A.1}$$

$$\gamma v_z = c\sqrt{\gamma^2 - 1}, \tag{A.2}$$

$$\mathcal{E}_\mathrm{i,kin} = m_\mathrm{i}\gamma c^2 - m_\mathrm{i}c^2, \text{ and} \tag{A.3}$$

$$c1 = \frac{qBb}{\sqrt{2m_\mathrm{i}}}, \tag{A.4}$$

the dispersion relation follows from

$$\Delta y = \frac{qBL_\mathrm{B}}{\gamma m_\mathrm{i} v} \left(\frac{L_\mathrm{B}}{2} + d_\mathrm{B} \right) \tag{A.5}$$

$$\Delta y = \frac{qBb}{m_\mathrm{i}c\sqrt{\gamma^2 - 1}} \tag{A.6}$$

$$\Delta y = \frac{1}{\sqrt{\left(\frac{\mathcal{E}_\mathrm{i,kin}}{m_\mathrm{i}c^2} + 1\right)^2 - 1}} \frac{qBb}{m_\mathrm{i}c} \tag{A.7}$$

$$\sqrt{\left(\frac{\mathcal{E}_\mathrm{i,kin}}{m_\mathrm{i}c^2} + 1\right)^2 - 1} = \frac{qBb}{m_\mathrm{i}c\Delta y} \tag{A.8}$$

$$\left(\frac{\mathcal{E}_\mathrm{i,kin}}{m_\mathrm{i}c^2} + 1\right)^2 = \left(\frac{qBb}{m_\mathrm{i}c\Delta y}\right)^2 + 1 \tag{A.9}$$

$$\frac{\mathcal{E}_\mathrm{i,kin}}{m_\mathrm{i}c^2} = \sqrt{\left(\frac{qBb}{m_\mathrm{i}c\Delta y}\right)^2 + 1} - 1 \tag{A.10}$$

$$\mathcal{E}_\mathrm{i,kin} = \sqrt{\left(\frac{qBb}{m_\mathrm{i}c\Delta y} m_\mathrm{i}c^2\right)^2 + (m_\mathrm{i}c^2)^2} - m_\mathrm{i}c^2 \tag{A.11}$$

$$\mathcal{E}_\mathrm{i,kin} = \sqrt{\left(\frac{qBbc}{\Delta y}\right)^2 + (m_\mathrm{i}c^2)^2} - m_\mathrm{i}c^2\,. \tag{A.12}$$

A.2. Image plate fading functions

The spontaneous decay of the meta-stable states in the active layer of an image plate can be corrected by utilizing fading functions. These function depend on the IP type, the radiation type, the scanner and the ambient temperature. Figure A.1 shows a selection of such fading functions that are available in literature.

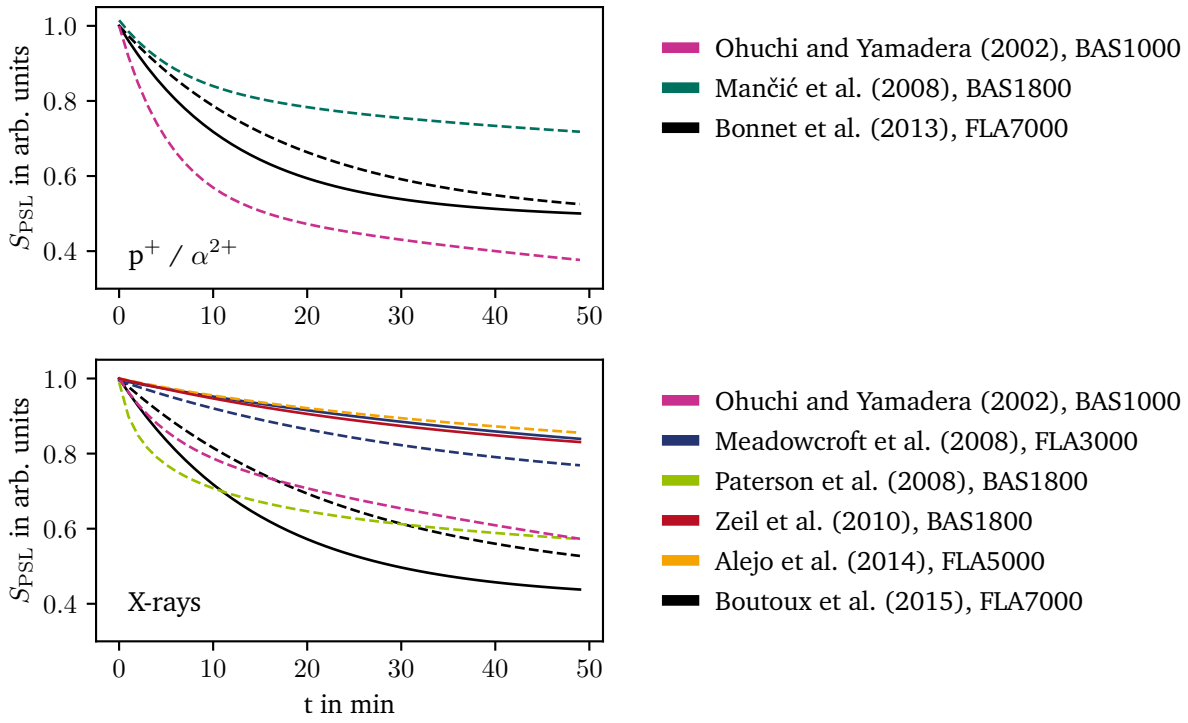

Figure A.1.: Overview of fading functions found in literature for protons and alpha particles (top) as well as X-rays (bottom) as a function of the time t between irradiation and scanning. The signal S_{PSL} is normalized, the continuous lines are for *BAS-SR* and the dashed lines for *BAS-TR* image plates. The legend includes the type of scanner used.

A.3. Parameter studies on titanium

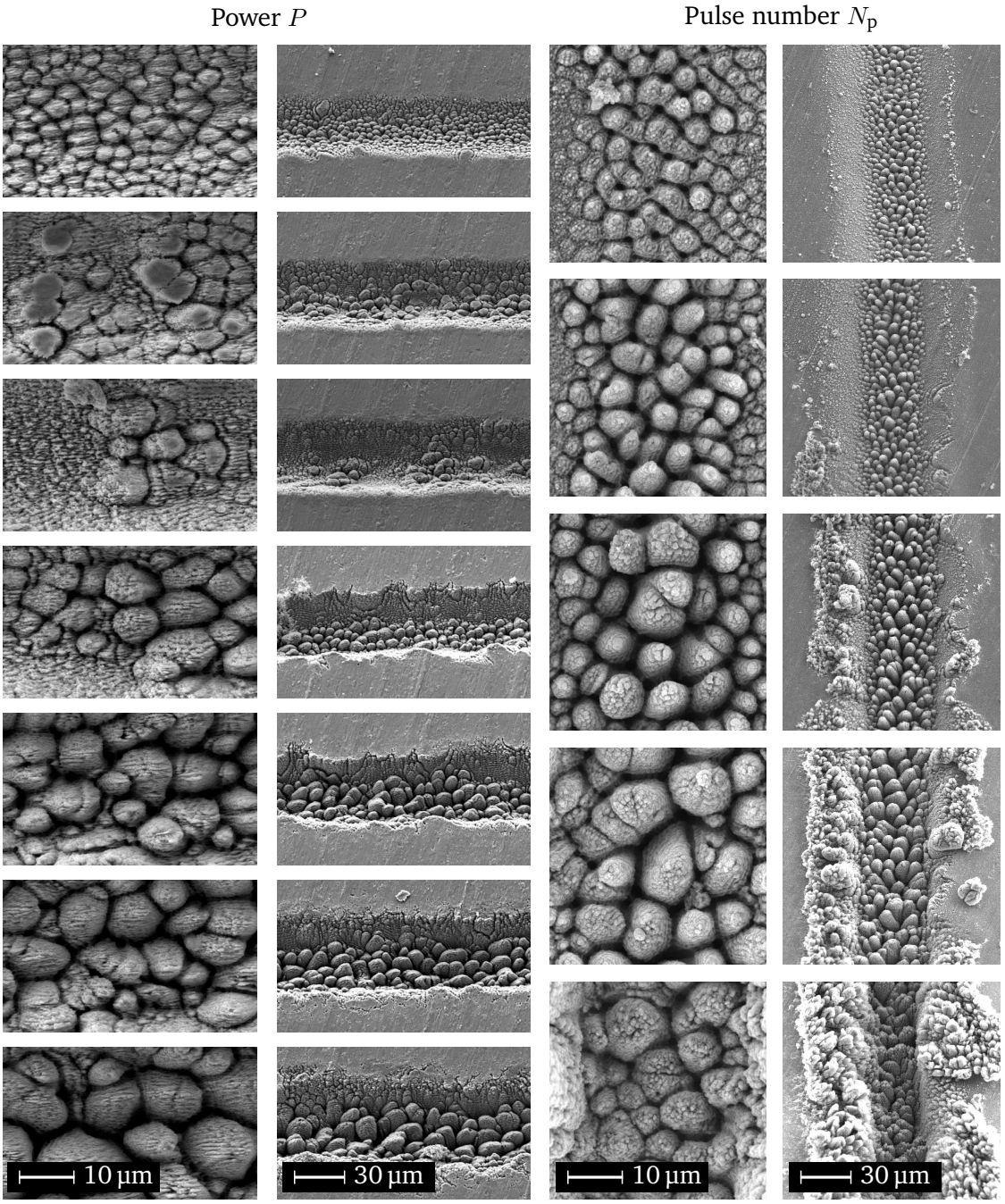

Figure A.2.: SEM images of titanium microstructures fabricated in a 10 mbar vacuum. Columns (a) and (b) show the structure formation with increasing power, namely 35 mW, 56 mW, 74 mW, 104 mW, 128 mW, 150 mW and 205 mW from top to bottom image. The pulse number was 500 for all samples. Columns (c) and (d) show the influence of the number of pulses N_p. Here, the power was kept constant at 125 mW while the pulse number was 250, 310, 420, 625 and 1250 from top to bottom frame. The images of column (a) and (c) were acquired with a view from top, while the samples were tilted by 30° for the recordings displayed in column (b) and (d). Each scale bar applies to the whole column.

A.4. Input file for PIC simulations with EPOCH

```
# SILICON TARGET WITH COPPER AND PROTON LAYER
# corresponds to 0 deg target of experimental PHELIX campaign
# laser: 500 fs (15 deg), electrons: 7 keV, 50 n_c, cell size: (8.4e-9)m^2

begin:control
  nx = 10714 # number of gridpoints in x
  ny = 9523 # number of gridpoints in y
  npart = nx * ny * 20 # number of macro-particles
  t_end = 3000 * femto # final time of simulation

  # size of domain
  x_min = -60 * micron # area of laser propagation and target
  x_max = 30 * micron # area of contamination layer and particle acceleration
  y_min = -40 * micron # so that laser focus fits inside and ...
  y_max = - y_min # ... boundaries are far enough away

  # faster computing on cluster
  nprocx = 1
  nprocy = 1024
  simplify_deck = T # for faster computing
  stdout_frequency = 100
  print_eta_string = T
end:control

begin:boundaries
  bc_x_min = simple_laser
  bc_x_max = simple_outflow
  bc_y_min_field = simple_outflow
  bc_y_min_particle =simple_outflow
  bc_y_max_field = simple_outflow
  bc_y_max_particle = simple_outflow
end:boundaries

begin:constant
  # general
  scale = 1 # 0: flat, 1: cone, ]0,1[: scaled cone
  tilted = 1 # 0: false, 1: true

  # laser parameters
  thetaphase = pi/180 * 15 # laser incidence angle
  lambda = 1.053 * micron # laser wavelength
  omega = 2 * pi * c / lambda # angular frequency
  starttime_laser = 0 * femto

  # target parameters
  den_cone = 50.0 * critical(omega) # density of target
  tiltangle = pi/180 * 15  # angle from needleflank to surface normal
  tiltdir = -1
  H_K = 25 * micron / sin(pi/2 - pi/180 *15) * scale # (scaled) height of cones
  b_K = 6 * micron * scale # (scaled) maximum diameter of cones
  d_G = 5 * micron # directly defined base thickness
  d_C = 5000 * nano # thickness of Cu coating layer

  # derived values
  x_shifted = x + d_C # shift x coord. to place Cu layer between Si and p+ layer
  dangle = pi/180 * 15 # angle of needle bisector to base
  tilt = if(x_shifted lt (-d_G), (x_shifted + d_G) * tan(dangle) / b_K ,0)
```

```
  h_K = if(tilted eq 0, H_K, H_K * sin(pi/2 - dangle) # derived height
  yt = (y - y_min) / b_K + tiltdir * tilt * tilted -4 *micron / b_K# coord.
    transformation
  r_K = 1/2 + (x_shifted + d_G) / (2 * h_K) # x dependent radius on an arbitraty position
  y_K = sqrt((yt - 1/2 - floor(yt))^2) # floor is used for generating multiple cones

  # exponential decay of cones
  a_exp = 0.8 * micron # length of exponential decay (in x direction)
  flanc = 0.334419 * micron # original thickness of the expanded region
  h_K_exp = h_K - flanc - 2* h_K * y_K
  rho_exp = den_cone * (exp(1/a_exp * (x_shifted + d_G) + 1/a_exp * (h_K_exp + a_exp))
    -1) / (exp(1) -1)

  # exponential decay of base
  rho_exp_base = den_cone * (exp(-1/a_exp * abs(x_shifted) + 1 + (d_G - flanc) / a_exp)
    -1) / (exp(1) -1)

  # contamination layer
  d_pro = if((abs(x_min) + abs(x_max)) / nx gt 1 * nano, 5 * (abs(x_min) + abs(x_max)) /
    nx , 5 * nano)
  rho_pro = den_cone * (exp(-1/d_pro * x + 1) -1) / (exp(1) -1)
  r = sqrt(y^2)

  # laser incidence angle
  ydelta = tan(thetaphase) * (- x_min -d_G -d_C) # laser hits target at y=0 at x=-d_G-d_C
  rdelta = sqrt((y+ydelta)^2)
end:constant

begin:species
  name = si_electron
  charge = -1.0
  mass = 1.0
  frac = 0.225
  density_max = den_cone
  temp_ev = 7000

  # base
  density = if((x_shifted gt (- d_G)) and ((x_shifted lt 0) or (x_shifted eq 0)),
    den_cone, 0.0)

  # cones
  density = if((scale gt 0) and (x_shifted lt (- d_G / 2)) and (y_K lt r_K), den_cone,
    density(si_electron))

  # exponentially decaying cones
  density = if ((scale gt 0) and (x_shifted lt (- d_G)), rho_exp, density(si_electron))

  # exponentially decaying base (if scale = 0)
  density = if ((scale eq 0) and (x_shifted gt (- d_G - a_exp + flanc)) and (x_shifted lt
     (- d_G + flanc)), rho_exp_base, density(si_electron))
end:species

begin:species
  name = si_ion
  charge = 14.0
  mass = 51181.8
  frac = 0.225
  temp_ev = 100
  density_max = 1/14 * den_cone
  density = 1/14 * density(si_electron)
```

```
end:species

begin:species
  name = cu_electron
  charge = -1.0
  mass = 1.0
  frac = 0.225
  density_max = den_cone
  temp_ev = 7000
  density = if((x gt (- d_C)) and ((x lt 0) or (x eq 0)), den_cone, 0.0) # base
end:species

begin:species
  name = cu_ion
  charge = 29.0
  mass = 115764
  frac = 0.225
  temp_ev = 100
  density_max = 1/29 * den_cone
  density = 1/29 * density(cu_electron)
end:species

begin:species
  name = protonProtonlayer
  charge = 1.0
  mass = 1836.2
  frac = 0.05
  temp_ev = 100
  density = if ((x lt d_pro) and ((x gt 0) or (x eq 0)), rho_pro, 0) # exp. decaying
    layer
end:species

begin:species
  name = electronProtonlayer
  charge = -1.0
  mass = 1.0
  frac = 0.05
  temp_ev = 7000
  density = density(protonProtonlayer)
end:species

begin:laser # simulation of PHELIX
  boundary = x_min
  intensity_w_cm2 = 1e+20
  lambda = lambda * cos(thetaphase)
  t_start = starttime_laser
  t_end = 1500 * femto + starttime_laser
  profile = gauss(rdelta, 0.0, 10 * micron / (2 * sqrt(loge(2))))
  t_profile = gauss(time, (500.0e-15 + 150.0e-15 + starttime_laser), 500.0e-15 / (2 *
    sqrt(loge(2))))
  phase = - 2 * pi * y * sin(thetaphase)/ lambda
end:laser

begin:output
  dt_snapshot = 100 * femto # number of timesteps between output dumps
  restart_dump_every = 5
  force_final_to_be_restartable = T

  # properties at particle positions
  particles = always
```

```
  particle_weight = always
  particle_energy = always
  ejected_particles = restart
  px = always
  py = always
  pz = always
  vx = restart
  vy = restart
  vz = restart
  id = always

  # properties on grid
  grid = always
  ex = always
  ey = always
  ez = always
  bx = always
  by = always
  bz = always
  jx = restart
  jy = restart
  jz = restart

  # derived variables
  ekbar = always
  charge_density = always
  number_density = always + species
  temperature = always + species

  # extended io
  distribution_functions = always
end:output
```

A.5. Target geometry optimization for individual parameters

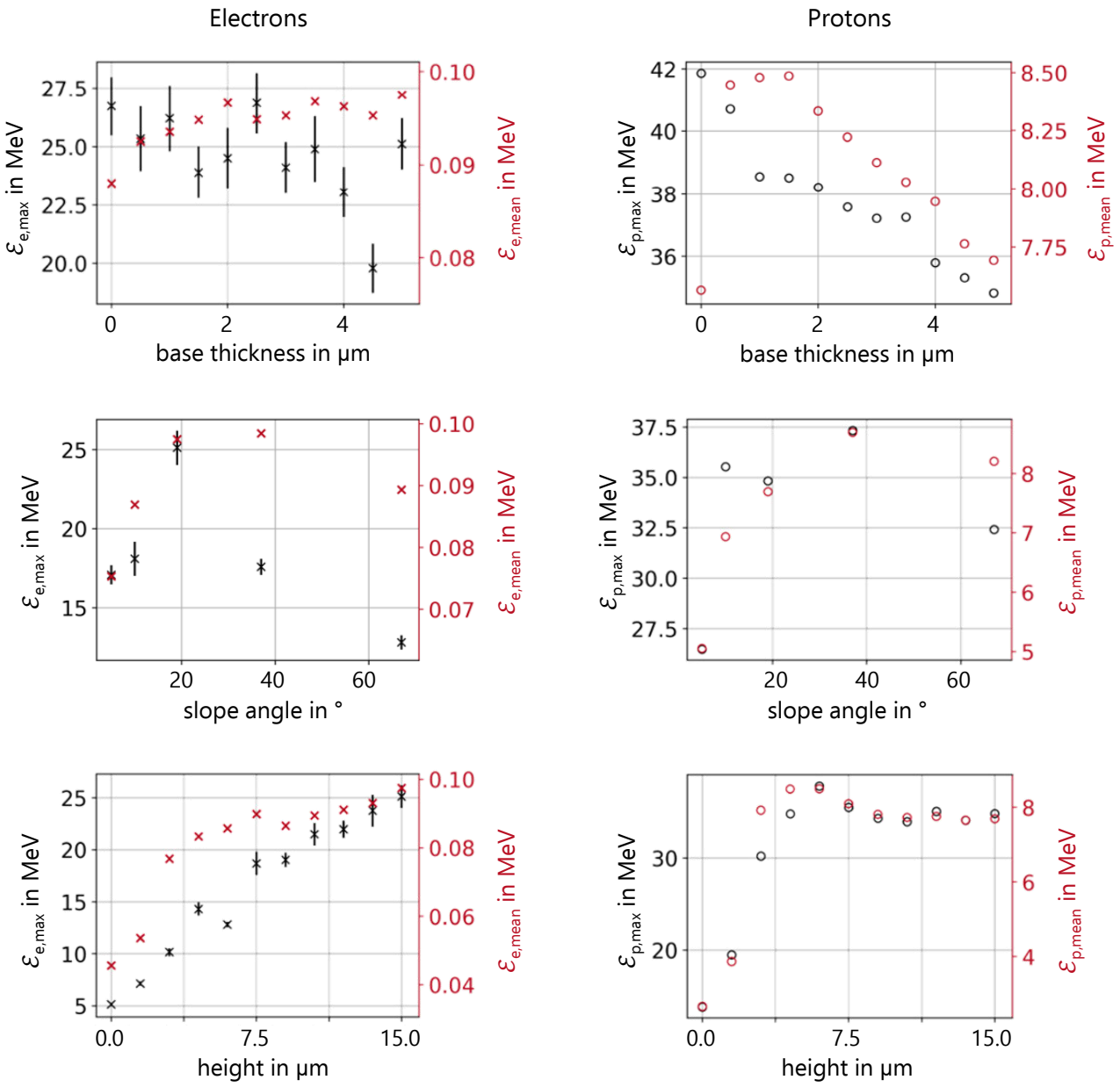

Figure A.3.: Simulated maximum (black) and mean (red) energies of electrons (left column) and protons (right column) for the individually studied target geometry parameters, namely the base thickness b (top row), the slope angle β (middle row) and the height h of the spikes (bottom row), for which the slope angle was kept constant. For a definition of the parameters and the values selected as optima see Fig. 5.25 and Section 5.2.4. Adapted from Grimm (2020) (Fig. 5.7, Fig. 5.9 and Fig. 5.11) with kind permission from Sarah Grimm.